

FLUORESCENCE STUDIES OF AMINE-SUBSTITUTED AZAANTHRACENE METAL COMPLEXES

Dissertation

zur Erlangung des mathematisch-naturwissenschaftlichen Doktorgrades

„Doctor rerum naturalium“

der Georg-August-Universität Göttingen

im Promotionsprogramm Chemie

der Georg-August University School of Science (GAUSS)



vorgelegt von **Arne Visscher**

aus Burgwedel

Göttingen, 2016

Betreuungsausschuss

Prof. Dr. Dietmar Stalke, Institut für Anorganische Chemie

Prof. Dr. Franc Meyer, Institut für Anorganische Chemie

Mitglieder der Prüfungskommission

Referent: Prof. Dr. Dietmar Stalke

Korreferent: Prof. Dr. Franc Meyer

weitere Mitglieder der Prüfungskommission

Prof. Dr. Ricardo A. Mata, Institut für Physikalische Chemie

Prof. Dr. Konrad Koszinowski, Institut für Organische und Biomolekulare Chemie

Prof. Dr. Thomas Waitz, Institut für Anorganische Chemie

Dr. Michael John, Institut für Organische und Biomolekulare Chemie

Tag der mündlichen Prüfung: 17.06.2016

DANKSAGUNG

Mein erster Dank gilt meinem Promotionsbetreuer Prof. Dr. Dietmar Stalke für die langjährige Unterstützung dieser Arbeit. Es war spannend, das im Arbeitskreis neue Thema der Acridin-Fluorophore frei erarbeiten zu dürfen und somit eine Alternative für das schon ausgiebig untersuchte Anthracen aufzeigen zu können.

Herrn Prof. Dr. Franc Meyer möchte ich für die freundliche Übernahme des Korreferats danken. Den weiteren Mitgliedern der Prüfungskommission danke ich ebenfalls für die Zeit, die sie sich genommen haben, meine Arbeit zu bewerten.

Meinen beiden langjährigen Labormitstreitern, David Dauer und Sebastian Wandtke, danke ich für die sehr angenehme Arbeitsatmosphäre und die vielen Gespräche auch außerhalb des Chemieuniversums. Dabei danke ich Sebastian für die immerwährenden Motivationsschübe, stets pünktlich im Labor zu erscheinen und David für die gegenseitige Unterstützung, die vorliegenden Ergebnisse auch endlich mal zu Papier zu bringen.

Meinen AC-F Praktikanten Grigory Shevchenko, Benjamin Gerdes, Michaela Bauer, Sayaka Shoji und Matheus Bukala danke ich für die synthetische Unterstützung im Labor.

Damit diese Dissertation verständlich und somit druckreif werden konnte, haben Lennard Krause, Thomas Niklas, Alexander Paesch und Timo Schillmöller ganze Arbeit geleistet. Vor allem Lennard und Thomas hatten scheinbar sehr viel Spaß den Verbrauch an roten Stiften bei Frau Gaugel zu erhöhen. Danke dafür!

Die Aufnahme von wirklich interessanten NMR Spektren war nur möglich, mit der fleißigen Hilfe von unserem NMR-Experten Sebastian Bachmann. Danke für die vielen abendlichen Messungen sowie auch für die Erklärung der Ergebnisse. Christoph Schnegelsberg danke ich für die superempfindlichen ESI-TOF Messungen meiner kaum löslichen Produkte. Bei Thomas Niklas bedanke ich mich für die wesentlich besseren ORCA-Rechnungen, so dass mir die Benutzung vom minütlich abstürzenden Avogadro weitestgehend erspart blieb.

Weiterhin bedanken möchte ich mich bei Thorsten Teuteberg und Ricardo Mata, die für mich sehr komplexe Rechnungen zu meinem „Super-Sensor“ durchgeführt haben. Deren Ergebnisse haben erheblich zum Verständnis der Acridin-Metall-Wechselwirkungen beigetragen. Erfreulicherweise hat Thorsten mir die Wechselwirkungen nicht nur anhand von Tabellen erklärt, sondern hat auch anschauliche Grafiken dazu angefertigt.

Was wäre unser Arbeitskreis ohne die vier durchweg laufenden Diffraktometer? Damit dies zumindest der Fall war, wenn meine Kristalle rotierten, möchte ich mich bei den fleißigen Maschinenschraubern bedanken. Besonders hervorzuheben sind dabei Felix Engelhardt und Lennard Krause, die zusammen mit Reent Michel auch meinen vielen kristallographischen Fragen standgehalten haben. Und wenn selbst deren Verfeinerungs-Knowhow irgendwann mal zu Ende ging, so konnte ich sicher sein, dass Regine Herbst-Irmer auch die kleinste Restelektronendichte noch zu verbessern wusste.

Dass ich diesem Arbeitskreis so lange treu geblieben bin, liegt unter anderem auch an der super Atmosphäre in dieser Gruppe. Immer wieder motivierend waren die vielen Kuchen mit noch mehr Kaffee, die sportlichen Einlagen am Kickertisch sowie auch das eine oder andere Feierabendbier

in Peters Pinte. In diesen kurz gehaltenen Pausen konnte man überaus wichtige Diskussionen über interdisziplinäre Themen führen.

Während des langjährigen Studiums wurden aus Kommilitonen schnell gute Freunde. Danke für die gemeinsame Zeit, die wir in Göttingen verbracht haben. Ich hoffe, dass diese Freundschaften auch noch lange nach der Uni-Ära anhalten werden.

Einen besonderen Dank möchte ich meinen Eltern aussprechen, die mich immer in jeder Hinsicht unterstützt haben. Danke, dass ihr so seid, wie ihr seid.

Zuletzt, und daher von größtem Stellenwert, danke ich meiner Frau Isis-Helena. Ich danke dir für deine Geduld, deine Unterstützung und deine Liebe. Und dafür, dass du mich geheiratet hast. Der Titel Ehemann macht einen weitaus glücklicher als der, den ich durch diese Arbeit erhalten werde.

Für meine Eltern

*„Alle sagten: Das geht nicht.
Dann kam einer, der wusste das nicht und hat's gemacht.“*

- o. V.

TABLE OF CONTENTS

1. Introduction	1
1.1 Photoluminescence	1
1.1.1 Photoinduced electron transfer	3
1.1.2 The fluorophore azaanthracene.....	5
1.1.3 The detection of metal ions using acridine systems.....	9
1.1.4 Intramolecular charge transfer (ICT).....	13
1.2 Scope	14
2. Results and discussion	17
2.1 Investigations of 2-azaanthracenes	17
2.1.1 5,10-Dimethyl-2-azaanthracene (3).....	17
2.1.2 Investigations to the bromination of 5,10-dimethyl-2-azaanthracene (3).....	19
2.2 Potential molecular sensors based on acridine	20
2.2.1 9-Methylacridine (4).....	20
2.2.2 9-(Bromomethylene)acridine (5)	22
2.2.3 Attempts to 4-aminoacridine	23
2.2.4 4,5-Bis(bromomethylene)acridine (8) and 4,5-bis(bromomethylene)-9-methyl- acridine (9).....	28
2.2.5 4,5-Bis(di(2'-methylthiobenzyl)aminemethylene)-9-methylacridine (10).....	32
2.2.6 Luminescence procedure and sample preparation	35
2.2.7 Luminescence properties of 4,5-bis(di(2'-methylthiobenzyl)aminemethylene)- 9-methylacridine (10)	37
2.2.8 4,5-Bis(<i>N,N',N'</i> -trimethylethylenediaminemethylene)acridine (11) and its 9- methyl derivative (12).....	41
2.2.9 Luminescence properties of 4,5-bis(<i>N,N',N'</i> -trimethylethylenediamine- methylene)acridine (11).....	44
2.2.10 4,5-Bis(<i>N</i> -methyl- <i>N</i> -phenylaminemethylene)acridine (13).....	52
2.2.11 Luminescence properties of 4,5-bis(<i>N</i> -methyl- <i>N</i> -phenylaminemethylene)- acridine (13).....	54
2.2.12 4,5-Bis(<i>N</i> -methyl- <i>N</i> -phenylaminemethylene)acridine hydrochloride (14).....	60
2.2.13 4,5-Bis(dimethylaminemethylene)acridine (15).....	64
2.2.14 Luminescence properties of 4,5-bis(dimethylaminemethylene)acridine (15)	64
2.2.15 4,5-Bis(dimethylaminemethylene)acridine hydrochloride (16).....	74
2.3 Investigations of metal complexes of 15	76
2.3.1 4,5-Bis(dimethylaminemethylene)acridine dibromido zinc(II) (17), dibromido cadmium(II) (19), and tetrakis(μ -acetate) bis(acetate) zinc(II) (20).....	76
2.3.2 Solid state analysis by X-ray diffraction.....	77
2.3.3 Computational studies on compounds 17–19	80
2.3.4 Investigation of the metal complexes in solution	83
3. Conclusion and outlook	89

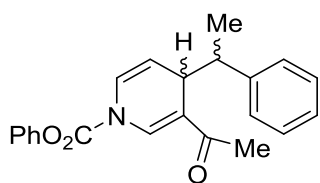
4. Experimental settings	93
4.1 General working procedure	93
4.2 Applied analytical methods	93
4.2.1 Computational studies	93
4.2.2 Elemental analysis	93
4.2.3 Fluorescence spectroscopy	93
4.2.4 Mass spectrometry	94
4.2.5 NMR spectroscopy	94
4.2.6 UV/Vis spectroscopy	95
4.3 Synthesis and characterisation	95
4.3.1 Synthesis of 1-phenoxy carbonyl-3-acetyl-4-(phenylethyl)-1,4-dihydro- pyridine (1)	95
4.3.2 Synthesis of 3-acetyl-4-(phenylethyl)pyridine (2)	96
4.3.3 Synthesis of 5,10-dimethyl-2-azaanthracene (3)	97
4.3.4 Synthesis of 9-methylacridine (4)	97
4.3.5 Synthesis of 9-(bromomethylene)acridine (5)	98
4.3.6 Synthesis of 2-bis(<i>p</i> -nitrobenzenesulfonyl)aminodiphenylamine (6)	99
4.3.7 Synthesis of 2-nitrodiphenylamine (7)	99
4.3.8 Synthesis of 4,5-bis(bromomethylene)acridine (8)	100
4.3.9 Synthesis of 4,5-bis(bromomethylene)-9-methylacridine (9)	101
4.3.10 Synthesis of 4,5-bis(di(2'-methylthiobenzyl)aminemethylene)-9-methyl- acridine (10)	101
4.3.11 Synthesis of 4,5-bis(<i>N,N',N'</i> -trimethylethylenediaminemethylene)acridine (11)	102
4.3.12 Synthesis of 4,5-bis(<i>N,N',N'</i> -trimethylethylenediaminemethylene)-9-methyl- acridine (12)	103
4.3.13 Synthesis of 4,5-bis(<i>N</i> -methyl- <i>N</i> -phenylaminemethylene)acridine (13)	104
4.3.14 Synthesis of 4,5-bis(<i>N</i> -methyl- <i>N</i> -phenylaminemethylene)acridine hydrochloride (14)	104
4.3.15 Synthesis of 4,5-bis(dimethylaminemethylene)acridine (15)	105
4.3.16 Synthesis of 4,5-bis(dimethylaminemethylene)acridine hydrochloride (16)	106
4.3.17 Synthesis of 4,5-bis(dimethylaminemethylene)acridine dibromido zinc(II) (17)	107
4.3.18 Synthesis of 4,5-bis(dimethylaminemethylene)acridine dibromido cadmium(II) (19)	108
4.3.19 Synthesis of 4,5-bis(dimethylaminemethylene)acridine tetrakis(μ -acetate) bis(acetate) zinc(II) (20)	109
5. Crystallographic section	111
5.1 Crystal selection and manipulation	111
5.2 Data collection and processing	111
5.3 Structure solution and refinement	111
5.4 Treatment of disorder	112
5.5 Determined structures	113
5.5.1 4,5-Bis(bromomethylene)-9-methylacridine (9)	113

5.5.2	4,5-Bis(di(2'-methylthiobenzyl)aminemethylene)-9-methylacridine (10).....	114
5.5.3	4,5-Bis(<i>N</i> -methyl- <i>N</i> -phenylaminemethylene)acridine hydrochloride (14).....	115
5.5.4	[(Me ₂ NHCH ₂) ₂ Acr]Cl ₂ ·(MeOH) (16).....	116
5.5.5	[(dmf)ZnBr{(Me ₂ NCH ₂) ₂ Acr}][(dmf)ZnBr ₃] (18).....	117
5.5.6	[CdBr ₂ {(Me ₂ NCH ₂) ₂ Acr}] (19).....	118
5.5.7	[Zn ₃ (μ-OAc) ₄ (OAc) ₂ {(Me ₂ NCH ₂) ₂ Acr}] (20).....	119
5.5.8	[Zn ₂ (μ-OMe) _{1.16} Br _{2.84} {(Me ₂ NCH ₂) ₂ Acr}]·(thf) (21).....	120
5.5.9	[(Me ₂ NHCH ₂) ₂ Acr]Br ₂ ·(MeOH) (22).....	121
6.	Crystal structure determination in collaborations.....	122
6.1	Structures determined for Mykyta Tretiakov (Prof. Dr. H. W. Roesky).....	122
6.1.1	I ₂ S=C[N(2,6- <i>i</i> -Pr ₂ -C ₆ H ₃)CH] ₂ (23).....	122
6.1.2	I ₂ S=C(CH ₂)(CMe ₂)(C ₆ H ₁₀)N-2,6- <i>i</i> -Pr ₂ -C ₆ H ₃ (24).....	123
6.1.3	I ₂ Te=C(CH ₂)(CMe ₂) ₂ N-2,6- <i>i</i> -Pr ₂ -C ₆ H ₃ (25).....	124
6.2	Structures determined for Bastian Milde (Prof. Dr. D. B. Werz).....	125
6.2.1	Dispirane: C ₆ H ₄ CCH ₂ O-(C ₅ H ₄ (CO ₂ Me) ₂) ₂ -C ₁₀ H ₆ CCH ₂ O (26).....	125
6.2.2	Dispirane: C ₁₂ H ₁₂ (CO ₂ Me) ₄ (CH ₂ OC ₆ H ₃ (CO ₂ Me)) ₂ (27).....	126
6.3	Structures determined for Tobias Schneider (Prof. Dr. D. B. Werz).....	127
6.3.1	Spiro[anthracene-9(10 <i>H</i>),1'(3' <i>H</i>)-isobenzofuran]-3'10-dione (28).....	127
6.3.2	10,15-Dihydro-5 <i>H</i> -tribenzo[<i>a,d,g</i>]cyclononen-5-ol (29).....	128
6.4	Structures determined for Matheus Bukala.....	129
6.4.1	[Ph ₂ SP(C ₁₄ H ₈)CH ₂ NH((CH ₂) ₂ OCH ₃) ₂] ⁺ [(thf)ZnBr ₃] ⁻ (30).....	129
6.5	Structures determined for Lianrong Liu.....	130
6.5.1	9,9'-Ethenediylldiacridine (31).....	130
6.5.2	Acridine-10-oxide·2H ₂ O (32).....	131
7.	Supplement.....	133
7.1	Lifetime measurement of 17	133
7.2	NMR spectra.....	133
7.3	Mass spectra.....	136
8.	References.....	139

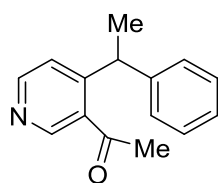
ABBREVIATION INDEX

Acr	acridine	Me	methyl
BMME	bromomethyl methyl ether	MeCN	acetonitrile
		MeOH	methanol
conc.	concentrated	MHz	megahertz
cps	counts per second	mmol	millimole
DCM	dichloromethane	MS	mass spectrometry
dem.	demineralised	NBS	<i>N</i> -bromosuccinimide
DMEDA	<i>N,N</i> -dimethylethylene-diamine	NMR	nuclear magnetic resonance
DMSO	dimethyl sulfoxide	PE	petroleum ether
EA	ethyl acetate	PET	photoinduced electron transfer
EI	electron ionisation		
eq.	equivalent(s)	Ph	phenyl
ESI	electrospray ionisation	ppm	parts per million
Et ₂ O	diethyl ether	<i>R_f</i>	retardation factor
HEPES	4-(2-hydroxyethyl)-1-piperazineethanesulfonic acid	rt	room temperature
		<i>sof</i>	site occupation factor
		THF	tetrahydrofuran
HOMO	highest occupied molecular orbital	TLC	thin layer chromatography
HSAB	hard and soft acids and bases	TOF	time-of-flight
		TrMEDA	<i>N,N,N'</i> -trimethyl-ethylenediamine
<i>I</i>	intensity		
IUPAC	<i>International Union of Pure and Applied Chemistry</i>	λ	wavelength
		λ_{det}	detected wavelength
		λ_{exc}	excitation wavelength
LUMO	lowest unoccupied molecular orbital		
M	molar		
<i>m/z</i>	mass/charge ratio		

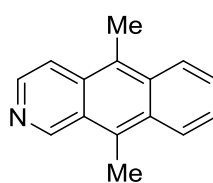
COMPOUND INDEX



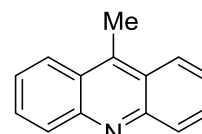
1



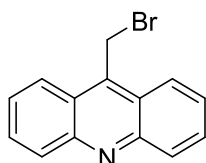
2



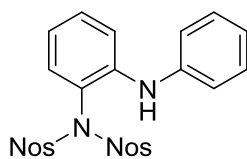
3



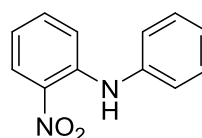
4



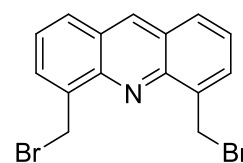
5



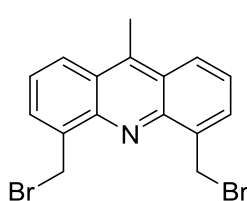
6



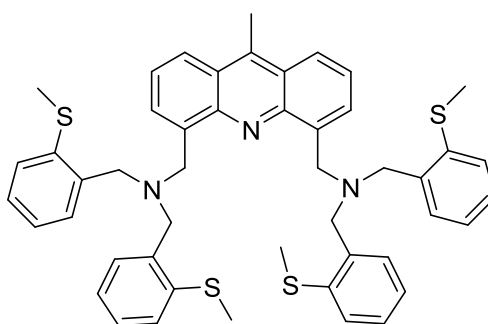
7



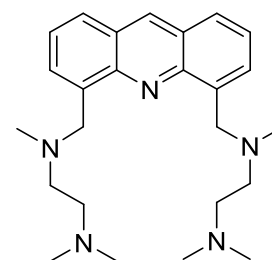
8



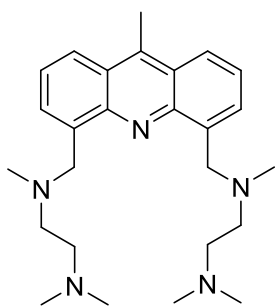
9



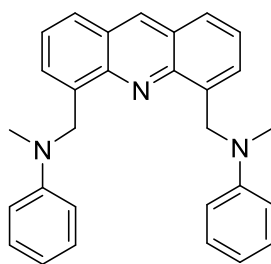
10



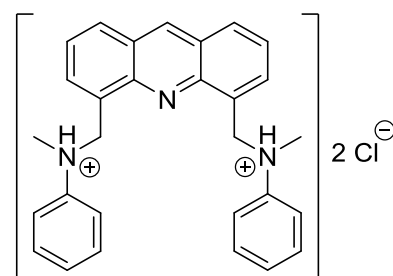
11



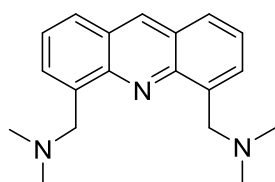
12



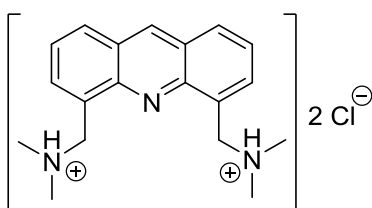
13



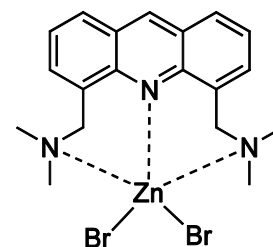
14



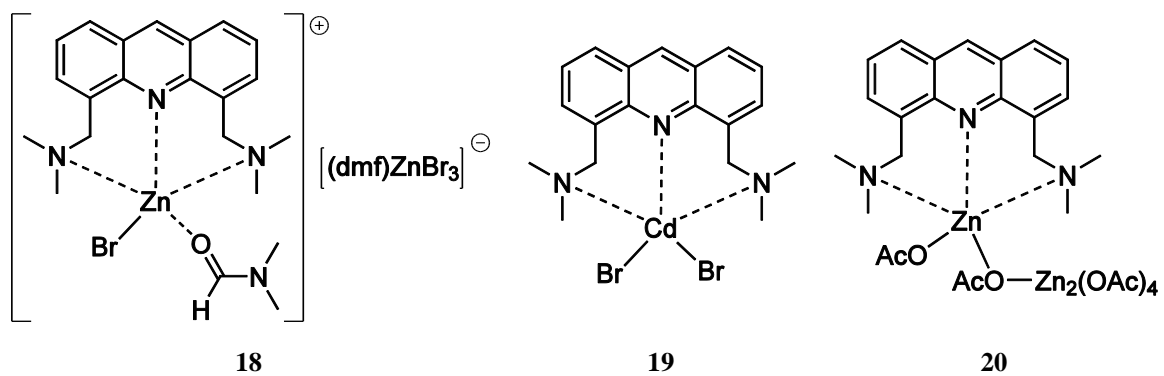
15



16



17



1. INTRODUCTION

1.1 Photoluminescence

The existence of fluorescent and phosphorescent substances has always been a fascinating phenomenon, not only limited to scientists. Luminescent appearances have been reported centuries ago, without having any knowledge about the underlying processes. For instance, in 1565 the Spanish physician and botanist *N. B. Monardes* reported the peculiar blue colour from an infusion of a Mexican wood, later called *Lignum nephriticum*.^[1] He was surprised by the fact that the water was coloured bluish “*though the wood is of white colour*”.^[2] In fact, the chemical evidence for the cause of this fluorescent phenomenon was only published in 2009.^[3] The pioneering physico-chemical investigations of important photoluminescence phenomena were made in the 19th century, namely by *E. Becquerel*, *D. Brewster*, *J. Herschel*, and *G. G. Stokes*. *Brewster* and *Herschel* examined similar substances like chlorophyll and the historically famous quinine sulphate solution.^[4] *Herschel* observed that light may be scattered by particles or dispersed at the surface of solutions similar to prisms. He used the words ‘epipolic dispersion’ which is only a superficial effect,^[4a] whereas *Brewster’s* analysis refuted the surface explanation. On the basis of polarisation measurements, he introduced the ‘internal dispersion’ effect which “*is a new property of light, produced by a peculiar action of certain solid and fluid bodies...*”.^[4b] Both scientists made great discoveries in this new field but they did not figure out the difference in the wavelength of the incident and the resulting light.

At the same time, *Stokes* was also interested in the behaviour of quinine sulphate solutions. He established the term fluorescence in 1852^[5] when he noticed the longer wavelength of the light emitted by the irradiated solution. In further experiments,^[6] he used sunlight with a blue glass filter which selectively transmitted light below 400 nm. This light was absorbed by the quinine solution causing the “*beautiful celestial blue colour*”.^[5] The crucial idea was to observe the solution through a glass filter only transmitting light above 400 nm. Since he could still see the blue colour, he knew that the light emitted at a 90° angle had to be of longer wavelength than the incident light. A schematic illustration of this experiment is depicted in Figure 1.1.

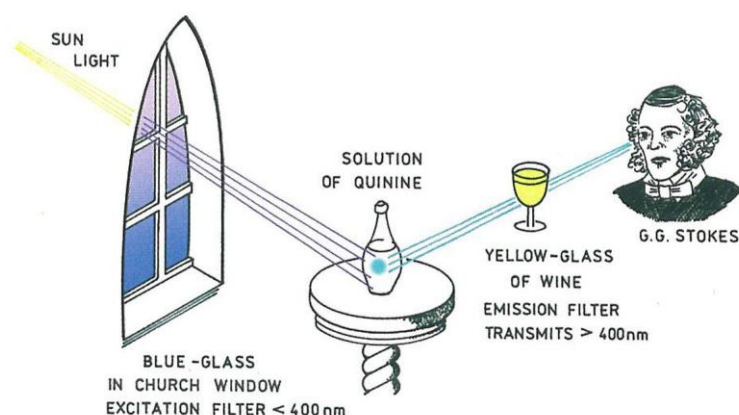


Figure 1.1: Schematic illustration of the experimental setup made by *Stokes*.^[7]

It needs to be mentioned that *Becquerel* first stated this discrepancy in the adjusted and detected wavelength ten years before. He published his observations with calcium sulphide exposed to solar light beyond the violet part of the spectrum.^[8] He coined the term phosphorescence without

making a difference between his observations and those of *Stokes* and stated that both are the same emission phenomenon only with different durations. It took some time until scientists like *A. Jabłoński* contributed to our modern-day understanding of fluorescence and phosphorescence processes.^[9] These phenomena originate from different electronic states which is easily demonstrated with the help of a (modified) *Jablonski* diagram (Figure 1.2).

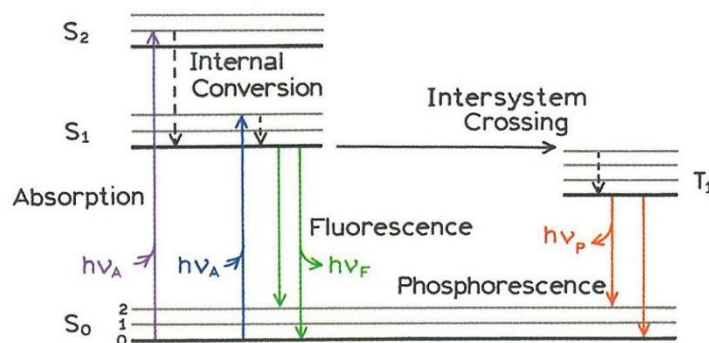


Figure 1.2: A possible illustration of a *Jablonski* diagram demonstrating several spectroscopic processes.^[7]

The diagram comprehensively describes the possible radiative and non-radiative transitions of an electronically excited sample. First of all, photons are absorbed by a chromophore in around 10^{-15} s resulting in various electronic states (S_1 , S_2 , ...). Within these states different vibrational levels may be populated which are illustrated in the figure as thinner horizontal lines. Nevertheless, luminescence always occurs from the lowest vibrational level of S_1 (apart from some rare exceptions) since the excess energy is quickly dissipated (internal conversion). This is due to a strong overlap of the states along with a short relaxation time of about 10^{-12} s. This non-radiative loss of energy explains the longer wavelength of the emission spectra, by now known as *Stokes* shift. According to this fact, the excitation wavelength does not influence the position of the emission spectrum as well as its shape. This is known as the *Kasha* rule.^[10]

The difference between fluorescence and phosphorescence, which led to a discussion between *Stokes* and *Becquerel*, is also explained by the *Jablonski* diagram. Fluorescence occurs from the S_1 state directly after the vibrational relaxation. It has a short lifetime of 10^{-6} – 10^{-9} s.^[11] Electrons in the S_1 state can additionally undergo a forbidden spin conversion to the triplet state T_1 which is called intersystem crossing. The transition to the singlet ground state is also forbidden concerning the selection rules which leads to slow rate constants in comparison to the fluorescence. Therefore, the lifetime of phosphorescence lies in dimensions of 10^{-3} – 10^2 s.^[11]

Excitation and emission spectra can have well-structured curves if the energy distances of the vibrational levels are big enough for the resolution of the spectrometer. Furthermore, several features of luminescence spectra can only be explained by inspection of the anharmonic potentials illustrated in Figure 1.3. According to *Boltzmann* statistics, virtually only the lowest vibrational state is populated in the ground state at standard conditions. The molecule can be excited electronically to various vibrational level in S_1 . The *Franck-Condon* principle requires the transitions to be vertical since the movement of the core can be neglected in comparison to electron movement.^[12]

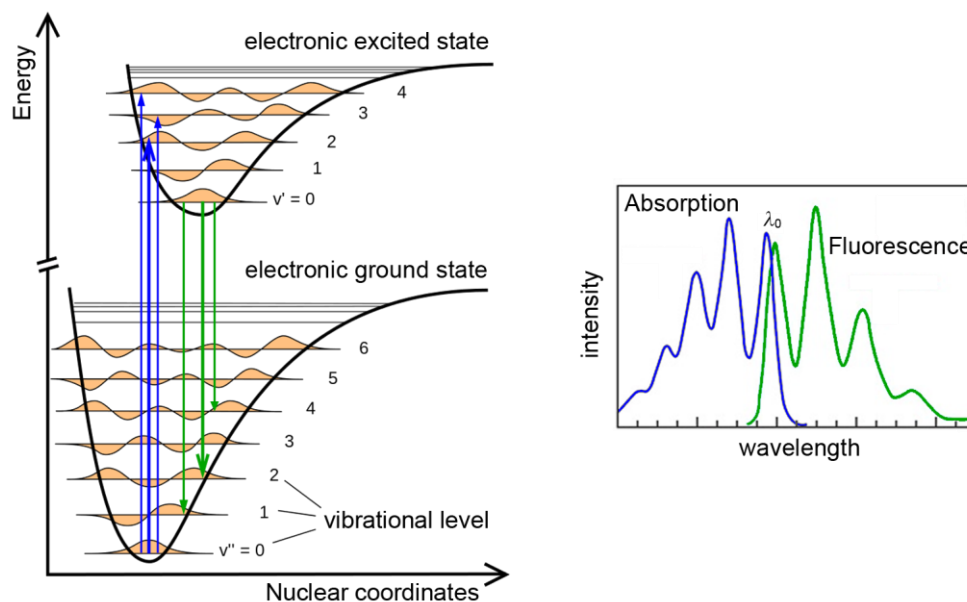


Figure 1.3: Illustration of the Franck-Condon principle and the origin of structured fluorescence spectra.

Additionally, transitions between vibrational states with a high orbital overlap are preferred. On the basis of this theory, the resulting spectra can have differently intensive band structures (Figure 1.3, right). Strong absorption due to high values of the wave function of both states results in more intense bands in the spectrum (e.g. $0 \rightarrow 2$, blue arrows). The same is true for the fluorescence emission marked in green.

The absorption of light by a fluorophore does not always imply the subsequent emission as luminescence occurrence. As already mentioned, the energy of molecules in higher electronic states is quickly dissipated by internal conversion to the lowest excited state S_1 . Furthermore, different excited vibrational levels will quickly relax to the lowest level ($v' = 0$). This is because the electronic configuration of a molecule changes upon excitation which leads to a fast reorganisation of the nuclei along with molecular vibration. The remaining energy can now be transformed to e.g. fluorescence occurrence or it is released in a non-radiative pathway due to collisions with other molecules. This is commonly present in concentrated solutions which is why fluorescence experiments are often realised with highly diluted samples. Hence, the analysed compound also collides with the solvent molecules. At ambient temperature, large compounds such as most dyes experience at least 10^{12} collisions per second.^[13]

Luminescent compounds are nowadays applied in a broad range of industrial, pharmaceutical, and analytical products.^[14] The ongoing development of luminescent substances with tailored features like lifetimes and quantum yields is still a promising field of research with huge possibilities.^[15] One possibility is the use of these kind of molecules as sensory devices. Fluorescent materials can be designed to work as switches by turning their emission of light selectively on and off.^[16] As explained before, this process is so fast that it opens a variety of useful applications. In the following, the most established mechanism for fluorescence quenching will be discussed.

1.1.1 Photoinduced electron transfer

Sensor molecules should be able to switch instantaneously between a fluorescent on and off state or change their emission wavelength significantly upon addition of an analyte. To achieve this

respond, several different mechanisms can be employed. Besides intramolecular charge transfer (ICT),^[17] metal-ligand charge transfer (MLCT)^[18] or excimer formation,^[19] an extensively investigated concept is the photoinduced electron transfer (PET)^[20] effect. Here, a poorly or non-fluorescent ligand starts to emit light upon coordination of an analyte under UV irradiation. The quenching of the fluorophore is realised by its structural design (fluorophore-spacer-receptor) resulting in a very efficient electron transfer. This process is illustrated in Figure 1.4.

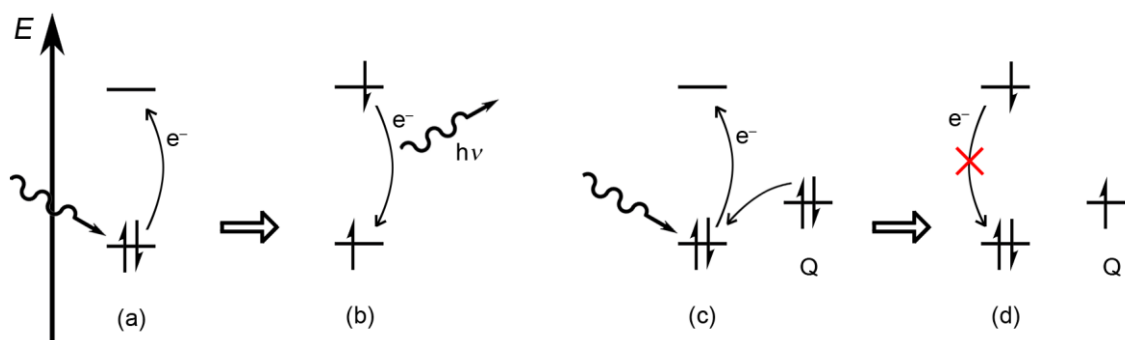
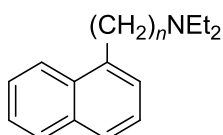
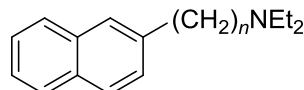


Figure 1.4: Mechanism of fluorescence (a, b) and its quenching by photoinduced electron transfer (c, d).

Usually, an electron in the ground state can be excited by irradiation of light (a). When it falls back to the ground state it loses its surplus energy and the phenomenon of fluorescence can occur (b). However, the excitation produces a vacancy in the ground state orbital, which may be filled with an electron from an orbital of a quencher (Q) which lies between these two states (c). In this case, no fluorescence emission can occur (d). The donating orbital can even belong to a separate molecule if it is in close proximity.^[21] In most cases it is a part of the fluorophore: here, especially amine moieties are chosen which are linked to the aromatic compound via a spacer unit. This spacer can be varied in its length, resulting in different efficiencies of the fluorescence quenching.^[22] Davidson and Trethewey have investigated this relation with derivatives of naphthylalkylamines.^[23] The results of this study are summarised in Table 1.1.

Table 1.1: Fluorescence quantum yields of different naphthylalkylamines.^[23] The derivatives with the most effective quenching properties are marked in blue.

					
Spacer	Φ_M	Φ_{Exciplex}		Φ_M	Φ_{Exciplex}
$n = 1$	0.006	0.001 (495 nm)	$n = 1$	0.018	0.006 (495 nm)
$n = 2$	0.008	0.040 (482 nm)	$n = 2$	0.003	0.028 (470 nm)
$n = 3$	0.012	0.015 (505 nm)	$n = 3$	0.010	0.010 (470 nm)
$n = 4$	0.008	0.002 (520 nm)	$n = 4$	0.012	0.012 (500 nm)

In the left example, a spacer length of one methylene unit yields the highest quenching of the fluorophore whereas an ethylene bridge is more efficient for the right molecule. In literature, only one methylene unit is mainly used^[24] which is also true for the molecules prepared in the course for this thesis. Its implementation between the aromatic compound and the receptor allows the latter to rotate easily around its bonds. This provides the conformational freedom to interact

electronically with the π -system of the fluorophore and results in an effective quenching of the fluorescence (Figure 1.5, a). At the same time the receptor is able to employ its lone pair in the complexation of analytes.

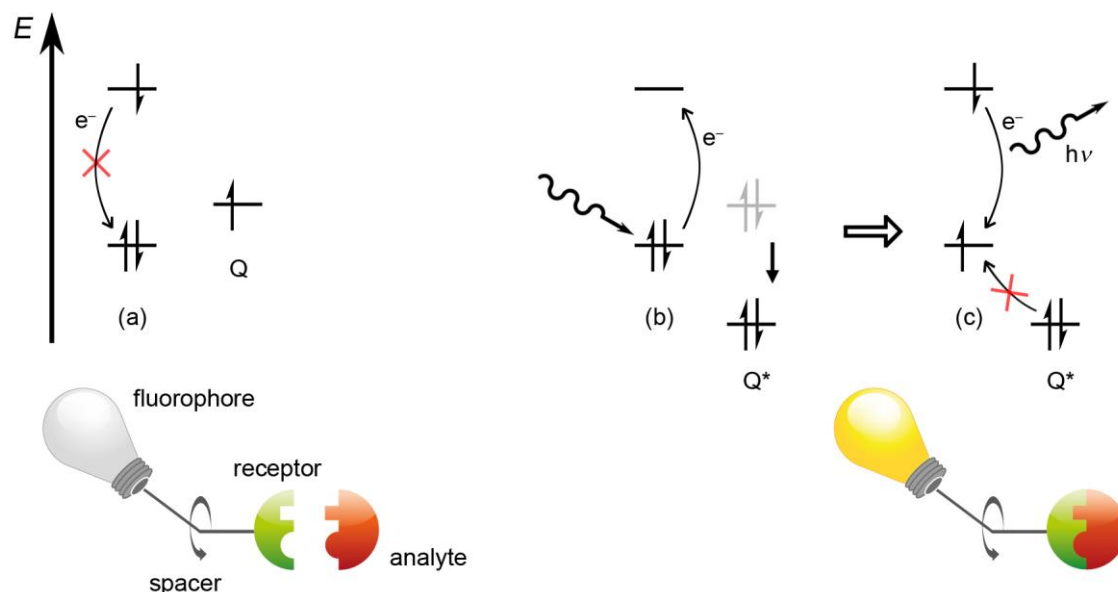


Figure 1.5: Left: Quenching of the fluorophore additionally illustrated by a scheme about the “fluorophore-spacer-receptor” principle. Right: Inhibition of the PET through bonding of the quencher (Q) to an analyte.

Through the binding of the quencher to e.g. a target metal ion, its redox potential is lowered resulting in an energetic state which lies underneath the energy of the excited fluorophore (b). If this is the case, the PET is hindered and the emission of light is facilitated (c). As already mentioned, amines are usually chosen for the role of the quencher/receptor. In order to donate an electron to the fluorophore, the amines need to have a higher potential energy than the aromatic compound.

1.1.2 The fluorophore azaanthracene

The choice of the fluorophore is not trivial since there is a variety of compounds described in the literature. Fluorophores mainly are polycyclic aromatic hydrocarbons with more or less extended π -systems. Anthracene is a very prominent example in this field, composed of three condensed benzene rings. Its derivatives and properties have also been investigated intensely by this working group.^[25] However, its congener azaanthracene, wherein one CH unit is substituted by a nitrogen atom, is far less investigated. Nevertheless, the usage of a nitrogen-containing aromatic system has the advantage of an additional donor function for the chelation of an analyte. This will be discussed exemplarily in the following chapter.



Scheme 1.1: Illustration of the Lewis diagrams of 2-azaanthracene (left) and 10-azaanthracene (right) including the correct IUPAC numbering of the atoms.

The substitution can be realised in several positions, this thesis concentrates on the two derivatives 10-aza- and 2-azaanthracene (Scheme 1.1). One advantage of the latter compound is its low symmetry (C_S) in comparison to anthracene (D_{2h}) which leads to higher $S_0 \rightarrow S_1$ transition rates and to an extent of spin-orbit coupling. In anthracene, the weak α -band is forbidden while it is allowed and clearly resolved in 2-azaanthracene (Figure 1.6). As a result, the fluorescence quantum yield of the latter is higher than of its isoelectronic hydrocarbon (0.36 to 0.24, respectively, measured in cyclohexane).^[26] However, it is a very rare representative of this group of fluorophores. A *SciFinder*[®] search of the term ‘2-azaanthracene’ yielded only 71 hits,^[27] containing every year since its first synthesis in 1895^[28]. A more expanded research with the words ‘az(a)anthracene’, and ‘benz(o)[g]isoquinoline’ (IUPAC nomenclature), which includes further congeners, resulted in 140 hits. These low numbers of scientific publications concerning this compound was the motivation to synthesise derivatives of the fluorophore and to investigate its luminescence properties.

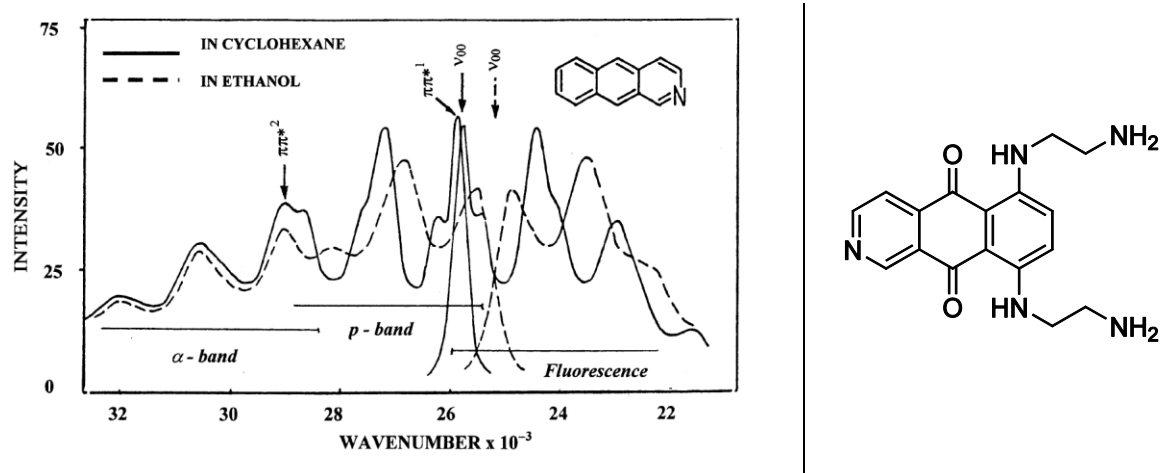
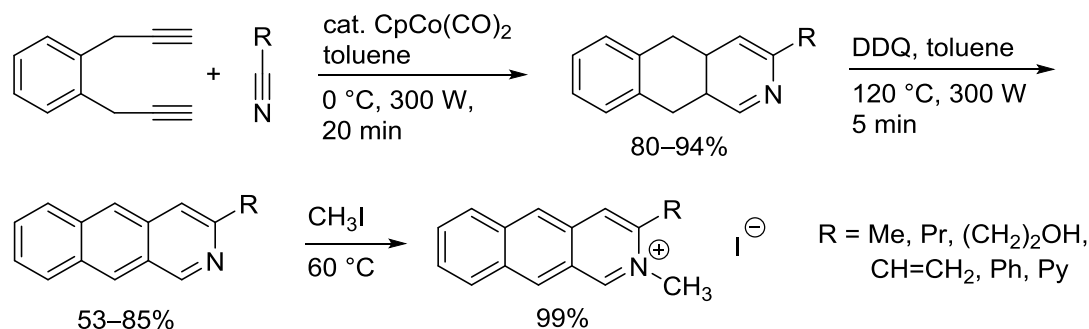


Figure 1.6: Left: Absorption and fluorescence spectra of 2-azaanthracene in different solvents.^[26] Right: Lewis diagram of the anti-cancer drug pixantrone.

Derivatives of the aromatic system are often used for DNA intercalation studies. Thereby, they may find application in the medicinal therapy of tumours. A well-known representative of these anti-cancer drugs is pixantrone which is used against aggressive lymphoma.^[29] It is based on the azaanthracene-5,10-dione structure and is depicted in Figure 1.6, right. Apart from the elaborate synthesis of this derivative,^[30] it could also be used as a possible molecular sensor. The ethylenediamine side arms in the 6- and 9-positions are good chelating receptors for e.g. cations.^[31] However, such derivatives have never been used for the fluorescence detection of metal ions according to the literature, apart from one publication.^[32] Here, the authors did brief investigations to possible metal ion interactions with the nitrogen atom of the fluorophore. Mainly, they focused on modern approaches to anthracenes and azaanthracenes by a [2+2+2] cyclotrimerisation. Here, the synthesis for the latter compound is introduced. The authors conducted the cyclotrimerisation under $CpCo(CO)_2$ catalysis in toluene using microwave irradiation (300 W), delivering the first intermediates in 80–94% yields. The following oxidation by DDQ resulted in six different substituted 2-azaanthracenes listed in Scheme 1.2. The reaction time of both steps is beneath half an hour involving good to excellent yields. A disadvantage is the usage of expensive starting materials and catalysts.



Scheme 1.2: Microwave assisted reaction pathway to 3-substituted 2-azaanthracene compounds.^[32]

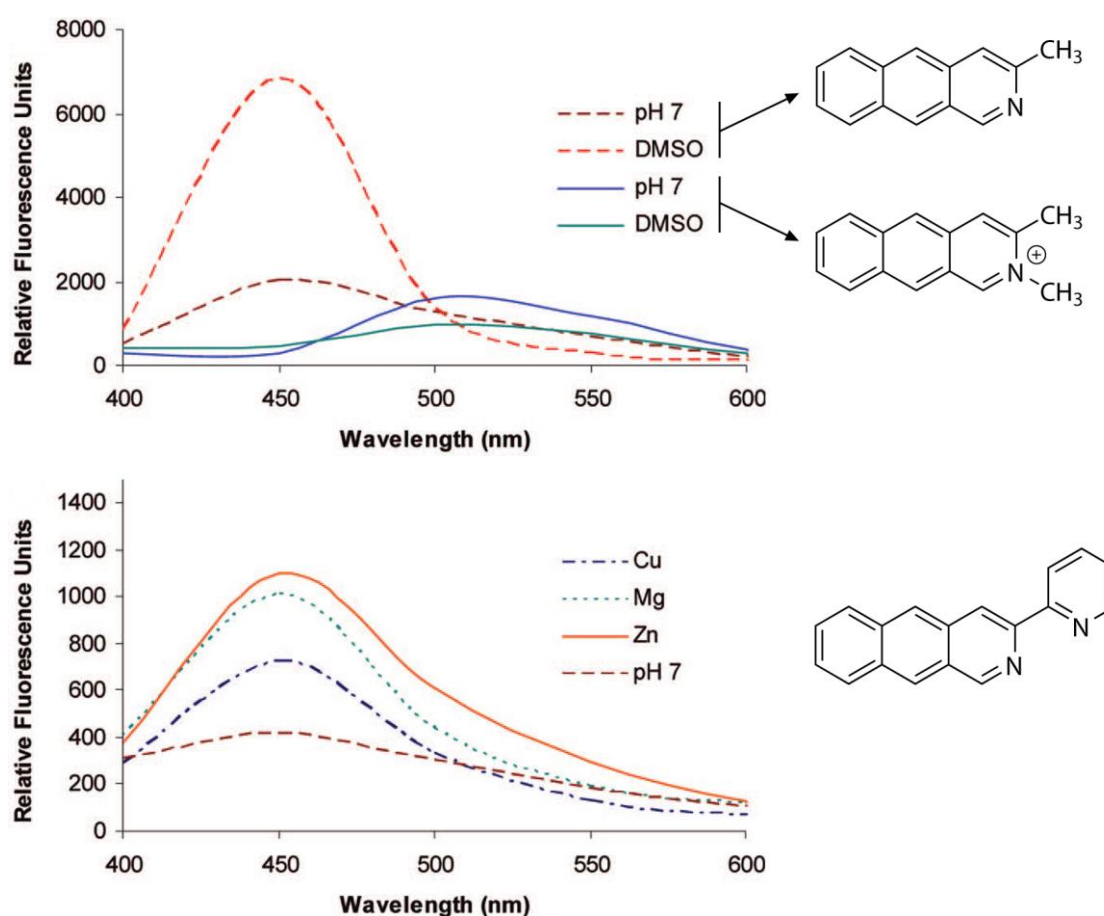


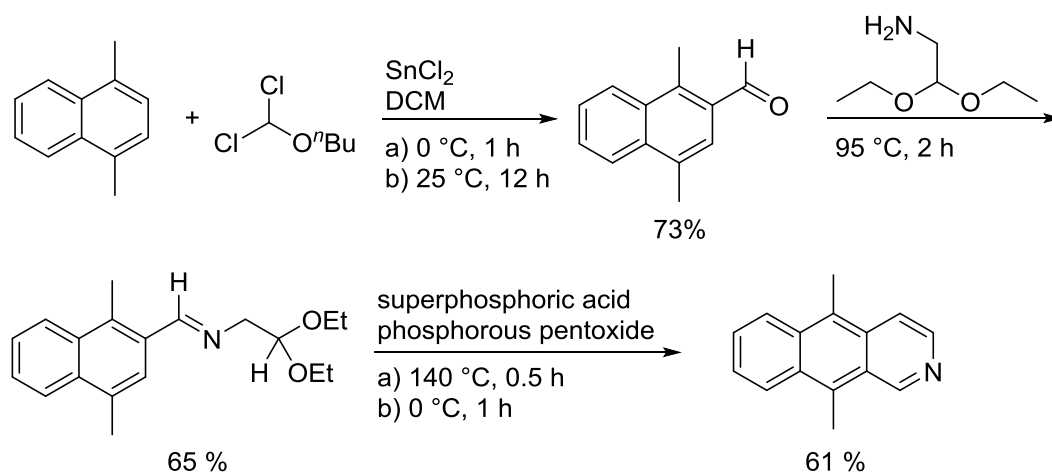
Figure 1.7: Emission spectra of different azaanthracene derivatives.^[32] Top: Comparison of mono- and dimethyl azaanthracene, demonstrating the effect of quaternisation on the fluorescence properties in DMSO and H₂O (pH 7); bottom: 3-pyridyl-2-azaanthracene in the presence of different divalent metal cations in aqueous solution.

Nevertheless, they introduced a fast and efficient approach to rare 2-azaanthracene derivatives. Additionally, they were able to methylate the nitrogen atom to induce a positive charge in the system which increases the solubility in an aqueous environment. Furthermore, the altering of the electronic properties of the fluorophore influences its emission spectrum investigated by the authors.

In the upper part of Figure 1.7, the emission spectra of 3-methyl-2-azaanthracene are shown, measured in protic (H₂O at pH 7) and aprotic (DMSO) solvents. The difference in intensity can be explained by the ability of the nitrogen centre to undergo coordination to the solvent, mainly to its

protons. Through the quaternisation of the nitrogen atom, a visible bathochromic shift in emission from blue to green was detected. This effect could also be generated in some cases by the use of dichloromethane as solvent. The use of a donating substituent closely associated to the nitrogen of the fluorophore (Figure 1.7, bottom) results in the coordination of some divalent metal cations (Mg^{2+} , Cu^{2+} , Zn^{2+}) increasing the emission intensity of the ligand. This small but very interesting effect was not further explained in the publication, but could be attributed to an intramolecular charge transfer (ICT, *vide infra*).

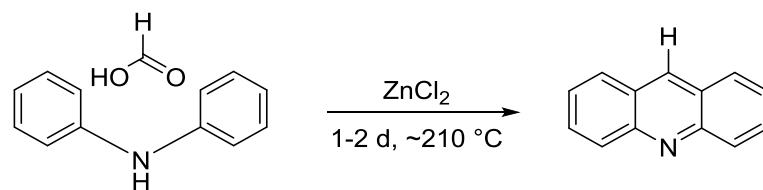
2-azaanthracene is commercially not available, and only a small number of further possible synthesis have been published in the last decades. All of them include at least three reaction steps with mainly small yields. In the following example, a dimethyl derivative is synthesised with a moderate yield of 29% (Scheme 1.3).^[33]



Scheme 1.3: Synthesis of 5,10-dimethyl-2-azaanthracene starting with a naphthalene derivative.^[33]

Usually, pyridine derivatives are chosen as starting materials to introduce the heteroaromatic ring.^[34] In this case, the authors are using 1,4-dimethyl naphthalene which is substituted in the 2-position. The synthesis involves three steps with acceptable yields. The reaction times are mainly short and the reagents are affordable. This is an important factor since the azaanthracene product is only the starting material for further reactions towards possible sensor systems. Therefore, the two methyl groups at the 5- and 10-positions are another advantage of this pathway since they should easily undergo substitution reactions with nucleophiles. This issue is again discussed in Chapter 2.1.1.

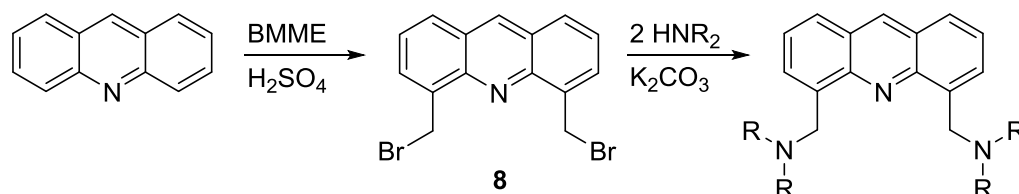
10-azaanthracene was discovered in 1870 by *Graebe* and *Caro* who found an unknown compound with basic properties when actually isolating anthracene out of coal tar.^[35] They gave it the name acridine due to its acridly effect to the skin. This name is still common today, apart from the systematic IUPAC name dibenzo[*b,e*]pyridine. Likewise, one of its first synthesis thirteen years later by *Berntsen*^[36] is also still applied in current literature^[37] as well as in this thesis (Scheme 1.4). Acridine derivatives are mainly established in the field of bioorganic chemistry. Here, they are used as fluorescence dye for e.g. DNA marker.^[38] In the medicinal area, several derivatives are applied as anti-malaria drug^[39] or even as a “*promising candidate for the treatment of aggressive, chemoresistant cancer*”.^[40]



Scheme 1.4: Reaction of diphenylamine with formic acid yielding acridine according to the procedure of *Bernthsen*.^[36]

However, the idea of using azaanthracenes as chemical sensors has mainly been pursued in the last decade. A *SciFinder*[®] search with the keywords ‘acridine’ and ‘sensor’ from 1870–2015 yielded 117 hits.^[27] 70 entries thereof have been published only in the period from 2010–2015. For comparison, the use of the single term ‘acridine’ results in 29,100 hits.

One possible reason for the increased interest is the publication of *Galy* and *Chiron* in 2003.^[41] They introduced the highly useful precursor **8** for an easy and straightforward synthesis of acridinyl amines utilising the “fluorophore-spacer-receptor” design (Scheme 1.5).



Scheme 1.5: Brief illustration of the synthetic route to potential molecular sensors based on acridine. The precursor **8** was implemented 2003^[41] and since then is used by numerous researchers.

The crucial reagent in this synthesis is the bromomethyl methyl ether (BMME) which allows to introduce two bromomethylene units to the aromatic system. This is carried out in a single step which is a tremendous advantage over further synthesis routes published only two years before.^[42] Here, the authors needed five steps to obtain the mono-bromomethylated species of acridine. The synthesis depicted in Scheme 1.5 will be explained in detail in Chapter 2.2.4.

1.1.3 The detection of metal ions using acridine systems

The detection of metal ions in solution has always been an important topic in analytical chemistry, environmental protection and medicinal applications. Metal ions like magnesium, calcium, or zinc are essential components of many enzymes in the human body.^[43] Especially Zn^{2+} plays a fundamental role in many different areas; e.g. in the emergence of Alzheimer’s disease.^[44] Moreover, its level of concentration could help to diagnose the growing of tumour cells in the prostate.^[45] Zinc deficiency increases the susceptibility to a variety of pathogens and is of central importance for the immune system.^[46] However, zinc ions are spectroscopically silent which makes it difficult to detect them by typical analytical methods like NMR spectroscopy. The heavier homologue Cd^{2+} is known to be a very toxic metal ion. Over several decades in the first half of the 20th century, hundreds of people in Japan were affected by the deadly *itai-itai* disease due to a cadmium polluted river.^[47] Therefore, it is vital to have a fast working and very sensitive method for the detection of metal ions in e.g. blood or water supplies. Fluorescence spectroscopy combined with suitable fluorescent sensors is a well-recognised method for such analysis. According to this, a multitude of publications is present in the literature, today.^[15, 25a, 48] However,

acridine based sensors for cationic analytes are less commonly used, although its number of publications is rising significantly in the last few years as mentioned before.

The first example introduced in this chapter (Figure 1.8) has been selected due to the comparison of the fluorophores anthracene and 10-azaanthracene – both equipped with the same receptor. Furthermore, Yoon et al. stated, “any acridine derivative bearing ligand on the 4,5-position via methylene linkage has not [yet] been studied as fluorescent chemosensors for metal ions.”^[49] They tested several metal ions in an aqueous buffer solution whereby selectivity towards zinc ions was detected.

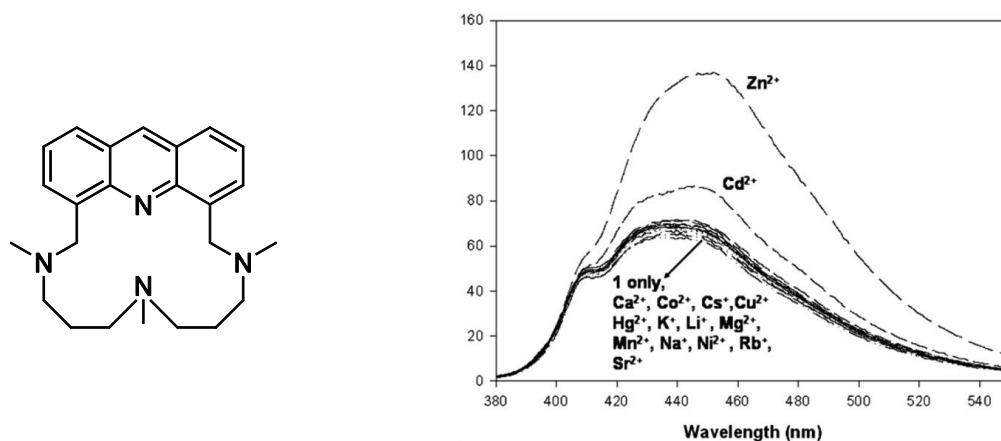


Figure 1.8: Molecular sensor for Zn^{2+} ions in an aqueous buffer solution.^[49]

Interestingly, only the acridine based compound showed fluorescence response to Zn^{2+} . The authors consider a binding contribution of the acridine nitrogen atom to the zinc ion due to these results. Nevertheless, they did not have any structural evidence for this hypothesis and the sensitivity of the sensor system is not very high. However, this publication confirms the application demand of acridine as a useful fluorescent part of sensor systems.

One year later, the same working group published another 4,5-substituted acridine derivative working as a chemical sensor.^[50] The published compound has the double number of donor sides, using two dipicolylamines as receptor units. In this case, they did not use the amines for the detection of metal ions like in the publication before, but for the preparation of a two-fold zinc complex (Figure 1.9, A).

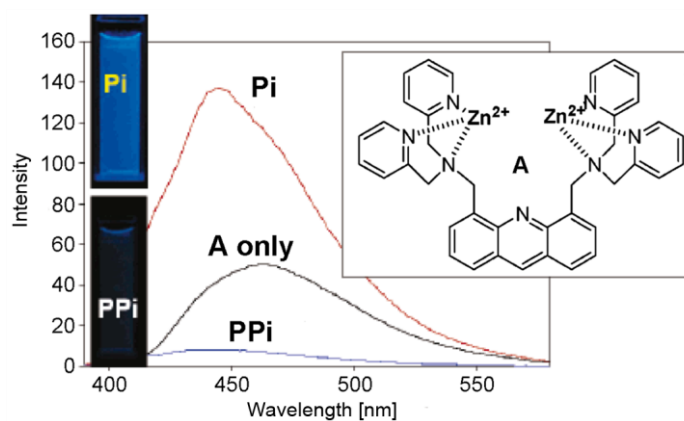


Figure 1.9: Fluorescence spectra of a Pi and PPI sensor, using a 4,5-bis(dipicolylaminemethylene)acridine which coordinates two zinc ions.^[50]

Each dipicolylamine coordinates a zinc ion involving three nitrogen atoms. The rest of the coordination sphere is filled with NO_3^- anions. This complex is now acting as a detector for pyrophosphate (PPi) and inorganic phosphate (Pi) anions which play important roles in signal transduction and energy storage in biological systems.^[51] Other anions like HSO_4^- , CH_3COO^- , and the whole group of halides do not alter the fluorescence spectrum significantly. The remarkable feature of this sensor system is the availability of two different mechanisms signalling the presence of Pi with a CHEF (chelation enhanced fluorescence) effect and the presence of PPi with a selective CHEQ (chelation enhanced fluorescence quenching) effect. The reduction of the fluorescence by the addition of a zinc complexing anion like PPi is easily comprehensible. When the metal ion is no longer bonded to the nitrogen atoms of the sensor, the amines act as quenchers due to the discussed PET effect. The CHEF mechanism is more complicated in this case. The authors state, that the effect can be attributed to additional hydrogen bonding between the hydrogen of the OH group in the Pi anion and the nitrogen atom of acridine. This correlation has been made by other authors as well.^[52] Additionally, they refer to the fluorescence enhancement observed by the coordination of zinc ions with the acridine unit, discussed before in Figure 1.8. Especially in this case, a structural proof would be a great advantage. However, they could show the affinity of the quencher side arms to the zinc ion by X-ray diffraction which is a rare exception in literature.

Besides the usage of amine groups for the receptor side arms of acridine, oxygen donors can be used, too. *Huszthy* et al. have synthesised acridone and acridine derivatives bearing 18-crown-6 ethers in the 4,5-position. With these compounds they are able to detect optically active salts (e.g. α -phenylethylamine hydrogen perchlorate)^[53] and also to separate these enantiomers by the use of stationary acridone phases^[54]. Some of their derivatives work as fluorescence sensors for Cu^{2+} and Pb^{2+} ions^[55] or for Ca^{2+} and Zn^{2+} ions^[56]. The latter will be presented here with the focus on the different fluorescent backbones.

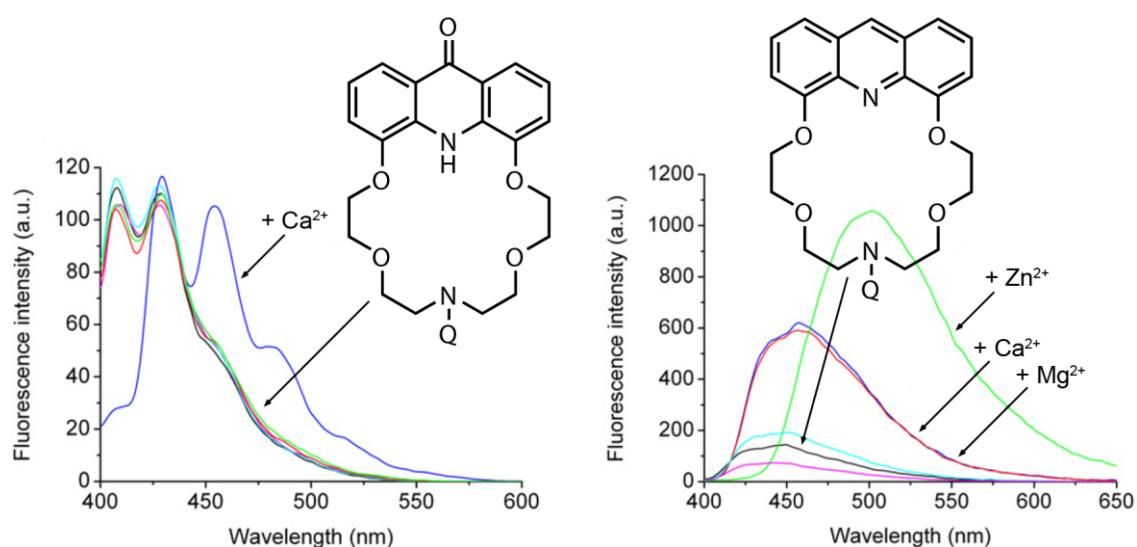


Figure 1.10: Emission spectra of 18-crown-6 ether derivatives based on acridone (left) and acridine (right) with Q = tetramethyl pyrroline.^[56] Spectral changes were shown upon addition of metal ions (1000 eq.) in MeCN: Na^+ : cyan, K^+ : magenta, Mg^{2+} : red, Ca^{2+} : blue, Zn^{2+} : green).

The coordination of metal ions is realised by an 18-crown-6 ether in both cases containing four oxygen and two nitrogen atoms as donor sites. However, they generate different results in the

selectivity of the analytes by the use of acridine on the one hand and the oxidised species acridone on the other hand. The acridone compound is only sensitive towards Ca^{2+} ions, signalled with a bathochromic shift of 20 nm but without any change in intensity (Figure 1.10, left). The reduced species responds to Ca^{2+} , Mg^{2+} , and Zn^{2+} ions. The two earth alkali metals influence the spectrum in the same manner with a significant increase of the intensity (Figure 1.10, right). With the addition of zinc ions, the intensity rises stronger and an additional appreciable bathochromic shift of 50 nm is observed. The authors only describe their results without any interpretation of the spectra. They did not provide further analysis of the complexes to get an idea about the coordination behaviour and the possible influence of the metal ions to the fluorophore. Nevertheless, an interaction of Ca^{2+} ions, respectively Zn^{2+} ions, with the π -system is probable since the shift of the emission wavelength can be attributed to changes within the electronic state of the aromatic systems.

The demand for structural insights into the ligand-metal complexes determined by fluorescence spectroscopy is fulfilled by the next example. However, this is done with a time lag of five years and by two different research groups. In the first place, the ligand 4,5-bis(*N,N*-di(2-hydroxyethyl)iminomethyl)acridine (BHIA) was synthesised 2011 by *Jin et al.*^[57] using the well-established route utilising BMME. The advantage of the published compound is the use of diethanolamines as they guarantee sufficient water solubility in combination with the binding ability to selected metal ions.

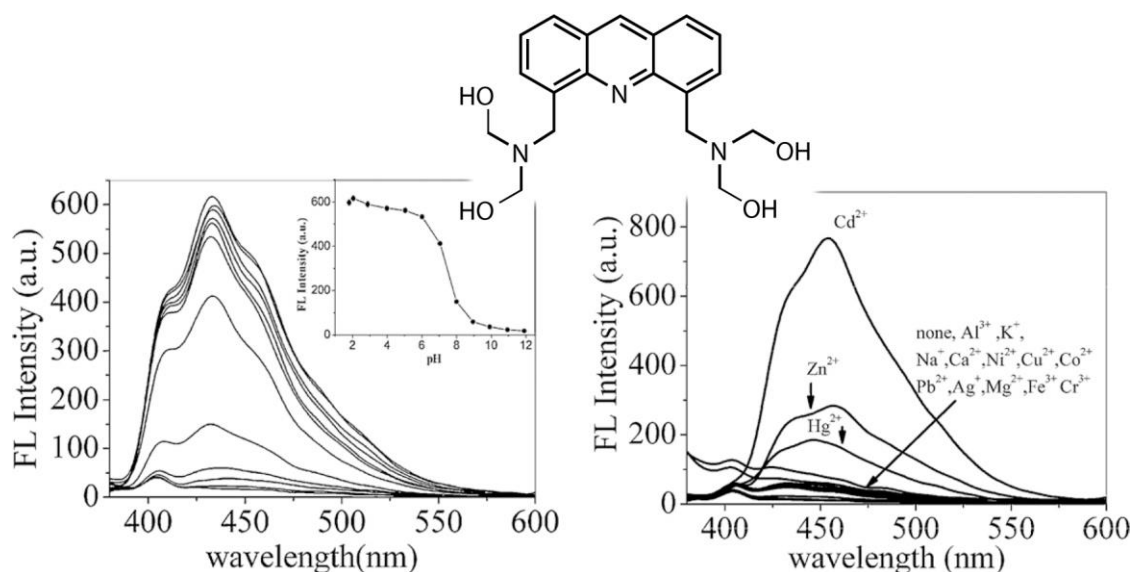


Figure 1.11: Emission spectra of the BHIA compound of *Jin et al.*^[57] showing the pH dependency in water (left) and the selectivity to Cd^{2+} ions in HEPES buffer with pH 7.4 (right).

The potential sensor compound shows a great dependency on the pH value of the aqueous solution (Figure 1.11, left). With decreasing pH the emission intensity rises due to the protonation of the amine. Since the lone pairs of the nitrogen atoms are no longer able to interact with the acridine, the PET is hindered and the fluorophore is “switched on”. The titration experiment with cadmium ions (Figure 1.11, right) can be analogously explained as well as for Zn^{2+} and Hg^{2+} ions, only less pronounced. As already mentioned, crystallographic studies were made with these complexes, discussing the free ligand^[58] and its metal complexes with Ag^+ , Cu^{2+} , and Cd^{2+} ions, published in 2016^[59]. The information of these publications are interesting, especially when

comparing the fluorescence studies with the solid state data. The discussion of these results as well as the comparison with the structures prepared for this thesis is done in Chapter 2.2.14 and 2.3.2.

1.1.4 Intramolecular charge transfer (ICT)

Besides the comprehensively discussed PET process, another mechanism used for the detection of analytes is the intramolecular charge transfer (ICT). In this case, no aliphatic spacer is present. The ICT occurs from an electron donor to an electron acceptor, both included in one conjugated compound.^[15] For this purpose, heteroaromatic systems are often used instead of pure hydrocarbon aromatic compounds. If excited by UV light, their dipole moments change significantly resulting in a large Stokes shift.^[60] Furthermore, interactions of the donor or acceptor with metal ions can change the photophysical properties of the fluorophores. The efficiency of the ICT process is altered and may result in a colorimetric respond of the compound.^[61]

The fluorophore 2-(4'-*N,N*-dimethylaminophenyl)imidazo[4,5-*b*] pyridine (DMAPIP-b) demonstrates this mechanism and its sensor abilities were investigated by *Krishnamoorthy et al.*^[62] Several metal ions were added to a solution of DMAPIP-b in acetonitrile without influencing its emission to a great extent (Figure 1.12, left). Only in the case of Zn^{2+} ions, the bathochromic shift of the emission maximum is pronounced strongly that the colour of the fluorescent solution changes from blue to green.

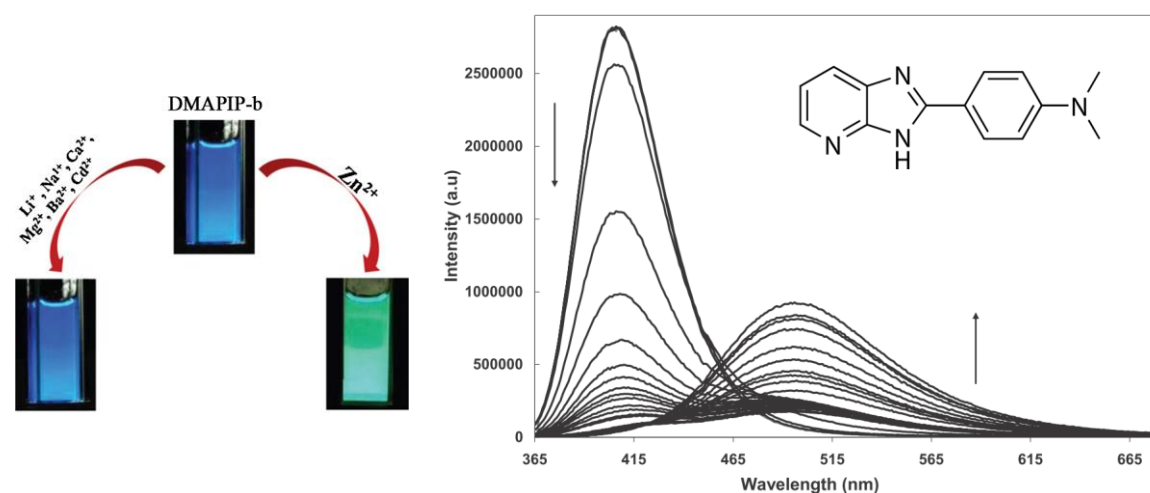


Figure 1.12: Left: Fluorescence of DMAPIP-b solutions in acetonitrile in presence of different metal ions. Right: Emission spectra of DMAPIP-b, illustrating the bathochromic shift upon addition of Zn^{2+} ions.^[62]

The emission spectra in Figure 1.12, right, illustrate the red shift of the emission maximum of approximately 100 nm upon addition of Zn^{2+} ions. The authors state that the cation is coordinated by the pyridine nitrogen atom since this enhances the conjugation of the system. The coordination by the dimethylamine would have the opposite effect, resulting in a blue shift of the emission. This was confirmed by protonation experiments of the different nitrogen atoms. The colorimetric respond is a great advantage in the field of molecular sensors, enabling the detection of an analyte even by the naked eye.

Similar investigations were made in the *Stalke* group with anthracene derivatives.^[25e] The compound 9-anthracene(*o*-(β -hydroxyethoxy)benzyl)amine was synthesised wherein the amine is

directly linked to the anthracene allowing a strong electronic influence to the π -system. Fluorescence experiments have shown that the compound is able to chelate zinc ions in DCM. Thereby, the emission maximum is significantly blue-shifted (100 nm) along with an increase of intensity (Figure 1.13). This strong respond to the analyte can be attributed to the fact that “*the fluorophore and the receptor share some critical atoms*”^[15] which is a further requirement for ICT sensors.

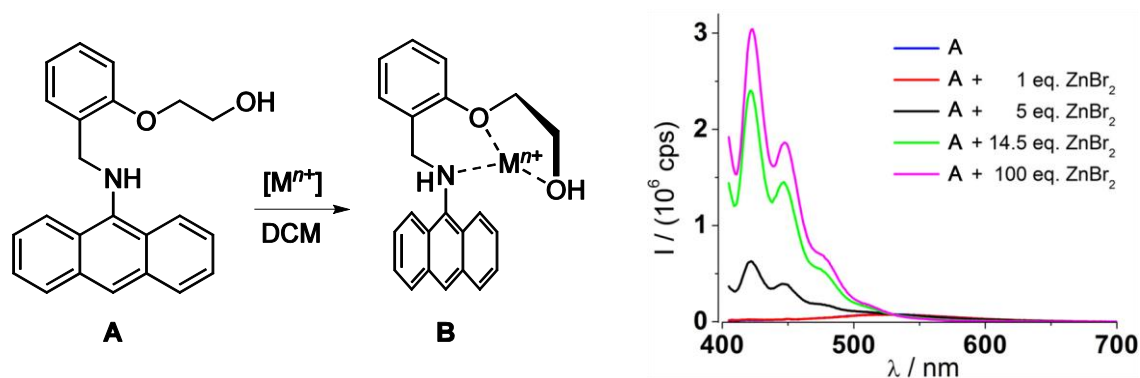


Figure 1.13: Left: Possible metal ion interaction of 9-anthracenepicolylamine. Right: Emission spectra of **A** with addition of ZnBr_2 in DCM.^[25e]

1.2 Scope

Former investigations of the *Stalke* group focussed on the hydrocarbon fluorophore anthracene. In this thesis, two representatives of the heteroaromatic congener azaanthracene with different fluorescence properties and potential usage as molecular sensors for metal cations were major fields of research. These compounds were 2- and 10-azaanthracene depicted in Figure 1.14, **A** and **B, C**, respectively.

2-Azaanthracene is a rare representative in the field of fluorescent sensors. Therefore, a suitable synthesis route for this aromatic system needed to be developed first. Its behaviour towards further substitution reactions to enable the “fluorophore-spacer-receptor” principle was of interest.

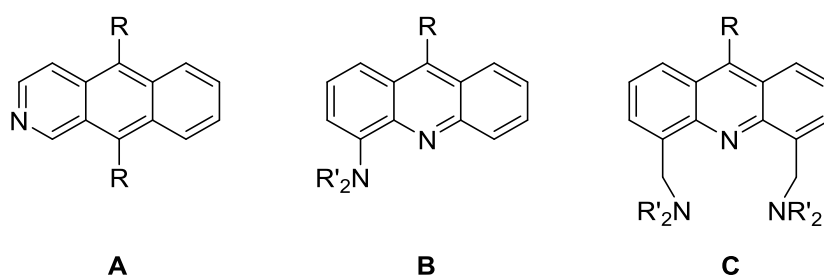


Figure 1.14: Structures of different azaanthracene derivatives investigated in this thesis. The possible substitution patterns which were of major interest are illustrated.

Concerning the second representative 10-azaanthracene, two various fluorescence mechanisms should be studied. Depending on the existence of a spacer unit between the quencher and the fluorophore, either the photoinduced electron transfer (PET) or the intramolecular charge transfer (ICT) effect can be utilised for cation detection. The latter effect is feasible if the receptor is directly bonded to the aromatic system (**B**) and has a strong electronic influence on the π -system.

This is a rare motif in the acridine literature which is why different syntheses towards new 4-aminoacridine compounds were studied.

The PET effect is present if the structural design depicted in Figure 1.14, **C** is used. Well established experimental procedures have led to the publication of various analogous structures in the last few years. For the course of this thesis, a variety of amine receptors were employed to determine their influence to the selectivity and sensitivity of the molecular sensor devices. The synthesised compounds and their metal complexes needed to be structurally investigated in detail by NMR and fluorescence spectroscopy in solution as well as in solid state by X-ray diffraction. With these analytical methods, the chelating motif of the ligand towards the target ion can be investigated. Especially the possible coordination of the acridine nitrogen atom to the analyte, often discussed in the literature, should be examined.

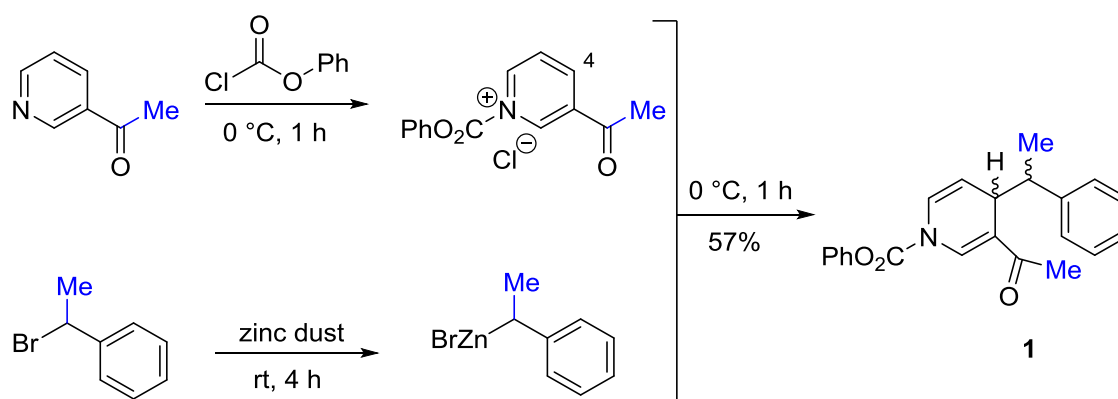
2. RESULTS AND DISCUSSION

2.1 Investigations of 2-azaanthracenes

During the prepeded master thesis, the synthesis of pure 2-azaanthracene could be established.^[63] The reaction involves three steps with isolable intermediates. But with this unsubstituted aromatic unit, further conversions to the desired fluorophore-spacer-receptor systems would expend a high amount of substance. Since the employment of BMME to the congener acridine was of great success, the reagent was applied to 2-azaanthracene, too. Unfortunately, no desired product could be obtained by this procedure. In this case, the methylene groups serving as spacer units were integrated already during the synthesis of the azaanthracene.

2.1.1 5,10-Dimethyl-2-azaanthracene (3)

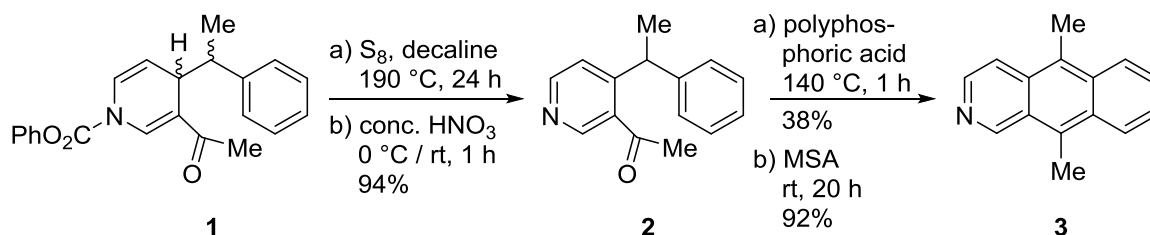
The already appropriated reaction by *Krapcho* and *Gilmor*^[64] during the master thesis will be used here in a modified way. Scheme 2.1 shows the first steps of the reaction pathway to 5,10-dimethyl-2-azaanthracene (3).



Scheme 2.1: First part of the synthesis of 5,10-dimethyl-2-azaanthracene, showing the reaction to 1-phenoxycarbonyl-3-acetyl-4-phenylethyl-1,4-dihydropyridine (1).^[64]

The modified starting materials provide the desired methyl groups highlighted in blue. In the upper part of the reaction, the protecting group phenyl formate is introduced to the nitrogen atom of the pyridine derivative. Additionally, this activates the species towards a *Michael* addition at position 4. In parallel, 1-bromo-1-phenylethane in THF was converted with zinc dust for four hours. After completion, the organozinc compound was added slowly to the pyridine derivative at 0 °C to obtain the diastereomeric intermediate **1**. After a column chromatographic work-up, the overall yield was 57%. According to the three reaction steps, the average yield amounts to 83% each. The intermediate could be purified by column chromatography. A separation of the diastereomers was not necessary since in the following reaction step only one of the possible enantiomers is forming. With a look at the integral intensities of the proton signals in the NMR spectrum, the diastereomeric ratio is about 3:1.

The next two steps contained some difficulties during the procedure. Firstly, the cleavage of the phenoxycarbonyl group and aromatisation of the pyridine ring was performed by oxidative sulfur at high temperatures (Scheme 2.2, a). Due to these harsh conditions, several side products were formed which needed to be removed. Additionally, the high-boiling solvent had to be distilled off.



Scheme 2.2: Further steps of the reaction pathway to **3** over the intermediate **2**, illustrating the reaction conditions by *Krapcho* and *Gilmor*^[64] (a) and the optimised conditions (b).

1 was dissolved in decaline together with sulfur and the mixture was heated to 190 °C for 24 h. After a vacuum distillation, the dark sticky residue was extracted with dichloromethane and dried over MgSO₄. The solvent was removed under reduced pressure to obtain a brown viscous oil. The yield of the synthesis of **2** was not determined due to some remaining decaline, but the ¹H NMR spectrum gave evidence that the conversion of the starting material was complete.

The last step was the acid catalysed cyclocondensation reaction of **2** with polyphosphoric acid. Both viscous reagents stirred sufficiently only at the needed high temperatures. After 1 h at 140 °C, the reaction mixture was neutralised, extracted with DCM and purified by column chromatography. The product was obtained as a yellow powder but in poor yields. This is why the conditions of these last two steps were optimised. Instead of the oxidation by sulfur in a high-boiling solvent, conc. HNO₃ was used. It is a strong oxidative acid which already reacts at much milder conditions. Therefore, **1** was cooled down to 0 °C when conc. HNO₃ was added slowly. It was stirred at room temperature for 45 min and poured onto ice afterwards. The crude product was extracted with DCM and also purified by column chromatography, to achieve a great yield of 94%. Since it was not possible to determine the yield with the oxidation conditions by *Krapcho* and *Gilmor*, one cannot reference the value directly. But according to the literature yield of 44%, the improvement is excellent. Additionally, an elaborate distillation of the solvent was not needed.

The use of polyphosphoric acid for the cyclocondensation reaction was not straightforward. The acid is highly viscous which impedes its handling and needs to be stirred sufficiently. The harsh reaction conditions can support the formation of undesired by-products which could be a reason for the low yield. An alternative reagent for this kind of cyclisation reactions can be found in the literature published by *Leon* and co-workers.^[65] They prefer using methanesulfonic acid (MSA) without heating. Therefore, **2** was dissolved in small amounts of MSA and was stirred at room temperature for 20 hours. After pouring onto ice, the solution was neutralised with NaHCO₃ and extracted with DCM. Under these new conditions, a yield of 92% after column chromatographic work-up could be achieved. The first step of the synthesis had a moderate yield of 57% (**1**) which reduced the overall yield of **3** to 49%. This is still a sufficient value with respect to the initially challenges.

In Figure 2.1, the ¹H NMR spectrum of 5,10-dimethyl-2-azaanthracene (**3**) is depicted. It demonstrates the almost pure product with only slight impurities in the aromatic region as well as some residual solvent dichloromethane. With this precursor in hand, further substitution reactions at the methyl groups at the 5,10-positions were studied.

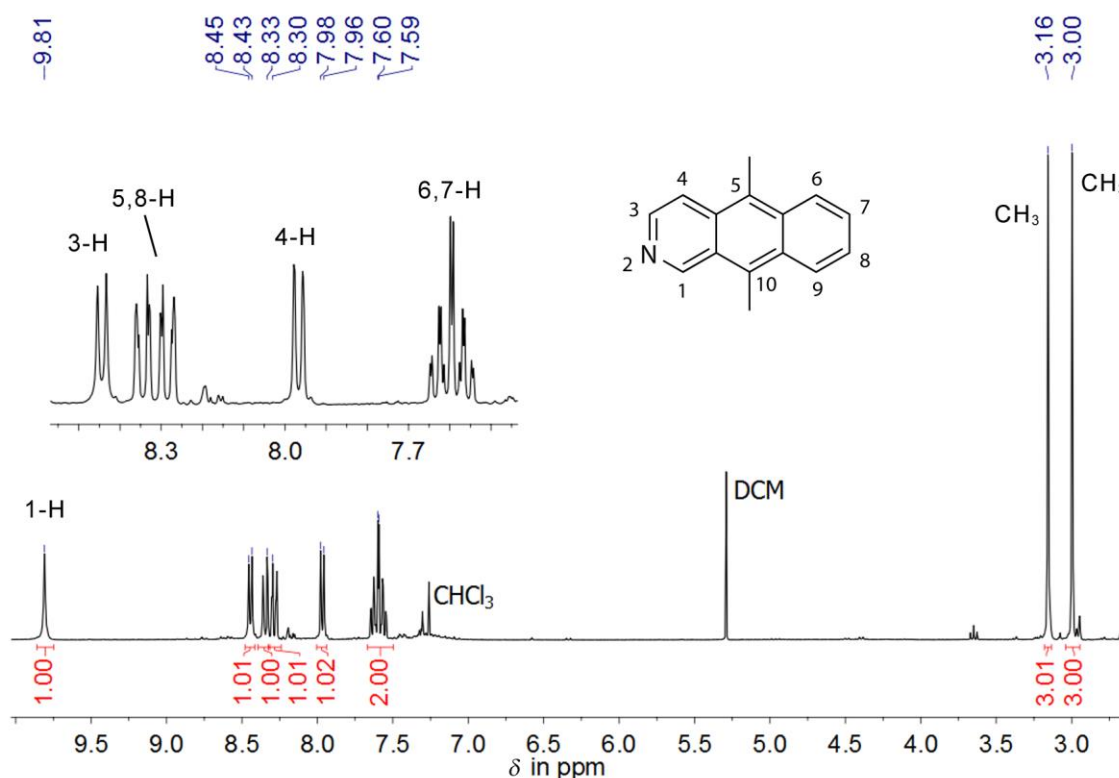
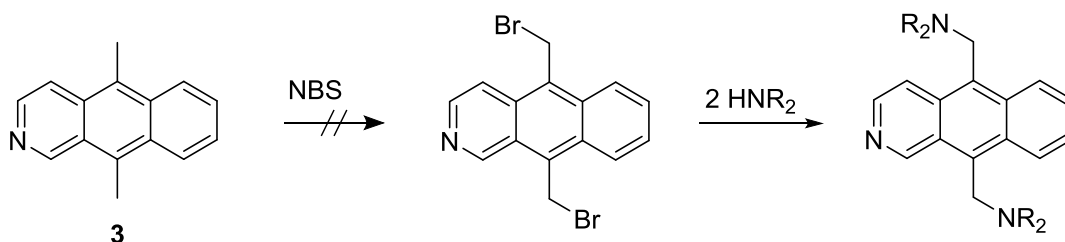


Figure 2.1: ^1H NMR spectrum of **3** in CDCl_3 .

2.1.2 Investigations to the bromination of 5,10-dimethyl-2-azaanthracene (**3**)

The next step for the build-up of a molecular sensor was the introduction of bromine atoms at the methyl groups, followed by a substitution reaction (Scheme 2.3). A common bromination of side arms like methyl groups can be realised with *N*-bromosuccinimide (NBS) and a radical initiator under high temperatures (*Wohl-Ziegler* reaction).^[66] NBS is used because of its polarised N–Br bond, leading to a partially positively charged bromine atom which can easily be cleaved. To initiate the radical reaction, benzoyl peroxide or *tert*-butyl peroxybenzoate has been used.



Scheme 2.3: Reaction pathway for the build-up of a molecular sensor system based on **3**.

Table 2.1: Different reaction conditions for the bromination approach of **3**.

No.	Solvent	Temperature	Reaction time	Radical starter
1	CHCl_3	70 °C	5 h	$(\text{PhC}(\text{O})\text{O})_2$
2	CHCl_3	70 °C	22 h	$(\text{PhC}(\text{O})\text{O})_2$
3	DMF	80 °C	4 h	$(\text{PhC}(\text{O})\text{O})_2$
4	DMF	25 °C	24 h	$t\text{BuOOC}(\text{O})\text{Ph}$

The bromination was carried out under four different reaction conditions, listed in Table 2.1. Other than expected, none of the approaches resulted in sufficient amounts of the desired product. Mostly, the starting material decomposed, whereas in some cases slight traces of the bromomethylene compound could be identified via $^1\text{H NMR}$ spectroscopy. However, these small amounts could not be isolated and purified for further analytics. In the literature, the successful bromination of the similar compound 9,10-dimethylantracene was demonstrated with NBS.^[66a] According to this, the nitrogen atom of the azaanthracene seems to hinder the radical conversion by unintended side reactions. However, the reaction of 9-methyl-10-azaanthracene with NBS, which is discussed in Chapter 2.2.2 of this thesis, resulted in the desired bromination of the methyl group.

A preceding oxidation of the aromatic nitrogen atom may prevent the decomposition of **3**. After the conversion with NBS, the nitrogen atom could be reduced with the oxophilic PPh_3 . Unfortunately, this hypothesis could not be investigated due to the lag of starting material based on its difficult synthesis. However, this would extend the synthesis of potential molecular sensors by two more steps, resulting in an overall reaction pathway including seven steps. This elaborate synthesis as well as the susceptible intermediates led to the decision to no longer pursue this type of azaanthracene. During the preceding master thesis, successful experiences were gained with the congener 10-azaanthracene which is why the focus was set on this fluorophore.

2.2 Potential molecular sensors based on acridine

The reactivity of acridine towards different reagents such as nucleophiles or electrophiles has been reviewed earlier by *Acheson*^[67] and lately by *Galy* and *Chiron*^[68]. The relevant positions for this thesis are 4, respectively 5, and to a certain extent the 9-position. In Figure 2.2, the frontier electron density for electrophilic substitution is shown.

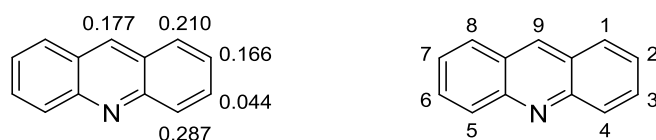
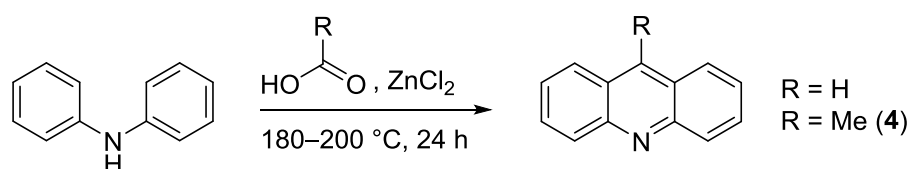


Figure 2.2: Calculated π -electron densities of acridine^[69] and its IUPAC numbering used in this thesis.

Electrophilic attacks should primarily occur at position 4 which is enhanced by the protonation of the nitrogen atom by an acid. It was taken advantage of this behaviour in the course of work for this thesis. In contrary, position 9 of acridine can be attacked by nucleophiles due to its lower electron density. This is attributed to the nitrogen atom at the *para*-position of the central ring.

2.2.1 9-Methylacridine (4)

On the one hand, the introduction of a methyl group at the 9-position can be achieved by a nucleophilic substitution with e.g. organolithium compounds at the aromatic system.^[70] On the other hand, a cyclocondensation reaction can be carried out to build-up the desired acridine derivative. The use of diphenylamine with either formic or acetic acid results in the synthesis of acridine and 9-methylacridine, respectively (Scheme 2.4).^[36b]

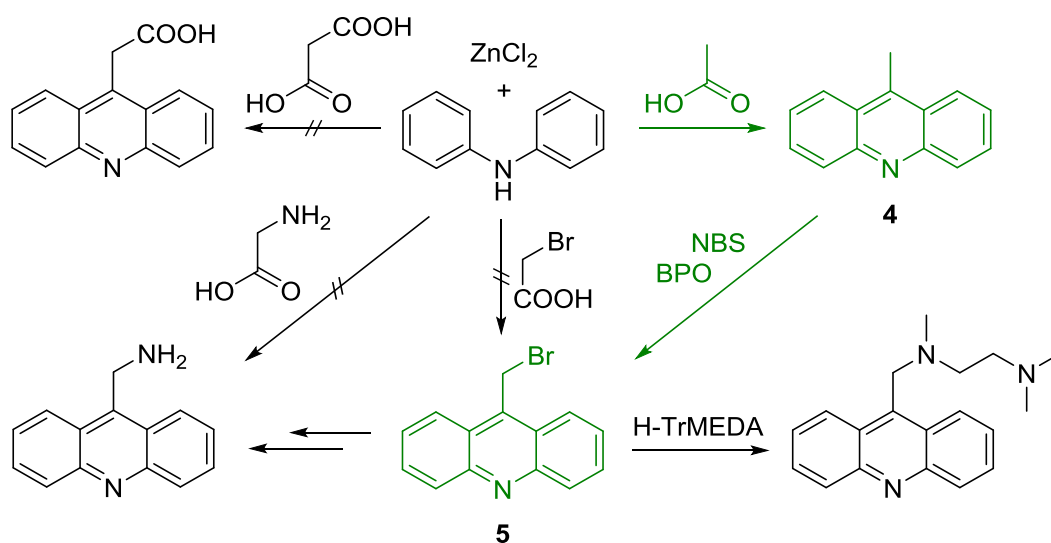


Scheme 2.4: Bernthsen synthesis of the fluorophores acridine and 9-methylacridine (4).^[36b]

Whereas pure acridine is commercially available and was not synthesised in this thesis, its 9-methyl derivative **4** was obtained by the use of 3 eq of glacial acetic acid and 4 eq of zinc chloride. High temperatures around 200 °C are needed for the cyclocondensation of the reagents. That is why the amount of acetic acid must be minimised due to its boiling point of 118 °C. Diphenylamine melts at 53 °C and acts as reagent as well as solvent. Mechanic stirring was needed to achieve a sufficient mixture of the starting materials. ZnCl₂ is used as Lewis acid and stabilises the intermediate. At the beginning of the reaction, the molten diphenylamine dyes the reaction mixture violet, whereas it changes the colour to dark green at temperatures above 180 °C. After one day, it was cooled to room temperature and the reaction was stopped by the addition of aqueous NaOH solution (2 M). The organic compounds were extracted with DCM and dried over MgSO₄. The obtained product was of sufficient purity with a yield of 57%.

The introduction of the methyl group had several reasons. On the one hand, it enhances the electron density of the aromatic system due to its positive inductive effect. This could improve the yields for further electrophilic reactions at the positions 4 and 5 which are discussed in Chapter 2.2.4. With regard to the nitrogen atom, a higher electron density could improve its donating properties for the coordination of metal cations, but only to a small extent. On the other hand, the methyl group can be utilised for further substitution reactions. For example, chelating amines can be used to coordinate target ions on both sides of the fluorophore – at position 9 and opposite to it at the 4- and 5-positions.

In the following, several attempts to further derivatives of acridine at the 9-position are discussed. They all originate from the previously shown reaction with diphenylamine as the starting material and an excess of ZnCl₂.

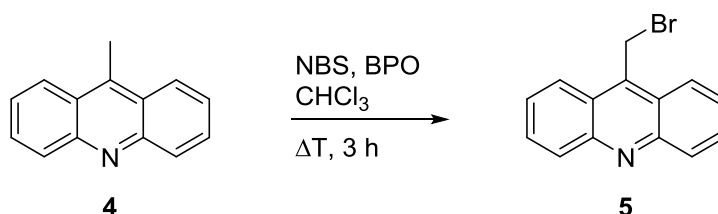


Scheme 2.5: Overview to a variety of potential compounds originated from diphenylamine.

Various reagents have been used to introduce functional groups in the *para*-position of the nitrogen atom by cyclocondensation reactions (Scheme 2.5). Unfortunately, most of them did not yield the desired product. In the case of glycine, no conversion of the starting material was observed, whereas the use of malonic acid only yielded 9-methylacridine likewise to the *Bernthsen* reaction with acetic acid. The latter can be explained by a decarboxylation of one of the carboxylic acid groups during the reaction. The achieved yield was lower in comparison to the standard procedure of Scheme 2.4.

2.2.2 9-(Bromomethylene)acridine (5)

A direct approach for the synthesis of **5** was tried with three equivalents of bromoacetic acid, depicted in Scheme 2.5. By this, an intermediate should be obtained which is convertible to potential molecular sensors by a following substitution reaction with e.g. amines. In the beginning of the reaction, the reagents were dissolved in the melted diphenylamine. After one hour at 200 °C, the reaction mixture became solid and it was cooled to room temperature. Most of the compound was dissolved in methanol and residues were filtrated off. The ¹H NMR spectrum showed that the introduction of the bromomethylene unit was not feasible by this method.



Scheme 2.6: Synthesis of 9-(bromomethylene)acridine (**5**).

With the use of **4** as precursor and *N*-bromosuccinimide as reagent, a second route to 9-(bromomethylene)acridine was performed. Both starting materials were dissolved in chloroform in equimolar amounts when 7 mol% of the radical initiator benzoyl peroxide (BPO) was added. The solution was heated to the boiling point of the solvent for three hours. After the solvent was removed under reduced pressure, a recrystallisation from ethanol was implemented to remove residual succinimide. After a column chromatographic work-up, **5** was obtained in a yield of 55%.

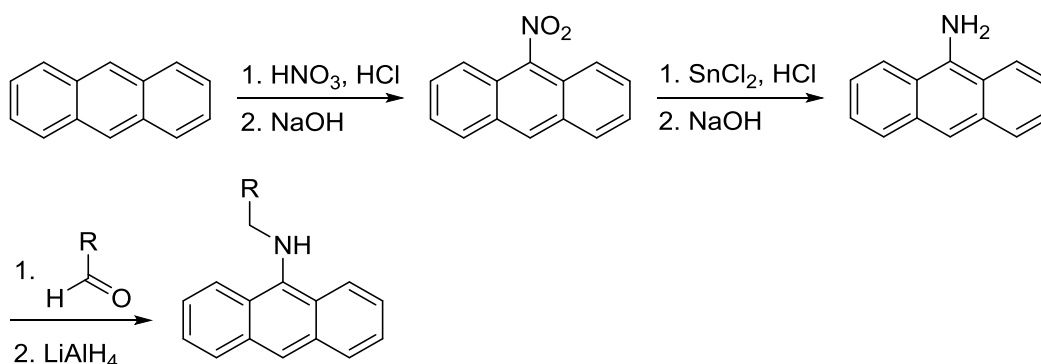
The bromine should now be replaced by an amine group. A primary amine can be obtained by the use of urotropine and hydrochloric acid.^[71] Afterwards it can be derivatised with e.g. aldehydes. Here, the direct substitution by a secondary amine was tried (Scheme 2.5). The amine *N,N',N'*-trimethylethylenediamine (H-TrMEDA) was chosen for the substitution of the bromine since it contains two nitrogen atoms for the coordination of an analyte. The three methyl groups enhance the donor ability of the diamine. For the conversion of **5**, one equivalent of the amine and an excess of K₂CO₃ was added. The basic salt improves the reaction by deprotonating the amine and it precipitates the bromide as KBr. The reaction was performed in chloroform overnight at a temperature of 50 °C. A ¹H NMR spectrum was recorded after 18 hours. It showed a significant upfield shift of the intense singlet of the CH₂ group by almost one ppm. This was a good indicator for the exchange of the bromine with a nitrogen atom. Furthermore, new signals in the aromatic region were found, whereas the spectrum indicated at least two present derivatives. To separate these, a column chromatography on alumina was applied. During the work-up, further derivatives were observed by the use of thin layer chromatography. Several fractions were isolated and

investigated by NMR spectroscopy. Unfortunately, no signals which belonged to the desired product were identified. Either the reaction did not yield the TrMEDA-substituted acridine or the chromatographic procedure led to the decomposition of the compound.

The main focus of this thesis laid on the determination of 4-mono- and 4,5-disubstituted acridine amines. This is why the derivatisation of the 9-position was not investigated further.

2.2.3 Attempts to 4-aminoacridine

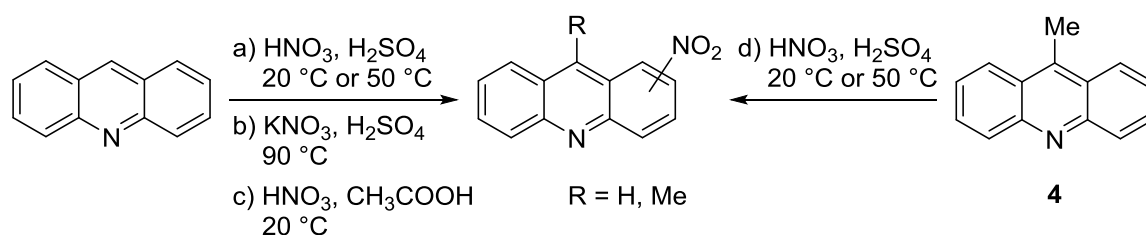
In the introduction, the molecular requirements for an intramolecular charge transfer (ICT) and its mechanism was discussed. In comparison to the methylene bridged derivatives mentioned in the chapter before, the receptor unit needs to be directly attached to the fluorophore. This was investigated in the *Stalke* group with anthracene derivatives.^[25e] The molecular sensor 9-anthracene(*o*-(β -hydroxyethoxy)benzyl)amine was synthesised and its sensor abilities were determined. The latter was already discussed in the introduction and its synthesis is presented here in detail.



Scheme 2.7: Reaction pathway to molecular ICT sensors based on 9-aminoanthracene.^[25e]

Wandtke used nitric acid for the nitration of anthracene at the 9-position, with a following reduction to the amine with SnCl_2 and HCl (Scheme 2.7). Based on this intermediate, different types of molecular sensors were synthesised. The reaction pathway should be adopted to acridine as fluorophore. Here, the amine should be introduced in the 4-position of acridine which allows to coordinate an analyte by the amine as well as by the aromatic nitrogen atom. This possibility is an advantage in comparison to the hydrocarbon congener anthracene.

The nitration of acridine has been studied by different researchers with modest results. The electrophilic nitration of the aromatic system not bearing directing substituents often leads to mixtures of nitrated products along with the oxidation of the starting material.^[72] In most cases, multiple nitration occurs at the aromatic system.^[73] Since the numbering of acridine is frequently mixed up in earlier literature^[74] and the identification of products was mainly realised by elemental analysis^[75], it often not became clear which nitro-substituted derivative was synthesised. However, by summarising different approaches, *Lehmstedt* figured out that changes of the reaction temperature and the ratio of the used acids yielded different substituted acridines.^[76] Therefore, various attempts to nitroacridine derivatives were performed which are listed in Scheme 2.8.



Scheme 2.8: Different attempts of the nitration of (9-methyl)acridine.

The commonly used reagents for the nitration of aromatic systems are nitric acid in combination with sulfuric acid. The resulting nitronium ion is able to perform electrophilic attacks. According to the calculated π -electron densities of acridine shown in Figure 2.2, the nitration should take place in position 1 and 4. In general, the aromatic compound was dissolved in acid and heated to the appropriate temperature. The reaction was stopped by pouring onto ice and the precipitates were filtrated off and washed with water. NH_3 or aqueous NaOH was added to the filtrate until it became alkaline. Further possible precipitates were filtrated and the solid products were dissolved in organic solvents. The solution was dried over MgSO_4 and the volatile components were removed under reduced pressure after filtration. In the case of procedure a) and d), the ^1H NMR spectrum was highly crowded. The crude product from procedure a) was recrystallised from glacial acetic acid resulting in a small amount of residue which could be characterised by NMR spectroscopy (Figure 2.3).

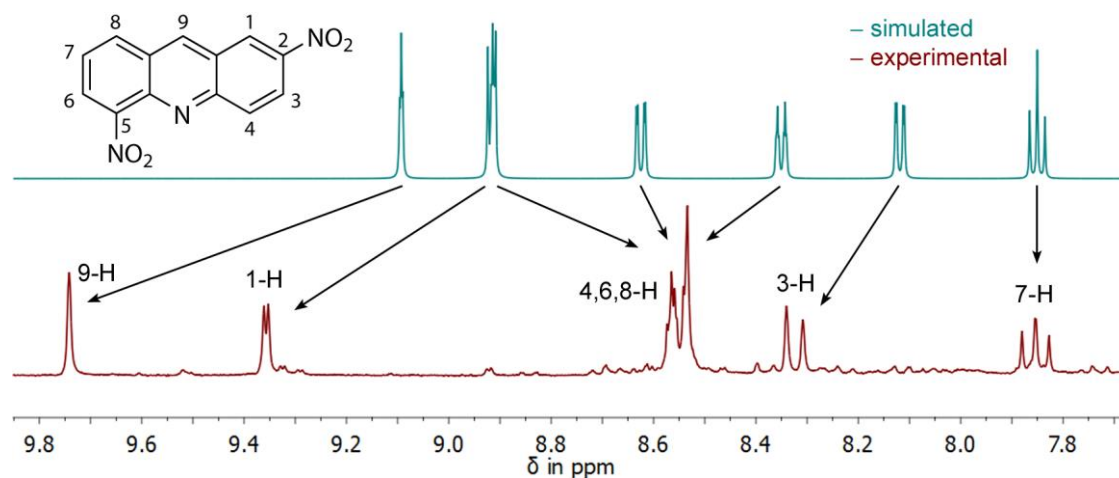


Figure 2.3: ^1H NMR spectrum of the proposed 2,5-dinitroacridine (red) and its simulated spectrum (turquoise).

The signals of the spectrum could be assigned to the relative protons with the help of a H,H-COSY NMR experiment and due to their multiplicity and chemical shift. Therefore, the measured spectrum was compared with a simulated spectrum calculated by the Mestrenova[®] software (v6.0.2). The integral intensities of the signals confirm the presence of seven protons. These results indicate that the disubstituted 2,5-dinitroacridine was isolated from the mixture of nitrated products.

With regard to the poor yields, the reaction conditions were modified. Nevertheless, the use of HNO_3 in glacial acetic acid did not lead to any reaction with the aromatic system. A further variation was the change of HNO_3 to its salt KNO_3 , also combined with H_2SO_4 .^[77] Likewise to the prior attempts, the ^1H NMR spectrum shows a variety of nitrated derivatives. After the usual

work-up, a column chromatography was performed to separate the different species. Due to their similar physical properties, no sufficient results were obtained. Only one fraction contained a disubstituted product which was analysed by NMR spectroscopy and compared with the simulated spectrum (Figure 2.4).

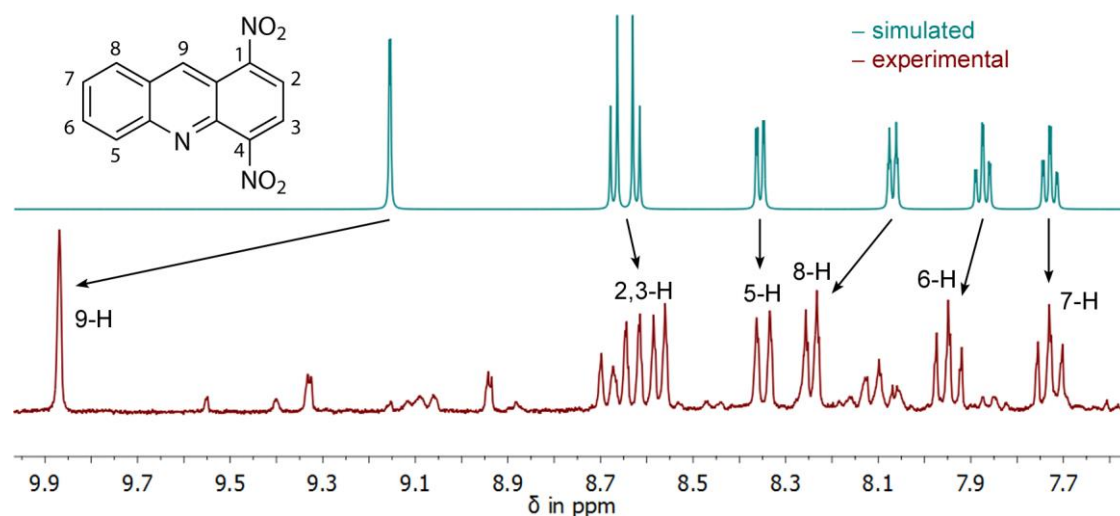
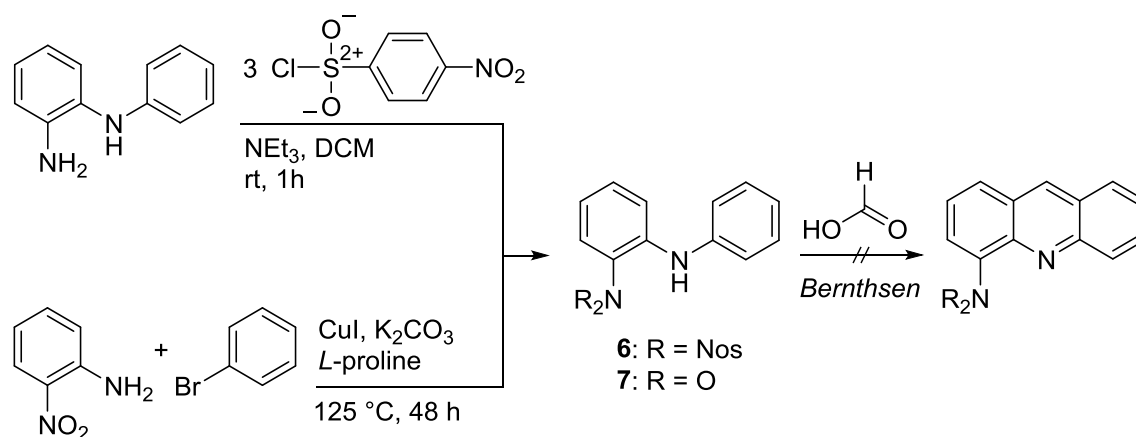


Figure 2.4: ^1H NMR spectrum of the proposed 1,4-dinitroacridine (red) and its simulated spectrum (turquoise).

In this case, the 1,4-dinitroacridine was formed which was determined in the same manner like the derivative described before. The analysis of the chemical shift, the integral intensity, and mainly the multiplicity of the signals resulted in the assumed compound. Again, only a small amount of the compound was isolated which still needs to be purified. This is why further attempts to the direct nitration of acridine were not followed although the substitution of the desired position 4, respectively 5, was successful.

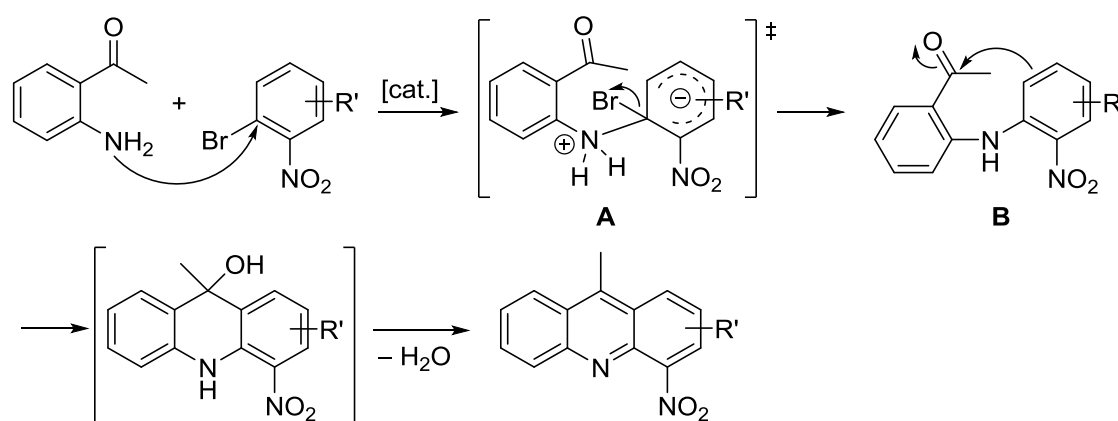
Another route for the introduction of an amino group is the use of appropriate starting materials for condensation reactions, yielding the desired acridine derivatives. One approach was the use of 2-aminodiphenylamine which should be able to undergo a condensation reaction with formic acid to 4-aminoacridine. However, the primary amino group would react with formic acid to form 1-phenyl-1*H*-benzimidazole.^[78]



Scheme 2.9: Two different approaches to derivatives of 2-aminodiphenylamine.

On the one hand, this unwanted reaction can be hindered by the use of a suitable protection group. On the other hand, a nitro group can be used instead which is afterwards easily reducible to the amine. Both methods were tried which synthetic routes are depicted in Scheme 2.9. 4-Nitrobenzenesulfonyl chloride was chosen as a suitable protecting group for the amine since it is stable towards acids which are used for the preceding cyclocondensation reaction. Triethylamine was added as base and the reaction mixture was stirred in DCM for one hour at room temperature. The protected amine **6** was isolated with a yield of 74%. It was tried to react this intermediate with formic acid in the presence of $ZnCl_2$ to form the 4-substituted acridine derivative. In this case, the two large protecting groups increase the melting point of the diphenylamine derivative drastically. Therefore, the solid reagents did not react sufficiently even at temperatures of 190 °C for 12 h.

2-Nitrodiphenylamine (**7**) has a melting point of 75 °C.^[79] Its synthesis was adopted from the proceedings of *Fu et al.* who studied the reactions of aniline and bromobenzene derivatives.^[80] The authors made use of the catalysts CuI (10 mol%) and *L*-proline (20 mol%) which enables the conversion of the starting materials in the presence of a base and temperatures around 110 °C. High boiling and polar solvents like DMF or DMSO were used in the publication. In the course of work for this thesis it has been founded that these conditions need very long reaction times. This can be reduced by higher temperatures, whereas 150 °C led to an unknown side reaction. A temperature of 125 °C was chosen along with the use of bromobenzene as solvent, which forces the equilibrium of the reaction to the side of the products. After 48 h, the crude product was purified by column chromatography to give **7** in a yield of 67%. Likewise to **6**, its reaction to 4-nitroacridine by the use of the *Berthsen* procedure was tested. During the reaction with 3 eq of formic acid, a dark brown solution was formed when the reaction mixture was heated to 190 °C. After 4 h, a black solid remained which is why additional 3 eq of formic acid were added and stirred for two more hours. A 1H NMR spectrum was recorded from a sample of this crude, black compound. Unfortunately, the spectrum showed the complete decomposition of the starting material. The nitro group is most probably not stable towards high temperatures which are needed for the cyclocondensation of the reagents.



Scheme 2.10: A possible approach to 9-methyl-4-nitroacridine derivatives via intramolecular condensation reaction.

To avoid these harsh reaction conditions, it was tried to enhance the reactivity of the diphenylamine derivative. If an aldehyde or ketone group was attached to the *ortho*-position, an intramolecular, nucleophilic attack from the neighbored phenyl ring would be possible. This is

depicted in Scheme 2.10, where 2-acetylaniline and 1-bromo-2-nitrobenzene are used as starting materials. The electron-withdrawing nitro group in *ortho*-position to the bromine atom enhances the nucleophilic attack of the amine. Furthermore, it stabilises the negative charge of the transition state **A**. After the cleavage of the bromide, the second nucleophilic attack to the carbon atom of the ketone should have a smaller activation energy than former intermolecular reactions with formic acid. Various attempts to the formation of intermediate **B** were investigated and are listed in Table 2.2.

Table 2.2: Different attempts to react *ortho*-substituted phenylamines with bromobenzene derivatives.

no.	starting materials		reagents & solvent	reaction conditions	
	phenylamine	bromobenzene		temp.	time
1a			K ₂ CO ₃ , CuI (10 mol%), <i>L</i> -proline (20 mol%) solvent: DMF	130 °C	40 h
1b				90 °C	144 h
2a			K ₂ CO ₃ , CuI (10 mol%), <i>L</i> -proline (20 mol%) solvent: DMF	130 °C	18 h
2b				90 °C	124 h
3a			1) K ₂ CO ₃ , Cu ⁰ (20 mol%), solvent: DME 2) conc. H ₂ SO ₄	85 °C	3 h
3b				110 °C	2 h

For the first two entries, the catalysts and solvents were chosen according to the mentioned investigations by *Fu et al.*^[80] They used similar starting materials but none of them contained an acetyl group at the aromatic systems. The temperature and reaction times have been varied as well as the substitution pattern of the starting materials. The reaction process of the first and second entry was discussed in Scheme 2.10. In all cases, ¹H NMR spectra were recorded of the reaction mixtures. Entry 1 only yielded an unwanted side product whereas 2 showed no conversion of the starting materials, independent of the applied reaction time and temperature. In the third entry, *ortho*-phenylenediamine and bromobenzoic acid were used as starting materials. Additionally, the catalyst was changed to Cu⁰ according to literature procedures.^[81] Here, all ¹H NMR signals of the starting materials were dissipated after 3 h, but the spectrum of the reaction mixture was too crowded to identify one definite product. Since the desired diphenylamine derivative is a dipolar ion, the separation from salts and other byproducts was not feasible. In a second approach, the crude product was directly treated with concentrated H₂SO₄ after the removal of the solvent and heated to 110 °C for 2 h. The strong and hygroscopic acid should favour the cyclocondensation reaction,^[81a] however, only the decomposition of the assumed intermediate was observed.

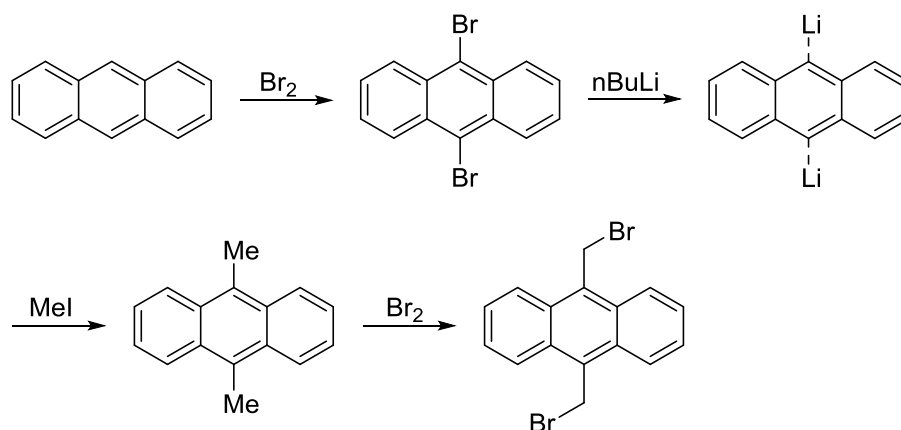
A variety of different attempts to obtain a 4-substituted acridinyl amine were performed. Neither the derivatisation of the acridine system nor the step-by-step formation of suitable intermediates led to the desired compounds. In some cases, the synthesis of intermediates was successful but the purification was too elaborate or the subsequent reaction was not realisable. *Kitahara et al.*

already published the reaction of intermediate **B** to the product **C**,^[82] however, they did not describe the synthesis of the starting material. Additional investigations of these types of reactions need to be done in the future but will not be discussed further in this thesis.

In the following chapters, the synthesis of acridine sensor systems is approached in a different way. A methylene unit between the fluorophore and the receptor allows the use of a more feasible and explored reaction pathway.

2.2.4 4,5-Bis(bromomethylene)acridine (**8**) and 4,5-bis(bromomethylene)-9-methylacridine (**9**)

For the synthesis of the fluorophore-spacer-receptor systems, the first challenge was the introduction of the methylene group, acting as the spacer unit. During the last years, the *Stalke* group has performed intense research in the field of anthracene based fluorophores.^[25] Thereby, a lot of different derivatives containing a methylene spacer unit were developed and synthesised. The reaction pathway to the desired anthracene systems was often realised in the following route (Scheme 2.11).

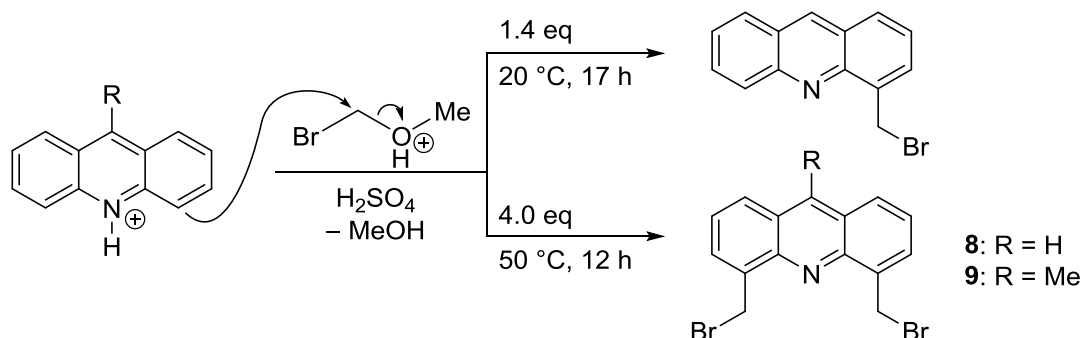


Scheme 2.11: Synthesis route to an anthracene precursor for molecular sensors.

This synthetic concept to the precursor 9,10-bis(bromomethylene)anthracene contains four steps, which implies a high synthetic effort. The bromide acts as a good leaving group in subsequent substitution reactions. Furthermore, they activate the methylene group towards nucleophilic attacks, due to their electron withdrawing properties. That is why in this thesis, the bromomethylene groups should be introduced to the acridine structure as well, but in a more efficient way.

This intention was reported by *Galy* and *Chiron* in 2003, already mentioned in the introduction.^[41] They made use of the reagent bromomethyl methyl ether (BMME), which is able to introduce one or two bromomethylene units to the aromatic system – in one step. The reaction needs to be carried out under strong acidic conditions. By that, the nitrogen atom of the acridine gets protonated and activates the neighbored positions 4 and 5 towards electrophilic substitution. Additionally, the halomethylether gets protonated at the oxygen atom as well, which supports the cleavage of the molecule (Scheme 2.12). With less than two equivalents of BMME and a temperature of 20 °C, the monosubstituted product can be obtained but only in small yields. When an excess of the ether is used (4 eq) with temperatures around 50 °C, the disubstituted acridine is

formed in a yield of 64%.^[41] The latter is the more interesting derivative which synthesis has already been studied in former investigations,^[63] but will again be described below. Furthermore, with the use of 9-methylacridine as starting material, the methyl derivative of the described product has been obtained, too.



Scheme 2.12: Usage of bromomethyl methyl ether for the synthesis of 4,5-bis(bromomethylene)acridine (**8**) and its 9-methyl derivative **9**.

For both preparations, acridine was dissolved in concentrated sulfuric acid and heated up to 50 °C when four equivalents of BMME were added. During the reaction time of 17 h, a significant amount of bromine gas was formed. The use of the strong acid could cause the formation of hydrogen bromide which again can be oxidised to bromine. This possible side reaction makes an excess of the added halomethyl ether useful. The crude yellowish brown product was crushed out by pouring onto ice, after what it was filtered and washed with dem. water. It was dissolved in chloroform, washed with brine and dried over MgSO₄. According to the literature, **8** can be purified by recrystallisation from Et₂O. In some cases, this procedure was almost sufficient, however, a repeated recrystallisation from chloroform was more satisfying. With the latter method, the yield drops down to the half of the reported value of 64%, but resulted in a purer product which was of higher importance with regard to the subsequent reactions. For the work-up of **9**, a column chromatography was applied (PE/EA, 10:1) which gave the desired product in a yield of 54%. The higher yield of **9** in comparison to **8** may be a result of the methyl group which enhances electrophilic reactions at the aromatic system.

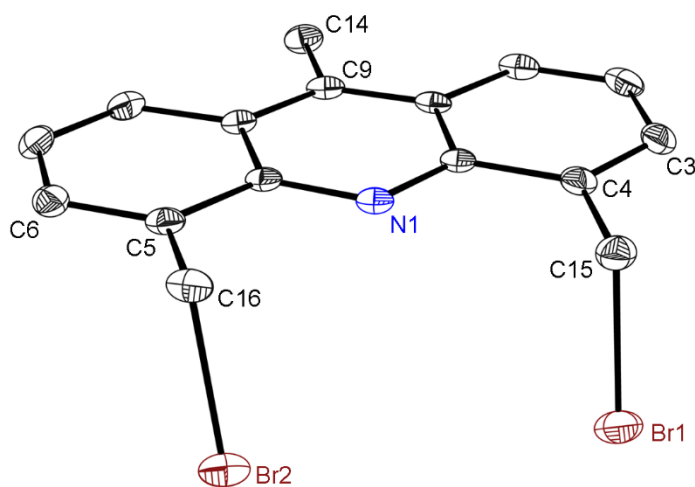


Table 2.3: Selected bond lengths [pm] and angles [°] of **9**.

Br1–C15	198.03(18)
Br2–C16	197.52(17)
C9–C14	151.0(2)
C4–C15–Br1	110.28(12)
C5–C16–Br2	111.72(12)
C3–C4–C15–Br1	–92.33(18)
C6–C5–C16–Br2	97.52(17)

Figure 2.5: Solid state structure of **9** illustrating the asymmetric unit.

In the case of **9**, a recrystallisation from DCM and a storage at $-30\text{ }^{\circ}\text{C}$ gave suitable crystals for X-ray diffraction. Due to their excellent stability and high μ_r value, the compounds crystals were chosen for an absorption comparison study of two different microfocus X-ray sources.^[83] In Figure 2.5, the asymmetric unit of compound **9** which crystallises in the monoclinic space group $P2_1/n$ is shown. The Br–C distances listed in Table 2.3 are slightly longer than the typical bond length of 195 pm ^[84] and their angles to the acridine backbone (C4–C15–Br1 and C5–C16–Br2, respectively) are a bit widened in comparison to the ideal tetrahedral angle. Although the structure is substituted symmetrically at the 4- and 5-positions, the torsion angle of C6–C5–C16–Br2 ($97.52(17)^{\circ}$) deviates stronger from the orthogonal angle of 90° than C3–C4–C15–Br1 ($-92.33(18)^{\circ}$). It is, therefore, more bended towards the inner centre. Differently from expectations, both bromine side arms point to the same direction although they have a high steric demand. The reason for that can be found in the packing of the crystal which is demonstrated in Figure 2.6. The two molecules have an opposite orientation in space and are shifted sideward by one benzene unit. Hence the bromine atoms lay on the same side, the π -systems of the fluorophores could get in closer contact. The distance between two planes generated through the inner six-membered ring of the neighboured acridine derivatives is 347.3 pm . A value around 350 pm has often been observed in publications with stacked fluorophores^[85] likewise in solid state investigations of anthracene derivatives in our working group.^[25d] In these publications, the influence of the packing effects on solid state fluorescence is determined. However, this will not be discussed here since it was not the focus of this thesis.

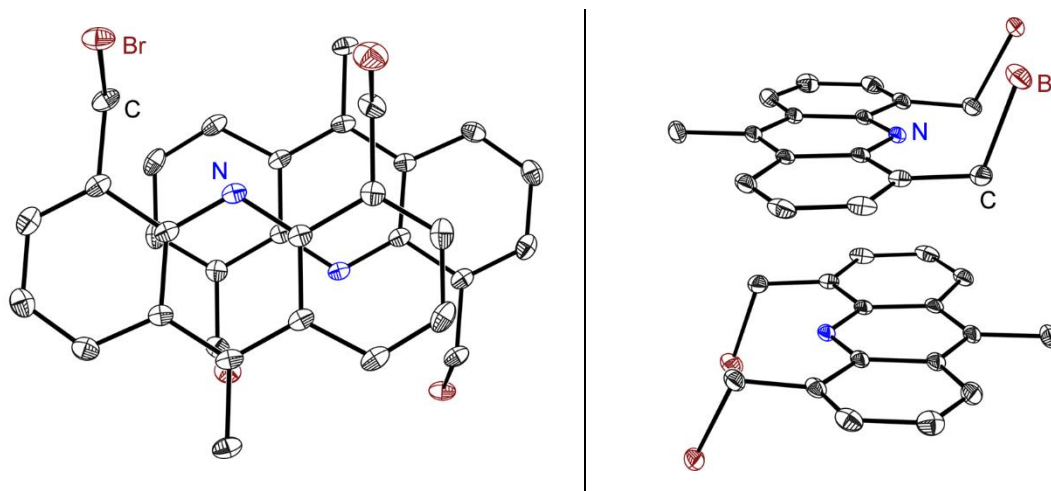
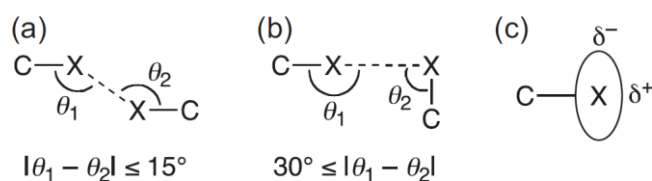


Figure 2.6: Different views of the solid state structures of **9** demonstrating the packing effect of the crystal.

At second glance at the packed structures, some interesting van der Waals interactions of the halogens have been found (Figure 2.7). The solid state structure of **9** involves $\text{CH}\cdots\text{Br}$ and $\text{Br}\cdots\text{Br}$ interactions. Especially the latter are attractive forces that have been utilised in crystal engineering.^[86] These forces are usually of weak character but they can have significant influences to the orientation of the molecules.



Scheme 2.13: Different kinds of halogen...halogen interactions. Type-I interaction (a), Type-II interaction (b), and the polar flattening effect in halogenated organic compounds (c).^[85d]

There are two different preferred geometries possible for the halogen...halogen contacts (Scheme 2.13). In general, these contacts are only termed as an interaction if the interhalogen distance is equal or less than the sum of the van der Waals radii (r_{vdW}). For two bromine atoms, r_{vdW} is 370 pm^[87] which is the same value measured for the Br1...Br1 distance in **9** (370.4 pm). The angles θ_1 and θ_2 are equal (151.9°) due to the intermolecular contact between the same bromine atoms (Br1). The resulting torsion angle of 180° indicates a Type-I geometry in this case, too. These geometries result from the polar flattening effect in halogenated organic compounds which is illustrated in Scheme 2.13, c. Thus, the polarised atoms can develop attractive forces. These structural determinations are rare in the literature concerning halogen-containing acridines,^[88] whereas *Nabeshima* et al.^[85d] have done similar interesting investigations to 2,7-dibromoacridine.

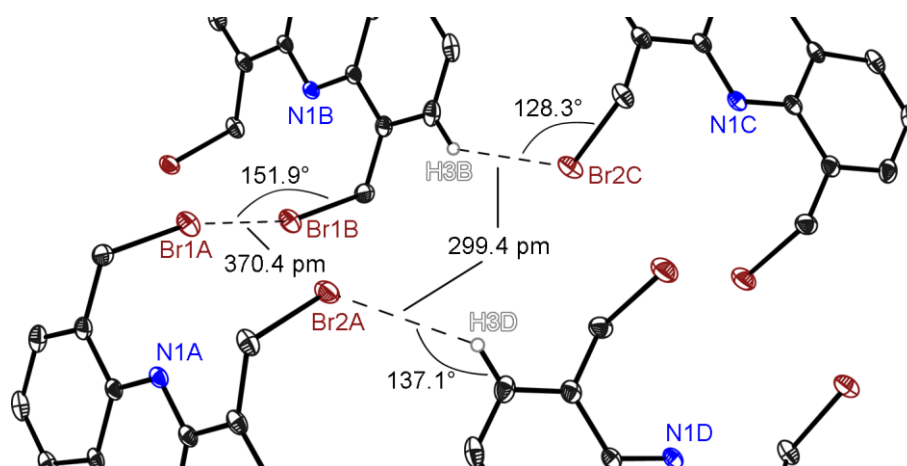


Figure 2.7: Detail of the packed cell visualising the Br...Br and CH...Br interactions.

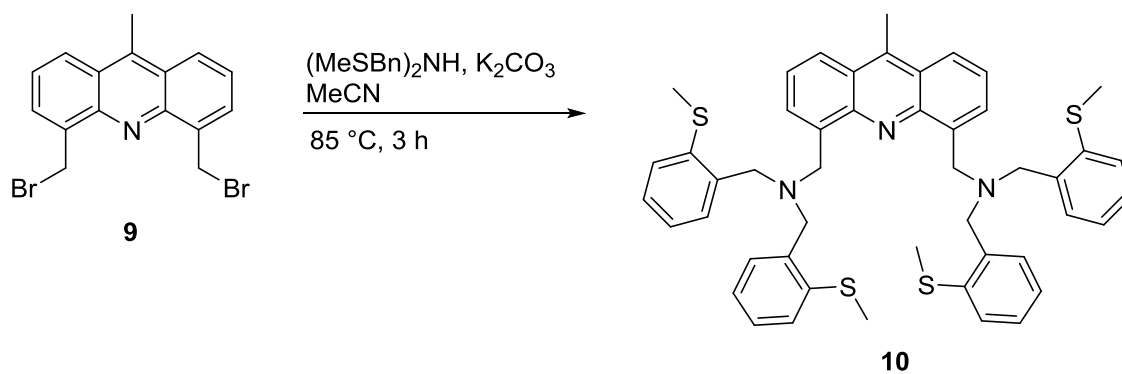
The second halogen interaction (CH...Br) can be termed either as the already discussed van der Waals force or eventually as a weak hydrogen bond. The hydrogen atom has an r_{vdW} value of 120 pm,^[87] resulting in a sum of 305 pm for H+Br. The measured distance in the solid state is 299.4 pm (H3...Br2) which is a smaller value than the van der Waals sum. It needs to be mentioned that the hydrogen atom H3 is not refined freely and, therefore, its geometry properties cannot be discussed in detail. Nevertheless, the interaction with the bromine atom is obvious and the resulting values should be seen as a rough approximation. According to *Steiner*,^[89] even the weak C–H donor groups are able to form “normal” hydrogen bonds. Their length should be less than 320 pm or better 300 pm which is the case here. The C–H...A angle should be above 110° for weak and above 130° for moderate hydrogen bonds. Here, the C–H...Br angle is 137.1° and 128.3° for H...Br–C, respectively.

The structures **8** and **9** feature the needed methylene units as spacer and, furthermore, the halides as a good leaving group. With these precursors in hand, only one more step was needed to replace the bromine atoms with amine receptor units.

2.2.5 4,5-Bis(di(2'-methylthiobenzyl)aminemethylene)-9-methylacridine (10)

A lot of different amine derivatives can be chosen for the substitution of the bromines. Apart from the nitrogen atom of the amine itself, it should have more heteroatoms like nitrogen, oxygen, or sulfur atoms to improve the chelating effect. The side arms can be sterically demanding to reduce the pocket size for a possible coordinated analyte. This should enhance the selectivity of the molecular sensor which is one of its most important properties. Concerning the precursor, the receptor units were introduced in the 4- and 5-positions of the acridine system. This arrangement is a great advantage since the side arms are in close proximity to each other and, therefore, are able to coordinate to the same analyte. This can also improve the selectivity of the system. Moreover, when both amines chelate a target cation, the analyte is forced in close proximity to the centred acridine nitrogen atom which then can act as a further donor side. This principle is demonstrated in the literature^[49, 56-57] and has been discussed in the introduction of this thesis. It would be of great benefit when this sparsely explored coordination motif would lead to a significant shift of the emission wavelength, resulting in a colorimetric response. However, the researchers investigating this phenomenon so far only reported bathochromic shifts of 16^[49] to 19 nm^[90]. The investigation of this possible coordination of the aromatic nitrogen atom to an analyte was one aim of this thesis.

In the following synthesis, each amine receptor is bonded to two benzyl groups bearing methylthio functionalities (Scheme 2.14). The benzyl groups provide the steric demand but can freely rotate due to their methylene bridge. The four sulfur atoms are able to coordinate an analyte, especially large and soft metal ions concerning to the *hard and soft (Lewis) acids and bases* concept (HSAB).^[91]



Scheme 2.14: Synthesis of **10** by a substitution reaction of **9** with bis(2-methylthiobenzyl)amine.

The bis(2-methylthiobenzyl)amine was synthesised by *Finkelmeier* during his PhD thesis in the *Stalke* group.^[25d] For the synthesis of **10**, two equivalents of the amine were given to a suspension of **9** and an excess of K_2CO_3 in acetonitrile. The oil bath was heated up to $90\text{ }^\circ\text{C}$ for three hours. During the reaction, a brown solid was formed which stuck at the surface of the flask. Therefore, the solvent was decanted after cooling to room temperature and the precipitate was washed inside the flask with hexane. The crude product was dissolved in toluene whereat the insoluble inorganic salts were filtered off. After the removal of the solvent under reduced pressure, compound **10** was almost pure with a yield of 48%, but for fluorescence spectroscopy analysis it needs to be highly purified. It was tried to separate the small amounts of side products with the help of column

chromatography (Al_2O_3 , PE/EA, 80:1 \rightarrow 1:20) but only mixed fractions were mainly obtained. In a small amount of test tubes, the purified product could be identified. Small crystals, suitable for X-ray structure determination, were isolated from these tubes (Figure 2.8). **10** crystallises in the triclinic space group $P\bar{1}$ with one molecule in the asymmetric unit. The nitrogen atoms of the amines exhibit a tetragonal environment due to their sp^3 hybridisation with an angular sum of 328.88° (N2) and 329.02° (N3), respectively. The ideal angular sum is 322.41° . Selected bond lengths and angles of the structure are listed in Table 2.4.

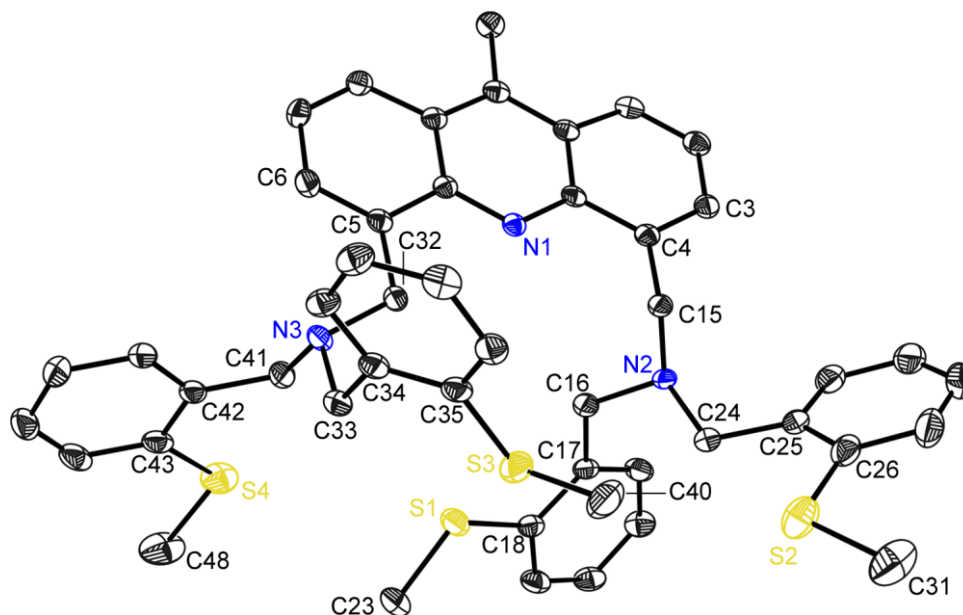


Figure 2.8: Solid state structure of **10**. Hydrogen atoms are omitted for the sake of clarity.

The torsion angles of the methylene bridged amine units vary considerably. The receptor groups at the 4- and 5-position are chemically equivalent, but due to their huge steric demand they turn in different directions. The torsion angle of C3–C4–C15–N2 with a value of 76.7° illustrates the rotation of the amine N2 more towards a perpendicular arrangement to the aromatic plane. In comparison to that, the amine N3 lies almost in the acridine plane, with an angle of 11.5° (C6–C5–C32–N3).

Table 2.4: Selected bond lengths and angles of **10**.

Bond [pm]		Angle [$^\circ$]		Torsion angle [$^\circ$]	
N2–C15	148.1(2)	C4–C15–N2	113.34(14)	C3–C4–C15–N2	$-76.7(2)$
N2–C16	147.0(2)	C15–N2–C16	109.48(13)	C6–C5–C32–N3	$11.5(2)$
N2–C24	146.6(2)	C5–C32–N3	112.65(14)	C15–N2–C16–C17	$171.38(14)$
N3–C32	146.5(2)	C32–N3–C33	110.03(13)	C15–N2–C24–C25	$-70.98(18)$
N3–C33	147.1(2)	C18–S1–C23	103.30(10)	C32–N3–C33–C34	$64.75(19)$
N3–C41	146.7(2)	C26–S2–C31	103.27(12)	C32–N3–C41–C42	$-159.72(14)$
S1–C18	177.2(2)	C35–S3–C40	103.07(10)	C23–S1–C18–C17	$176.43(15)$
S1–C23	180.2(2)	C43–S4–C48	104.04(12)	C31–S2–C26–C25	$167.30(15)$
S4–C43	176.5(2)			C40–S3–C35–C34	$-166.25(15)$
S4–C48	179.5(2)			C48–S1–C43–C42	$168.05(15)$

Nevertheless, both receptors show to the same side of the aromatic structure, which is demonstrated in Figure 2.9, left. The N–C distances are in good agreement with typical bond length for sp^3 hybridised atoms (147 pm). The same is true for the S–C(sp^2) bond lengths whereas the S–C(sp^3) distances are all shortened (typical values are 176 pm and 183 pm, respectively).^[84] In Table 2.4, the longest (S1) and shortest (S4) values are listed for the sulfur environments. The C–S–C angles are quite similar and all smaller than the ideal tetrahedral angle due to the strong steric demand of the two lone pairs at each sulfur atom. Additionally, all torsion angles containing the sulfur and nitrogen atom are listed to visualise the difference of the geometry, especially in the case of the amines.

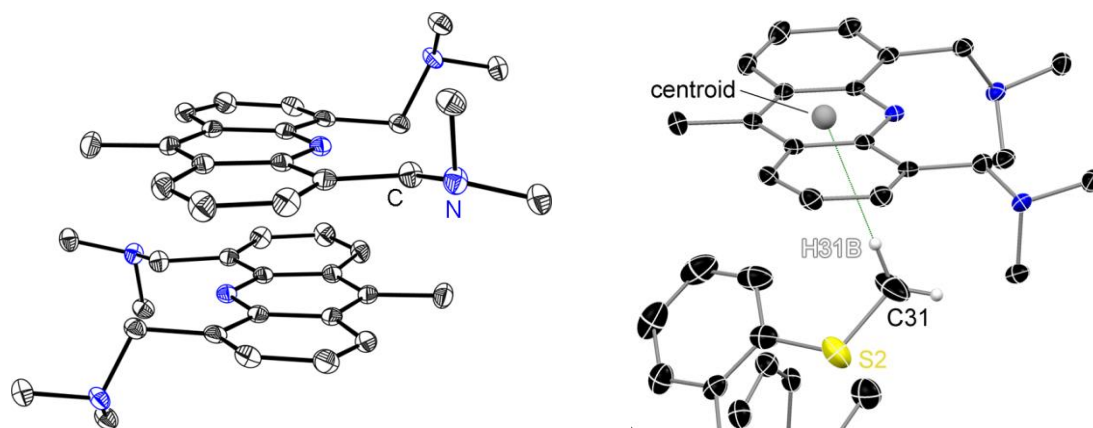


Figure 2.9: Left: side view of the packing effect of the acridine systems in **10**; right: visualising the intermolecular CH \cdots π -interaction. The positions of the hydrogen atoms at C31 were refined freely for the discussion.

The solid state structure of the precursor **9** showed a packing effect of the acridine backbone. The same is true for this structure, demonstrated in Figure 2.9, left. The distance between the two aromatic π -systems is 339.6 pm, an even smaller value than for **9** (347.3 pm). Likewise, the acridine units are pointing in opposite directions, however, they are less shifted resulting in a higher overlap. This could explain the stronger attraction. Furthermore, one of the phenyl rings bonded to C41 shows an additional overlap to its next counterpart (Figure 2.10) with a distance of 356.5 pm.

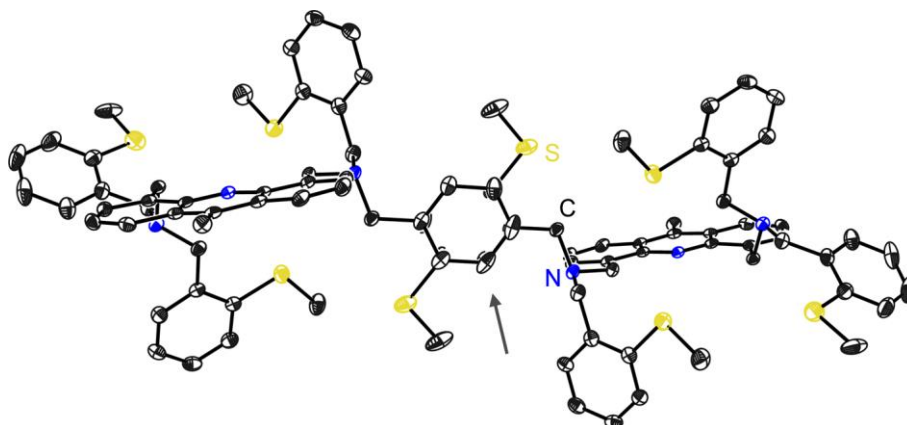


Figure 2.10: π - π -overlap of two phenyl groups marked with an arrow.

Another interaction which stabilises the geometry of the solid state structure is an intermolecular CH $\cdots\pi$ -interaction of a hydrogen to the centre of an acridine ring. The hydrogen atom (H31B) is linked to the methyl group of S2. To determine the strength of this interaction, a centroid was calculated in the centre of the inner six-membered ring of acridine. The distance between H31B and the centroid is 283(2) pm and 258(2) pm orthogonal to the aromatic plane. The distances are in line with the averaged literature value of 272(18) pm, calculated by 9520 entries in the CSD database with CH $\cdots\pi$ interactions.^[92] The CH $\cdots\pi$ angle to the centroid is 175(2) $^\circ$. This angle is nearly linear indicating a strong interaction for this type of phenomenon.

The pureness of the single crystals obtained from the column chromatography allowed analysing the compound by fluorescence spectroscopy.

2.2.6 Luminescence procedure and sample preparation

Before realising the fluorescence measurements, several important issues have to be considered carefully. At first, a series of common errors in sample preparation are possible. The compound to be analysed has to be absolutely pure since small impurities can have a significant effect on the fluorescence spectra. An aromatic side product can overlap with the actual emission spectrum and alters the curve. Additionally, an incorrect excitation wavelength could be used due to a wrongly assigned spectrum. That is why it is useful to record spectra at different excitation wavelengths to determine if the emission spectrum remains the same. This should be the case since emission spectra are usually independent of the incident light.^[93]

For appropriate measurements, the correct concentration level of the samples needs to be set. On the one hand, a strongly diluted sample can lose too much intensity which results in a bad signal-to-noise ratio. On the other hand, too strong concentrated samples are sources of several

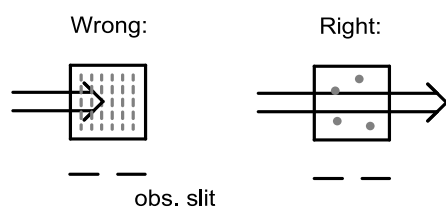


Figure 2.11: Absorption of the incident beam at highly concentrated samples (left).

significant errors. The absorption of the fluorophore leads to a reduction of the emitted light at too high concentrations (Figure 2.11), which is termed the inner filter effect. Furthermore, a large amount of molecules results in a higher number of collisions of excited fluorophores. By that, the absorbed energy decays in a non-radiative pathway whereby the molecules return to their ground state.^[7] This suppresses the actual intensity of the measured sample.

Some fluorophores like pyrene show another concentration-dependent behaviour. If sufficient molecules are present in solution, they can form excited-state dimers, called ‘excimer’.^[19, 94] Thus, new excimer peaks at higher wavelength show up at the emission spectrum. This topic will be discussed more intense in chapter 2.2.11.

The right range of concentration needs to be determined experimentally by titration of the analyte with the used solvent. These dilution experiments have already been carried out in the master thesis with comparable compounds.^[63] The resultant concentration ranges differ for each fluorophore, which is why the low concentration of $1.0 \cdot 10^{-5}$ M was chosen. At this value, the intensity decreases in linear relation with the decrease of concentration.

The next important issue was the choice of the solvent. It is essential to have completely clear solutions without any precipitates. Therefore, one demand to the solvent is the ability to dissolve organic compounds (molecular sensor) as well as inorganic metal salts (target ions). Otherwise, the used concentrations would differ in the experiment or remaining solids could scatter the incident beam, distorting the results. A second demand deals with the possibility to use a molecular sensor in medicinal applications. For this purpose, e.g. the detection of metal ions in blood, the sensor should be able to operate in water. Hence, this is a very ambitious goal and causes more challenges which will be discussed later on in this thesis (Chapter 2.2.14). A good alternative to that is the polar protic solvent methanol. It is able to dissolve most organic compounds and a wide range of metal salts. For a good comparison of the spectroscopic results, every tested metal ion should have the same counter anion. It should not be able to strongly complex the cations like acetate or carbonate ions, avoiding a competition with the added sensor. Available for a wide range of metal salts and soluble in methanol are the metal bromides and, therefore, mainly used in this thesis.

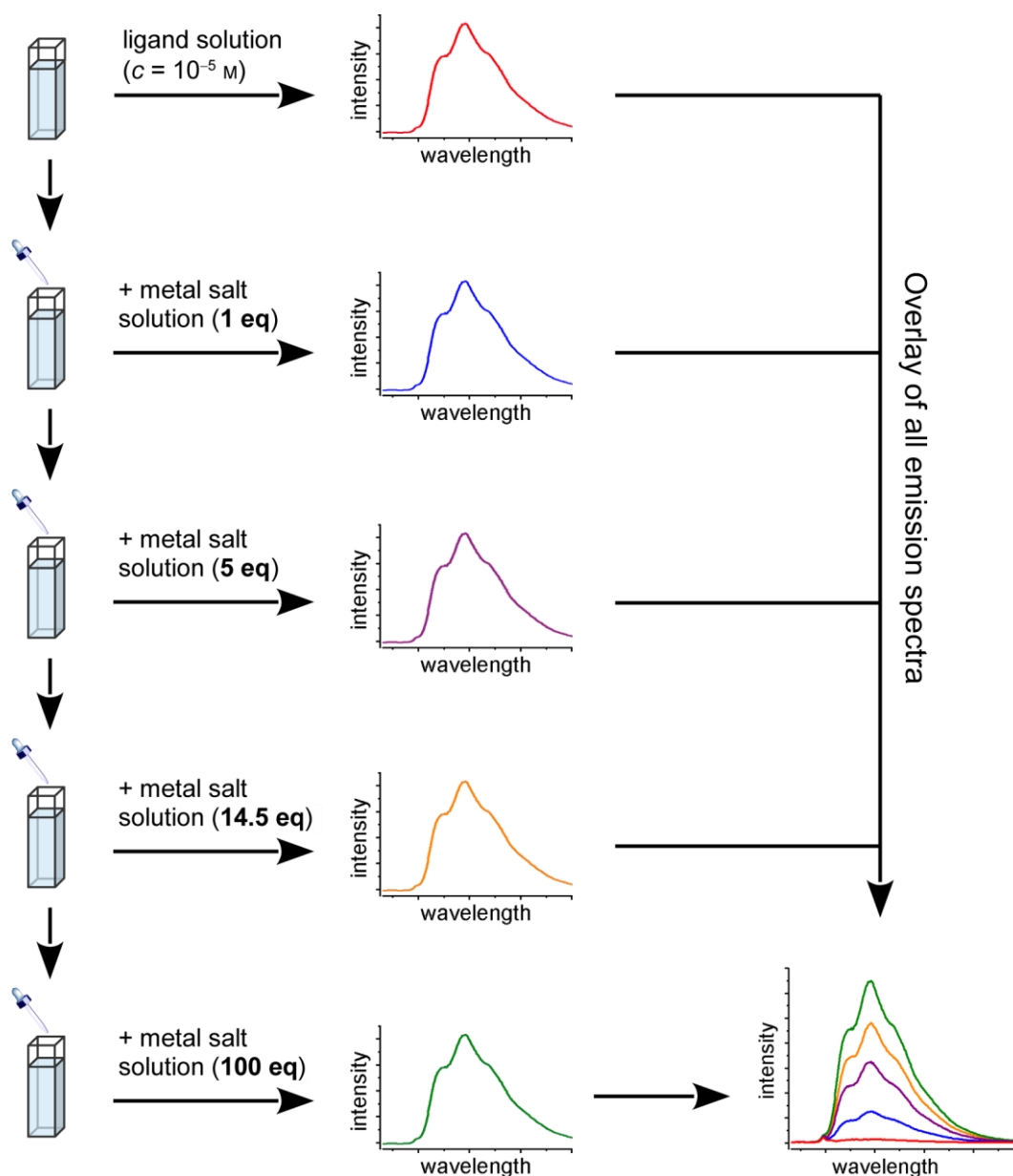


Figure 2.12: Screening procedure for metal ions used in this thesis.

The synthesised compounds with the “fluorophore-spacer-receptor” structure had to be tested for their possibility to work as a molecular sensor for metal cations. To get a wide and quick overview if the addition of an analyte alters the emission spectrum of a sensor system, a screening procedure was established (Figure 2.12). Sixteen different metal ions were chosen across the periods of elements (Figure 2.13). Each was added as a solution to the dissolved ligand in four steps in a range from 1 to 100 equivalents. If any effect was observed, a more intense study of this analyte was performed.

1																	18
H	2											13	14	15	16	17	He
Li	Be											B	C	N	O	F	Ne
Na	Mg	3	4	5	6	7	8	9	10	11	12	Al	Si	P	S	Cl	Ar
K	Ca	Sc	Ti	V	Cr	Mn	Fe	Co	Ni	Cu	Zn	Ga	Ge	As	Se	Br	Kr
Rb	Sr	Y	Zr	Nb	Mo	Tc	Ru	Rh	Pd	Ag	Cd	In	Sn	Sb	Te	I	Xe
Cs	Ba	La	Hf	Ta	W	Re	Os	Ir	Pt	Au	Hg	Tl	Pb	Bi	Po	At	Rn

Figure 2.13: Periodic table of the chemical elements. Metalloids and non-metallic elements are grey-shaded. The utilised metal ions for the screening procedure are marked in green.

The dissolving of the metal salts was carried out with the same solvent as for the ligand, unless it was stated otherwise. As described before, the most frequently used solvent was methanol, but in some cases tetrahydrofuran, dichloromethane, or even water were used, too. To be able to add an equivalent range from 1 to 100 into the small cuvettes, two different concentrated solutions of the metal salts were prepared (Table 2.5). The quantities shown in the legend of the fluorescence spectra are added up values (from bottom to top). This is valid for all experiments discussed in this thesis.

Table 2.5: Used concentrations for the spectroscopic investigations.

	ligand	salt: 1 eq	5 eq	14.5 eq	100 eq
c [mol/l]	$1 \cdot 10^{-5}$	$2.4 \cdot 10^{-4}$	$2.4 \cdot 10^{-4}$	$2.28 \cdot 10^{-3}$	$2.28 \cdot 10^{-3}$
V [ml]	2.4	0.1	0.4	0.1	0.9

2.2.7 Luminescence properties of 4,5-bis(di(2'-methylthiobenzyl)aminomethylene)-9-methylacridine (10)

The first two luminescent experiments which should be carried out with a new compound are the recordings of an excitation and an emission spectrum. For the excitation spectrum, the detector is set to a specific emission wavelength whereas the sample solution is irradiated at varied energy of light. From this spectrum, the information for the setting of the proper wavelength for the record of the emission spectrum can be gained. In this case, the sample is irradiated at the defined wavelength and the detector records the emitted light.

In the previous chapter, methanol was described as the solvent of choice for the metal ion screening. In this case, acetonitrile was used to dissolve the metal salts and, due to a better solubility, tetrahydrofuran for the ligand. These solvents form less strong solvent shells around the metal ions in comparison to methanol. Otherwise, the high polar methanol would be in strong competition to the amine groups of the chemical sensor. Since in this case only 1.4 mg of purified crystalline material of **10** could be isolated, only a few spectroscopic experiments could be

performed. With this amount, an overall sample volume of 35 ml was obtained with a concentration of 10^{-5} M. That is why the conflict with a too polar solvent should be reduced. THF was chosen because of its less polarity in comparison to methanol and it readily dissolves the ligand.

The excitation and especially the emission spectrum of **10**, depicted on the left side of Figure 2.14, show a strongly broadened band. These unstructured curves can appear when only small energy distances are present between the vibrational states which cannot be resolved by the spectrophotometer.

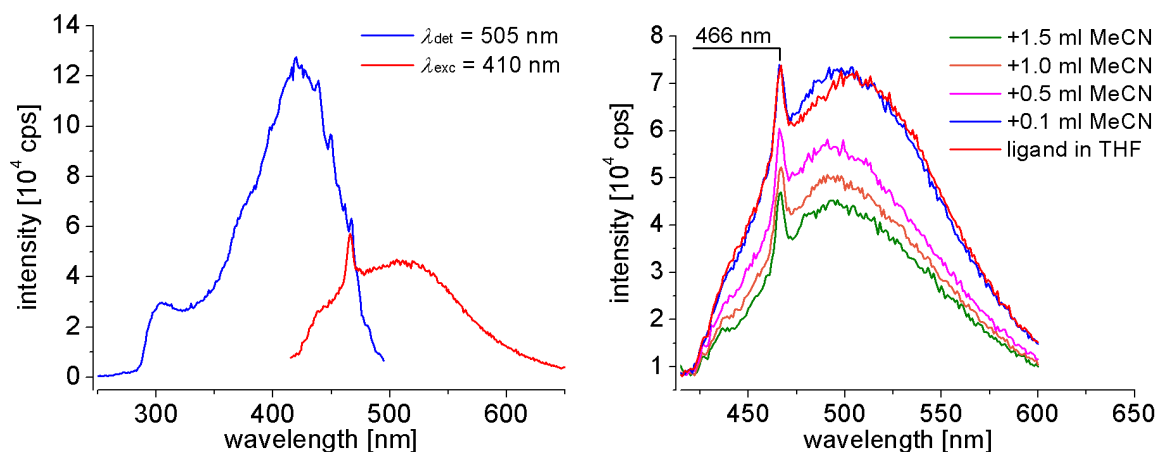


Figure 2.14: Left: Excitation (blue: $\lambda_{\text{det}} = 505$ nm) and emission (red: $\lambda_{\text{exc}} = 410$ nm) spectrum of **10** in THF (10^{-5} M); right: emission spectra of **10** in THF with addition of acetonitrile ($\lambda_{\text{exc}} = 410$ nm).

In comparison to the luminescence properties of pure acridine (Figure 2.15, left), the emission intensity is lowered by a factor of 11, which hints to a working PET effect. Furthermore, the emission band is shifted to longer wavelengths (bathochromic shift) for about 100 nm. Thus, it lies more in the visible region which makes it easier to detect the altering of the emission intensity by the naked eye.

The noticeable peak at 466 nm is a result of Raman scattering of the used solvent tetrahydrofuran. On the one hand, these peaks can be identified by comparison with literature data,^[95] on the other hand, by varying the excitation wavelength. Signals due to Raman scattering move their position in dependency of the incident light, in contrary to the emission of the fluorophore.

On the right side of Figure 2.14, emission spectra are depicted of a THF solution of **10** while titrated with acetonitrile. The added volumes are equal to the titration of the metal ions. Thereby, the altering of the emission intensity by dilution can be examined as well as possible changes by mixing two different solvents. Especially in the case of charged compounds or with the presence of strong dipoles, the polarity of the solvent can significantly influence the emission wavelength. Here, only the expected decrease of intensity was observed by reducing the sample concentration.

In the next experiment, it was tested if the PET effect is working at all. As already mentioned, the first indication is the low emission intensity of the ligand in comparison to pure acridine. To check if the fluorescence can be switched back on, the lone pairs of the nitrogen atoms were forced in a bonding situation to another atom. An appropriate way for this is the protonation of the amines with an acid. Therefore, two different concentrated solutions of diluted hydrochloric acid

were prepared (0.001 M and 1 M) and were added dropwise to the ligand solution (Figure 2.15, right). One drop out of a glass pipette has an approximate volume of 25 μl which was determined experimentally. Nevertheless, the indications of equivalents in the legend are rounded values.

Regarding the emission spectra, there is a noticeable decrease of intensity by adding the first two amounts of HCl (0.001 M). After changing to 1 M concentrated acid, the emission intensity rises, but only slightly higher than the beginning value. This could assume a poor working PET effect but the strong hypsochromic shift of the wavelength needs to be taken into account.

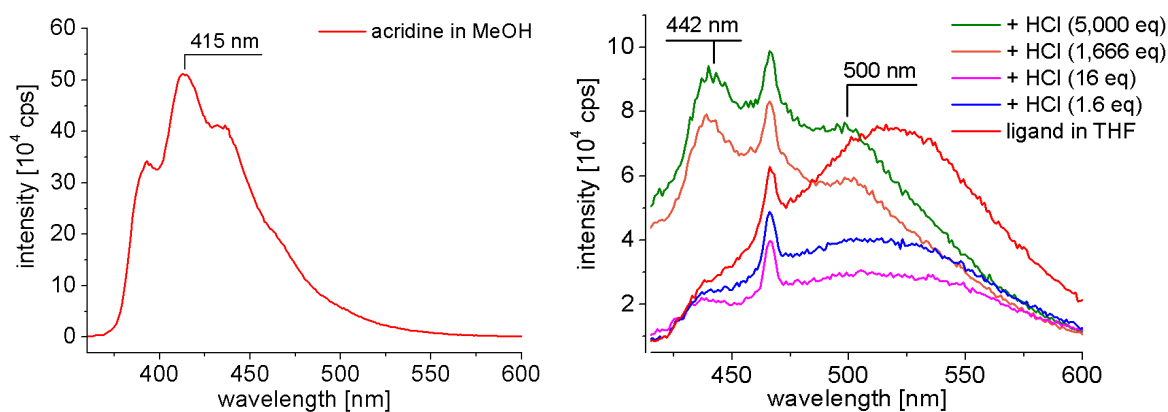


Figure 2.15: Left: Emission spectrum of acridine in methanol (10^{-5} M, $\lambda_{\text{exc}} = 353$ nm); right: Emission spectra of **10** in THF (10^{-5} M) titrated with aqueous hydrochloric acid at one defined wavelength ($\lambda_{\text{exc}} = 410$ nm).

The spectra were recorded at a defined excitation wavelength of 410 nm, according to the excitation spectrum of the pure ligand (Figure 2.14, left). If the excitation spectrum is altered significantly by the addition of acid, the wavelength needs to be adjusted. What can be seen in the right spectrum of Figure 2.15 is a rising new band at 442 nm. This wavelength was chosen for recording a second excitation spectrum and is depicted in Figure 2.16 (left, green curve) in comparison to the wavelength used before (blue curve). Both spectra were recorded with an excess of HCl.

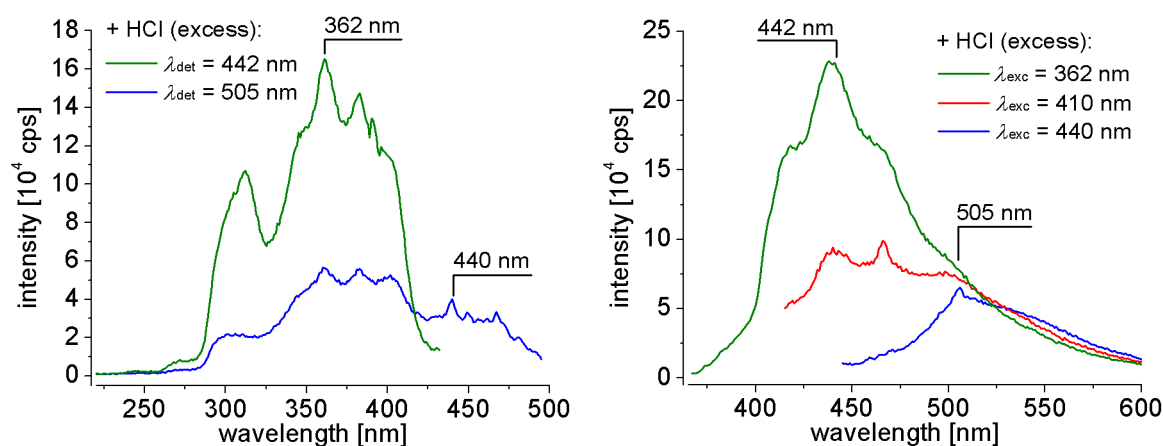


Figure 2.16: Excitation spectra (left: green: $\lambda_{\text{det}} = 442$ nm, blue: 505 nm) and emission spectra (right: green: $\lambda_{\text{exc}} = 362$ nm, red: 410 nm, blue: 440 nm), measured at different wavelengths after addition of aqueous HCl to **10** in THF (10^{-5} M).

On the basis of this new spectrum, the more appropriate excitation wavelength of 362 nm was adjusted and compared with emission spectra at different wavelengths (Figure 2.16, right). Now, the emission curve has a well-defined shape with a strong intensity enhancement as expected for the protonation of the amine receptors.

As mentioned before, the amount of sample solution was only sufficient for several investigations. That is why the two heavy metal salts cadmium and mercury bromide were chosen which are classified as soft metal ions according to the HSAB concept of Pearson.^[91] The sulfurous receptor units of the ligand should rather be able to coordinate to these analytes.

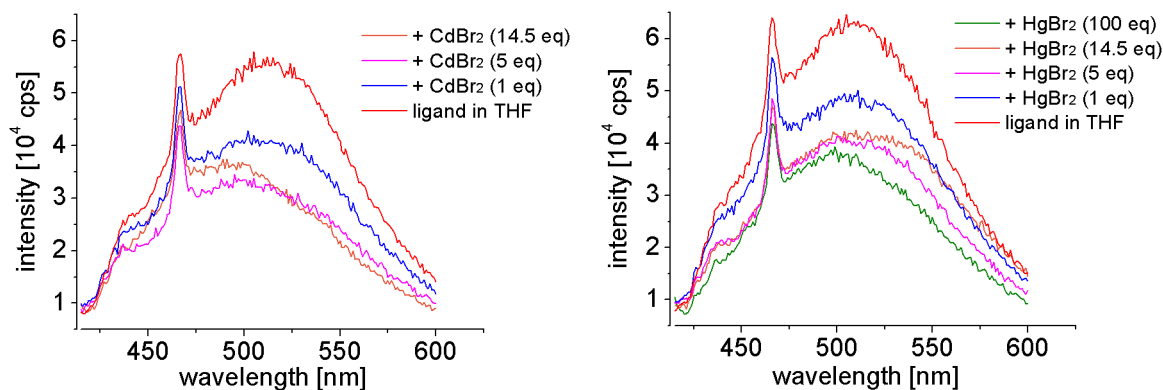


Figure 2.17: Emission spectra of **10** in THF (10^{-5} M, $\lambda_{\text{exc}} = 410$ nm) with addition of CdBr_2 (left), respectively HgBr_2 (right); both metal salts were dissolved in MeCN.

Unfortunately, the titration of Cd^{2+} and Hg^{2+} solutions in MeCN did not alter the emission spectrum of **10** (Figure 2.17). The decrease of intensity can directly be attributed to the dilution effect shown in Figure 2.14, right. In the case of CdBr_2 , only a maximum of 14.5 eq could be added to the sample cuvette, due to the worse solubility of the salt in MeCN. Hence, there is no indication that the addition of a larger amount of metal ion would change the spectra significantly. Having a closer look at the receptor side arms, the assumption could be made that the methylthio benzyl groups could coordinate metal ions outside the range of the amines. If they do not coordinate to the analyte, no molecular response can be observed in the emission spectrum (on-switch) since they are responsible for the PET effect. To get an idea about what kind of structure could get formed by adding a metal ion to compound **10**, the computer program Avogadro v1.1.1 was used.^[96] The x,y,z-file of the solid state structure was imported with the software and the geometry was optimised using the universal force field (UFF). After a cadmium ion was added close to the side arms, the geometry was optimised again. (Figure 2.18). In the case of mercury, similar observations have been made and are not shown here. First of all, it needs to be clarified that the geometry optimisation by the computer program does not necessarily reflect the solid state structure or even the conformation in solution. Hence, it can give a hint to a possible interaction of the ligand with metal ions. It is interesting to see that the cadmium ion is arranged between two of the four sulfur atoms, possibly interacting with their lone pairs. The other sulfur atoms are not able to rotate around their S–C axis to coordinate to the metal ion since the phenyl rings would otherwise get in close contact to other groups. The coordination sphere of the Cd^{2+} ion is filled with at least three hydrogen bond interactions, which are not shown here.

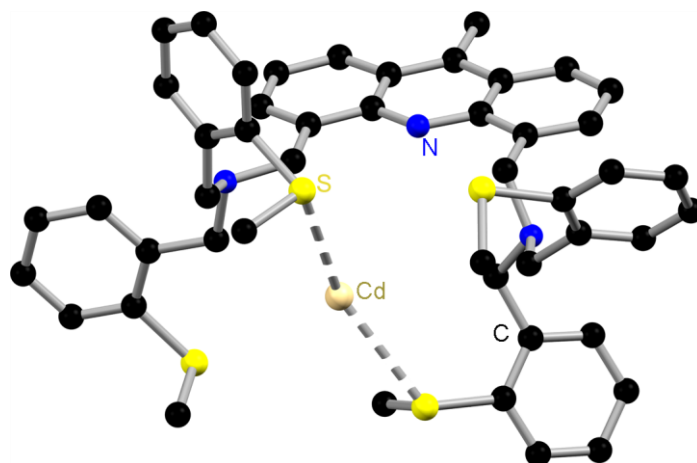


Figure 2.18: Possible interaction of **10** with a Cd^{2+} ion. The geometry was optimised with Avogadro v1.1.1^[96] using the universal force field.

What more can be seen are the long N–Cd distances which could explain the lack of changes in the spectra. Their lone pairs even point in the opposite direction which is due to the steric demand of the large receptor units and because of the repulsion of the multitude of hydrogen atoms. As mentioned before, without a coordination of the nitrogen lone pair to the analyte, the quenching mechanism of the PET effect is still present and no notable fluorescence emission can occur.

In conclusion, a new acridine derivative was synthesised and could be characterised completely by analytical methods like NMR spectroscopy and mass spectrometry. The X-ray diffraction of the single crystal provided structural information about the potential molecular sensor and, especially, the arrangement of the six possible donor atoms of the chelate. The compound was furthermore investigated by fluorescence spectroscopy and tested for metal ion recognition by the example of Cd^{2+} and Hg^{2+} ions. The envisaged PET effect by the use of the fluorophore-spacer-receptor system was proven and could be switched off by protonation of the amines. Further measurements with a variety of analytes would have been interesting. However, the synthesis of the amine itself and the subsequently synthesis of the target compound was declared as a too elaborate procedure considering the sparsely promising results.

2.2.8 4,5-Bis(*N,N',N'*-trimethylethylenediaminemethylene)acridine (**11**) and its 9-methyl derivative (**12**)

On the basis of the results of the investigation of **10**, the amine *N,N',N'*-trimethylethylenediamine (H-TrMEDA) was chosen for the substitution of the bromine atoms at the 4,5-positions. It has a less steric demand and its ethylene group offers more flexibility in comparison to the phenyl containing substituent. Another substantial factor is the selection of a receptor containing only nitrogen atoms. This improves the chance to coordinate a target ion by the PET initiating amine groups. Heteroatoms like sulfur have a different target affinity due to their large and high polarisable electron shell. This could lead to the possibility that they do not share a target ion with the smaller and harder nitrogen atoms. According to the receptor unit, various examples can be found in the literature,^[31, 98] illustrating the good chelating effect of the amine. In Figure 2.19, a very promising compound is illustrated published by *Czarnik et al.*^[97]

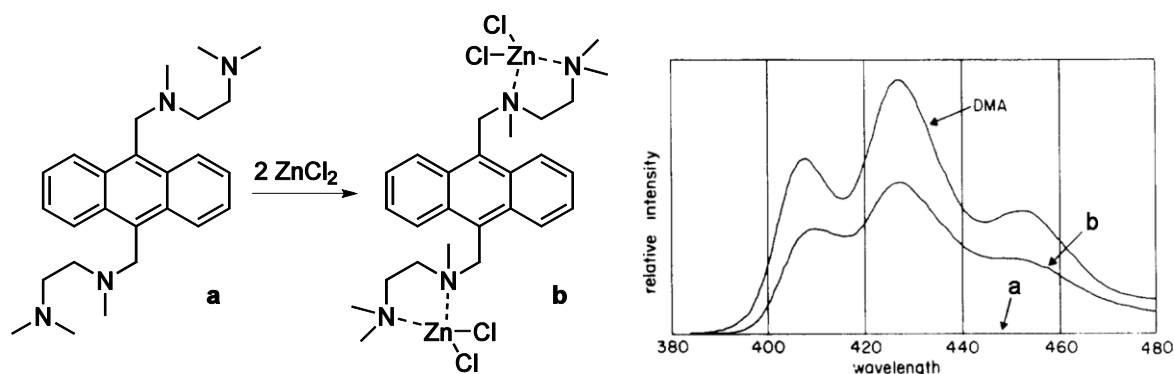
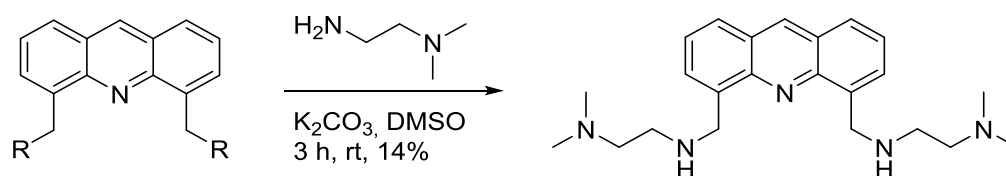


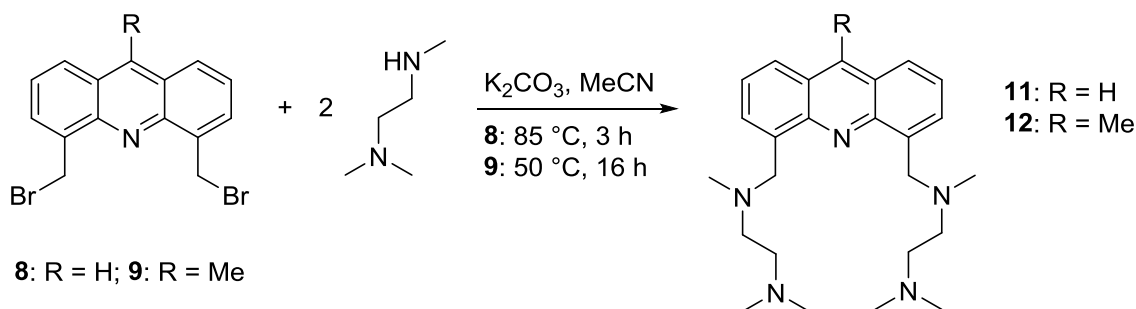
Figure 2.19: Left: Proposed coordination motif of bis(tmeda)anthracene with ZnCl_2 ; Right: Fluorescence emission spectra of compounds **a**, **b**, and 9,10-dimethylantracene (DMA) in acetonitrile (10^{-4} M).^[97]

They are using the related fluorophore anthracene and the same quenching mechanism (PET). When the authors add ZnCl_2 to a solution of 9,10-bis(tmeda)anthracene in acetonitrile, the emission intensity of the system is enhanced by a factor of 1000. With acridine as fluorophore unit, only one similar structure could be found in the literature, published by *Sapi et al.* in 2009 (Scheme 2.15).^[99] The aim of the authors was the evaluation of the derivatives as telomeric G-quadruplex binding agents. Therefore, no information was available about their sensing properties for e.g. metal ions.



Scheme 2.15: Synthesis of 4,5-bis(N,N' -dimethylethylenediaminemethylene)acridine ($\text{R} = \text{Cl}$).^[99] 2.2 equivalents of the primary amine were used.

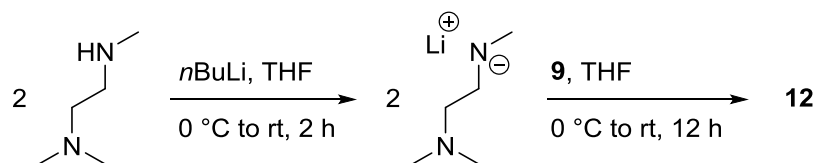
They synthesised several 4,5-bis(dialkylaminoalkyl)-substituted acridines starting from the hydroxymethyl ($\text{R} = \text{OH}$) or halogenomethyl derivative ($\text{R} = \text{Cl}, \text{Br}$). In this thesis, the reaction pathway was modified at various points. As already used before, the bromomethylene derivative as starting material should lead to higher yields because of the better leaving group (Br vs Cl). The solvent DMSO is exchanged by acetonitrile which allows a direct work-up with brine to remove the excess of salt. Secondly, it can be more easily removed under reduced pressure. However, the main important part is the choice of a primary or secondary amine. Primary amines tend to undergo oligomeric reactions,^[42] which is why the amine H-TrMEDA was chosen for this synthesis.



Scheme 2.16: Reaction pathway to the TrMEDA derivatives **11** ($\text{R} = \text{H}$) and **12** ($\text{R} = \text{Me}$).

Another positive benefit is the +I effect of the methyl groups. They push electron density into the nitrogen atoms and, therefore, enhance the donor ability of their lone pair. This is crucial for an efficient receptor unit. Both derivatives **8** and **9** were used as starting materials, whereas **8** has already been used for the synthesis of **11** in the master thesis.^[63] In this thesis, the synthesis has to be optimised and the fluorescence measurements have to be repeated because the first where so low that the material could not be obtained in useful quantities and in the letter there were some systematic errors identified. The synthesis was performed several times with slight changes in the reaction temperature, time and used solvent. It turned out that the reaction conditions in Scheme 2.16 were the best. Reaction temperatures below 50 °C did not lead to the desired product over a couple of days. Unfortunately, the yield of **11** could only be improved to 14%. After the extraction of the product with ethyl acetate in a brine solution, the ¹H NMR spectrum showed some small but unwanted signals left. Since they were especially in the aromatic region, this side-product could affect the fluorescence studies. However, every attempt to remove this compound was unsuccessful. The column chromatography could in some cases reduce the amount of the side-product but always along with a strong reduction of the yield. Other attempts like the quaternisation of the product or the precipitation with a zinc salt were not satisfying. Since **11** is an oily product, a (re-)crystallisation could not be implemented.

The synthesis of the methyl derivative **12** was carried out in MeCN at 50 °C with an excess of K₂CO₃ and 2.1 equivalents of the amine. The reaction mixture was stirred for 16 hours and afterwards purified by column chromatography on alumina. This procedure gave a yield of 17% which was the highest value along with a pure product.



Scheme 2.17: Second approach to **12** with *n*BuLi and *N,N',N'*-trimethylethylenediamine (H-TrMEDA).

Since the yields of the desired products were not very pleasing, a second approach for the synthesis of **12** was tried (Scheme 2.17). Therefore, the used amine was deprotonated before with the strong base *n*-butyl lithium and was afterwards added to the dissolved acridine derivative **9**.

This attempt yielded a variety of side-products which reduced the solubility in the commonly used NMR solvents CDCl₃ and DMSO-*d*₆. However, the ¹H NMR spectrum of the reaction mixture showed an almost complete conversion of the starting material and most likely signals of the desired product (Figure 2.20, b). As can be seen from the comparison of the spectra (b) and (c), the quantity of non-defined signals using *n*BuLi is higher than with the common used and milder base K₂CO₃. This is why the second approach to **12** was no promising alternative.

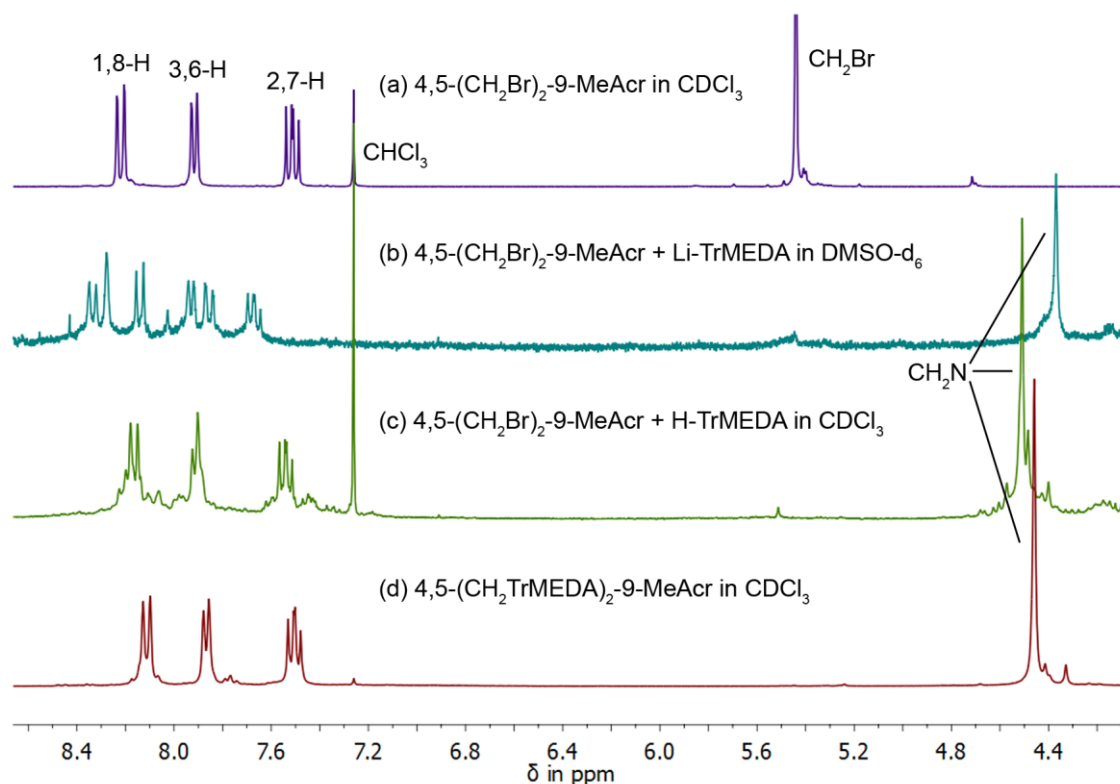


Figure 2.20: Illustration of the ^1H NMR spectra of the starting material **9** (a) and the purified product **12** (d). The spectra in-between compare the conversion of **9** with the lithiated amine (b) and with K_2CO_3 and H-TrMEDA (c); both are measured out of the reaction mixture before purification.

2.2.9 Luminescence properties of 4,5-bis(N,N',N' -trimethylethylenediamine-methylene)acridine (**11**)

As mentioned before, **11** has already been synthesised during the master thesis.^[63] However, the fluorescence measurements were performed with an excess of $n\text{Bu}_4\text{NBF}_4$ at that time, to keep the ionic strength constant. Later investigations showed that this salt contained impurities which led to an unintended protonation of the ligand and distorted results.

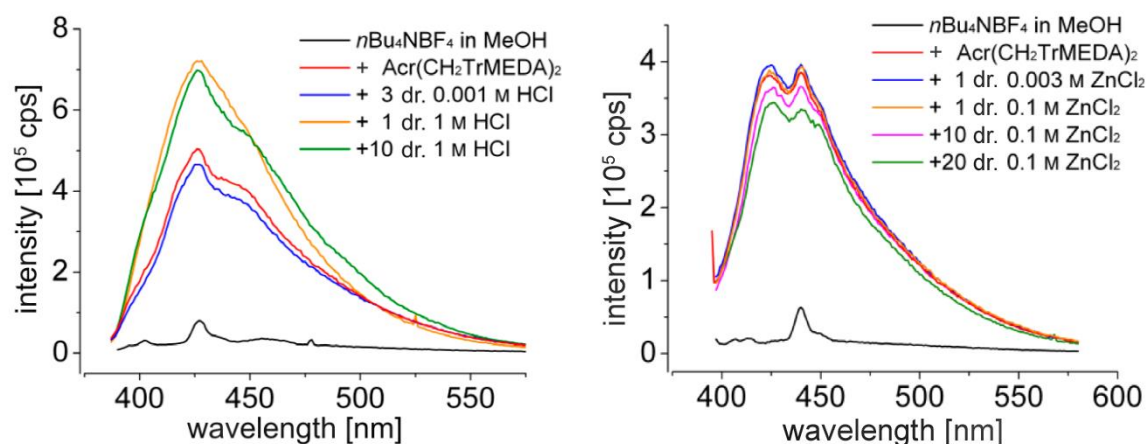


Figure 2.21: Former investigations to **11** in MeOH ($c = 1 \cdot 10^{-4} \text{ M}$, $\lambda_{\text{exc}} = 380 \text{ nm}$) with an excess of $n\text{Bu}_4\text{NBF}_4$.^[63] Left: addition of aqueous HCl; right: addition of ZnCl_2 .

Actually, the ligand **11** should show similar fluorescence properties like **10** as its structure has the same “fluorophore-spacer-receptor” design. Therefore, only less emission intensity should be expected for a 10^{-4} M solution in methanol. The starting intensity of $5 \cdot 10^5$ cps (red line) is, however, very high and is only slightly enhanced with an excess of aqueous hydrochloric acid (Figure 2.21, left). Consequently, a screening procedure with a variety of metal salts did not alter the spectra significantly, exemplarily illustrated by a titrating experiment with ZnCl_2 (Figure 2.21, right).

In this thesis, it was of great interest whether **11** would react to different analytes when the right conditions are applied. The $n\text{Bu}_4\text{NBF}_4$ salt has been left out with regard to the noted problem and the concentration was lowered to a 10^{-5} M solution in methanol. The resulting emission spectrum (Figure 2.22, left) differs significantly by its intensity ($<1 \cdot 10^4$ cps) and wavelength in comparison to the spectrum depicted above. Without the protonation of the amines, the PET effect seems to work as expected and quenches the fluorescence emission. The highest peaks at 405 nm for the excitation spectrum and 421 nm for the emission spectrum are a result of Raman scattering of the used solvent.^[100] The broad band of the emission spectrum has its maximum at about 462 nm which is less red-shifted as compound **10** (505 nm).

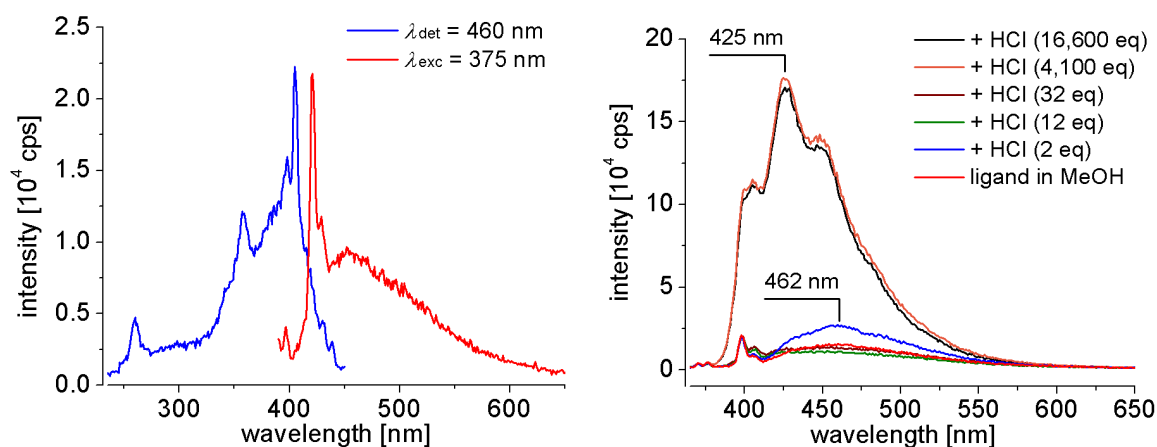


Figure 2.22: Left: Excitation (blue: $\lambda_{\text{det}} = 460$ nm) and emission (red: $\lambda_{\text{exc}} = 375$ nm) spectrum of **11** in MeOH (10^{-5} M); right: emission spectra of **11** in MeOH with addition of aqueous HCl ($\lambda_{\text{exc}} = 357$ nm).

The addition of small amounts of aqueous hydrochloric acid (2 to 32 eq) did not lead to a significant change of the emission shape or intensity (Figure 2.22, right). An excess of HCl, however, resulted in a huge altering of the spectrum. The emission wavelength is blue-shifted from 462 to 425 nm and the intensity rises from $1.0 \cdot 10^4$ cps to $17.5 \cdot 10^4$ cps. In contrast to **10**, the structure of the excitation spectrum of **11** was not significantly altered by the addition of HCl. Therefore, the change in emission intensity can directly be compared. Additionally, the broad band becomes more structured with three well-defined maxima. The protonation of the ligand has likely led to larger energy distances between the vibrational states which can be resolved now.

With a view at the strong shift of the wavelength, it is worth thinking about the possibility that also the nitrogen atom of the acridine backbone gets protonated by the addition of larger amounts of acid. The $\text{p}K_{\text{a}}$ values of the amine groups lie around 9 for the outer nitrogen^[101] and around 10 for the inner nitrogen atom^[102]. Acridine itself has a $\text{p}K_{\text{a}}$ value of 5.45, but it rises to 10.7 when getting excited in the fluorescence spectrometer.^[103] Consequently, the fluorophore in the excited

state should get protonated first, but with a slight excess of acid the amine groups take up a proton, too. In contrast to this consideration is a publication of *Tripathi et al.*^[104] They investigated the fluorescence properties of 9-aminoacridine at various pH values (Figure 2.23).

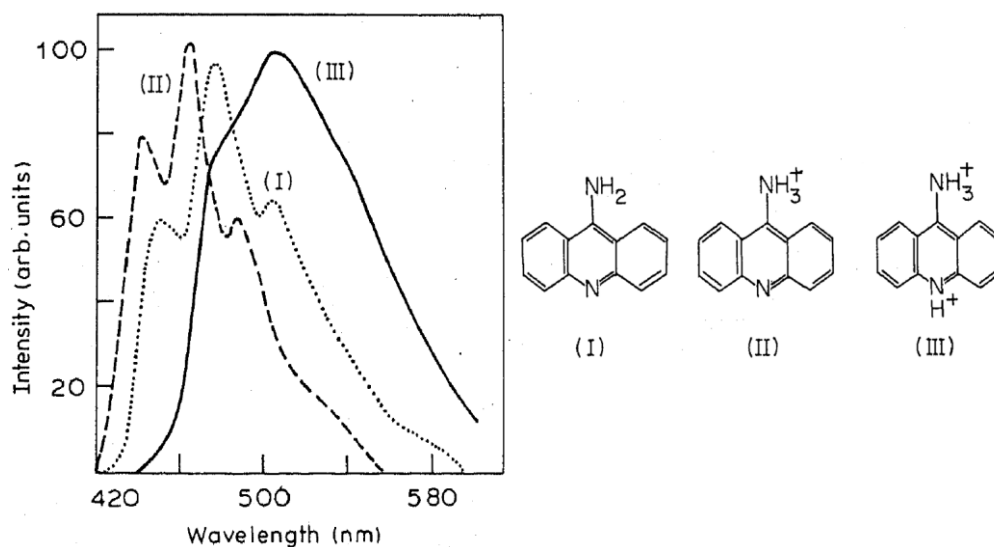


Figure 2.23: Emission spectra of 9-aminoacridinium hydrochloride at different pH values^[104]: pH = 12 (I), pH = 6 (II), and in conc. H₂SO₄ (III).

They have shown that the emission spectrum of 9-aminoacridine in water is slightly blue-shifted when it gets protonated at the primary amine (pH = 6). Only when the compound is measured in concentrated H₂SO₄, the emission is strongly red-shifted with some loss of structure. The formed emission curve is similar to that of acridinium ion which often can be found in literature^[105] as well as in the investigations of the master thesis.^[63] The same observations like the blue shift and the structured emission curve was made during the HCl experiment of **11** (Figure 2.22, right). It is, therefore, very likely that either the p*K*_a of the excited acridine backbone is not reaching this high value of 10.7 if it is substituted with the receptor units; or the wavelength-dependent proton transfer to the aromatic system is not favoured at the used excitation wavelength.^[105a] These considerations will be supported by later investigations in this thesis.

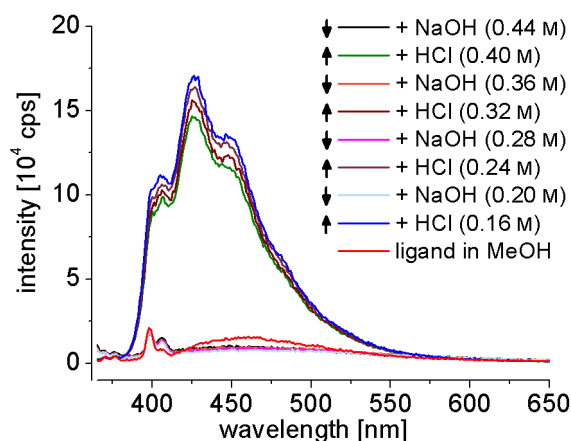


Figure 2.24: Reversibility study with alternating addition of aqueous HCl and NaOH to a solution of **11** in methanol (10⁻⁵ M, λ_{exc} = 357 nm).

A further important analysis upon the addition of a strong acid is the question if the compound gets protonated as expected or if a decomposition product generates the altered spectrum.

Therefore, a reversibility experiment of the protonation/deprotonation process of the ligand was implemented. A specified amount of aqueous HCl and NaOH was alternately added to the compound solution (Figure 2.24). The experiment demonstrates the good stability of the ligand in a low concentrated alcoholic solution. The fluorescence emission rises strongly with the addition of HCl and is completely quenched after the addition of an appropriate amount of NaOH. The maximum emission intensity decreases only slightly after each cycle which is not necessarily due to decomposition processes. The amount of acid and base was given dropwise with a glass pipette which could have small variations in volume. Moreover, the added Cl^- ions are known to act as fluorescence quencher.^[106]

These results are nice features for a molecular sensor. It reacts to an analyte (H^+ ions) with a strong increase in fluorescence intensity as well with a significant shift of the emission wavelength. The process is reversible along with a stable sensor ligand. Accordingly, a metal ion screening (Chapter 2.2.6) was carried out to check if **11** would react equally to some of the tested cations. The screening was performed in methanol (10^{-5} M) with an excitation wavelength of 357 nm and is summarised in the following bar chart (Figure 2.25).

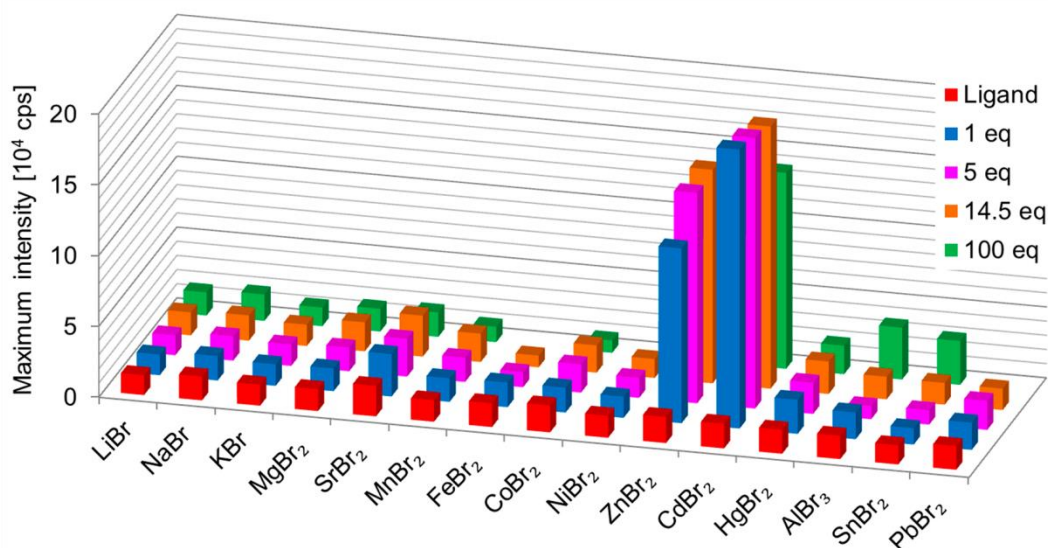


Figure 2.25: Cation screening of **11** in methanol (10^{-5} M, $\lambda_{\text{exc}} = 357$ nm) with different metal salts from 1 to 100 equivalents. The maximum emission intensity is depicted for each metal ion addition.

For every addition, the maximum emission intensity is illustrated and can directly be compared among each other. In the case of FeBr_2 , the solution got coloured at higher concentrations which only resulted in the absorption of the beam. NiBr_2 and PbBr_2 were not soluble enough for measurements with 100 eq of the salts. What is conspicuous is the high selectivity of the ligand towards Zn^{2+} and Cd^{2+} ions among the tested metal salts. The intensity rises strongly and the wavelength of the maximum is shifted from 462 nm to 456 or 450 nm, respectively, in the case of a Zn^{2+} or Cd^{2+} coordination (Figure 2.26). The difference of 6 nm between the two metal ion titrations is quite small and can just be differentiated by fluorescence spectroscopy. The emission intensity is a bit more increased by the addition of cadmium ions to the ligand solution. However, the maximum intensity is already reached with the addition of one or five equivalents in both cases. The factor of the enhancement lies around 10 (8 for Zn^{2+} and 11 for Cd^{2+} ions) which is the

same as for the protonation experiment. With 100 eq added, the intensity decreases mainly due to dilution effects (0.9 ml of ZnBr_2 onto 3.0 ml solution in the cuvette).

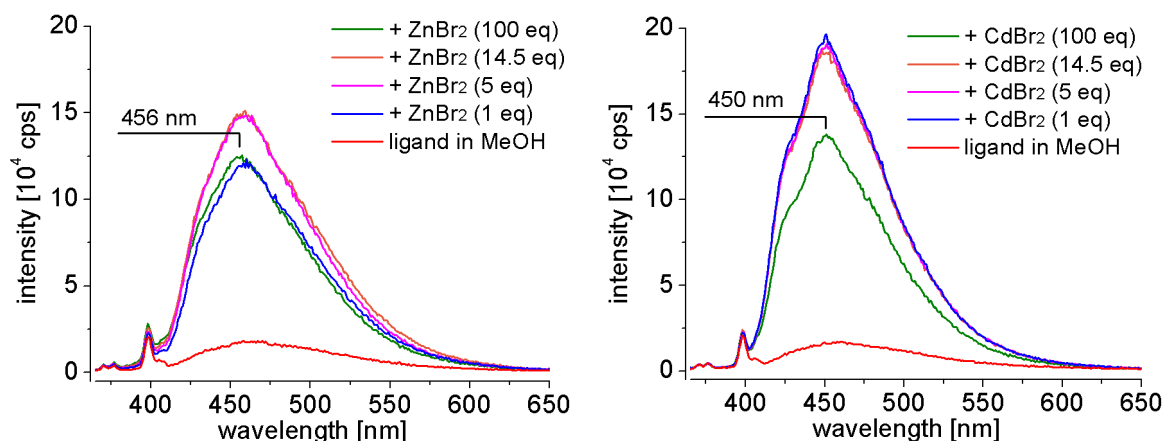


Figure 2.26: Emission spectra of **11** in methanol (10^{-5} M, $\lambda_{\text{exc}} = 357$ nm) with addition of ZnBr_2 (left) and CdBr_2 (right). The emission wavelength of the pure ligand (red line) is around 462 nm.

In the case of zinc, a second salt was dissolved and titrated to the ligand to check how the anion influences the emission spectrum. In contrast to the used halide salts a chelating anion was chosen: $\text{Zn}(\text{NO}_3)_2 \cdot 6\text{H}_2\text{O}$. Furthermore, the higher Lewis basic character of the nitrate oxygen atoms may reduce the positive charge of the zinc ion which makes it less attractive for the lone pairs of the nitrogen atoms of **11**. Nevertheless, an even higher fluorescence enhancement in comparison to ZnBr_2 was observed after the addition of $\text{Zn}(\text{NO}_3)_2$ (Figure 2.27).

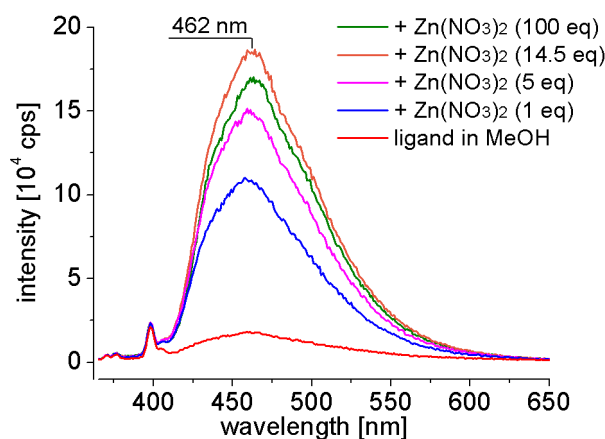


Figure 2.27: Emission spectra of **11** in methanol (10^{-5} M, $\lambda_{\text{exc}} = 357$ nm) with addition of $\text{Zn}(\text{NO}_3)_2 \cdot 6\text{H}_2\text{O}$.

The emission intensity rises strongly and reaches a value which lies somewhere between the results of the zinc and cadmium bromide titrations. More interestingly, the wavelength of the formed complex has the same value than the pure ligand (462 nm). This is in contrary to the bromide experiments where the wavelengths shift to 456 and 450 nm for zinc and cadmium, respectively. As mentioned before, the zinc ion is maybe reduced in its positive charge by the counter ions and, therefore, does not get this close to the acridine ring. This lowers its influence to the π system which is reflected in the emission wavelength. The differentiation between zinc and cadmium ions with this sensor system is hardly possible if nothing is known about the anions in solution. More investigations with different anions were needed for more accurate statements.

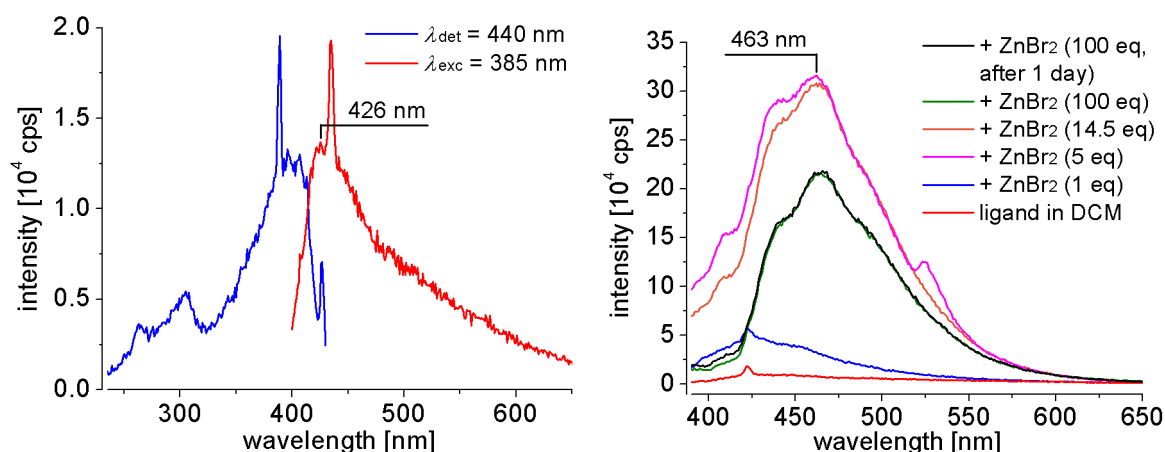


Figure 2.28: Left: Excitation (blue: $\lambda_{\text{det}} = 440$ nm) and emission (red: $\lambda_{\text{exc}} = 385$ nm) spectrum of **11** in DCM (10^{-5} M); right: emission spectra of **11** in DCM with addition of ZnBr_2 ($\lambda_{\text{exc}} = 375$ nm).

In addition, it was interesting to know if the ligand behaves different in a less polar and aprotic solvent. That is why dichloromethane was chosen for a comparison experiment. The metal salts of the screening procedure are non-soluble in DCM except ZnBr_2 . So, an excitation and emission spectrum of **11** was recorded, which was afterwards titrated with ZnBr_2 (Figure 2.28). The emission spectrum of **11** is shifted hypsochromic (426 nm) in comparison to the measurement in methanol (462 nm, Figure 2.22). This is a known effect caused by the difference in polarity of the used solvents.^[107] The fluorophore usually has a larger dipole moment in the excited state (μ_E) than in the ground state. Polar solvents are able to reorient around μ_E and lower the energy of the excited state. This results in an emission at higher wavelengths. Less polar solvents have only a small effect to μ_E and do not shift the emission maximum strongly. This behaviour can only be observed with polar fluorophores. An unsubstituted anthracene would not show any solvent dependency. The theory to this effect as well as an illustrative experiment with 4-dimethylamino-4'-nitrostilbene (DNS) is depicted in Figure 2.29.

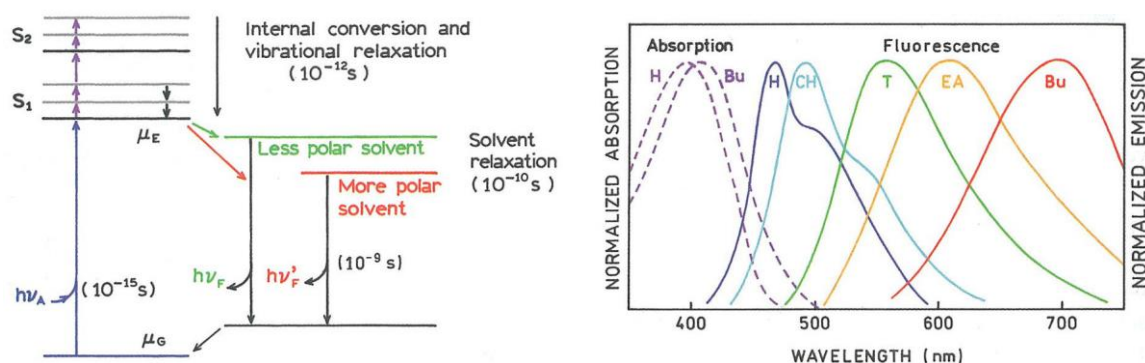


Figure 2.29: Left: Jablonski diagram for the illustration of the solvent relaxation effect depending on the solvent polarity. Singlet state (S), dipole moment of the excited state (μ_E) and of the ground state (μ_G), absorption ($h\nu_A$), fluorescence ($h\nu_F$); right: Emission spectra of DNS in solvents of increasing polarity. Hexane (H), cyclohexane (CH), toluene (T), ethyl acetate (EA), *n*-butanol (Bu).^[107]

As already described before, the sharp and highest peaks in Figure 2.28, left, are caused by Raman scattering of the used solvent (389 and 435 nm).^[108] The intensity of the excitation and emission spectrum is quite low, but with the addition of ZnBr_2 , the emission rises tremendously.

The increase is approximately four times stronger than with the solvent methanol (a factor of 32 in comparison to 8). However, with only one equivalent of zinc ions added, the effect is less pronounced. Likewise to the addition of CdBr_2 , the emission intensity decreases when too high concentrations of the salt are reached. Additionally, a bathochromic shift of the emission wavelength along with an altering of the curve shape is observable. The maximum is shifted by approximately 37 nm. This is a significant value which is as high as at the addition of hydrochloric acid to the ligand solution. The shape of the emission curve after the zinc addition has one maximum with two shoulders on both sides. In general, it becomes more structured. Furthermore, the stability of the complex in solution was tested in this experiment. The cuvette was sealed with a lid for 24 hours whereupon a further emission spectrum was recorded. No alteration of the spectrum was noticed after this period of time.

Since the shape and the wavelength of the emission curve changes during the titration, the excitation spectrum needs to be observed, too. In Figure 2.30, the excitation spectra of the pure ligand and with an amount of ZnBr_2 are depicted, as well in DCM as in methanol. The long black line perpendicular to the spectra shows the wavelength at which the solution was excited.

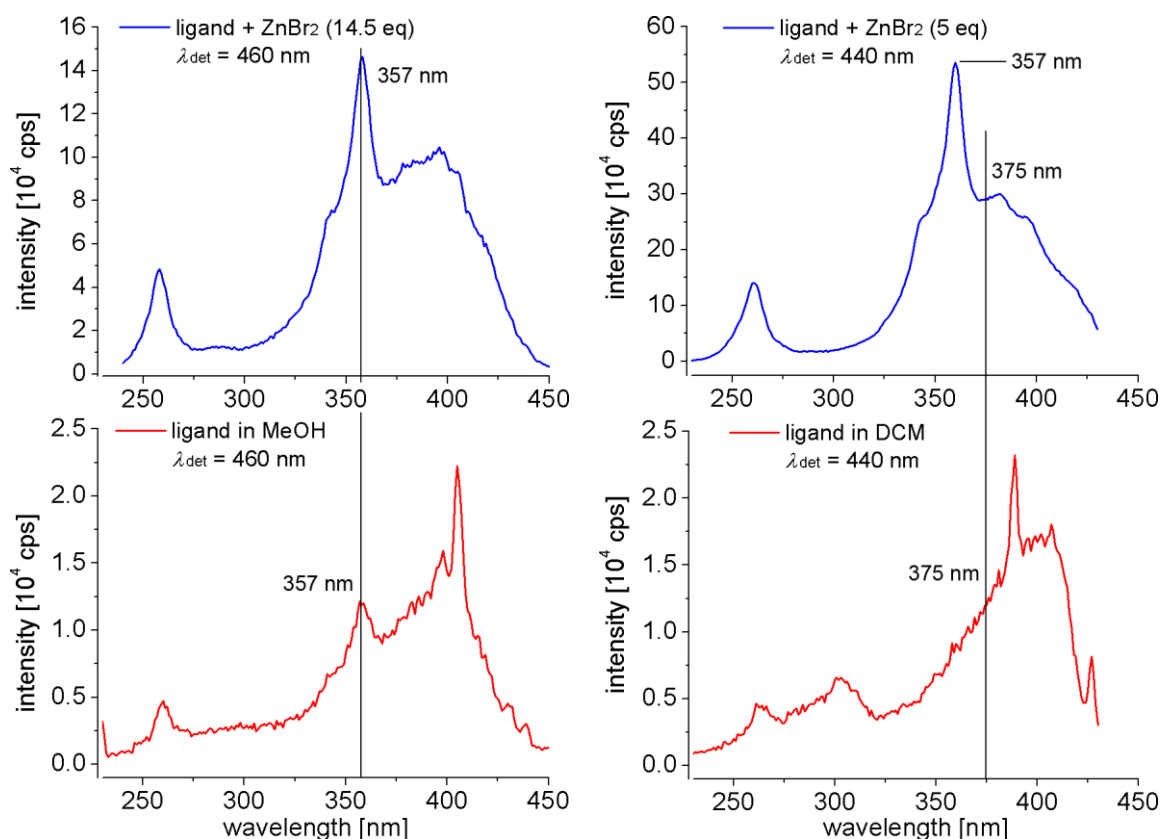


Figure 2.30: Comparison of the excitation spectra of **11** without (bottom) and with addition of ZnBr_2 (top); (left: in MeOH with $\lambda_{\text{det}} = 460$ nm; right: in DCM with $\lambda_{\text{det}} = 440$ nm).

In the case of methanol measured before, the spectrum looks quite the same before and after the addition of zinc ions (left picture). Only the intensity output is higher for the latter which is why the Raman signal above 400 nm vanishes. Looking at the spectra in DCM, a complete new band is rising at 357 nm, the same value as in methanol. If the DCM sample was excited at 357 nm, the emission intensity would have been even higher than it is already.

When comparing the shifts of the emission maxima between the methanol and the dichloromethane experiment, it is apparent that the zinc ions in DCM have a greater effect to the fluorescence system ($\Delta\lambda$ 6 nm vs 37 nm). This observation is maybe due to the weaker donor ability of the chlorinated solvent in comparison to the polar alcohol. As a consequence, the zinc ions have a higher positive charge and bind stronger to the amines of the receptor ligand. This should at first suppress the PET effect resulting in stronger emission intensity, which is the case here. Secondly, the shorter N–Zn distances may have an electronic influence to the π -system of the fluorophore. Accordingly, varying the solvents with different dielectric constants can have significant influences to the fluorescence spectra. The starting emission wavelength differs if the sensor ligand is polar, too, which can be an important property for some experimental demands. The influence of the solvent shell to the analyte should never be neglected. This can have an effect to different sensory aspects as already discussed before. However, concerning the worse solubility of a variety of metal salts in less polar solvents than methanol, it is more useful to stick with one polar solvent. The comparability of the experiments and the similarity to water are crucial reasons for that.

A general disadvantage of the compound is its non-solid state of aggregation. The oily product hampers the usual work-up procedures as well as the crystallisation of the compound. The latter is a serious disadvantage since the solid state structures of the free ligand and especially of its metal complexes provides a lot of information. The manner of the analyte complexation is needed to understand the fluorescence behaviour described in this thesis. As already mentioned before in Chapter 2.2.7, computational studies can give a hint how a possible interaction of the ligand with a metal ion might look like. The organic ligand was geometry optimised by Avogadro^[96] and again optimised after the addition of a zinc ion close to the receptor units. In this case, two structures with different coordination spheres were obtained depending on the initial position of the metal ion. The resulting atom coordinates were imported to the ORCA^[109] program package to determine the minimum energies of both complexes. The optimised structures are illustrated in Figure 2.31.

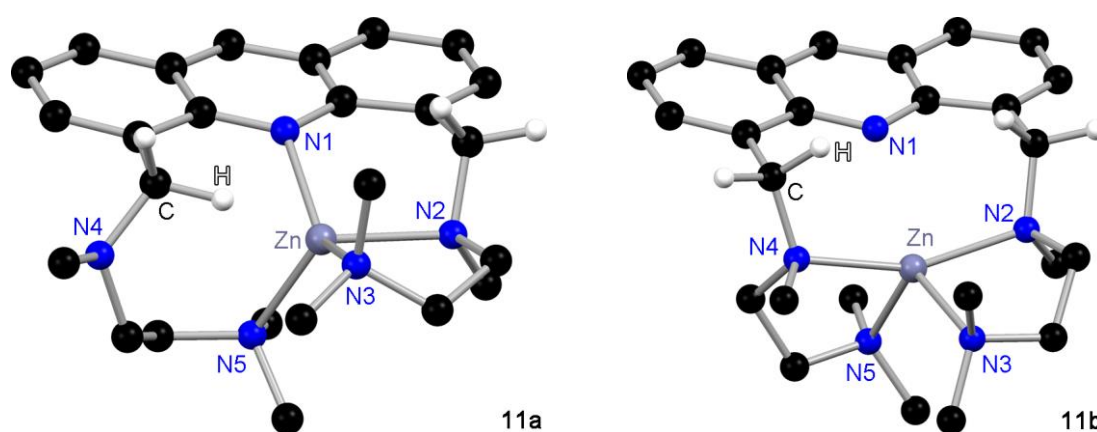


Figure 2.31: Possible interactions of **11** with a Zn^{2+} ion. The geometries were optimised with ORCA^[96] including all hydrogen atoms. In these illustrations, only the hydrogen atoms at the methylene units are shown.

During the geometry optimisation, the zinc ion gets chelated by the amine receptors. In the case of **11a**, N4 is not involved in the complexation. However, this interaction is crucial for the fluorescence properties of the ligand system since N2 and N4 are relevant for the electron

transfer. On the one hand, the emission intensity of the sensor system would only be ‘switched on’ half because the PET effect would still be present at this receptor site. On the other hand, the acridine nitrogen atom is strongly involved in the coordination of the cation, which is demonstrated by the calculated distances listed in Table 2.6. All N–Zn distances have similar values and are shorter than the distances of **11b**. Here, the acridine shows no or only very weak interaction, with a N1–Zn distance of 273.7 pm (210.9 pm in the case of **11a**). The calculated distances of both structures represent the gas phase and are only comparable to each other. To determine which coordination motif is more likely, the Gibbs free enthalpies were computed. **11b** has a smaller minimum energy indicating a more stable geometry. The complexes have an energy difference of 52.1 kJ·mol⁻¹, which additionally demonstrates the main formation of **11b**.

Table 2.6: Selected atom distances [pm] of the calculated structures.

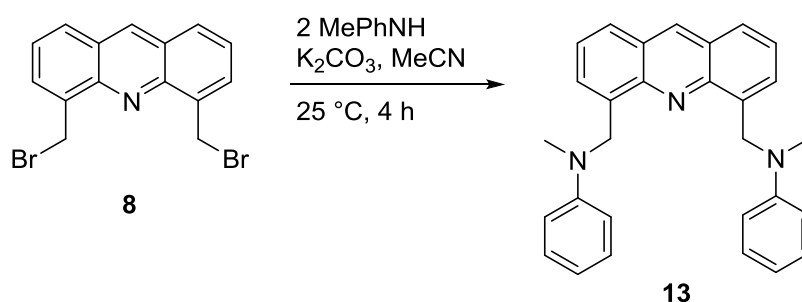
	11a	11b
N1–Zn	210.9	273.7
N2–Zn	210.9	212.9
N3–Zn	216.9	226.5
N4–Zn	---	214.8
N5–Zn	210.2	212.3
H–Zn	203.2	---

To conclude, 4,5-bis(*N,N',N'*-trimethylethylenediaminemethylene)acridine has shown very interesting sensory abilities. It is able to detect small amounts of zinc or cadmium ions in a polar alcoholic medium. The present PET effect is working well with an easily visible ‘off/on’ principle. In contrast to some anthracene based chemical sensors investigated in 2014 in this working group,^[25e] **11** is stable in a 10⁻⁵ M solution for at least 24 hours even with the addition of ZnBr₂ (Figure 2.28, right, black line). The alternating addition of an excess of aqueous HCl and NaOH also did not seem to decompose the ligand. Despite all these positive properties of **11**, its synthesis involves several side-products resulting in a very low yield. The calculations with ORCA hinted to a coordination of a Zn²⁺ ion by the amine receptors not involving the acridine nitrogen atom. But without any experimental data of solid state structures, it is hard to make a statement. Nevertheless, two acridine derivatives were synthesised and characterised by NMR spectroscopy. **12** was synthesised for the first time, whereas **11** was already isolated during the master thesis. The latter could now be characterised in detail by fluorescence spectroscopy. It was waived to investigate the fluorescence properties of **12** since the methyl group at the 9-position should not alter the spectra significantly as well as its selectivity towards the selected metal ions.^[26, 110] It was of greater interest to study the sensing abilities of the acridine derivatives substituted with different amines which is furthermore investigated in the next chapters.

2.2.10 4,5-Bis(*N*-methyl-*N*-phenylaminemethylene)acridine (**13**)

Some of the information written in this chapter has already been published in: A. Visscher, S. Bachmann, C. Schnegelsberg, T. Teuteberg, R. A. Mata and D. Stalke, *Dalton Trans.* **2016**, 45, 5689–5699.^[111]

Based on the information gained from preceded sensor systems, a more condensed amine is needed which does not exclude its own nitrogen atom from the coordination of metal ions. The most obvious solution is to omit additional donor groups at the side arms of the amine. A methyl group with its +I effect has already proven beneficial in the chapter before and should be retained. The second residue should be sterically demanding to increase the size-selectivity of the molecular sensor towards target cations. Additionally, more rigid side arms than *N,N,N'*-trimethylethylenediamine were favourable to prevent the formation of an oily product. This is why *N*-methyl-*N*-phenylamine was chosen as receptor unit. The rigid phenyl group with its ability to perform π - π -interactions, as it was observed in the X-ray structure of **10**, should contribute to obtain a solid compound.



Scheme 2.18: Synthesis of the potential molecular sensor 4,5-bis(*N*-methyl-*N*-phenylaminemethylene)-acridine (**13**).

The well-established starting material **8** was used again in acetonitrile with K₂CO₃ as base. Two equivalents of the amine were added and the reaction mixture was stirred for four hours at room temperature. The reaction progress can be monitored by different dissolving properties. In the beginning, **8** and K₂CO₃ are only partly soluble in MeCN forming a yellow suspension. At the end of the reaction, the product is completely dissolved and only the excess of salt added or formed during the reaction precipitates. The solvent was changed to ethyl acetate and washed several times with brine. The organic layer was dried over MgSO₄, filtrated and the solvent was removed under reduced pressure. In the ¹H NMR spectrum only signals referring to the desired product and used solvents were observed. However, the fluorescence emission spectrum showed a huge, broad band at small wavelengths which is unusual for acridine derivatives. This band could be identified as the starting material *N*-methylaniline. Its proton signals could then be assigned in the ¹H NMR spectrum (Figure 2.32), in particular by the comparison of the integral intensities.

Without being aware of the impurity, the signals of *N*-methylaniline can hardly be found in the spectrum. The signals of the phenyl protons of the starting material (marked with blue ellipsoids) are completely covered by the product signals. The signal of the methyl group at 2.67 ppm is easily being mixed up with residual solvent signals. Solvent investigations showed that **13** is poorly soluble in methanol, slightly soluble in ethyl acetate and good soluble in tetrahydrofuran. Hence, the HNMePh amine is a liquid, a recrystallisation from methanol was performed and the impurities were filtrated off.

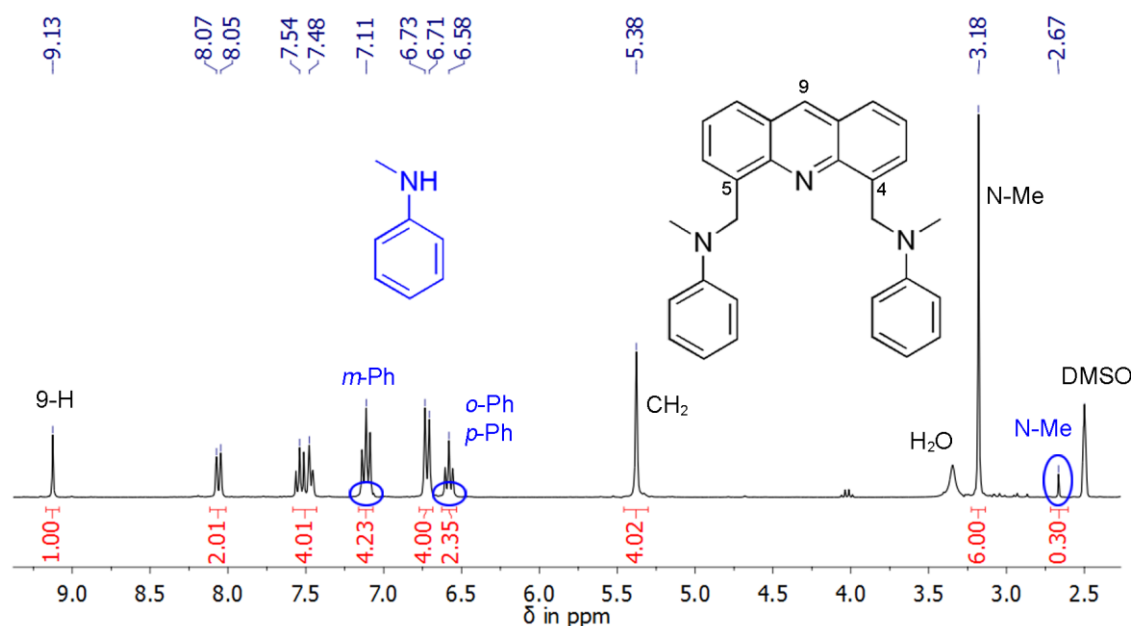


Figure 2.32: ^1H NMR spectrum of **13** in $\text{DMSO-}d_6$. The signals of *N*-methylaniline are covered by the signals of the product and are marked with blue ellipsoids.

2.2.11 Luminescence properties of 4,5-bis(*N*-methyl-*N*-phenylaminemethylene)-acridine (**13**)

In comparison to the investigated compounds **10** and **11**, the acridinyl amine **13** has less donating groups. Only the two nitrogen atoms of the amines at the 4- and 5-position trigger the PET effect. This could be an advantage according to the efficiency of the off/on switch (see discussion to Figure 2.31). The commonly used irradiation wavelength of 357 nm for the fluorescence measurements did not result in any significant emission of light. Therefore, an absorption spectrum of the ligand solution in methanol was recorded (Figure 2.33).

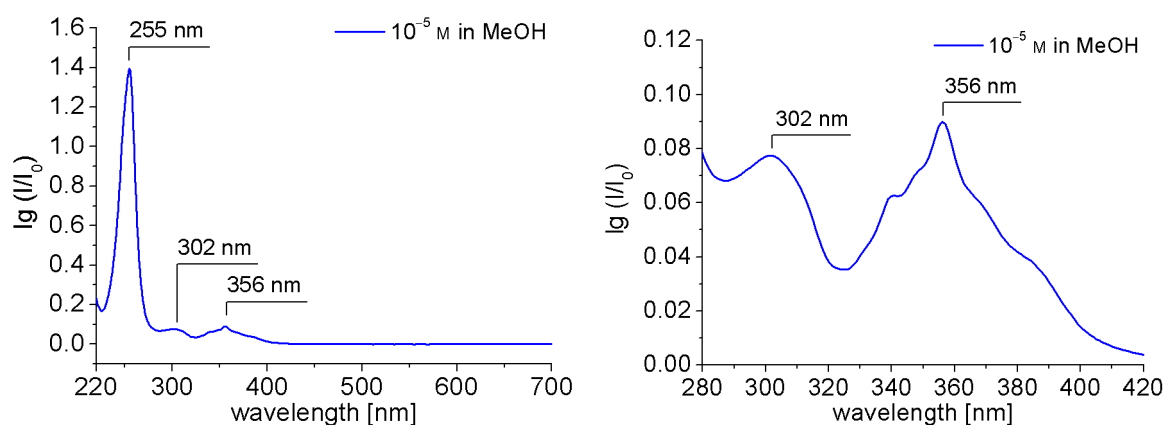


Figure 2.33: UV/vis absorption spectrum of **13** in MeOH (10^{-5} M) showing the complete wavelength range (left) and the significant wavelength region in detail (right).

The absorption spectrum is corrected by subtraction of a methanol reference spectrum. The experiment yielded three observable signals with a large and narrow one at 255 nm, a broad signal at 302 nm and a slightly structured signal at 356 nm. The two highest energy transitions at 255

and 356 nm are π - π^* in nature and are referred to the acridine backbone.^[112] The broad band at 302 nm was not determined. The experiment shows that the same excitation wavelength which was used before can be applied to **13**, too. The absence of any fluorescence emission demonstrates the excellent quenching mechanism of the PET.

In Figure 2.34, left, both excitation and emission spectra of **13** in methanol are depicted. Apart from the Raman scattering of the solvent at 398 nm including the two smaller bands before and after,^[100] no significant emission of light can be observed. However, this positive result concerning the PET effect was slightly diminished by the next experiment. Aqueous HCl was added to the cuvette to protonate the amine groups and prevent them from fluorescence quenching. Similar to the acridine derivatives investigated before, the emission intensity only rises after an excess of HCl was added to the sample (Figure 2.34, right).

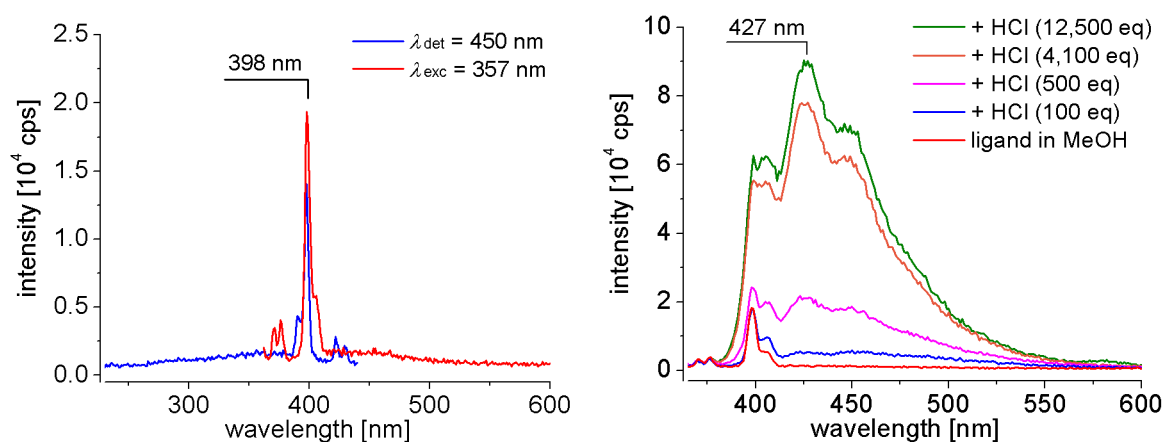


Figure 2.34: Left: Excitation (blue: $\lambda_{\text{det}} = 450$ nm) and emission (red: $\lambda_{\text{exc}} = 357$ nm) spectrum of **13** in MeOH (10^{-5} M); right: emission spectra of **13** in MeOH with addition of aqueous HCl ($\lambda_{\text{exc}} = 357$ nm).

An excitation spectrum recorded afterwards now shows the typical curve with the highest band at 357 nm (Figure 2.35). **13** seems to behave similar to **11** which responded to the presence of zinc and cadmium ions. A full fluorescence screening was therefore performed on this new compound.

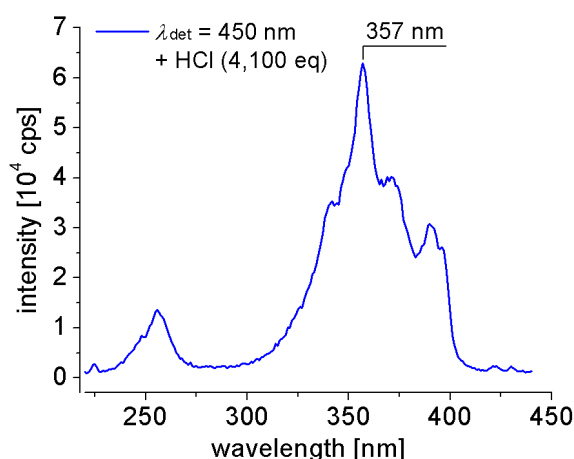


Figure 2.35: Excitation spectrum of **13** in methanol ($\lambda_{\text{det}} = 450$ nm, 10^{-5} M) with addition of aqueous HCl.

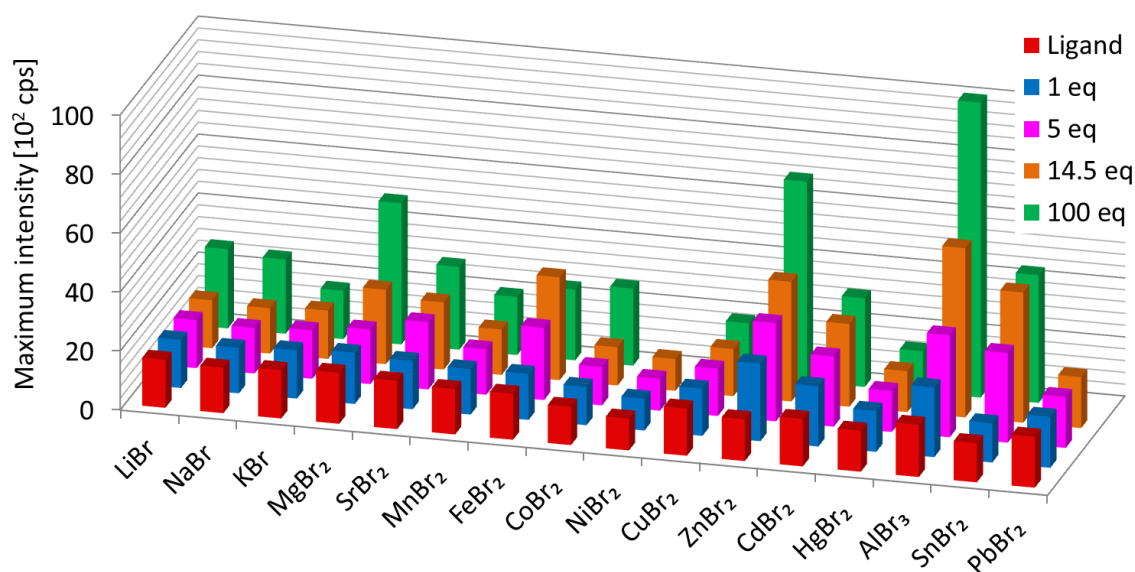


Figure 2.36: Cation screening of **13** in methanol (10^{-5} M, $\lambda_{\text{exc}} = 357$ nm), with a metal salt concentration ranging from 1 to 100 equivalents. The maximum emission intensity is depicted for each metal ion addition.

The three dimensional bar chart in Figure 2.36 illustrates the low response of **13** to the tested salts. Only a small enhancement of the intensity is observed after the addition of 100 equivalents of ZnBr_2 or AlBr_3 . However, this is not a significant response in contrast to the results of **11** in Figure 2.25. By looking at the emission spectra of the mentioned metal salts, two different wavelengths are observed (Figure 2.37). The maximum for ZnBr_2 (456 nm) is in line with the studies of the former acridine derivatives. The titration of AlBr_3 , however, led to a hypsochromic shift of the emission maximum to 427 nm. This value is known for the protonated ligand as can be seen in Figure 2.34, right. The aluminium ion is a Lewis acid which is able to make the solvent release protons which in turn protonates the organic ligand. The same observations were made with SnBr_2 to a lesser extent.

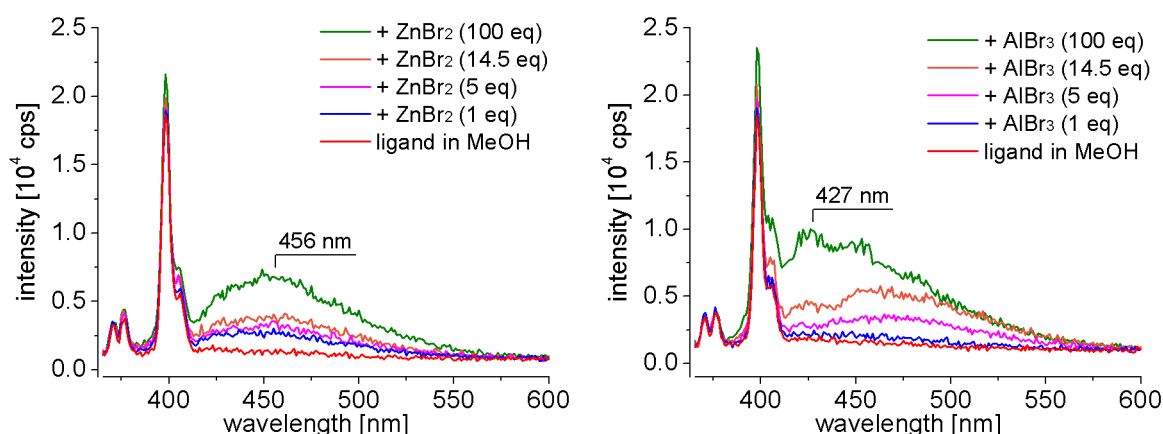


Figure 2.37: Emission spectra of **13** in MeOH (10^{-5} M, $\lambda_{\text{exc}} = 357$ nm) with addition of ZnBr_2 (left) and AlBr_3 (right).

These results clearly indicate that the lone pairs of the nitrogen atoms only show a weak basicity. On account of the aniline like structure, the lone pair of the nitrogen atom is partly delocalised into the phenyl ring which results in a lower basicity (+M effect).^[113] This is confirmed by the large excess of hydrochloric acid which was needed to achieve an enhancement of the emission

intensity. The shielding of the metal ions by the methanol molecules seems to be stronger than the chelating ability of **13**. This is why the aprotic, less polar solvent dichloromethane was used for further experiments.

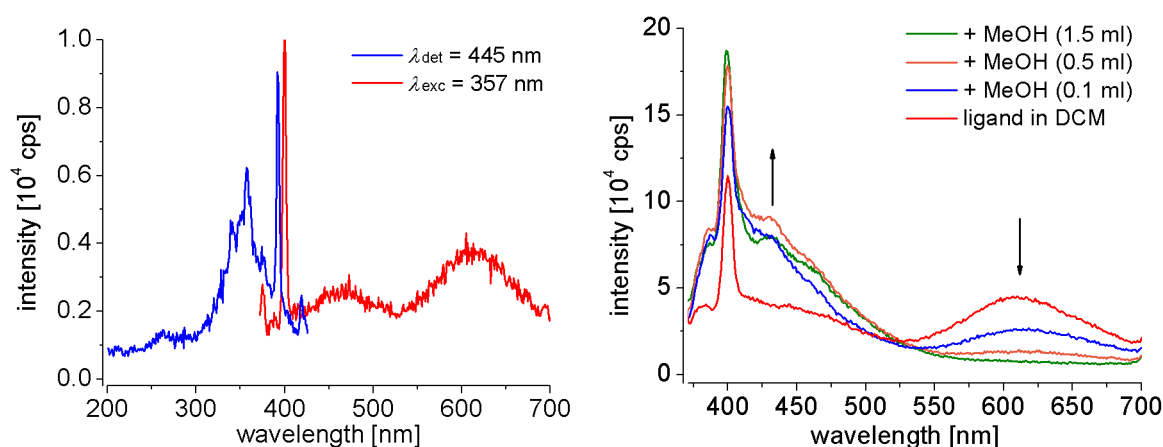


Figure 2.38: Left: Excitation (blue: $\lambda_{\text{det}} = 445 \text{ nm}$) and emission (red: $\lambda_{\text{exc}} = 357 \text{ nm}$) spectrum of **13** in DCM (10^{-5} M); with the usual front and exit slit bandpass of 2 nm; right: the same emission spectrum of **13** but with a bandpass of 4 nm and with addition of pure methanol.

As can be seen in Figure 2.38, left, the excitation and emission spectrum of **13** in DCM is very low in its intensity. But in contrary to the measurements in methanol, a rough curve can be observed. Unusual for the emission spectrum is the existence of two separate bands; one in the expected region around 470 nm and the other at longer wavelengths of 610 nm. This lower energy hints to the formation of excimers which was already mentioned in Chapter 2.2.6. Excimers are usually found in glasses at very low temperatures. In solution, this is only observable in non-polar solvents at specified concentrations. That is why the addition of polar methanol (Figure 2.38, right) reduces the band at 610 nm along with an increase of intensity at the short wavelength region.

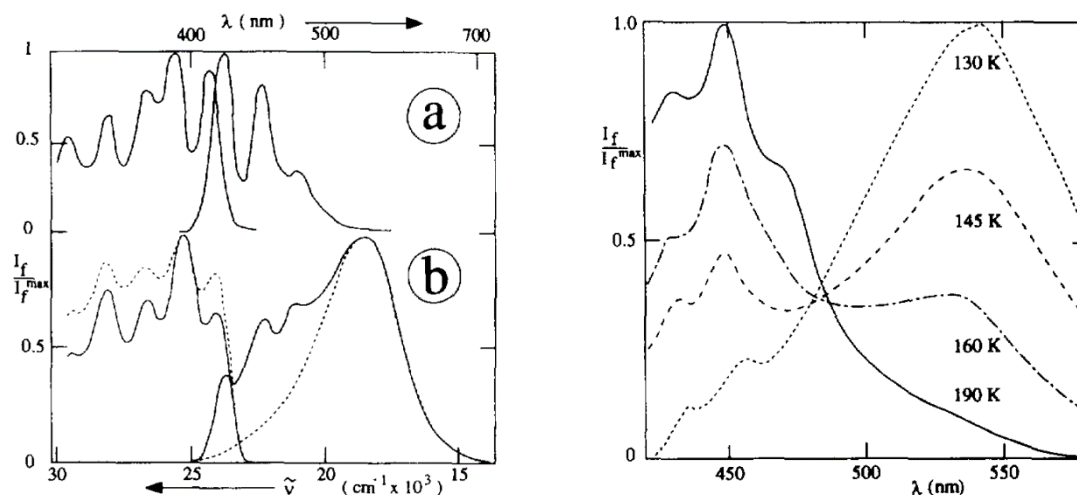


Figure 2.39: Left diagram: Fluorescence excitation (left) and emission (right, $\lambda_{\text{exc}} = 353 \text{ nm}$) spectra of 9-phenyl-2,10-diazaanthracene at 77 K in MCH (0.02 mM; $\lambda_{\text{det}} = 450 \text{ nm}$) (a) and in D-P (0.12 and 0.45 mM, full and broken lines respectively; $\lambda_{\text{det}} = 580 \text{ nm}$) (b); right diagram: Fluorescence spectra (non-corrected) for 8-methyl-9-phenyl-2,10-diazaanthracene in D-P at 130, 145, 160 and 190 K; MCH: methylcyclohexane; D-P: 2,2-dimethylbutane/*n*-pentane (8:3).^[114]

Excited-state dimers of acridine systems are rarely present in literature. *Nikolov* and *Görner* studied this phenomenon with an diazaanthracene derivative.^[114] In Figure 2.39, they show both the concentration and temperature dependency of its excimer formation. The concentration dependency is investigated in non-polar glasses at 77 K. At a concentration of 0.12 mM, both the monomer and the excimer species are observed (b). At almost quadrupled concentration, only the fluorescence emission of the excimer is detectable. The same is true for varying temperature experiments. In the right diagram, the temperature dependency is illustrated in a non-polar solution. Here, the ratio of monomer/excimer decreases with increasing temperature. When the excimer formation is not visible anymore, the temperature reaches 190 K. This is still a very low value as the experiments in this thesis were carried out at 295 K. It is therefore a rarely phenomenon under these measurement conditions.

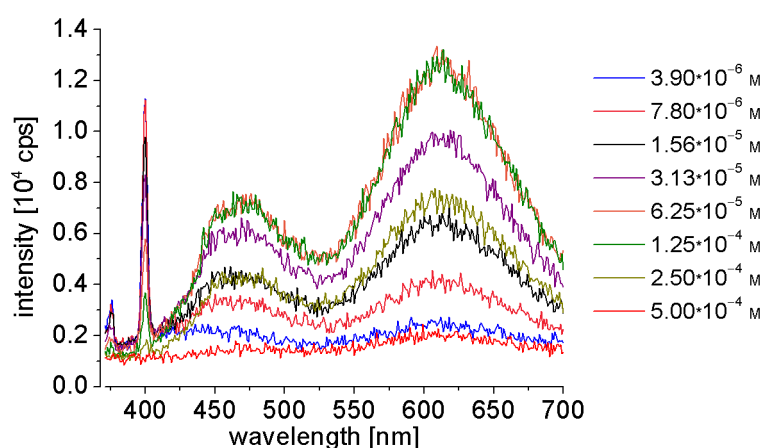


Figure 2.40: Emission spectra of **13** in DCM ($\lambda_{\text{exc}} = 357$ nm) at different concentrations.

In Figure 2.40, a dilution experiment in DCM was performed to examine if various concentrations of **13** influence the emission spectrum significantly. The experiment was started with a concentration of $5.0 \cdot 10^{-4}$ M and was then diluted by half several times. Higher concentrations only led to absorption of the incident beam. During the experiment, different intensity ratios of the two bands were observed. At high or low concentrations, the monomer/excimer ratio is about 1:1, whereas at $1.25 \cdot 10^{-4}$ M and $6.25 \cdot 10^{-4}$ M the intensity of the assumed excimer rises. Both experiments, the concentration dependency and the varied solvent polarity should verify the existence of the described phenomenon. The question how the ligand responds to Zn^{2+} ions in a non-polar solvent will be discussed in the following.

In Figure 2.41, left, an increase in intensity after the addition of ZnBr_2 is readily observable. Furthermore, the shape and the emission wavelength alters during the titration. A very broad band is observed in the beginning when one equivalent of the metal ion is present in solution. With five equivalents present, four significant peaks are observable. Another ten equivalents lead to the formation of a single band at 470 nm. When 100 equivalents of zinc ions are added, the shape of the curve remains the same but is lowered in intensity due to dilution. According to these observations, it is possible that two metal complexes which emit light at different wavelengths are formed with small amounts of ZnBr_2 added. With further addition (around 15 eq), the complex emitting at 470 nm is favoured. In contrary to the emission spectra measured before, no band could be observed at higher wavelengths (> 550 nm).

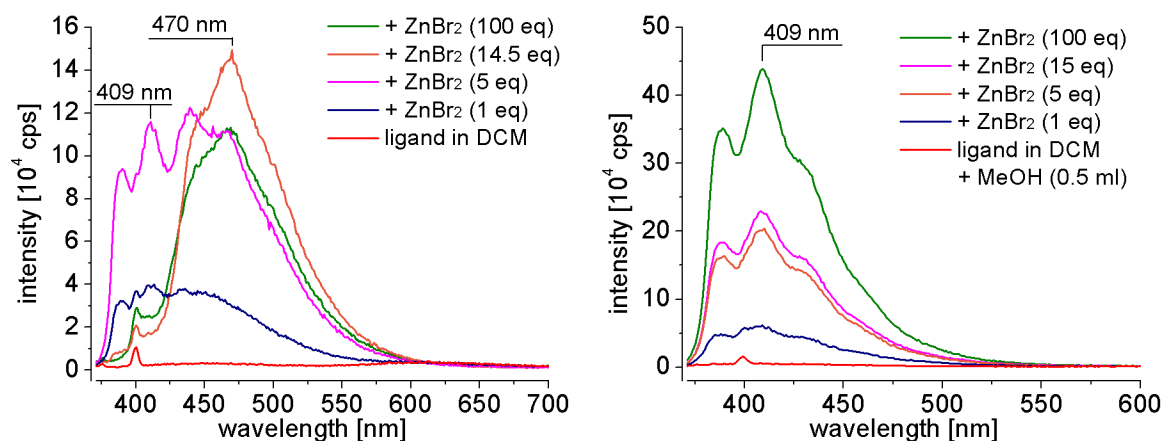


Figure 2.41: Emission spectra of **13** in DCM (10^{-5} M, $\lambda_{\text{exc}} = 357$ nm) with addition of ZnBr_2 . In the right diagram, methanol was added before ZnBr_2 was titrated to the sample.

Since the polarity of the solvent strongly influences the behaviour of the synthesised molecular sensor, another experiment with ZnBr_2 was performed. Half a millilitre methanol was added to the free ligand in DCM before the solution was titrated with the metal ion (Figure 2.41, right). In this case, only the structured band at 409 nm was observed – independent of the added amount of zinc ions. These experiments suggest that the band at 470 nm in pure DCM results from an excimer complex containing one or more zinc ions. The latter is more likely since the band at higher wavelengths is only favoured when an excess of metal ions is present.

Similar investigations with a pyrene based sensor were made by *Wu et al.* in 2012.^[115] They combined the nucleobase thymine, working as a Hg^{2+} ion receptor, with the fluorescence dye pyrene, which is known to form intra- and intermolecular excimers.^[116] The publication describes a strong bathochromic shift of almost 100 nm of the fluorescence emission upon addition of mercury ions (Figure 2.42).

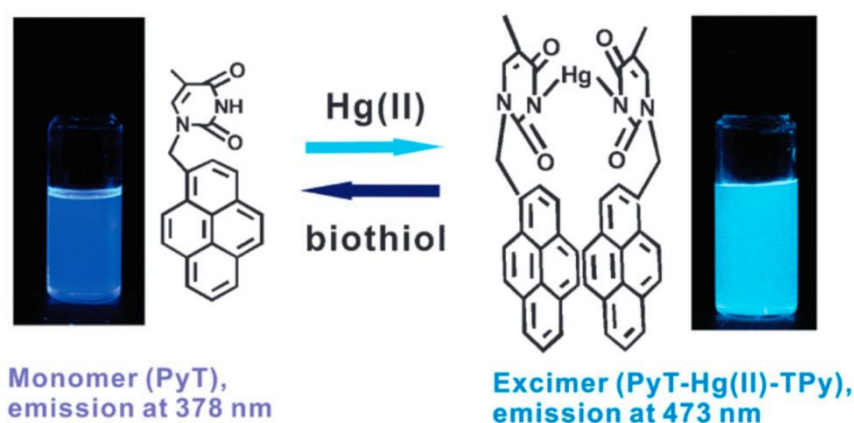


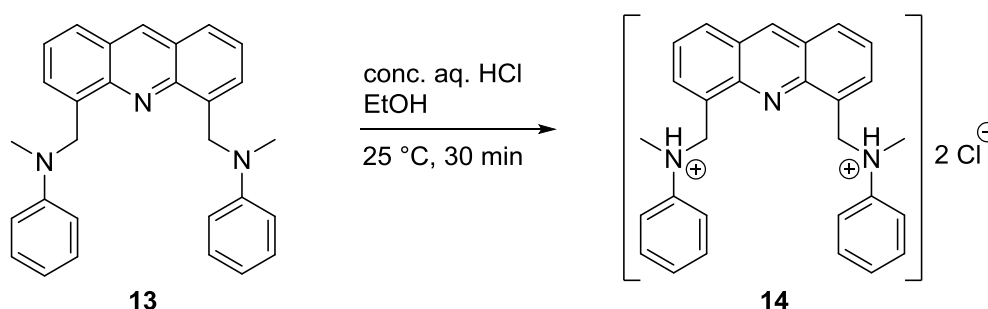
Figure 2.42: Illustration of the proposed sensing mechanism of PyT (pyrene-thymine) in the presence of Hg^{2+} ions. The process is reversible by the addition of biothiol (glutathione). The measurements were performed in a HEPES buffered water/DMSO mixture (7:1, pH 7.0).^[115]

The results of *Wu et al.* are similar to those described here and could explain the observations made by the fluorescence experiments. Although the results obtained by the use of DCM were interestingly, this solvent was not in the focus of this thesis. As already mentioned in Chapter

2.2.9, neither the comparability with other metal ions nor the similarity to the biological important solvent water is given with DCM.

2.2.12 4,5-Bis(*N*-methyl-*N*-phenylaminemethylene)acridine hydrochloride (**14**)

Several attempts to crystallise **13** were not successful. That is why it was precipitated as hydrochloride salt, since the saline ionic character can support the formation of crystalline material. **13** was suspended in ethanol and an excess of conc. aqueous HCl was added. The reaction mixture was stirred at room temperature for 30 min whereby it became a clear solution. The crude product was extracted three times with hexane, then the volatile compounds were removed under reduced pressure.



Scheme 2.19: Hydrochlorination of the amine functionalities led to the formation of the saline **14**.

The different analytical methods were not conclusive in all cases. The elemental analysis gave results which did not allow to distinguish if two or three chloride anions are present. A third chloride would assume the protonation of the acridine nitrogen atom as well. Unfortunately, only an EI mass spectrum was recorded which showed m/z fragments without the significant chlorine patterns. This can be attributed to the hard ionisation technique. Other techniques like electrospray ionisation (ESI) or fast atom bombardment (FAB) yield lower fragmentation rates and would have been more suitable for the identification of the saline compound.

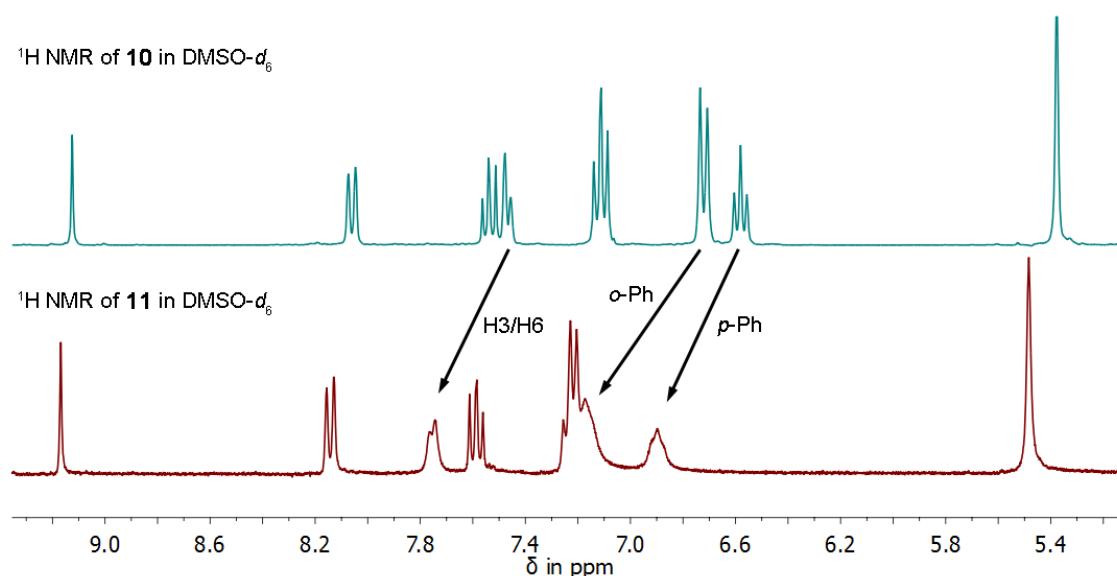


Figure 2.43: Comparison of the chemical shifts of **13** (top) and **14** (bottom) of their $^1\text{H NMR}$ spectra.

The investigation of **14** by NMR spectroscopy gave a good hint towards the protonation of the amines. All proton signals are shifted to lower magnetic fields (Figure 2.43) whereas some of the signals are broadened and show a stronger shift (marked with arrows). These signals belong to the protons of the phenyl groups and of the acridine ring at C3/C6. The latter are the neighbored positions of the methylene spacer and therefore more effected than the other aromatic protons. These results from the NMR spectrum are in line with the proposed synthesis of **14** in Scheme 2.19, although no NH proton was visible. This is mainly due to a rapid exchange of acidic protons with the used DMSO- d_6 or with residual water in the NMR solvent.^[117] The latter is very likely, since the water signal is shifted by 0.6 ppm. The broadened signals could be explained by the presence of dynamic effects in solution.^[118] The chlorides act as counter ions to the aminium cations and are in close proximity to them. If they exchange slowly enough, the dynamic effect could be monitored by NMR spectroscopy.

Besides the spectroscopic analysis, the aim of the synthesis of the saline **14** was the crystallisation of the compound to compare its geometry with the similar arranged sensor ligands. The crystallisation was realised in an equivalent mixture of ethanol/hexane, in which the HCl adduct was dissolved at boiling temperature. After cooling to room temperature, the solution was stored for four weeks. During this time, suitable crystals for X-ray analysis formed (Figure 2.44).

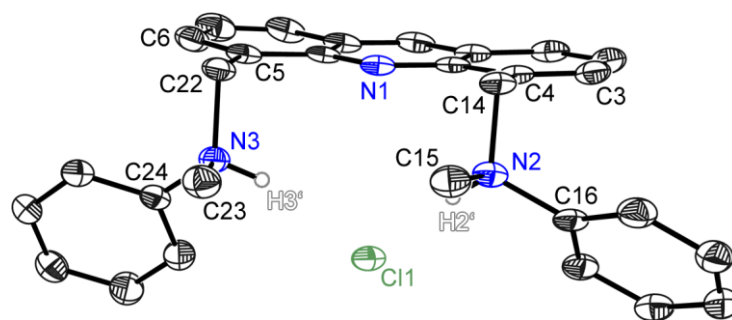


Figure 2.44: Solid state structure of **14** crystallised from an ethanol/hexane mixture. Not freely refined hydrogen atoms, the disordered solvent molecules (EtOH and H_3O^+), and two more chloride ions were omitted for clarity.

In the above figure the asymmetric unit of **14** is depicted, showing the organic ligand with two protons attached to the amine side arms. The disordered solvent molecules (EtOH and H_3O^+) as well as two more chloride ions were omitted in this illustration. However, these additional molecules can explain the inconsistent values of the elemental analysis. The comparison of this data is listed in the experimental settings. The compound crystallises in the monoclinic space group $C2/c$ and the receptor side arms are arranged almost symmetrical. Both positions of the hydrogen atoms of the amines ($\text{H2}'$ and $\text{H3}'$) were refined freely. They point towards the centred Cl1 atom forming hydrogen bonds which will be discussed in the following section. First, the packed structure was studied to determine further hydrogen-chlorine interactions as well as the already discussed packing effects between two acridine or phenyl systems. In comparison to **10**, the phenyl rings in this structure do not show any π - π -interactions. Here, $\text{CH}\cdots\pi$ interactions between a hydrogen atom (H23C) of the methyl group C23 and the phenyl ring of N2 are present with a distance of 261.2 pm. Additionally, the acridine backbones get close to each other, resulting in a short π - π -distance of 338.9 pm. This value is 0.7 ppm smaller than the distance in

the packed structure **10**. The overlap of the acridine ring systems is shown in Figure 2.45. These different types of interactions play a crucial role for the arrangement of the crystal structure.

The N–C bond lengths listed in Table 2.7 are significantly elongated compared to typical bond lengths of N(sp³)–C(sp³) and N(sp³)–C(sp²) that are 147 pm and 143 pm, respectively.^[84] Here, the longest bond is N3–C22 with 152.7(3) pm. Compared to the relative acridine amine **10**, the highest deviation is 6.2(5) pm. The bonds between the nitrogen atoms and the *ipso*-C of the phenyl groups are as long as a bond to an sp³ hybridised carbon atom (both are 147.9(3) pm). These values could be attributed to the present tertiary ammonium ions. The nitrogen atoms N2 and N3 are positively charged through the protonation resulting in a smaller electronegativity value and less attraction to the carbon atoms. This leads to the elongation of the N–C bonds.

Table 2.7: Selected bond lengths and angles of **14**.

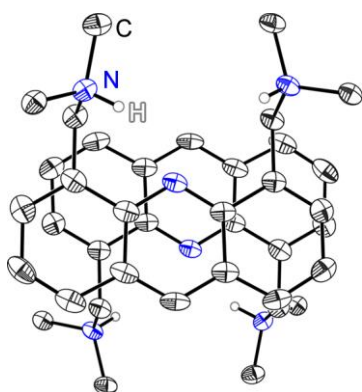


Figure 2.45: Detail of the π - π -overlap of the acridine moieties of **14**.

Bond [pm]		Angle [°]	
N2–C14	152.5(3)	C4–C14–N2	112.77(19)
N2–C15	150.4(3)	C14–N2–C15	109.16(19)
N2–C16	147.9(3)	C14–N2–C16	112.46(19)
N3–C22	152.7(3)	C15–N2–C16	113.55(19)
N3–C23	149.2(3)	C5–C22–N3	109.6(2)
N3–C24	147.9(3)	C22–N3–C23	110.78(19)
N1...Cl1	332.7	C22–N3–C24	113.61(19)
		C23–N3–C24	111.4(2)
		C3–C4–C14–N2	–89.5(3)
		C6–C5–C22–N3	97.1(3)

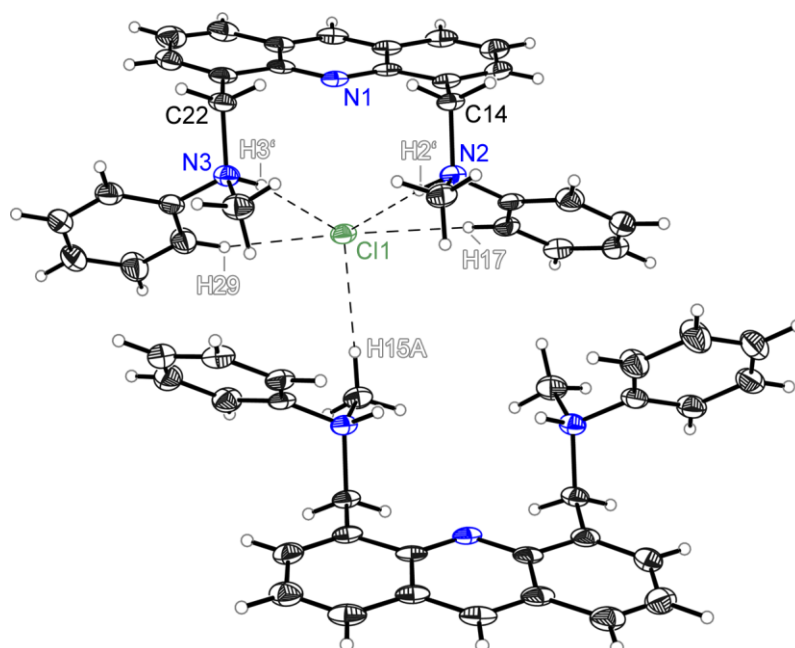


Figure 2.46: Two molecules of **14** demonstrating the hydrogen bonds to the centred chlorine atom Cl1.

The usually tetrahedral C–N–C angles are likewise affected. The bonded hydrogen atom is sterically less demanding than the former lone pair, leading to larger angles (e.g. C23–N3–C24: 113.61(19)°). The torsion angles of the receptor side arms are very close to the perpendicular angle with values of 89.5(3)° and 97.1(3)°. This is probably due to the formation of hydrogen bonds between the ammonium ions and the chloride.

In Figure 2.46, the environment of Cl1 is illustrated, including five hydrogen-chloride interactions which are marked with dashed lines. Two of them have a nitrogen as donor (D) and are stronger than the hydrocarbon counterparts. Nitrogen atoms possess a higher electronegativity than carbon atoms, forming partially positive charged hydrogen atoms. This results in a stronger interaction with the acceptor (A). According to the literature, DH...A interactions can be stated as hydrogen bonds if they are shorter than 320 pm and have a greater DHA angle than 90°. [89] When comparing the values for the NH...Cl interaction with the defining parameters in Table 2.8, the interactions can be classified as moderate hydrogen bonds. The H...Cl distances are quite long with values of 216(2) and 224(2) pm for H2'...Cl1 and H3'...Cl1, respectively. The first parameter can be stated as a moderate interaction, whereas the second distance lies in the range for weak hydrogen bonds. The DHA angles are large with values of 174(2) and 163(2)°, respectively. The first angle can be attributed to a strong interaction with an almost linear arrangement. Referring to these properties, the H2'...Cl1 interaction is significantly stronger than its H3' counterpart. Another classification can also be gained by the comparison of the values with the data of the diagram, depicted in Figure 2.47. Here, NH₃⁺...Cl⁻ interactions are illustrated in an angular scatter plot of N–H...Cl angles against H...Cl distances. The values of the N–H...Cl interactions are marked in red in the figure, assuming strong bonding situations in comparison to the relative literature values demonstrated as black dots.

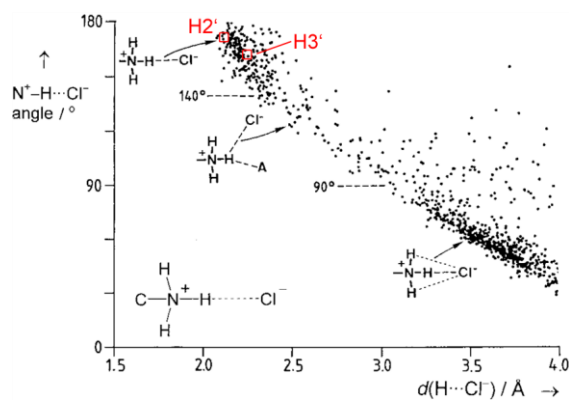


Figure 2.47: Angular scatter plot of N–H...Cl⁻ angles against H...Cl⁻ distances for –NH₃⁺ donors. [119]

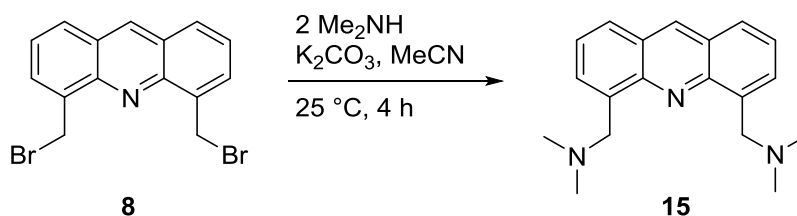
Table 2.8: Part of the classification of hydrogen bonds after Jeffrey. [120] Distances are given in [pm] and angles in [°].

	Strong	Moderate	Weak
interaction type	strongly covalent	mostly electrost.	electrost./dispers.
d (H...A)	120-150	150-220	> 220
d (D...A)	220-250	250-320	> 320
Φ (DHA)	170-180	> 130	> 90

2.2.13 4,5-Bis(dimethylaminemethylene)acridine (**15**)

Major parts of this chapter have already been published in: A. Visscher, S. Bachmann, C. Schnegelsberg, T. Teuteberg, R. A. Mata and D. Stalke, *Dalton Trans.* **2016**, 45, 5689–5699.^[111]

The fluorescence investigations of **10**, **11**, and **13** showed interesting and especially different behaviour, amongst other things, the recognition of analytes and the influence of various solvents. Nevertheless, none of them combined sufficient requirements to be used as a chemical sensor. Equally to H-TrMEDA, another amine which has already been utilised during the master thesis was chosen for further investigation. It features the simplest structure of secondary amines: dimethylamine. In contrast to the *N*-methyl-*N*-phenylamine used in the chapter before, the basicity of dimethylamine is higher due to the twofold +I effect and the non-existent +M effect. The fluorescence measurements of the master thesis contained the same systematic error as mentioned in context with **11**. Similarly, no solid state structure of the pure compound or of any metal ion complex was determined.



Scheme 2.20: Synthesis of 4,5-bis(dimethylaminemethylene)acridine (**15**).

The synthesis of **15** was almost the same as for the other substitution reactions. No heating was needed to obtain the almost pure product after a few hours. The volatile components were removed under reduced pressure and the remaining solids were dissolved in an ethyl acetate/brine mixture. The solution was washed with brine and afterwards dried over MgSO_4 . After filtration, the solvent was removed under reduced pressure and a partly oily, partly solid product was obtained. Storing the flask in the refrigerator for a couple of hours resulted in a complete yellow-brown solid. A ^1H NMR spectrum demonstrated the purity of the target compound without any elaborate purification. Furthermore, the yield was almost tripled (63%) in comparison to the synthesis in the master thesis (22%). Since the full spectroscopic characterisation of **15** confirmed its purity, the luminescence properties of the molecular sensor were investigated in the following chapter.

2.2.14 Luminescence properties of 4,5-bis(dimethylaminemethylene)acridine (**15**)

Likewise to **13**, an UV/vis spectrum of **15** was recorded to evaluate its absorption properties. A suitable excitation wavelength for the emission studies can directly be abstracted by this experiment (Figure 2.48). The absorption spectrum of **15** does not differ significantly to the spectrum of **13**. The two highest signals are observed at the same wavelength (253 and 356 nm), whereby the not determined broad band at 302 nm was not detectable in this case. This leads to the assumption that it belongs to a transition originated by the phenyl rings of **13**. The signal with its maximum at 356 nm is a bit more structured in this experiment by what its shoulders can be assigned to the values 340, 368, and 386 nm. The possible observation of this pattern is attributable to resolved vibrational energy levels.

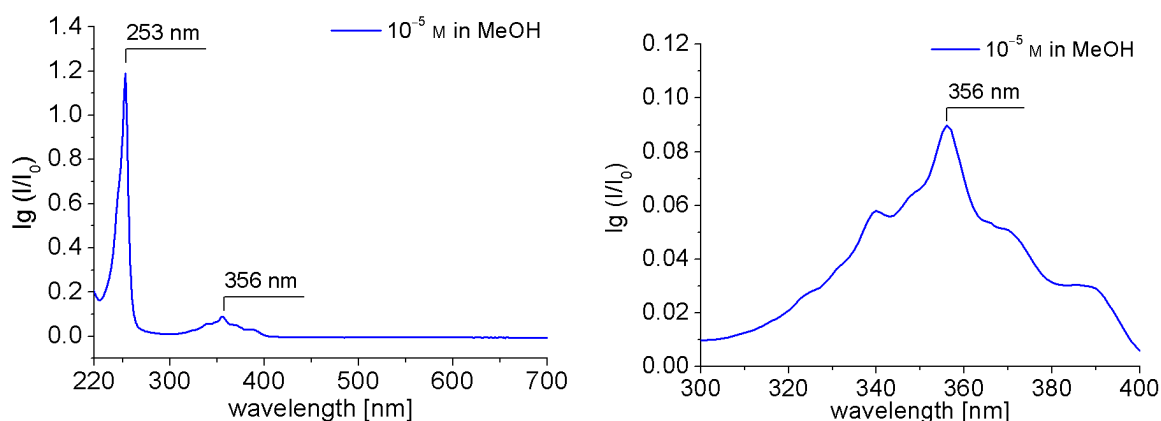


Figure 2.48: UV/vis absorption spectrum of **15** in MeOH (10^{-5} M) showing the complete wavelength range (left) and a detail of the significant wavelength region (right).

As expected, the excitation and emission spectrum in Figure 2.49 are completely different than those obtained during the master thesis with the overall use of $n\text{Bu}_4\text{NBF}_4$. The resulting bands are higher in intensity in comparison to **12** and **13**. The emission curve lies in a similar wavelength region with its maximum at 450 nm. Again, the peak at 398 nm can be assigned to the Raman scattering of methanol.

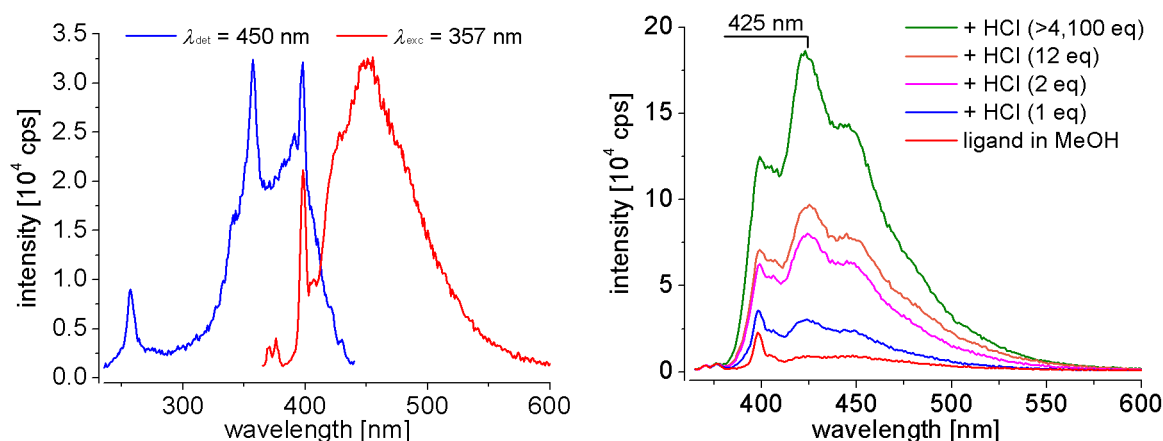


Figure 2.49: Left: Excitation (blue: $\lambda_{\text{det}} = 450$ nm) and emission (red: $\lambda_{\text{exc}} = 357$ nm) spectrum of **15** in MeOH (10^{-5} M); right: emission spectra of **15** with addition of aqueous HCl ($\lambda_{\text{exc}} = 357$ nm).

The second highest peak in the excitation spectrum is at a wavelength of 357 nm, which is in line with the results from the absorption study and was used for the excitation of the compound in every following experiment. The protonation of the ligand depicted in Figure 2.49, right, yielded the expected blue shift of the emission band with a maximum of 425 nm. However, the addition of only one equivalent of aqueous hydrochloric acid leads to the hypsochromic shift along with an increase of the fluorescence intensity. Additional amounts of HCl enhance the intensity until the already known structured curve is formed. In contrast to **12** and **13**, the respond to the acid is considerably more pronounced and already present at fewer equivalents. This observation proves the good donor abilities of the amine receptors according to their high basicity.

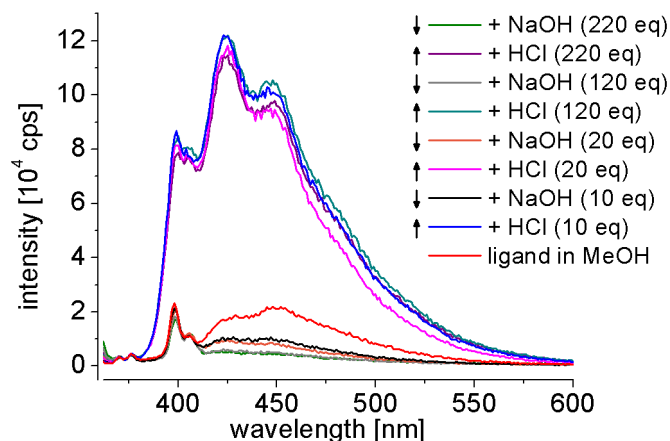


Figure 2.50: Reversibility study with alternating addition of aqueous HCl and NaOH to a solution of **15** in MeOH (10^{-5} M, $\lambda_{\text{exc}} = 357$ nm).

As already been shown (Figure 2.24), a reversibility study of the protonation/deprotonation process is useful to determine the stability of the fluorophore. The emission spectra in Figure 2.50 clearly demonstrate the stability of **15** towards acids and bases. If diluted hydrochloric acid is added to the sample, the emission intensity strongly rises whereas it is effectively quenched by the addition of sodium hydroxide. Each cycle was repeated four times without any alterations. Only the emission curve of the pure ligand in methanol shows a different behaviour. It has a higher intensity than the spectra with an excess of NaOH. The first assumption was the presence of already protonated sensor molecules in the sample. This could be excluded since the wavelength of the starting emission spectrum is above 450 nm. In the case of a protonation of the ligand, the wavelength is shifted to 425 nm. The second possibility would be a small impurity of a metal salt which induces this higher intensity by coordination to the quenching amines. When aqueous NaOH is added to the solution, possible metal ions should precipitate as hardly soluble metal hydroxides and are no longer available for coordination.

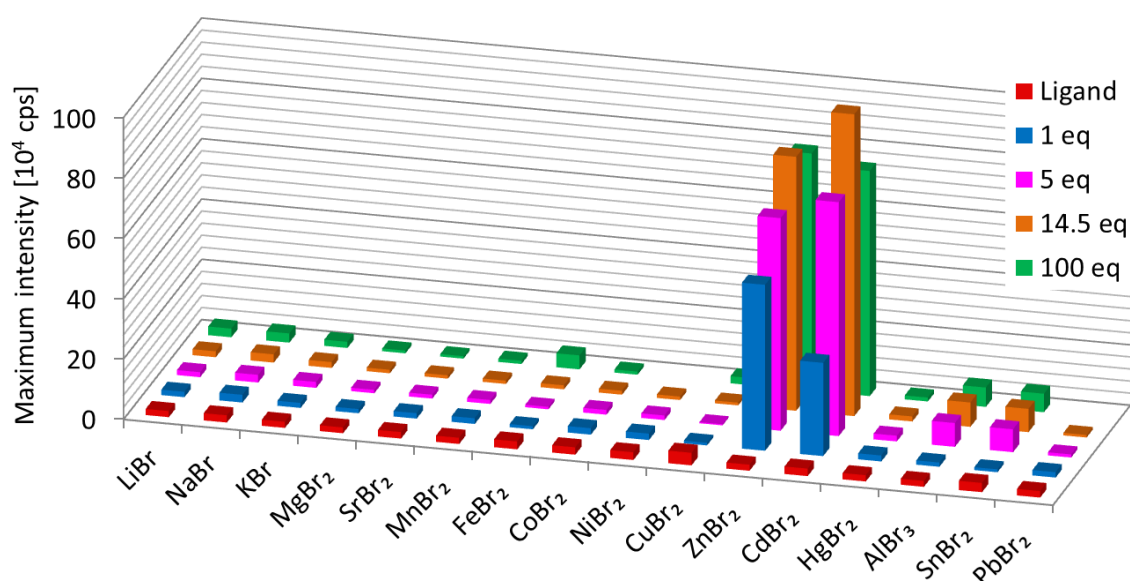


Figure 2.51: Cation screening of **15** in MeOH (10^{-5} M, $\lambda_{\text{exc}} = 357$ nm) with different metal salts from 1 to 100 equivalents. The maximum emission intensity is depicted for each metal ion addition.

The fluorescence response of **15** towards different metal ions is depicted in Figure 2.51, demonstrating the screening procedure in methanol. Among the tested sixteen metal salts this ligand shows a very high selectivity towards Zn^{2+} and Cd^{2+} ions. The emission intensity increases enormously – even higher than in the case of **11**. The minute emission enhancement with AlBr_3 and SnBr_2 is solely due to the strong Lewis acidity of these metal ions which leads to slight protonation of the ligand. This was evidenced by the different resulting emission wavelengths. If the ligand is protonated, the wavelength of the emission maximum is blue-shifted to 425 nm, whereas in the case of Zn^{2+} or Cd^{2+} coordination the maximum is observed at 457 nm and 445 nm, respectively. In this context it should be mentioned that, although the emission shift between the two metal ions is only 12 nm, this is sufficient to differentiate the metals by fluorescence spectroscopy. A closer look at the emission spectra depicted in Figure 2.52 additionally demonstrates the high sensitivity of this sensor molecule.

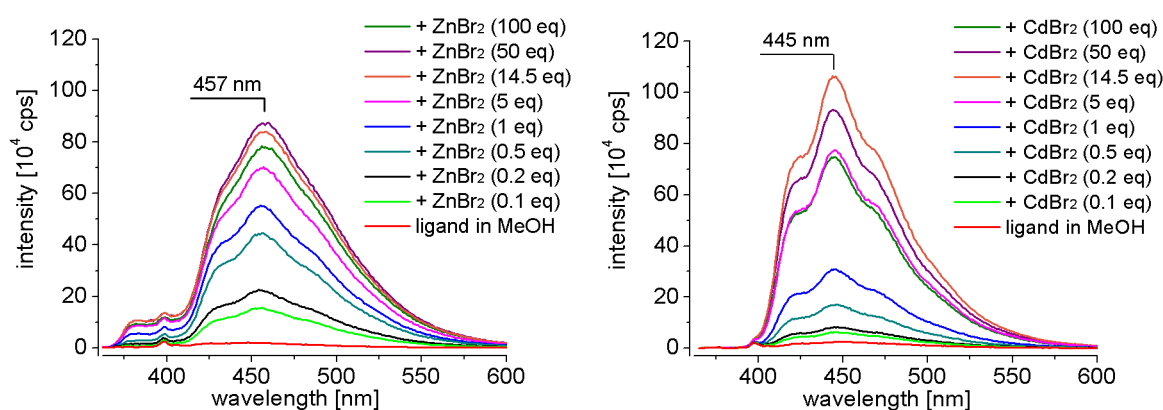


Figure 2.52: Emission spectra of **15** in MeOH (10^{-5} M, $\lambda_{\text{exc}} = 357$ nm) with addition of ZnBr_2 (left) and CdBr_2 (right), respectively.

After the addition of only 0.1 eq. of ZnBr_2 , a significant increase of emission intensity was observed. It continued rising until around 50 eq. of the metal ion were titrated into the cuvette. Another 50 eq. resulted in a lowering of the fluorescence signal. At this point all fluorophores are saturated with zinc ions and the dilution effect exceeds. In the case of CdBr_2 the altering of the emission spectra is similar to zinc, whereas the fluorescence enhancement rises more slowly and reaches a higher maximum at around 15 equivalents. Since the starting intensities of the pure ligand differ slightly, the emission enhancement is the same for both cases with a factor of around 42.

In Figure 2.53, the UV/vis absorption spectrum of the pure ligand **15** is compared with the spectra of its metal complexes as well as with the protonated form. In general, the absorption is reduced by the addition of the metal ions whereas it is slightly enhanced through protonation. A shift of the wavelength cannot be observed in any case. In the literature, where similar acridine derivatives were investigated, the altering of the absorption spectra by the addition of metal salts were declared as an evidence for the participation of the acridine nitrogen atom in the complexation with the target metal ion.^[57, 121]

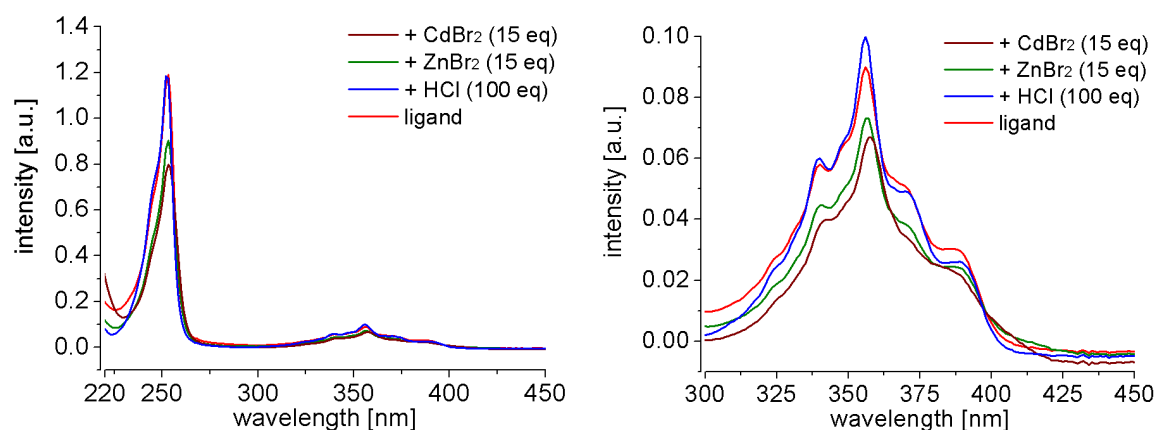


Figure 2.53: UV/vis absorption spectra of four samples: pure **15** in MeOH (10^{-5} M, red), with addition of 100 eq HCl (blue), with 15 eq ZnBr₂ (green), and with 15 eq CdBr₂ (brown). In the left figure, the wavelength range from 220–450 nm is shown whereas in the right figure, a detail of the significant wavelength region around 360 nm is depicted.

It is stated, that the analyte is affecting the electronic density of the acridine ring and thus affects the electronic transitions. This can be an explanation for the slightly different spectra, but it needs to be considered that the amines of the receptor unit can also influence the aromatic backbone electronically when coordinating to an analyte. Further investigations need to be done before stating possible interactions of the acridine moiety. In this thesis, the coordination of the acridine nitrogen atom to the metal ions is explored in detail in the further chapters.

Regarding the metal ion screening again, the varying starting intensities are the second hint to the existence of contaminations in the sample. The first indication was mentioned during the protonation/deprotonation study. Since the analytics of **15** do not hint to any significant impurities, the focus was placed on the solvent for the fluorescence experiments. The used methanol was purchased from VWR Chemicals[®] (AnalaR NORMAPUR) which provides analytical data for their solvents. Each kilogram contains impurities of < 0.2 mg Zn²⁺ and < 0.01 mg Cd²⁺ ions. Converted to the employed volume and concentration for the measurements, every sample could contain an amount of < 0.3 eq Zn²⁺ ions and < 0.009 eq Cd²⁺ ions with respect to the ligand. This is a significant amount which needs to be considered when comparing the results. In addition, this could explain the higher excitation and emission spectrum of **15** in comparison to **13**, which is not sensitive to the mentioned metal ions. To prove this statement, two further batches of purified methanol were ordered from Sigma-Aldrich[®] (puriss. p.a.) and Fisher Chemicals[®] (analytical reagent grade). The batch of the latter company should have less amounts of zinc ions (< 0.05 mg; Cd²⁺ was not specified), but the emission spectra measured with this methanol all resulted in higher starting intensities; up to $8.4 \cdot 10^4$ cps. Sigma-Aldrich[®] stated to have less than < 0.1 mg of Zn²⁺ impurities and < 0.05 mg of Cd²⁺ in their fillings. The experiments with this methanol gave intensities lower than $1.5 \cdot 10^4$ cps (Figure 2.54). What is more is the difference of the emission wavelength between these batches. The pure ligand seems to emit at smaller wavelengths since the contamination with metal ions (mainly Zn²⁺) shifts the emission maximum to 454 nm (green and blue line). That is why the excitation and emission spectrum of **15** was recorded again, measured in methanol from Sigma-Aldrich[®] (Figure 2.54, right). Here, the emission maximum was observed at lower wavelengths at a range of 420 nm to

450 nm. The result of these measurements underlines the sensitivity of the synthesised sensor system which is able to even detect traces of impurities.

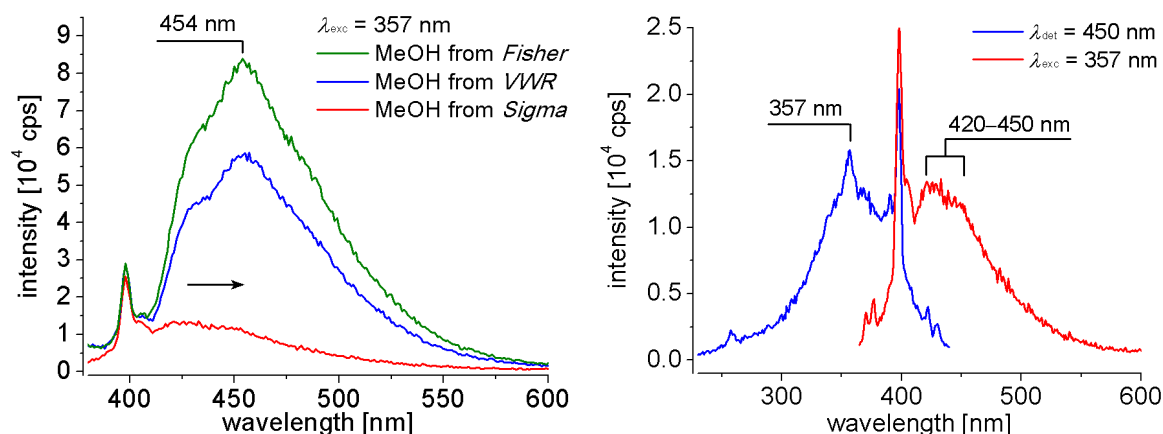


Figure 2.54: Left: Emission spectra of **15** (10^{-5} M, $\lambda_{\text{exc}} = 357$ nm) with different batches of methanol from various companies; right: repeated excitation (blue: $\lambda_{\text{det}} = 450$ nm) and emission (red: $\lambda_{\text{exc}} = 357$ nm) spectrum of **15** in MeOH from Sigma-Aldrich® (10^{-5} M).

For a good comparability of the resulting spectra, only metal bromides were chosen during the cation screening. Nevertheless, it is interesting to know if, and how other anions would influence the sensing ability of the acridine derivative. For this reason, two more zinc salts were tested under the same conditions: $\text{Zn}(\text{NO}_3)_2 \cdot 6\text{H}_2\text{O}$ and $\text{Zn}(\text{OAc})_2 \cdot 2\text{H}_2\text{O}$. Their fluorescence spectra are shown in Figure 2.55.

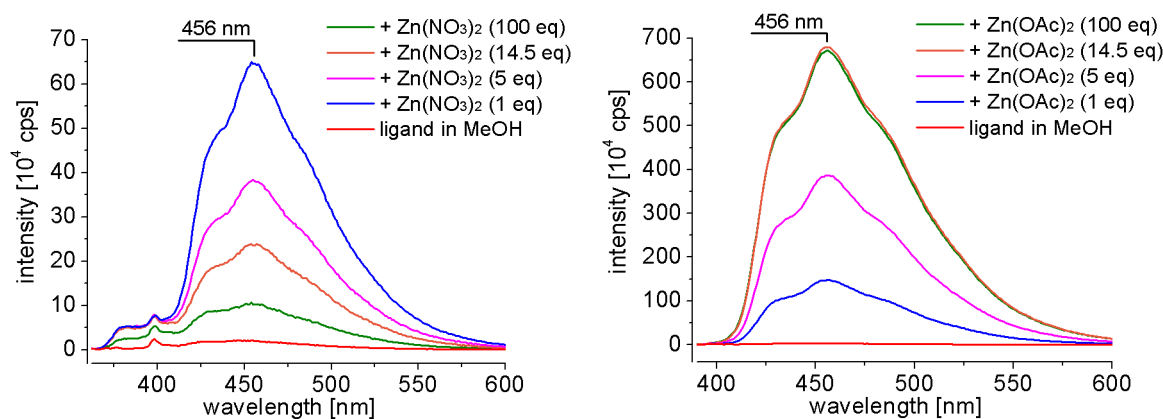


Figure 2.55: Emission spectra of **15** in MeOH (10^{-5} M, $\lambda_{\text{exc}} = 357$ nm) with addition of $\text{Zn}(\text{NO}_3)_2 \cdot 6\text{H}_2\text{O}$ (left) and $\text{Zn}(\text{OAc})_2 \cdot 2\text{H}_2\text{O}$ (right), respectively.

On the one hand, the titration experiment with $\text{Zn}(\text{NO}_3)_2 \cdot 6\text{H}_2\text{O}$ shows a similar behaviour like ZnBr_2 . The wavelength of the fluorescence band is the same and a strong enhancement of the emission intensity is visible (factor of 30). On the other hand, the maximum is already reached with one equivalent of metal salt added. Further addition directly led to a strong decrease in intensity which cannot be explained only by dilution. In the case of $\text{Zn}(\text{OAc})_2 \cdot 2\text{H}_2\text{O}$, a tremendous increase of fluorescence is observable which reaches its maximum at around 15 eq. The determined 217-fold increase in intensity is the highest value reported in this thesis. It needs to be mentioned that the used detector in the spectrofluorometer is only able to report intensities up to two million cps reliably.^[122] Since the emission intensity lies above this limit, the value of

the factor contains an unknown error. Nevertheless, the different anions strongly influence the fluorescence output. Since halides are known to be able to quench luminescence, the complexes with metal bromides maybe show lower fluorescence emission, in general, than those without halides. This would explain the much stronger response to zinc with acetate as anions. An explanation for the fast decreasing intensity with an excess of $\text{Zn}(\text{NO}_3)_2 \cdot 6\text{H}_2\text{O}$ could not be found, yet. The influence of the crystallisation water should not be very significantly. A comparison of the emission spectra of **15** with dry CdBr_2 and with its hydrate $\text{CdBr}_2 \cdot 4\text{H}_2\text{O}$ did not show any difference. What is important to mention is the same shift of the emission wavelength in the cases of all three zinc salts. This supports the hypothesis of the ability to differentiate zinc and cadmium ions by the use of **15** in combination with a spectrofluorometer.

In Figure 2.50, it was shown that the protonation of the ligand is a reversible process without any significant decomposition. The same can be demonstrated with the reaction of the two coordinating metal ions. Therefore, the bidentate ligand ethylenediamine (en) was chosen to compete with the new sensor compound **15** (Figure 2.56).

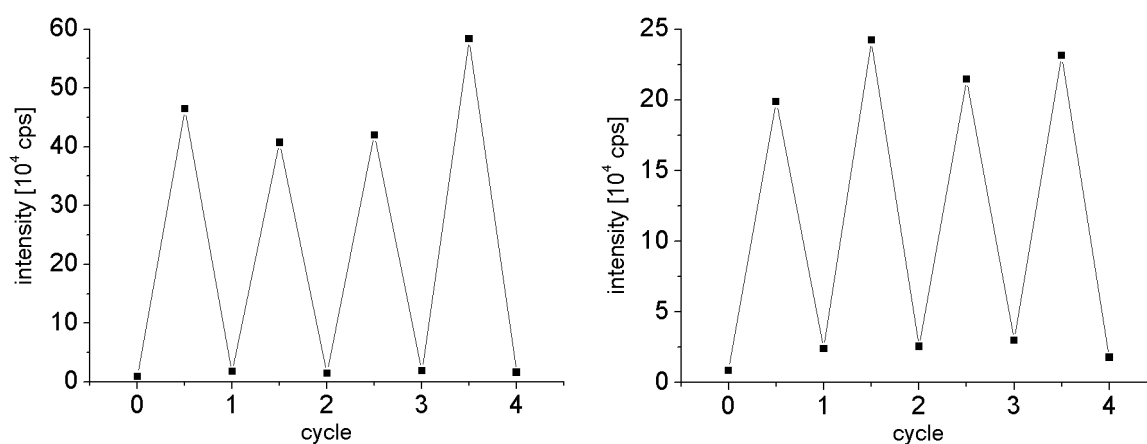


Figure 2.56: Fluorescence intensity changes of **15** in MeOH (10^{-5} M, $\lambda_{\text{exc}} = 357$ nm) upon alternate addition of ZnBr_2 (left) respectively CdBr_2 (right) and ethylenediamine (en).

In both experiments, the PET effect with its clearly visible off/on switch becomes apparent. Every reagent was added in a slight excess to ensure a full quenching or enhancement of the fluorescence. According to this, the maximum emission intensity varies. This reversibility is a very important feature for a chemical sensor if the compound is used or applied to industrial screening processes. For these purposes, it can be fixed to a polymer or resin surface and only needs to be washed with an e.g. ethylenediamine solution after the usage and thus can be used very often.

The experiments provide further information. Since the addition of five equivalents of ethylenediamine already quenches the fluorescence, the resulting complex must have a higher stability constant than the metal ion complex with **15**. Positive charged zinc and cadmium ions form octahedral complexes with three en molecules each ($[\text{M}(\text{en})_3]^{2+}$).^[123] The stability constant of these complexes is in both cases $1.23 \cdot 10^{12}$, whereas the successive formation constants do vary.

As already mentioned, zinc is classified as a harder Lewis acid in comparison to cadmium. The nitrogen atoms of the receptor side arms are classified likewise and should therefore bind stronger

to the zinc ions. This is why an experiment was set up to investigate the behaviour of the competing metal ions (Figure 2.57).

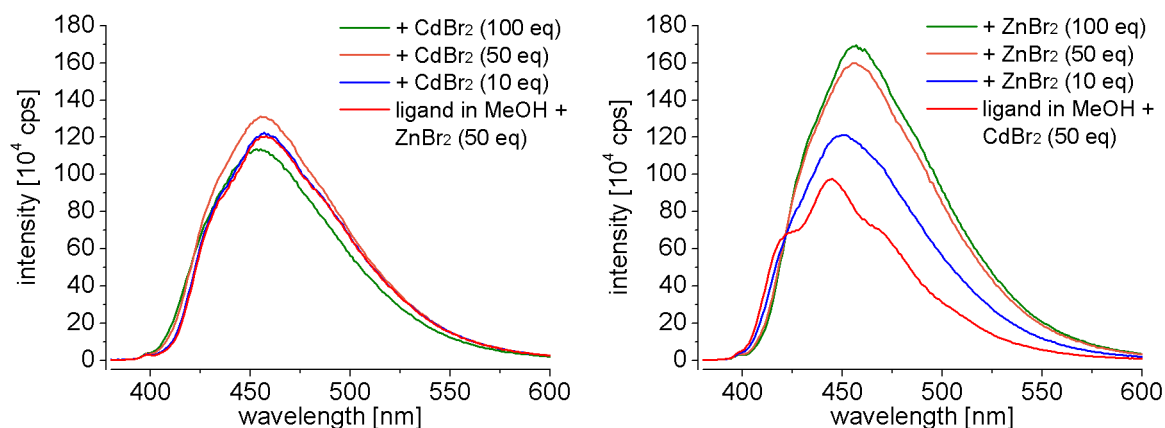


Figure 2.57: Emission spectra in MeOH (10^{-5} M, $\lambda_{\text{exc}} = 357$ nm): First, **15** with 50 eq of ZnBr_2 were added, then CdBr_2 was titrated into (left) and vice versa (right).

This experiment clearly demonstrates the stronger binding of zinc ions to the sensor ligand in comparison to Cd^{2+} . In the left figure, 50 equivalents of zinc bromide were added to **15**, then cadmium bromide was titrated into with 10, 50, and 100 equivalents. Even with twice of the Cd^{2+} amount, no significant change of the wavelength or emission intensity was observable. The zinc ions still bind to the amine receptors of the ligand. In the opposite experiment, the results were clearly different (Figure 2.57, right). Already ten equivalents of Zn^{2+} ions were sufficient to alter the spectrum. In the case of a 1:1 ratio of Zn^{2+} and Cd^{2+} , the spectrum reflects the bonding situation of the zinc complex ($\lambda_{\text{max}} = 457$ nm).

In the introduction, the short lifetime of the fluorescence phenomenon (10^{-6} – 10^{-9} s) was discussed. To prove if these values are consistent with the observed emission of the complexes, the lifetime of the excited state of compound **17** was measured exemplarily. Since this experiment could not be carried out in our department, the sample was taken to a workshop of the company *Horiba Scientific* in Essen. Here, a single exponential decay with a lifetime of $13.9 \cdot 10^{-9}$ s was measured (Figure 7.1) which fits good in the expected region for fluorescent compounds.

All these experiments gave a good overview about the sensing abilities of **15** in methanol. The next step was, therefore, the investigation of the possibility to use pure water as a solvent. Since the ligand is less polar and does not have any water-soluble substituents like carbon acid or sulfonyl groups, its solubility in water was quite low. For a 10^{-5} M solution only 2 mg of the ligand needs to be dissolved in 682 ml water. However, during the dissolution process the ligand got protonated by the water. The emission spectrum of its solution showed a highly intense band at 425 nm with exactly the same structure as after protonation with HCl. Even with the use of an aqueous phosphate buffer system (0.01 M, pH 7.4), the ligand only went into solution along with its protonation.

Similar observations were made with the addition of water to the alcoholic sample solution (Figure 2.58). Here, the wavelength of the emission maximum is only altered significantly after addition of 1.5 ml water. This is the same volume needed to add 100 eq. of a metal ion. The intensity of the band is, however, not enhanced strongly.

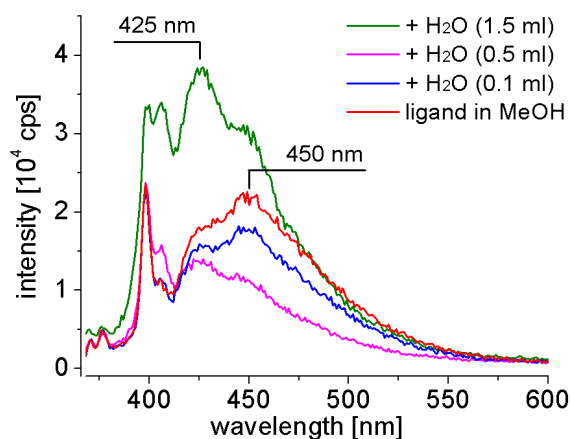


Figure 2.58: Emission spectra of **15** in MeOH (10^{-5} M, $\lambda_{\text{exc}} = 357$ nm) with addition of purified water.

This gave rise to the possibility to use water as the solvent for the metal ions, but to stay with methanol for the dilution of the organic compound. By this means, the ligand will not be protonated but can be titrated to aqueous samples in the biological or medicinal analysis. In Figure 2.59, the experiments with ZnBr_2 and CdBr_2 dissolved in water are illustrated.

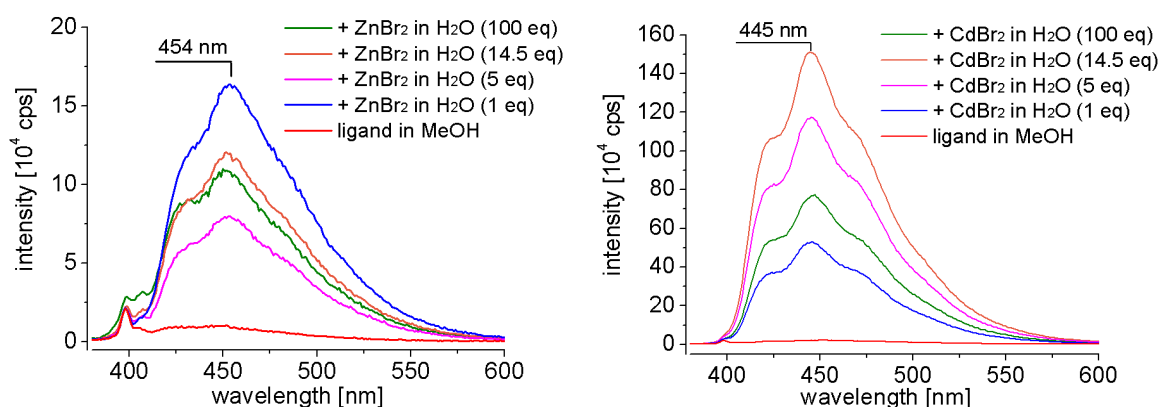


Figure 2.59: Emission spectra of **15** in MeOH (10^{-5} M, $\lambda_{\text{exc}} = 357$ nm) with addition of ZnBr_2 (left) and CdBr_2 (right). Both metal salts were dissolved in purified water.

The addition of one equivalent of zinc ions led to the expected enhancement of the intensity. Unfortunately, five equivalents of the metal ion reduce the emission of light by its half whereas further titration again increases the fluorescence; but only to a smaller extent. This behaviour is hard to explain. In general, the higher donor capability of the H_2O molecules in comparison to methanol may lead to a lower intensity. The strong solvent shell hardly releases zinc ions for the complexation with **15**. To understand the strange leap in the spectrum, the different concentrations of the metal ion solutions need to be considered (Table 2.5). The addition of five equivalents of Zn^{2+} is accompanied with 0.5 ml of water. This amount already decreases the emission intensity in comparison to the first addition. 14.5 equivalents, however, are added in a higher concentrated solution; only 0.1 millilitres of water are needed for this rise by 9.5 eq. Due to this higher $\text{Zn}^{2+}/\text{H}_2\text{O}$ ratio, the fluorescence rises again. Further addition only leads to the often observed effect of dilution.

Surprisingly, this behaviour cannot be observed in the case of cadmium. Here, the addition results in the typical strong increase of the emission intensity. The overall enhancement is even higher as

with the use of methanol. The different concentrations of the metal solutions did not influence the titration experiment at all. The aqueous solvent shell seems to be less strong in this experiment, which could be attributed to a weaker interaction of the hard Lewis base water with the soft Lewis acid Cd^{2+} compared to Zn^{2+} . These results demonstrate that sensor compound **15** dissolved in methanol can be used to detect Cd^{2+} ions even in aqueous solutions.

For a better assessment of the measured fluorescence values, the emission intensities of several compounds are compared with the typical fluorophore anthracene. In Table 2.9, the maximum intensities of the used compounds and their relative intensities divided by the fluorescence of anthracene are shown. In all cases, the compounds were excited at maximum intensity of the excitation spectrum. The maximum emission intensities of the measured compounds are lower than the intensity of anthracene. Zinc and cadmium bromide in methanol have values close to each other, whereas the addition of CdBr_2 dissolved in water reaches a higher relative intensity (0.21). The most powerful enhancement was achieved by the use of $\text{Zn}(\text{OAc})_2$ which has almost the same fluorescence intensity as the strong fluorophore anthracene (0.95).

Table 2.9: The maximum emission intensities of the metal complexes of **15** and their relative emission intensities compared with anthracene. All measurements were realised with 10^{-5} M solutions in methanol.

compound	λ_{exc} [nm]	abs. intensity [10^4 cps]	rel. intensity to anthracene
15 + ZnBr_2	357	84.15	0.12
15 + ZnBr_2 (aq)*	357	16.40	0.02
15 + CdBr_2	357	105.83	0.15
15 + CdBr_2 (aq)*	357	151.02	0.21
15 + $\text{Zn}(\text{NO}_3)_2$	357	65.01	0.09
15 + $\text{Zn}(\text{OAc})_2$	357	678.63	0.95
anthracene	373	711.91	1.00

* The metal salt was dissolved before in water.

With regard to the results of the metal ion screening in Figure 2.51, it needs to be discussed why the ligand responds selectively towards Zn^{2+} and Cd^{2+} ions in alcoholic solution. The effective ionic radii of the targets only play a minor role since the radius of Zn^{2+} (74 pm) differs stronger to Cd^{2+} (95 pm) than to most of the other tested cations (e.g. $r(\text{Mg}^{2+}) = 72$ pm, $r(\text{Cu}^{2+}) = 73$ pm).^[124] Furthermore, the receptor side arms can rotate around their methylene bridge to vary the pocket size of the sensor. The electron configuration of the metal ions tends to be more crucial because zinc and cadmium are both d^{10} elements. In general, the electron configuration of the transition metal ions has a strong influence to the stability constant of possible metal complexes (*Irving-Williams series*).^[125] However, the heavier homologue Hg^{2+} did not alter the fluorescence spectrum. This could have other reasons like the presence of fully occupied f-orbitals which leads to a more diffuse electron cloud and a greater ionic radius (116 pm). The radius is 21 pm larger than Cd^{2+} and could be too big for the chelation by both receptor units. For further investigations, it would be interesting if Cu^+ and Ag^+ ions, both d^{10} metal ions, influence the emission spectrum likewise to Zn^{2+} and Cd^{2+} . Since their bromide salts are non-soluble in methanol, they have not been tested in the course of this thesis. One example is present in the literature where this hypothesis is not fulfilled. In the introduction, the ligand 4,5-bis(*N,N*-di(2-

hydroxyethyl)iminomethyl)acridine (BHIA) was discussed as a molecular sensor for Cd^{2+} ions and, to a smaller extent, for its homologues Zn^{2+} and Hg^{2+} , too. Ag^+ ions were also tested but did not influence the present PET effect at all.^[57] A different research group were able to crystallise metal complexes of BHIA with Cu^{2+} , Ag^+ , and Cd^{2+} .^[59] All structures demonstrate the interactions of the nitrogen-containing side arms with the metal ions. Accordingly, the PET should be hindered along with the return of fluorescence emission. However, this was only observed by the use of the cadmium salt. Cu^{2+} ions behave different with regard to their paramagnetism. They are able to quench fluorophores e.g. through electron transfer from the paramagnetic cation to the excited molecule (Figure 2.60, a) or by an energy transfer process via the metal ion (b).^[126] This phenomenon was observed by the authors of the fluorescence study. An explanation for the absence of fluorescence by the addition of silver ions to the sensor solution could be found in the experimental conditions of both experiments. The metal ion screening was performed in buffered water whereas the crystals for X-ray diffraction were obtained from an acetone solution. The donor capability of the organic ligand may not be strong enough to compete with the polar aqueous solvent shell.

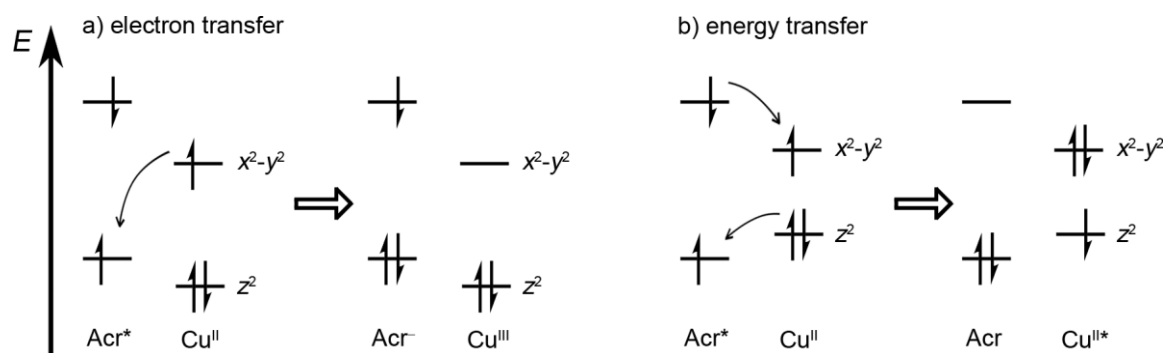


Figure 2.60: Two possible quenching mechanisms of paramagnetic metal ions exemplified by Cu^{2+} and anthracene.^[126b]

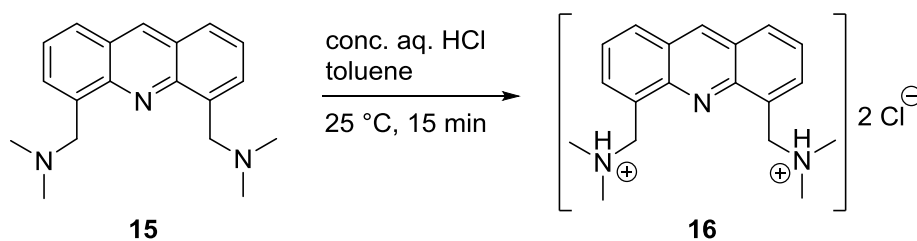
To conclude, it is possible that some of the tested paramagnetic transition metal ions interact with **15**, but do not enhance the emission intensity due to the mentioned quenching mechanisms. Since the ligand is already quenched by the PET of the amine receptor, no significant change was observed upon the titration with the paramagnetic metal ions. Alkaline and earth alkaline metals prefer to bind to oxygen-donor ligands^[127] and may stay solvated by the alcoholic environment.

Concerning the interesting studies of the BHIA ligand, crystallographic investigations of several metal ion derivatives of **15** are done in Chapter 2.3. To begin with, the hydrochloric adduct of the ligand will be discussed in the following.

2.2.15 4,5-Bis(dimethylaminemethylene)acridine hydrochloride (**16**)

Likewise to the synthesis of **14**, hydrochloric acid was used to convert **15** to its saline derivative (Scheme 2.21). In this reaction, toluene was used as a solvent for **15** in which conc. HCl was titrated into. Thereby, the product precipitated and was filtered off. After several washings with toluene, the pure product was dried under reduced pressure and a bright yellow powder was obtained with a good yield of 93%. The compound could be fully characterised by ESI MS, elemental analysis and NMR spectroscopy. With the latter analysis, the protons attached to the nitrogen atoms became apparent and could be identified by their couplings to the neighbouring

groups. In contrast to the determination of **14**, the elemental analysis gave sufficient results in this case, verifying the existence of two chloride counter ions. Final evidence was given by the solid state structure of the compound.



Scheme 2.21: Hydrochlorination of the amine functionalities led to the formation of the saline **16**.

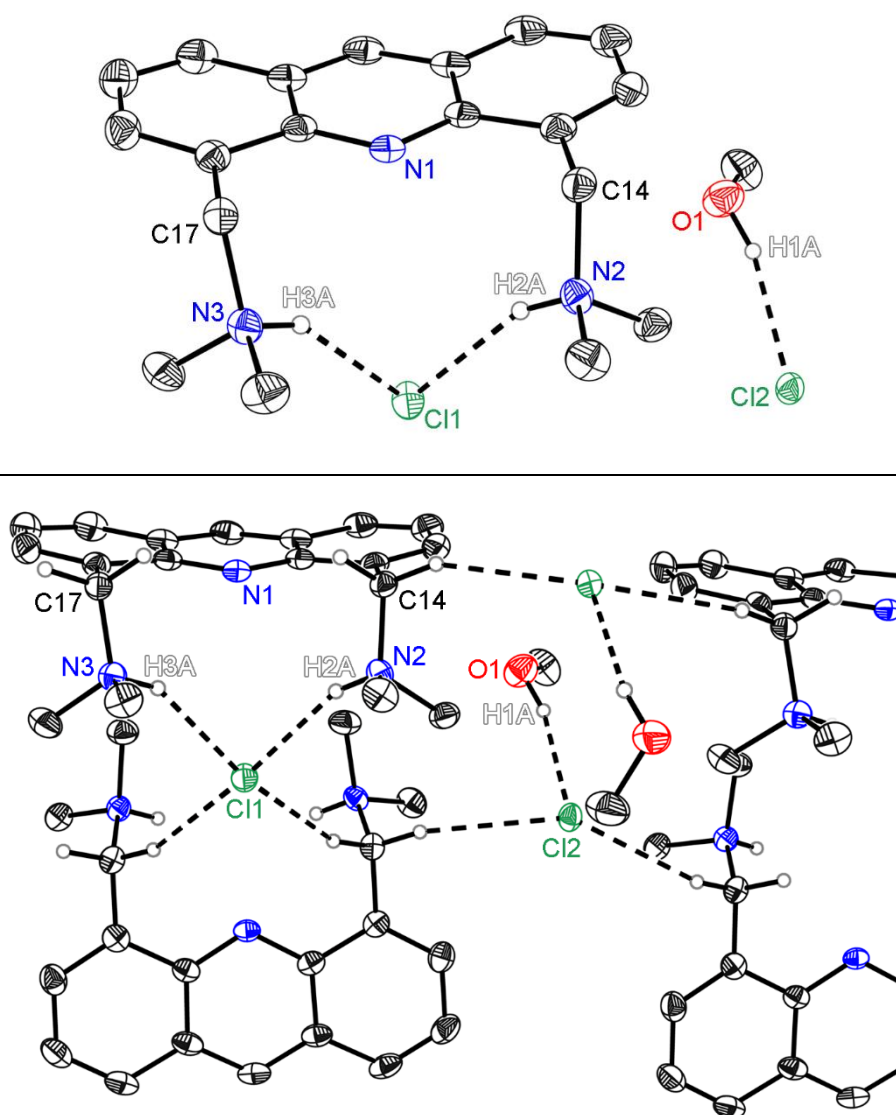


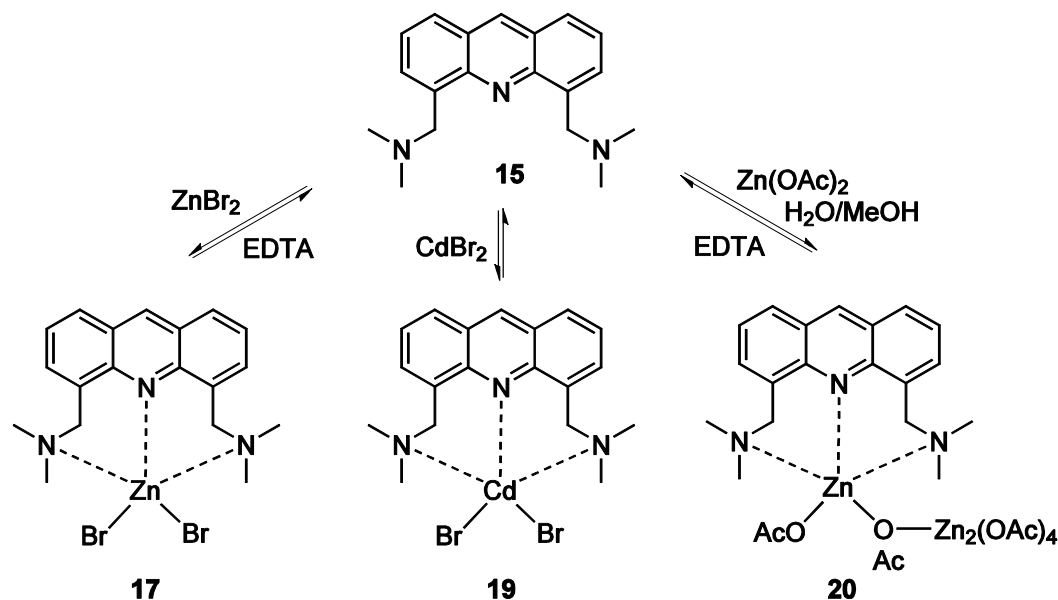
Figure 2.61: Solid state structures of $[(\text{Me}_2\text{NHCH}_2)_2\text{Acr}]\text{Cl}_2 \cdot (\text{MeOH})$ (**16**) with the asymmetric unit (top) and with an illustration of the hydrogen bonds (bottom). The hydrogen atoms of the acridine and of the methyl groups were omitted for clarity. The positions of the hydrogen atoms H1A, H2A, and H3A were refined freely. Anisotropic displacement parameters are depicted at the 50% probability level.

A recrystallisation from methanol gave suitable crystals for X-ray analysis. In Figure 2.61, the solid state structure of **16** with the co-crystallisation of one methanol is illustrated. The asymmetric unit contains one molecule which crystallises in the orthorhombic space group $Pna2_1$ and is shown in the upper part of the figure. The positions of the hydrogen atoms H1A, H2A, and H3A were refined freely but U_{iso} were constrained to $1.2 \cdot U_{\text{eq}}$ of the pivot atom. The second picture demonstrates the linkage of the compounds by hydrogen bonds. One of the chlorine atoms (Cl1) is thereby encaged by two acridine moieties with two stronger (NH...Cl) and two weaker hydrogen bonds (CH...Cl). The latter interaction derives from the methylene bridges which also forms hydrogen bonds to the second chloride. This is surrounded by a third hydrogen bond from the methanol molecule (OH...Cl). Unfortunately, the character of these interactions cannot be determined further. Likewise, the significant bond lengths and angles cannot be discussed since the completeness of the data set is too low (completeness to $\Theta_{\text{full}} = 77.2\%$). This was caused by a blockage of the cooling system during the measurement along with the loss of the crystal. But in general, the side arms at the 4- and 5-positions are arranged similarly and are comparable with those of their relative precursor **9**.

2.3 Investigations of metal complexes of **15**

2.3.1 4,5-Bis(dimethylaminemethylene)acridine dibromido zinc(II) (**17**), dibromido cadmium(II) (**19**), and tetrakis(μ -acetate) bis(acetate) zinc(II) (**20**)

To gain a better understanding of the observed fluorescence properties of **15**, it is necessary to know how the metal ions are linked to the ligand. Therefore, the synthesis of the metal complexes and their investigation with a variety of analytical methods is of major importance and is discussed in the following.



Scheme 2.22: Reaction pathways to different metal complexes based on **15**.

For the synthesis of **17**, the ligand and ZnBr_2 were dissolved in THF whereas MeOH was used for the preparation of **19** (Scheme 2.22). In both cases, one equivalent of the metal salt was added dropwise to **15**, resulting in an immediate precipitation of the metal complex. The suspension was

filtrated and washed with the same solvent used for the synthesis. The formation of the zinc complex resulted in a moderate yield of 47%. The cadmium complex could be isolated with a yield of 90%. Both zinc complexes were checked for the possibility to reobtain the pure ligand system. Therefore, aqueous $\text{Na}_2\text{H}_2\text{EDTA}$ and NaHCO_3 solutions were used to remove the metal salts and to isolate **15** in good yields (Chapter 4.3).

The crystallisation of **15** with $\text{Zn}(\text{OAc})_2$ to give **20** was endeavoured to check whether complexes with different zinc salts behave the same which is indeed the case here. The metal salt was only soluble in water and was added in a slight excess to an alcoholic solution of the organic ligand. The yield was not determined for this compound. A toluene/DMF mixture was used to dissolve **20** at room temperature. The solution was stored at $-30\text{ }^\circ\text{C}$ for ten days resulting in the formation of suitable crystals.

2.3.2 Solid state analysis by X-ray diffraction

Single crystals of **17** and **19** were obtained through crystallisation from a THF/DMF mixture by slowly cooling the boiling solution to room temperature. By X-ray diffraction experiments, it was possible to determine their solid state structures (Figure 2.62). The zinc complex crystallises in the monoclinic space group $P2_1/c$ and the cadmium derivative in the chiral orthorhombic space group $P2_12_12_1$. Both complexes are almost isostructural. In the zinc structure one bromide ion is substituted by a coordinating solvent molecule DMF and is in the following numbered as **18**. The positively charged complex is counterbalanced by a solvent-separated $[\text{ZnBr}_3]^-$ anion in the asymmetric unit (Figure 5.4).

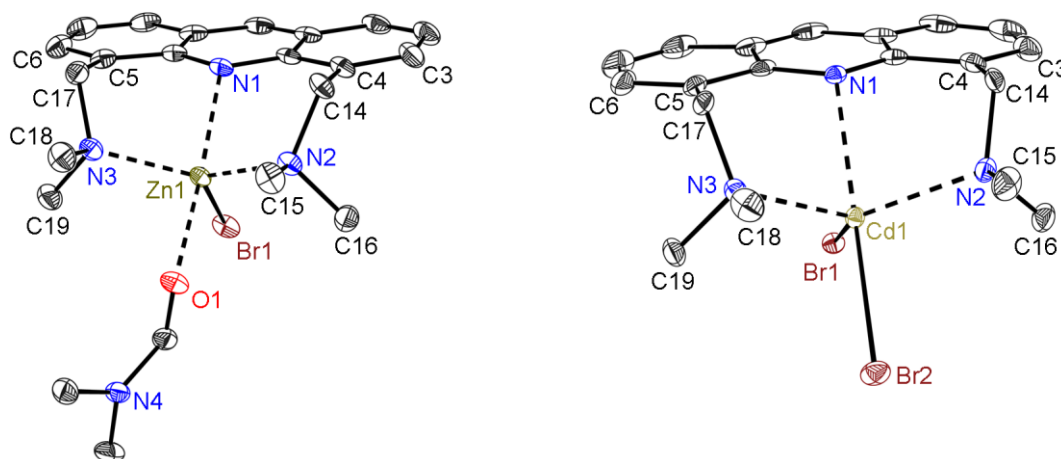


Figure 2.62: Solid state structures of $[(\text{dmf})\text{ZnBr}\{(\text{Me}_2\text{NCH}_2)_2\text{Acr}\}]^+$ (**18**, left) and $[\text{CdBr}_2\{(\text{Me}_2\text{NCH}_2)_2\text{Acr}\}]$ (**19**, right); crystallised from a THF/DMF mixture. The omitted counter anion in the asymmetric unit of the zinc structure is a solvent-separated $[(\text{dmf})\text{ZnBr}_3]^-$ unit. All hydrogen atoms were omitted for clarity. Anisotropic displacement parameters are depicted at the 50% probability level.

The solid state structures indicate a coordination of the Zn^{2+} and Cd^{2+} ions by all three present nitrogen atoms. This binding motif, where the methylene bridged amines in the 4- and 5-positions and the aromatic nitrogen atom of the acridine all are involved in a metal ion coordination, is currently only present with one entry in the CSD. The solid state data was published in 2016^[59] during the writing of this thesis. Other two examples with methylene bridged phosphorous atoms coordinating a ruthenium ion can be found in the database.^[128] Overall, a structure search concerning a coordination of an acridine unit to any metal ion merely results in 56 hits.^[129]

Table 2.10: Selected bond lengths and angles of **18** and **19**. The angular sums arise from the C–N–C angles.

Bond [pm]	18 (Zn)	19 (Cd)	Angle [°]	18 (Zn)	19 (Cd)
N1–M	230.39(16)	254.07(18)	N1–M–N2	90.05(6)	82.91(6)
N2–M	207.89(16)	232.31(19)	N1–M–N3	89.81(6)	82.81(6)
N3–M	209.09(17)	231.70(19)	N1–M–O1/Br2	175.31(6)	174.08(4)
Br1–M	239.83(4)	259.13(4)	N2–M–N3	128.68(6)	120.87(7)
O1/Br2–M	218.82(14)	266.16(4)	angular sum of N2	325.0(5)	327.1(6)
			angular sum of N3	324.0(5)	327.0(6)
			C3–C4–C14–N2	–114.8(2)	–105.3(3)
			C6–C5–C17–N3	112.7(2)	105.9(3)

From the nitrogen-metal bond lengths in Table 2.10 it is obvious that the averaged distances from the amine nitrogen atoms to the metal ion (208.49(17) pm for Zn^{2+} and 232.01(19) pm for Cd^{2+}) is shorter than from the acridine nitrogen atom (230.39(16) pm and 254.07(18) pm, respectively). The shorter distances are in perfect agreement with literature values found in the CSD, compared to general $\text{N–Zn}^{2+}/\text{Cd}^{2+}$ bonds. The longer N–M distances can still be found in the database but less frequently. One reason for this different bonding situation results from the rotational ability of the amines to improve the orbital overlap with the target ions. The C–N–C angles of the sp^3 hybridised amines are very close to the ideal tetrahedral angle. The resulting geometry forces the metal ion underneath the acridine plane which reduces the dative bonding of the ring nitrogen atom. Moreover, the lone pair of the sp^2 hybridised nitrogen atom is partly delocalised in the π -system of the aromatic system and has therefore a reduced donor capacity. The N–M bond incloses an relatively acute angle of 44.5° (**18**) and 38.5° (**19**), to the plane of the central acridine ring. A closer look at the bonding situation and the angle values in Table 2.10 reveals the coordination polyhedron of a trigonal bipyramid at each metal atom. This geometry is depicted in Figure 2.63.

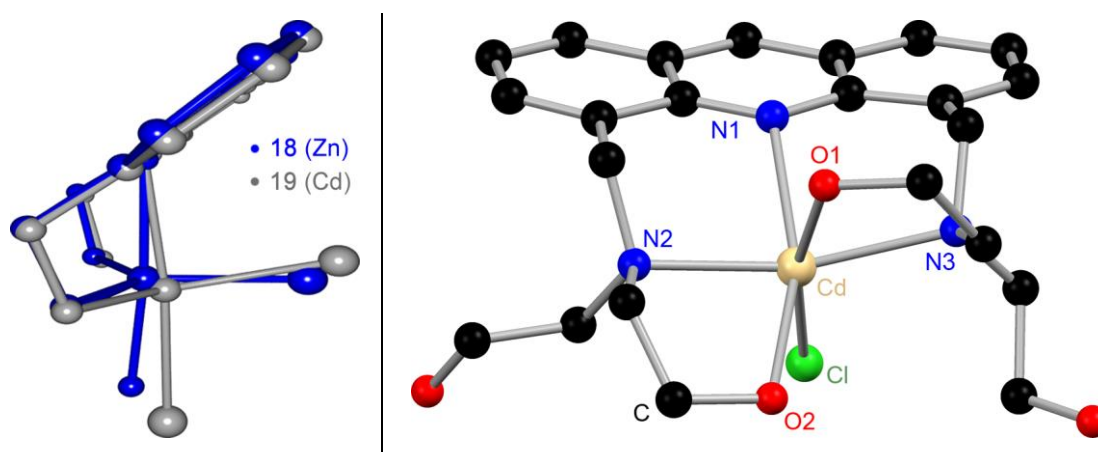


Figure 2.63: Left: Superposition of both metal ion structures (**18** and **19**), showing the trigonal bipyramidal geometry of the coordination motif. The methyl groups at the amines and the main part of the DMF molecule are omitted for clarity. Right: Solid state structure of $[\text{CdCl}(\text{BHIA})]^+$, illustrating the similar structure motif of an acridinyl amine sensor system.^[59] The solvent-separated counter ion was omitted for clarity.

The illustration was made by fixing the positions of the inner ring atoms of the acridine backbones. In the zinc complex (blue), the acridine nitrogen atom and the nitrogen atoms of the amines form an almost perfect right angle. In **19** (grey), they are bended to smaller angles due to the higher space requirements of the cadmium ion. Additionally, the torsion angles of the receptor side arms demonstrate this different steric demand. A higher value represents a stronger N–M interaction along with a smaller drift of the metal ion underneath the acridine plane (**18**: 113.8(4)° vs **19**: 105.6(6)°; averaged values). The π -stacking of the aromatic systems, already discussed in several structures before, can also be observed in the case of **18**. The distance between the two acridine units is 360.1 pm, which is the highest value measured in this thesis. The cadmium complex is not showing any interactions between the aromatic backbones.

In Figure 2.63, right, the solid state structure of $[\text{CdCl}(\text{BHIA})]^+$ is shown, published by *Denisova* and co-workers.^[59] It illustrates the similar structure motif of an acridinyl amine sensor system and its fluorescence properties has been discussed in the introduction (Figure 1.11). In contrast to **19**, two more oxygen donors fill the coordination sphere of the metal ion and a chloride acts as counter ion. According to this, the Cd^{2+} ion has an octahedral coordination geometry which is supported by almost perpendicular angles between the chelating atoms (except O2). The distances of the amines to the metal centre are comparable with those measured for this thesis, whereas the N1–Cd distance is only 246.0(3) pm in comparison to 254.07(18) pm in **19**. This stronger interaction may be explained by the five-dentate BHIA ligand inclosing the metal ion to a greater extent. Furthermore, only one chloride ion is bonded, whereas two bromides are present in **19**. The anions reduce the positive charge of the cation and makes it less attractive for the lone pairs of the nitrogen atoms.

Table 2.11: Selected bond lengths and angles of **20**.

Bond [pm]		Angle [°]	
N1–Zn1	232.53(14)	N1–M–N2	87.88(5)
N2–Zn1	210.35(15)	N1–M–N3	89.67(5)
N3–Zn1	210.25(15)	N1–M–O1	85.10(5)
O1–Zn1	197.98(12)	N1–M–O3	175.85(5)
O3–Zn1	212.50(12)	N2–M–N3	122.63(6)
O4–Zn2	193.86(13)	C3–C4– C14–N2	–112.06(19)
		C6–C5– C17–N3	110.84(18)

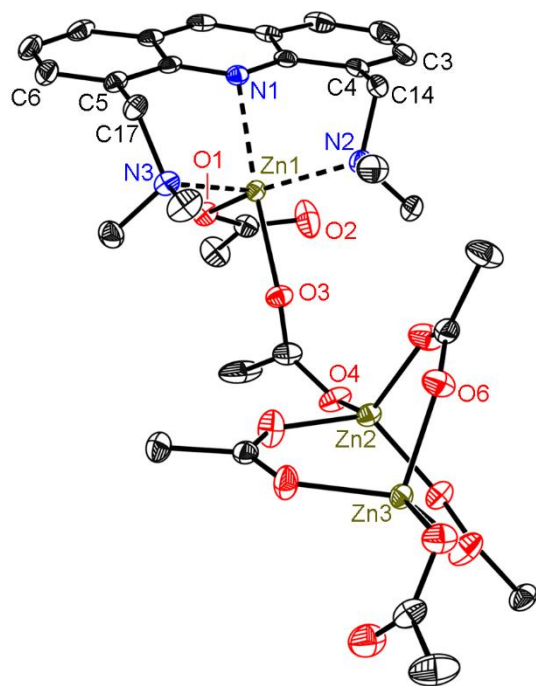


Figure 2.64: Solid state structure of $[\mu\text{-(OAc)}_4(\text{OAc})_2\text{Zn}_3\{(\text{Me}_2\text{NCH}_2)_2\text{Acr}\}]$ (**20**). All hydrogen atoms were omitted for clarity. Anisotropic displacement parameters are depicted at the 50% probability level.

In addition to **18**, two more zinc containing structures were crystallised and determined by X-ray diffraction. One of the compounds was crystallised from a THF/MeOH mixture whereby parts of

the methanol solvent molecules were deprotonated. Two zinc ions are present in the asymmetric unit which are μ^2 -coordinated by a methoxide anion. The organic ligand is chelating one of the metal ions whereas the second is surrounded by three bromides. One of the bromides is disordered with another methoxide with a site occupation factor of 0.84 and 0.16, respectively. Additionally, two THF molecules were disordered each over two positions. Since the structure was obtained by chance and the coordination sphere of the metal ions is disordered, it will not be discussed here in detail but can be found in the crystallographic section.

The more interesting structure was obtained by the addition of $\text{Zn}(\text{OAc})_2$ to **15**. The metal salt was used to investigate the influence of the counter ion. The difference in their fluorescence behaviour has already been discussed in Chapter 2.2.14, now the properties of the solid state structures will be compared. **20** crystallises in the same monoclinic space group ($P2_1/c$) with one molecule in the asymmetric unit (Figure 2.64). The geometry of the zinc chelation is the same as in the case of **18**. The only difference is that two anionic acetate groups fill the coordination sphere of the metal ion. One of the acetate groups is bridging to a second zinc ion which is in turn coordinated by another three bridging acetate molecules, linking to a third zinc ion. The N–Zn1 distances are elongated by 1.16(32) to 2.46(31) pm in the case of **20** which can be explained by the higher Lewis basic character of the acetate oxygen atoms.^[91] Therefore, the positive zinc ion is reduced in its charge and is less attractive for the lone pairs of the nitrogen atoms. This weaker bonding situation can additionally be seen by the smaller torsion angles of the amine groups (C3–C4–C14–N2 and C6–C5–C17–N3, respectively).

The N1–Zn1–O3 angle is quite the same as for compound **18** ($\sim 175^\circ$). However, the O3–Zn1 bond is with 212.50(12) ppm very high in comparison to the other Zn–OAc interactions; they range from 193.86 ppm (O4–Zn2) to 199.92 ppm (O6–Zn3). Since it is an anion-cation interaction, the oxygen-metal bond lengths should be much shorter as in the case of the neutral DMF coordination in **18**. Here, the oxygen-zinc distance is only 6.3 pm longer (218.82 pm) than the O3–Zn1 bond of the acetate group. A reasonable explanation for this unusual bond lengths is the shielding of the dimethylamine groups. The mentioned methyl groups would otherwise get in close contact to the methyl groups of the bridging acetate groups of Zn2 and Zn3.

2.3.3 Computational studies on compounds 17–19

Unfortunately, the results from the solid state investigations do not agree with the observations made during the fluorescence measurements. The nitrogen atom distances (especially N2 and N3) to the central zinc ion should be shorter in the case of **20**, since its observed emission intensity was much higher than with ZnBr_2 . The deactivation of the PET effect of the free ligand **15** should be more effective when a strong target coordination is present. Apparently, the situation in the solid state cannot be transferred directly to the experiments in solution. Furthermore, the longer N1–M²⁺ distances can still be found in the CSD, however, the solid state investigations are not a sufficient evidence for the existence of a bonding situation.^[130] In order to judge on the main binding forces of the metal ion coordination, and to relate the findings to the chemistry in solution, a series of electronic structure calculations on compounds **17** to **19** were conducted.

All structures were optimised at the B3LYP-D3/def2-TZVPP^[131] level of theory. Included were the complexes **18** and **19**, identified in the solid state structures, as well as the hypothetical

complex **17**. The structures obtained (see subsequent figures) are in good agreement with the crystal data which has been discussed before. A natural bond orbital (NBO) analysis^[132] was carried out to gain insight into the coordination of the metals to the acridine derivative **15**. The data in Table 2.12 give the second order perturbation theory energies^[133] for the interaction between the lone pairs of the different nitrogen atoms and the zinc or cadmium ion. Furthermore, the calculated N–M distances of the complexes are shown. As expected, in these structures the metal has a weaker coordination to N1, compared to the other nitrogen atoms.^[134] Substitution of one bromide anion by a DMF solvent molecule increases this value from 5.6 to 17.0 kcal·mol⁻¹ (**17** in comparison to **18**). Two different effects could serve as an explanation to this trend. The weaker interaction could be due to a lower positive charge at the metal, since Br⁻ should be a better electron density donor than DMF. Another possibility would be that the bulky bromide anion pulls the metal away from the acridine ring nitrogen atom. The NPA charges for the two compounds are 1.49 (**17**) and 1.60 (**18**), so that the charge difference is not very significant. The second possibility, hence the interaction with a second bromide to weaken the coordination to the acridine seems to be the most likely explanation for this effect.

Table 2.12: NBO second-order perturbation theory analysis of the metal ion (Zn/Cd) coordination to **15** at the B3LYP-D3/def2-TZVPP level of theory.

compound	$E^{(PT2)}$ [kcal·mol ⁻¹]			$d^{(N-M)}$ [pm]		
	N1	N2	N3	N1	N2	N3
[(dmf)ZnBr{(Me ₂ NCH ₂) ₂ Acrid}] ⁺ (18)	17.0	25.4	25.1	277.0	221.3	220.1
[ZnBr ₂ {(Me ₂ NCH ₂) ₂ Acrid}] (17)	5.6	24.7	25.4	---	---	---
[CdBr ₂ {(Me ₂ NCH ₂) ₂ Acrid}] (19)	4.7	22.8	22.7	283.0	241.7	241.6
[(MeOH) ₂ Zn{(Me ₂ NCH ₂) ₂ Acrid}] ²⁺ (in MeOH)	21.9	25.4	26.5	215.7	207.0	207.0
[(MeOH) ₂ Cd{(Me ₂ NCH ₂) ₂ Acrid}] ²⁺ (in MeOH)	15.0	32.1	31.8	237.3	225.0	225.2

Furthermore, calculations on the hypothetical complexes, [(MeOH)₂Zn{(Me₂NCH₂)₂Acrid}]²⁺ and [(MeOH)₂Cd{(Me₂NCH₂)₂Acrid}]²⁺ formed in solution, were conducted. The replication of the conditions in solution as close as possible is of great interest, which is why the COSMO continuum solvation model was applied (for standard methanol solution conditions).^[135] The NBO results show that the coordination to the acridine nitrogen is strengthened (21.9 and 15.0 kcal·mol⁻¹ for Zn²⁺ and Cd²⁺, respectively). This is in line with the observations made when comparing **17** and **18**. The complexes formed in the solid state have a weaker binding to the acridine moiety due to the crystallisation with bromide anions. The computed structures show smaller N1–Zn/Cd distances in agreement with this observation. The values are 216 and 237 pm, for Zn²⁺ and Cd²⁺ respectively. In methanol solution, sizeable interactions between the metal ion and the N1 nitrogen atom can be confirmed. The interactions with the side arm nitrogen atoms are relatively constant, just slightly enhanced in solution. For the illustration of the difference electron density maps of the discussed compounds, the electron densities of the individual parts were computed and subtracted from the electron density of the whole complex, respectively. Thereby, the geometry of the atoms is untouched. The individual parts are always the organic ligand **15**, the metal ion (Zn²⁺/Cd²⁺), and the coordinating counterparts (Br⁻, DMF, MeOH). This facilitates the

illustration of the regions where the electron density is enhanced due to the interaction of the relevant atoms. The green clouds represent the accumulated electron density.

In Figure 2.65, the interaction of the lone pairs of all three nitrogen atoms with the zinc ion is accentuated in both structures with a slightly higher accumulated electron density in the methanol compound. This is in line with the results of the computational studies. In the case of the cadmium structures, the interaction with the metal ion is accentuated to a lesser extent. In the compound calculated in solution small electron density clouds are still observable in the region of the nitrogen atoms pointing towards the metal ion centre (Figure 2.66, left). However, the CdBr_2 structure does not have any observable interactions, using the same isosurface level. In Figure 2.67, two more electron density maps of **19** are shown with smaller isosurface levels. With $0.009 \text{ e}\text{\AA}^{-3}$ the interaction with the side arm amines becomes apparent and at a level of $0.005 \text{ e}\text{\AA}^{-3}$, the N1–Cd interaction can be observed as well.

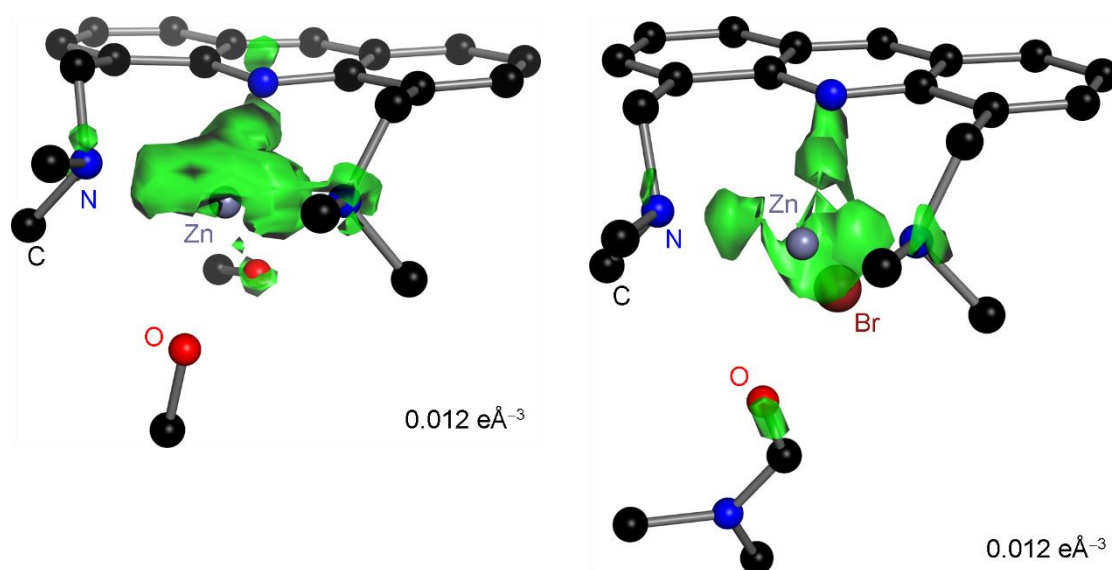


Figure 2.65: Computed electron density map of $[(\text{MeOH})_2\text{Zn}\{(\text{Me}_2\text{NCH}_2)_2\text{Acr}\}]^{2+}$ (left) and $[(\text{dmf})\text{ZnBr}\{(\text{Me}_2\text{NCH}_2)_2\text{Acr}\}]^+$ (**18**, right) at an isosurface level of $0.012 \text{ e}\text{\AA}^{-3}$, whereof the electron densities of the individual parts have been subtracted.

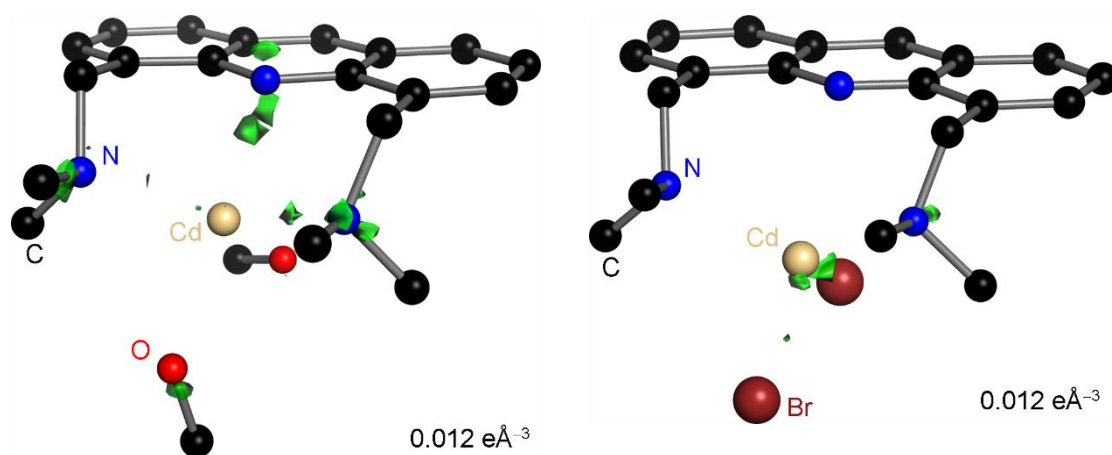


Figure 2.66: Computed electron density map of $[(\text{MeOH})_2\text{Cd}\{(\text{Me}_2\text{NCH}_2)_2\text{Acr}\}]^{2+}$ (left) and $[\text{CdBr}_2\{(\text{Me}_2\text{NCH}_2)_2\text{Acr}\}]$ (**19**, right) at an isosurface level of $0.012 \text{ e}\text{\AA}^{-3}$, whereof the electron densities of the individual parts have been subtracted.

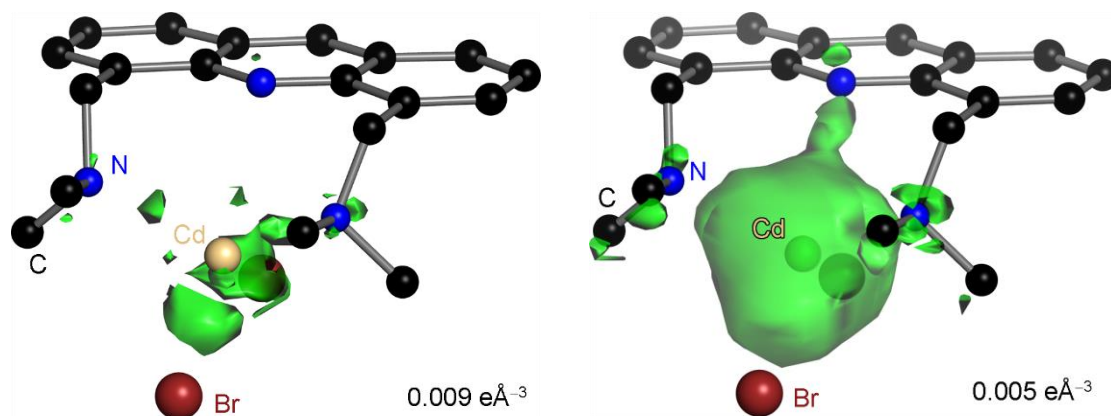


Figure 2.67: Computed electron density map of **19** at different isosurface levels, whereof the electron densities of the individual parts have been subtracted. Left: $0.009 \text{ e}\text{\AA}^{-3}$, right: $0.005 \text{ e}\text{\AA}^{-3}$.

When comparing the results of the computational studies with the fluorescence properties, it is apparent from the difference density plots that the metal coordination does not affect the π -density significantly in agreement with the almost unchanged emission wavelength. A possible explanation would be that the coordination does not influence the π -system significantly. Considering the geometry optimisations for the complex in methanol solution, both metal ion interactions with the aromatic nitrogen atom become stronger. This should also be the case for the titration experiment of the fluorescence measurements.

2.3.4 Investigation of the metal complexes in solution

For a deeper insight into the liquid phase, ^1H NMR spectra in $\text{DMSO-}d_6$ were recorded of the relevant compounds depicted in Figure 2.68. In comparison to the spectrum of the pure ligand, the metal complexes show significantly broadened signals. This is often caused by dynamic processes.^[118] Consequently the spectra of **17** and **19** were measured at different temperatures.

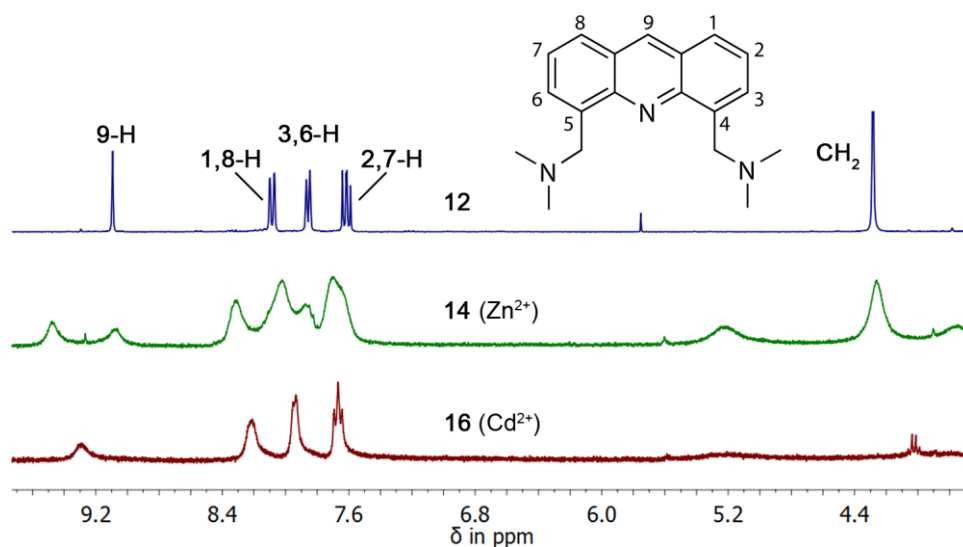


Figure 2.68: ^1H NMR spectra of compounds **15**, **17**, and **19** in $\text{DMSO-}d_6$ at ambient temperature.

Therefore, the NMR solvent was changed to $\text{DMF-}d_7$ due to its wide temperature range of liquidity from -61 to 151 $^\circ\text{C}$. Another advantage is the higher comparability to the solid state structures since they were crystallised from the same solvent. Especially the zinc structure

contains a DMF molecule coordinating to the metal ion. This motif will be discussed in this chapter, too. With the use of DMF- d_7 for the NMR experiments, the signals are likewise broadened at ambient temperature. An increase of the temperature sharpens the broad signals until one definite set of signals is obtained (Figure 2.69, 353 K). At the coalescence temperature of nearly 303 K, the diastereotopicity of the CH₂ protons becomes visible. The signal of the four methyl groups at the amines also splits into two signals.

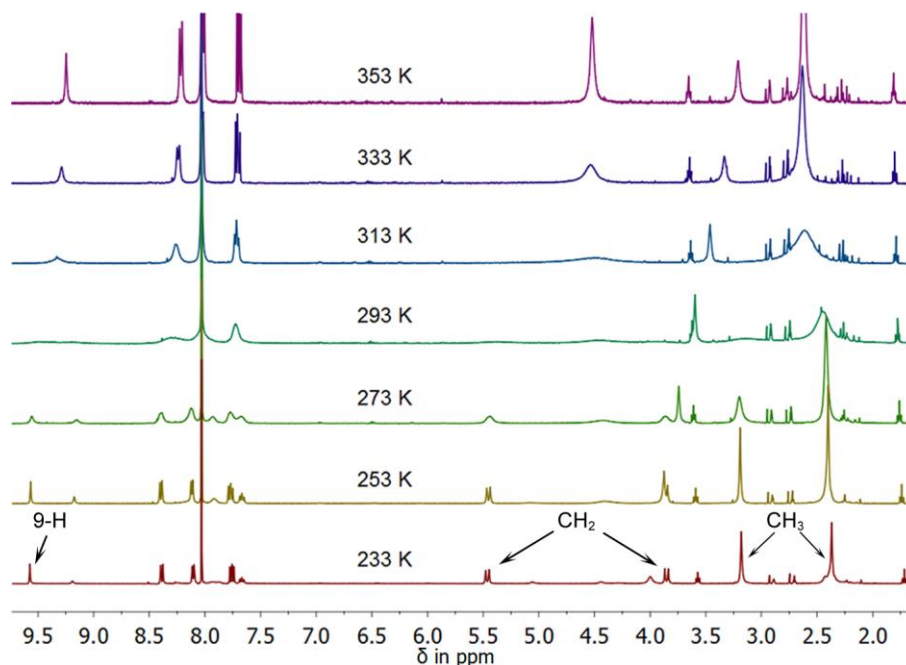
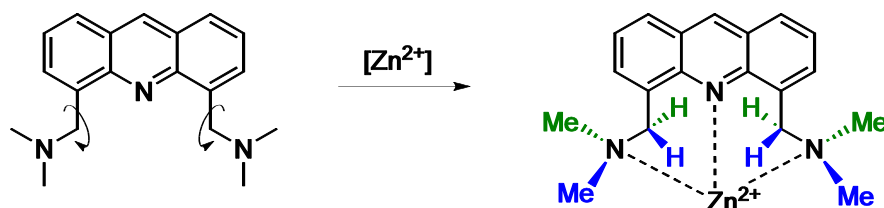


Figure 2.69: Temperature-dependent ^1H NMR spectra of **17** in DMF- d_7 . The discussed signals are marked at 233 K.



Scheme 2.23: Visualisation of the hindered rotation of the amines after the coordination of zinc. The coloured protons and methyl groups are no longer chemically equivalent and can be monitored.

The velocity of their hindered rotation caused by the coordination of the zinc ion (Scheme 2.23) lies underneath the NMR timescale at lower temperatures and can be monitored. At lower temperatures, the spectrum splits into two different sets of signals with a maximum intensity at around 253 K. At this temperature they exhibit an intensity ratio of around 2:1 what can be monitored by the singlet of the H-9 proton at 9.57 ppm and 9.17 ppm, respectively (Figure 2.70). This splitting is most likely to be attributed to the exchange of the bromine atoms with the solvent DMF, which has already been observed in the solid state structure. To prove this statement, an excess of NaBr was added to the sample, altering the ^1H NMR spectrum significantly: a third set of signals appears whereby the intensity ratio of the other two sets of signals is reversed (Figure 2.71). To distinguish between these different species, two pseudo 2D ^1H -DOSY experiments at

low temperature were carried out, with and without the presence of NaBr salt (Figure 2.72; for full spectrum see Figure 7.3).

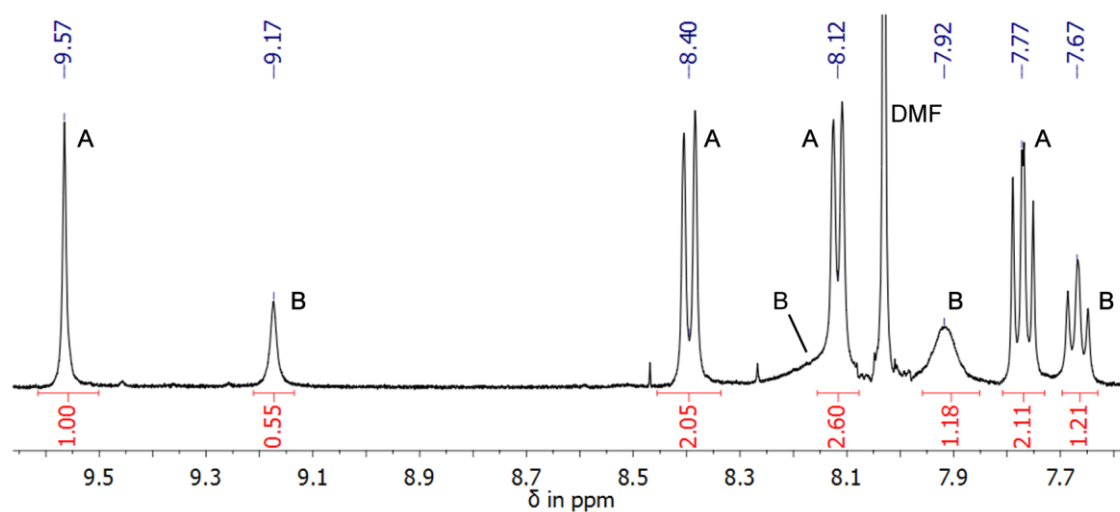


Figure 2.70: Aromatic region of the ^1H NMR spectrum of **17** in $\text{DMF-}d_7$ at 253 K, illustrating the two sets of signals (A and B) observed at lower temperatures.

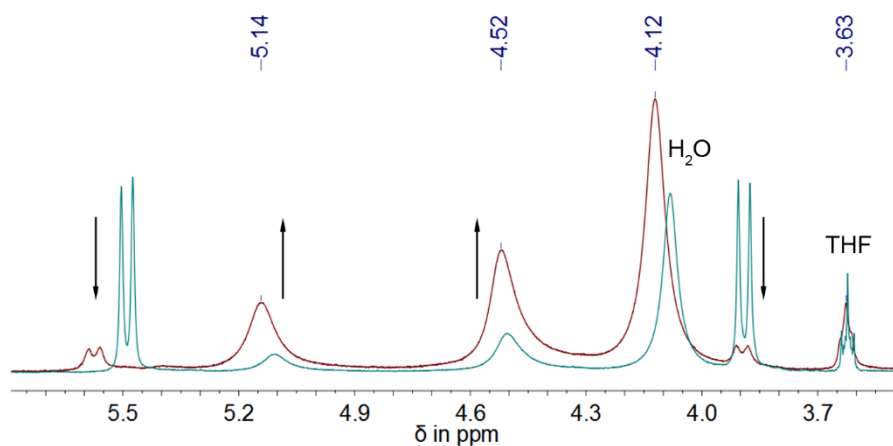


Figure 2.71: Extract of the superimposed ^1H NMR spectra of **17** without (turquoise) and with addition of 10 eq NaBr (red) in $\text{DMF-}d_7$ at 243 K. After the addition of the salt, the signal intensity of the diastereotopic methylene protons (CH_2) decreases, while two different signals at 5.14 and 4.52 ppm rise.

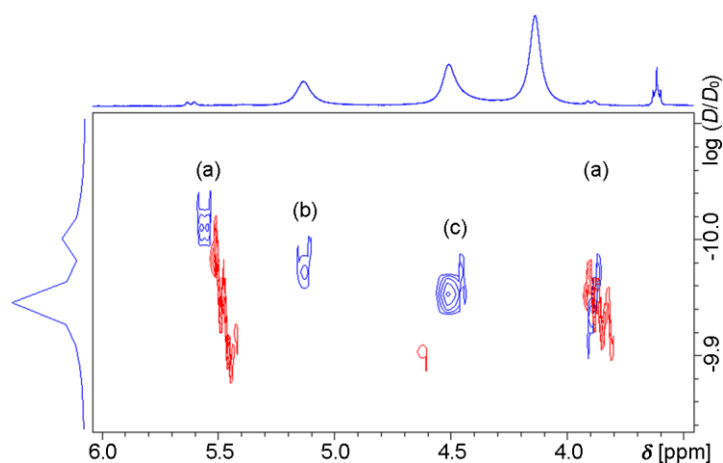


Figure 2.72: Overlay of the ^1H -DOSY NMR spectra of **17** showing the signals of the CH_2 groups without (red) and with addition of 10 eq NaBr (blue) in $\text{DMF-}d_7$ at 243 K;

a) $[(\text{dmf})_2\text{Zn}\{(\text{Me}_2\text{NCH}_2)_2\text{Acr}\}]^{2+}$,
 b) $[(\text{dmf})\text{ZnBr}\{(\text{Me}_2\text{NCH}_2)_2\text{Acr}\}]^+$,
 c) $[\text{ZnBr}_2\{(\text{Me}_2\text{NCH}_2)_2\text{Acr}\}]$.

Additionally, tetramethylbutane (TMB) was added as internal reference for the ^1H -DOSY NMR experiments. Its diffusion coefficient was kept constant to generate comparability of the different spectra. The diffusion coefficient of the rising signals decreases slightly from (a) to (c) which can be explained by the smaller radius/mass ratio of a bromine atom compared to a DMF molecule (van der Waals volume of bromine: 2.74^{-29} m^3 ; DMF: 1.31^{-28} m^3).^[87, 136] Consequently, (c) should represent the dibrominated species (**17**). The new signal (b) has a diffusion coefficient that lies between the two others and is therefore assigned to the monobrominated compound (**18**). Furthermore, the signals at room temperature are no longer broadened after the addition of NaBr (Figure 7.2). Due to these results, the dynamic processes can be attributed to the exchange between bromide ions and solvent molecules.

Zinc ions are spectroscopically silent making it difficult to detect a ligand-metal interaction by NMR spectroscopy. However, the ^{15}N NMR chemical shifts of the free ligand and of the zinc complex were measured using the ^1H , ^{15}N -HMBC experiment (Figure 7.5 and Figure 7.6, respectively). The comparison of the resulting shifts shows a small but significant deshielding of $\Delta\delta = 8.6 \text{ ppm}$.^[137]

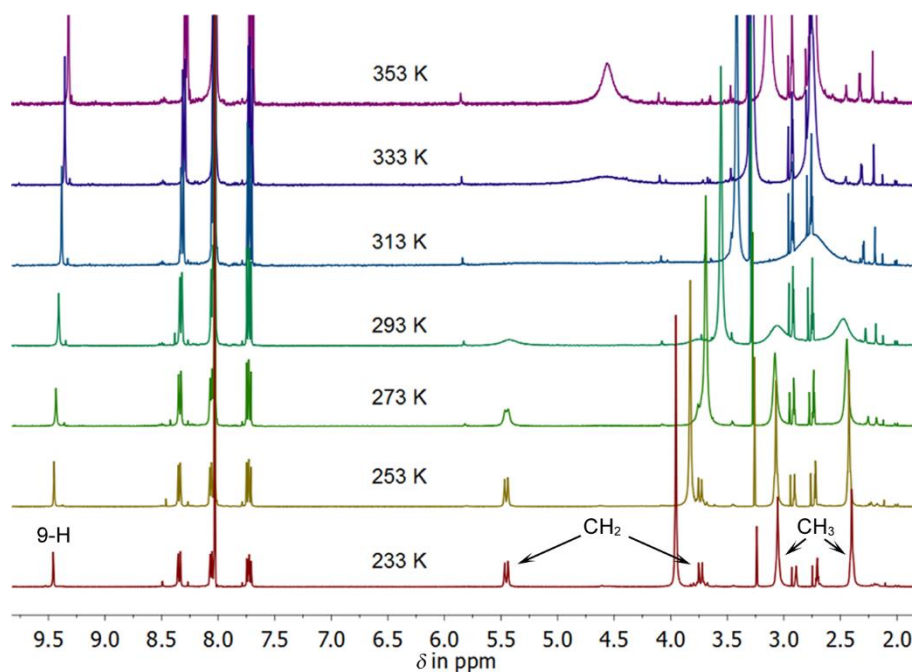


Figure 2.73: Temperature-dependent ^1H NMR spectra of **19** in $\text{DMF-}d_7$. The discussed signals are marked at 233 K.

In principle, the ^1H NMR spectra of **19** show similar dependencies upon temperature variation as shown for compound **17** (Figure 2.73). The coalescence temperature in $\text{DMF-}d_7$ is around 313 K where the diastereotopicity of the CH_2 protons becomes visible as well as the mentioned splitting of the signal of the methyl groups. But in this case no second set of signals appears and the spectrum is less broadened. Most likely, the soft Lewis acid Cd^{2+} does not exchange its large and soft bromides with the small oxygen donor DMF at all or at a smaller rate. However, the advantage of this complex is the NMR active ^{113}Cd nucleus. Employing a 2D ^1H , ^{113}Cd -HMBC experiment at low temperature, the identification of vicinal couplings of the methyl and methylene protons to the metal ion were possible (Figure 7.7). The chemical shift of the cadmium isotope is -345 ppm , referenced to Me_2Cd . Interestingly, a coupling to the ^{113}Cd nucleus was only

observed for one proton of each methylene group. The coupling to the other proton is likely not to be observed due to an unfavourable angle between the related atoms.^[138] From the NMR spectroscopic experiments it is clear that the complexes adopt the same contact ion pairs in solution as observed in the solid state.

Another analytical method which allows investigating the transferability of the solid state structure to solution is electrospray ionisation mass spectrometry. A time-of-flight (TOF) spectrometer was chosen because of the poor solubility of **17** and **19** in most of the common solvents (e.g. THF, MeOH, MeCN). The measurements were performed in pure THF for the zinc complex and in THF/H₂O for the cadmium complex due to the even lower solubility. However, both complexes were sufficiently present in solution for the TOF spectrometer. Figure 2.74 depicts two comparisons of the mass patterns of **17** and **19**. The black lines represent the experimental data, whereas the red lines illustrate the simulated spectrum for the proposed structural motif (in the positive ion mode one bromide anion was omitted for the calculated spectrum).

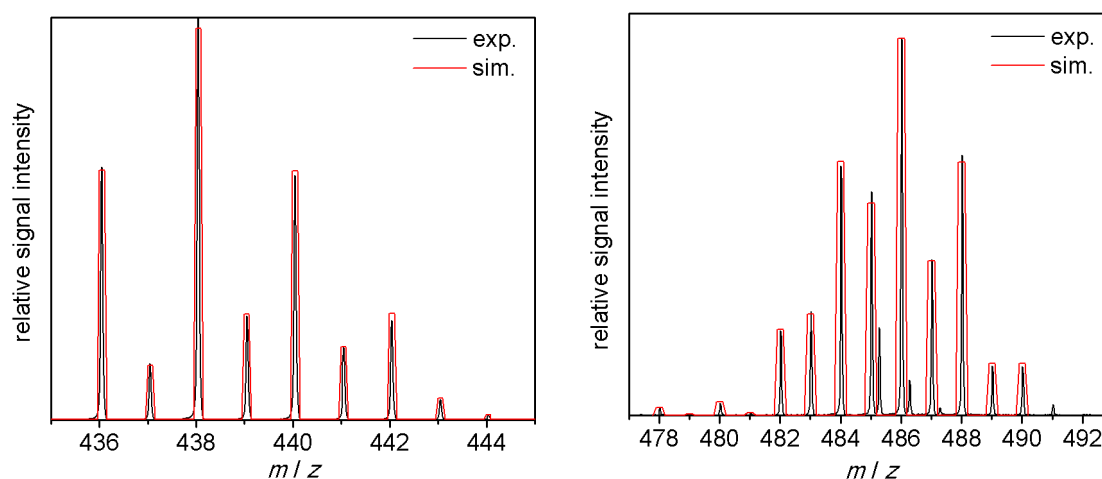


Figure 2.74: Parts of the mass spectra showing the simulated (red) and the experimental (black) isotope pattern of the cationic [(C₁₉H₂₃N₃)ZnBr]⁺ (left) and [(C₁₉H₂₃N₃)CdBr]⁺ (right).

The simulated isotope patterns were calculated using the COMPASS[®] software package from Bruker Daltonik. The comparisons demonstrate perfect matches of the predicted and observed species, which is also given in precise *m/z* data in Table 2.13. Furthermore, the full mass spectrum is free of any ionic fragments because only signals generated by the acridine derivative, with and without metal ion, and related fragments can be detected (Figure 7.8).

Table 2.13: Measured and theoretical *m/z* ratios of cations observed upon ESI-TOF-mass spectrometric analysis of **17** and **19** in THF or in a THF/H₂O mixture, respectively.

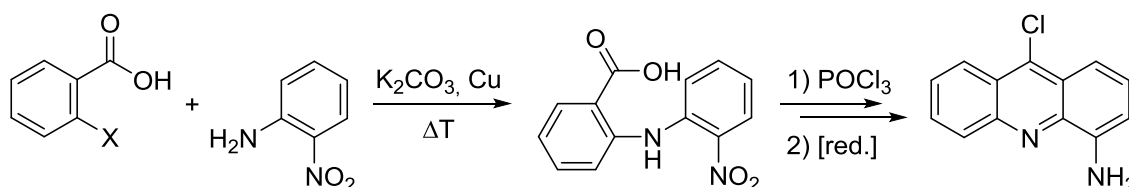
Cation	M = Zn (17)		M = Cd (19)	
	<i>m/z</i> (measured)	<i>m/z</i> (theoretical)	<i>m/z</i> (measured)	<i>m/z</i> (theoretical)
[(C ₁₉ H ₂₃ N ₃)H] ⁺	294.20	294.20	294.21	294.20
[(C ₁₉ H ₂₃ N ₃)MBr] ⁺	438.05	438.03	486.02	486.01
[(C ₁₉ H ₂₃ N ₃) ₂ HMBBr ₂] ⁺	813.15	813.15	861.15	861.12
[(C ₁₉ H ₂₃ N ₃) ₂ M ₂ Br ₃] ⁺	957.00	956.99	1050.95	1050.94

The same is valid for the Cd^{2+} complex (Figure 7.9). Both methods, NMR spectroscopy and mass spectrometry, emphasise that the solid state structure is maintained in solution. Apart from the expected complexes shown in Figure 2.74, additional interesting species were found during the measurement. In Table 2.13, two dimeric complexes were identified. One consists of two ligands with an MBr_2 centre and a significant abundance. The second is involving two ligand systems but also two metal ions with the molecular formula $[(\text{C}_{19}\text{H}_{23}\text{N}_3)_2\text{M}_2\text{Br}_3]^+$. In both metal ion cases, the abundance of the latter species was very low. However, with the help of a CID spectrum (collision induced dissociation) the mass pattern could be resolved precisely and its fragments could all be assigned to the used compounds. Additionally, the simulated spectra perfectly match the measured data which is true for all listed cations (Figure 7.10 and Figure 7.11). These complexes are most likely formed during the measurement, especially the aggregates with a high molecular mass. But the structure with the formula $[(\text{C}_{19}\text{H}_{23}\text{N}_3)_2\text{HMBR}_2]^+$ is conceivable in solution if the ligand to metal salt ratio would be increased. Further investigations with varied ratios would be an interesting study.

3. CONCLUSION AND OUTLOOK

Two different fluorophores were investigated in this thesis on their potential usability as molecular sensors. A modified and greatly improved reaction procedure^[64] was established for the scarcely explored 5,10-dimethyl-2-azaanthracene (**3**). The methyl groups act as spacer units for further substituted amine receptors. Different from what was expected, their bromination was not feasible and resulted in the decomposition of the compound. Former substitution studies with the pure 2-azaanthracene were equally unsuccessful.^[63] Unless easy derivatisation is not guaranteed, this fluorophore is not consistent with the requirement for sensor devices.

The second approach was based on the heteroaromatic system acridine. In this case, a variety of new amine substituted ligands were synthesised and examined with special emphasis on their fluorescence properties. It was found that the introduction of an amine group in 4-position is not straightforward. Only a few publications are present considering the synthesis. Future investigations of 4-aminoacridine derivatives should focus on the very recently reported copper catalysed *Ullmann* coupling with a subsequent condensation reaction by the use of POCl₃ (Scheme 3.1).^[139]



Scheme 3.1: Proposed reaction pathway for the synthesis of 4-amino-9-chloroacridine, inspired by the publication of *Jiang* and co-workers.^[139]

More feasible than the monosubstitution was the introduction of two bromomethylene units which bromine atoms were subsequently substituted by secondary amines. The resulting new acridine derivatives (**10–16**) were characterised in detail by NMR and fluorescence spectroscopy. Apart from the oily TrMEDA derivatives **11** and **12**, the solid state structures of all fluorophore-spacer-receptor systems were examined by X-ray diffraction. Their geometrical arrangements and the packing effects of the crystal structures were discussed and compared. The synthesised acridinyl amines respond differently towards the tested metal ions and show interesting behaviour in various solvents. For instance, an extraordinary excimer formation of **13** was observed by the use of a non-polar solvent at a defined concentration.

The PET based sensing abilities of the acridine systems were improved by the variation of the functionality of the amine side arms, resulting in the molecular sensor 4,5-bis(*N,N*-dimethylaminemethylene)acridine (**15**). Its fluorescence spectra show a remarkable metal ion selectivity and increase in fluorescence emission upon titration with dissolved ZnBr₂ and CdBr₂ in methanol (Figure 3.2). For the latter, even water can be used to dissolve the metal salt without influencing the detectability threshold. The high sensitivity of the acridine based sensor molecule and its good stability was demonstrated successfully. The very efficient electron transfer features **15** as a valuable ligand for medical or environmental purposes. Besides the detection of metal ions, the addition of acids and bases resulted in an instantaneously switch between the fluorescent on/off states by protonation/deprotonation of the amine receptors, repeatable without degeneration. Thus, **15** is as well applicable as a pH sensor.

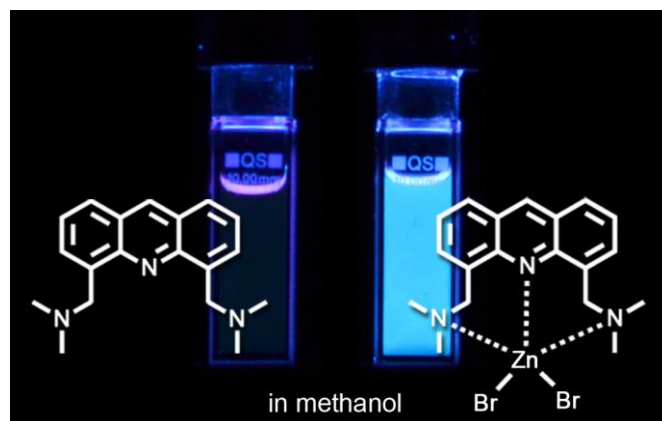


Figure 3.1: Fluorescence phenomenon of **15** in methanol (10^{-5} M, left) and with addition of ZnBr_2 (1 eq, right). The cuvettes were irradiated with UV light at 365 nm.

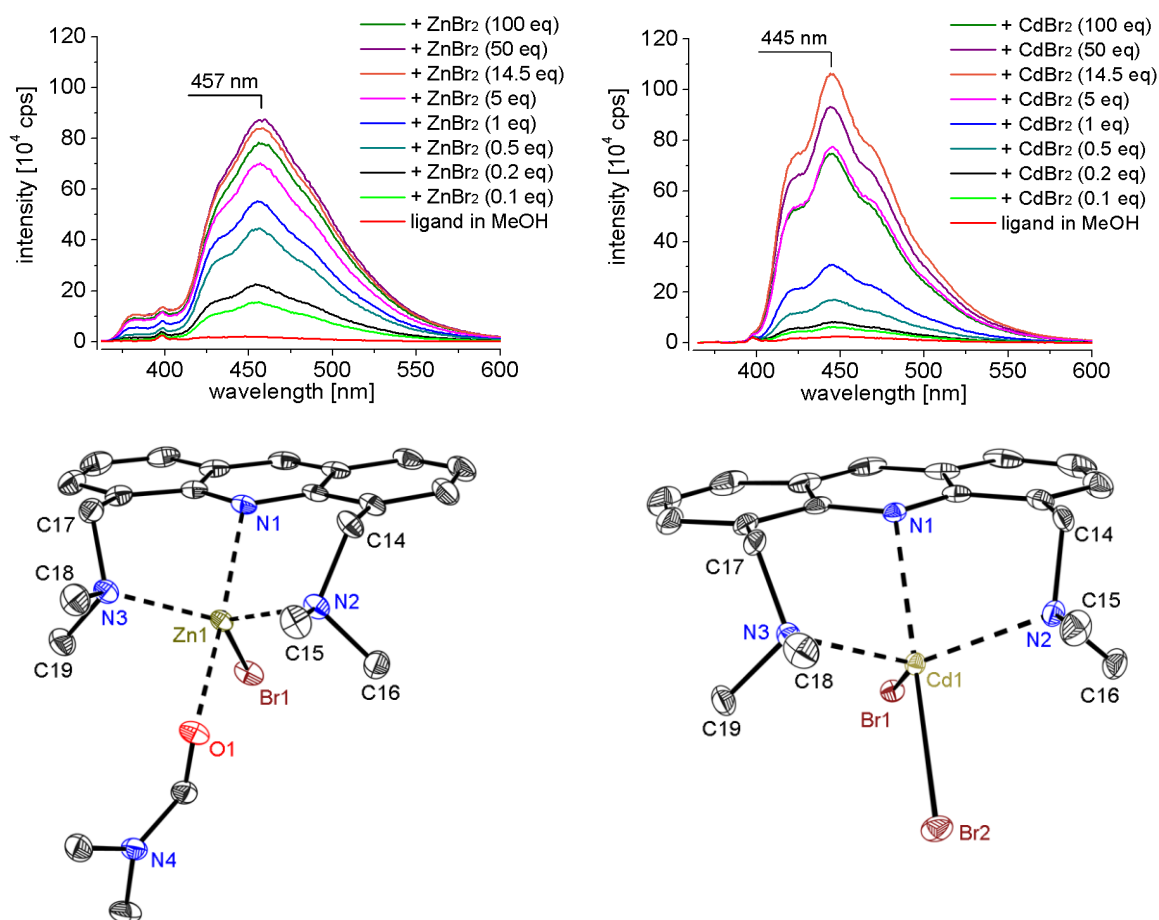


Figure 3.2: Titration experiment with dissolved Zn^{2+} and Cd^{2+} ions to a solution of **15** in methanol demonstrating the huge enhancement of the emission intensity (top). The corresponding solid state structures of the metal complexes **18** and **19** are depicted underneath.

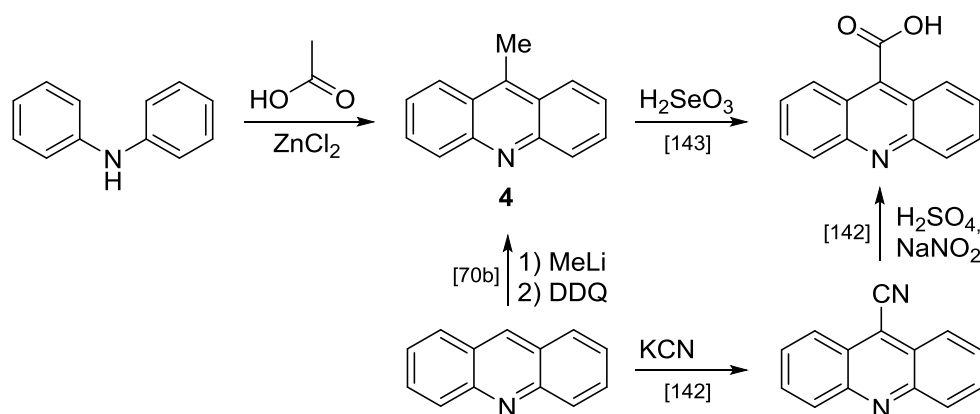
The solid state contact ion pairs **18** and **19** determined by X-ray diffraction were confirmed to be present in solution by NMR spectroscopy and ESI mass spectrometry. Compared to the numerous publications concerning zinc sensors, only very few provide structural evidence of the metal ion coordination, although this is fundamental for the understanding of fluorescence processes. The

solid state structures indicate a coordination of the Zn^{2+} and Cd^{2+} ions by all three nitrogen atoms, additionally proven by computational studies.

With respect to these computational results, the coordination of zinc is stronger than its heavier homologue cadmium which was supported by fluorescence measurements. To classify the strength of the chelation, the determination of the stability constant is of interest. Therefore, initial attempts have been made in the course of this thesis: Job plots^[140] were generated with values obtained from fluorescence titration experiments. The graphs indicated a ligand to metal coordination of 2:1 which is not in line with the results discussed above. Interestingly, complementary NMR experiments in the course of a master thesis stated a ligand to metal coordination of 1:1 and in some cases 1:2.^[141] Due to the inconsistent results, a reliable value for the stability constant could not be calculated. This unexpected behaviour should be investigated in more detail.

In the case of zinc, spectroscopic studies concerning the influence of the anion were made. For instance, the exchange of bromide with acetate ions gave a tremendous increase of the fluorescence emission, reaching 95% of the intensity of pure anthracene (under the same experimental conditions). In comparison, the use of ZnBr_2 yielded a value of 12%. Additionally, the geometrical parameters of both solid state structures were discussed and compared with each other.

Fluorescence measurements in pure water were not feasible in the course of this thesis due to the water-insolubility of the organic ligand. However, according to the high demand for molecular sensors in medical applications, its solubility behaviour should be improved. The 9-position of the acridine ring is suitable for the introduction of functional groups. This was shown with the synthesis of 9-methyl- (**4**) and 9-bromomethyleneacridine (**5**). These compounds can easily be modified by oxidation or substitution reactions. For instance, Scheme 3.2 illustrates two synthetic routes to 9-carboxyacridine whose polar group strongly enhances the water-solubility of acridine.



Scheme 3.2: Synthesis of 9-carboxyacridine by two different reaction pathways. ^[70b] ^[142] ^[143]

The reaction pathway via 9-cyanoacridine was already established in the *Stalke* group in 2015.^[144] This intermediate could also be of interest for further studies since the strong electron-withdrawing cyano group is known to shift the emission of fluorophores to longer wavelengths.^[145] Thus, the emitting range of the compounds lie more in the visible region of the electromagnetic spectrum and is easily detectable by the naked eye.

4. EXPERIMENTAL SETTINGS

4.1 General working procedure

Air and moisture sensitive reactions were carried out using modified *Schlenk*^[146] techniques in dried nitrogen or argon atmosphere and resulting sensitive substances were stored in an argon glovebox. The used solvents were purchased in high quality and dried due to standard laboratory techniques if necessary. For the fluorescence measurements, water was purified first through a Millipore water purification system Milli-RO 3 plus and finally with a Millipore ultrapure water system Milli-Q plus 185. All employed reactants were commercially available or reproduced according to the given literature procedure.

4.2 Applied analytical methods

4.2.1 Computational studies

For the geometry optimisations of **11**, the basis *Ahlrichs-TZV/def2-TZV*^[131e, 147] were used for calculations (including the atom-pairwise dispersion correction^[131f, 148] with the *Becke-Johnson* damping scheme (D3BJ)^[149]). The LIBINT2 library^[150] was used for the computation of two-electron integrals. The geometry optimisations of **17–19** were carried out at the B3LYP-D3/def2-TZVPP^[131, 151] level of theory (including *Becke-Jones* type damping^[149] of the dispersion correction^[131f]). In the case of Cd, the Stuttgart/Dresden ECP28MDF^[152] was used. The electronic densities and the corresponding NBO analysis^[132-133] were computed at the same level. The B3LYP calculations were performed under the RIJCOSX approximation.^[153]

All calculations (**11**, **17–19**) were realised with the ORCA^[109] program package.

4.2.2 Elemental analysis

Elemental analyses were carried out by the *Analytische Labor des Instituts für Anorganische Chemie der Georg-August-Universität Göttingen*. The determination of the organic elements (C, H, N, S) were realised with an *Elementar Vario EL3* and the metal ions were analysed with the *AAS 5FL Analytik Jena*. The amount of halides (Cl, Br) was determined potentiometric or titrimetric.

4.2.3 Fluorescence spectroscopy

The fluorescence measurements were performed on a *Horiba Jobin-Yvon* Fluoromax-4 spectrometer. A general setup of a spectrofluorometer is depicted in Figure 4.1. The Fluoromax-4 is equipped with a 150 W xenon arc lamp (1) which provides a continuous spectrum of light. This is focused on the entrance slit of the *Czerny-Turner* excitation monochromator (2) by elliptical mirrors. The beam with the selected wavelength is split and a small partition of light is directed to a reference detector (4). The main part of the beam hits the sample which perpendicular emitted light is directed to the emission monochromator (5). From here, the signal is detected by a photomultiplier (6).

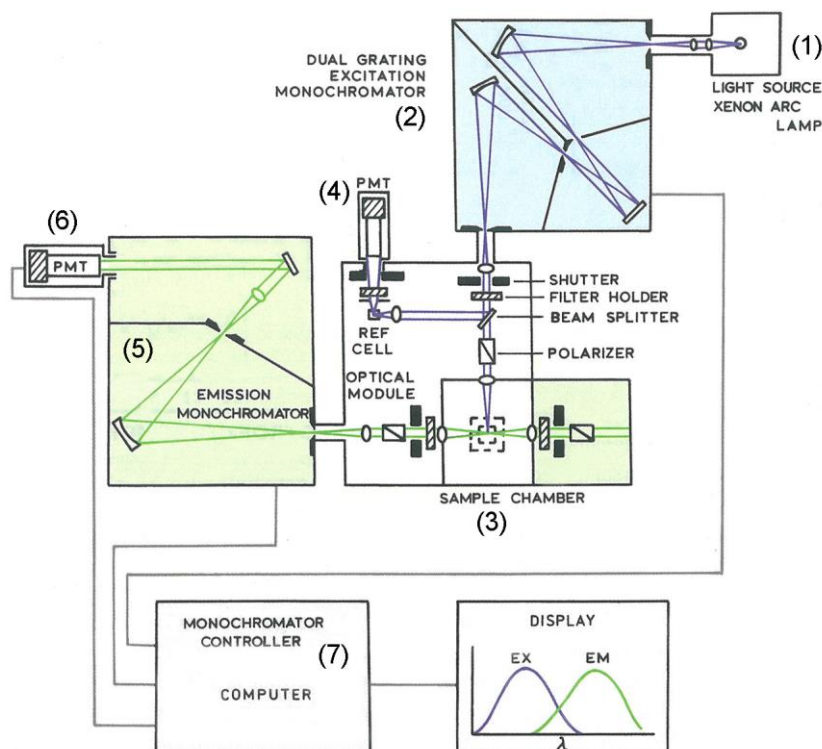


Figure 4.1: General setup of a spectrofluorometer, illustrating the beam path.^[154]

The spectra were recorded and modified graphically using the software *FluorEssence*TM v.3.0 at a computer terminal (7).^[155] The entrance and exit slit widths of each monochromator can be adjusted to vary the amount of passing light. If the slits are wider, a more intense spectrum is obtained but with loss of resolution. On the one hand, the overflow of the detector due to too strong emitting samples can be prevented. On the other hand, the signal-to-noise ratio of low fluorescent compounds can be improved.

4.2.4 Mass spectrometry

Most of the mass spectrometry experiments were carried out on a *MAT 95* (70 eV) instrument for EI-MS^[156] experiments as well as on a *HCT Ultra* instrument for ESI-MS^[157] experiments. For the electrospray ionisation mass spectrometric studies of **17** and **19**, sample solutions of $c \approx 5$ mM were continuously administered into the ESI source of a micrOTOF-QII mass spectrometer (*Bruker Daltonik*) by a step motor-driven gas-tight syringe (flow rate: 0.5 ml/h). This instrument combines a quadrupole mass filter with a time-of-flight analyser. The simulated isotope patterns were calculated using the COMPASS[®] software package from *Bruker Daltonik*. The mass to charge ratios of the molecular ions and the fragment ions are based on the isotopes bearing the highest natural abundances (^1H , ^{13}C , ^{14}N , ^{16}O , ^{32}S , ^{64}Zn , ^{114}Cd , $^{79}\text{Br}/^{81}\text{Br}$).

4.2.5 NMR spectroscopy

The NMR measurements were performed on a *Bruker Avance III 300* and *Bruker Avance III HD 400* spectrometer. Unless it was stated otherwise, the measurements were carried out at room temperature in 1-10 % solutions of deuterated solvents. The chemical shifts (δ) are reported in parts per million (ppm) and the coupling constants J in Hz. The residual proton signals of the

incompletely deuterated solvents were chosen as internal standards for ^1H NMR spectra.^[158] For ^{13}C spectra, the carbon resonances of the solvents were used for calibration. The assignment of the peaks was accomplished by two dimensional NMR techniques ($^1\text{H}, ^1\text{H}$ -COSY, $^1\text{H}, ^{13}\text{C}$ -HSQC, $^1\text{H}, ^{13}\text{C}$ -HMBC). In the case of **17** and **19**, further specialised experiments were used for the evidence of ligand-metal interactions (^1H -DOSY, $^1\text{H}, ^{15}\text{N}$ -HMBC, $^1\text{H}, ^{113}\text{Cd}$ -HMBC). The observed multiplicities are abbreviated as follows: s = singlet, d = doublet, t = triplet, q = quartet, m = multiplet. Combined abbreviations are derived from their components (e.g. dd = doublet of doublets).

4.2.6 UV/Vis spectroscopy

Absorption spectra (UV/vis) of **13** were recorded at a *Jasco* V-650 double beam spectrophotometer and of all other compounds at an *Agilent* 8453 diode array spectrophotometer. The samples contained 10^{-5} M solutions in methanol. The data were corrected by subtraction of a reference measurement of the pure solvent. In contrast to the fluorescence experiments, the detector is placed behind the cuvette, in linear arrangement to the beam. The transmitting light which is not absorbed by the sample solution is detected. Non-radiative processes can be observed in this way.

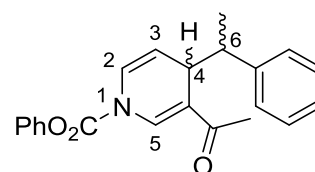
4.3 Synthesis and characterisation

4.3.1 Synthesis of 1-phenoxyacetyl-3-acetyl-4-(phenylethyl)-1,4-dihydropyridine (**1**)

1-Bromo-1-phenylethane (3.65 ml, 26.4 mmol, 1.0 eq.) was added over 5 min to a suspension of zinc dust (2.58 g, 39.5 mmol, 1.5 eq.) in THF (30 mL) and was stirred at room temperature for 4 h. Separately, to a solution of 3-acetylpyridine (4.35 g, 35.9 mmol, 1.4 eq.) in THF (45 ml) phenylchloro formiate (5.63 g, 35.9 mmol, 1.4 eq.) was added slowly at room temperature and the mixture was stirred for one hour.

After completion of the reactions, the organozinc compound was given dropwise to the activated pyridine derivative at $0\text{ }^\circ\text{C}$, where it was stirred for 60 min. The reaction mixture was quenched with aqueous NH_4Cl solution (20%, 15 ml) and extracted with EA (2x 100 ml). The organic phase was washed with saturated, aqueous Na_2CO_3 solution (60 ml) and dem. water (40 ml) and was dried over MgSO_4 . The pure product was filtrated and the solvent was removed under reduced pressure. **1** (5.38 g, 15.5 mmol, 59%) could be obtained after purification by column chromatography (PE/EA, 10:1) as a yellow oil. The diastereomeric ratio of the two formed compounds is approximately 3:1.

Chemical formula:	$\text{C}_{22}\text{H}_{21}\text{NO}_3$
Molecular weight:	347.41 g/mol
DC (SiO_2):	$R_f = 0.30/0.24$ (PE/EA, 10:1)



¹H NMR

(300 MHz, CDCl₃): *main product*: δ [ppm] = 7.68 (s, 1 H, H₅), 7.49-6.86 (m, 10 H, H_{Ph}), 6.86-6.78 (m, 1 H, H₂), 5.32 (br, 1 H, H₃), 3.76 (dd, ³J = 10.2, 4.8 Hz, 1 H, H₄), 3.04 (dq, ³J = 7.2, 4.8 Hz, 1 H, H₆), 2.32 (s, 3 H, COCH₃), 1.30 (d, ³J = 7.2 Hz, 3 H, CH₃).

side product: δ [ppm] = 8.06 (s, 1 H, H_{5'}), 7.49-6.86 (m, 10 H, H_{Ph}), 6.86-6.78 (m, 1 H, H₂), 4.88 (br, 1 H, H_{3'}), 3.81-3.71 (m, 1 H, H_{4'}), 3.27-3.16 (m, 1 H, H_{6'}), 2.37 (s, 3 H, COCH₃), 1.18 (d, ³J = 7.2 Hz, 3 H, CH₃).

¹³C NMR

(75 MHz, CDCl₃): *main product*: δ [ppm] = 196.97 (1 C, C=O), 156.13 (1 C, C_{OPh}), 134.85 (1 C, C₅), 110.84 (1 C, C₃), 37.86 (1 C, C₄), 44.12 (1 C, C₆), 25.37 (1 C, COCH₃), 17.44 (1 C, CH₃).

side product: δ [ppm] = 196.97 (1 C, C=O), 156.13 (1 C, C_{OPh}), 134.85 (1 C, C_{5'}), 110.15 (1 C, C_{3'}), 39.09 (1 C, C_{4'}), 41.53 (1 C, C_{6'}), 25.44 (1 C, COCH₃), 13.31 (1 C, CH₃).

The carbon atoms of the phenyl groups could not be identified due to a too crowded spectrum.

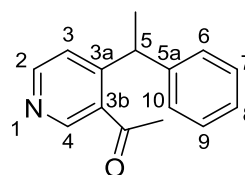
4.3.2 Synthesis of 3-acetyl-4-(phenylethyl)pyridine (2)

1 (160 mg, 0.46 mmol, 1.0 eq.) was converted slowly with conc. HNO₃ (30 ml) at 0 °C and stirred for 45 min at room temperature. For neutralisation, the reaction mixture was poured onto ice and treated with K₂CO₃. After extraction with DCM (3x 30 ml), it was washed with dem. water (2x 30 ml) and dried over MgSO₄. The title compound (98 mg, 0.43 mmol, 94%) was obtained after a column chromatographic work-up (PE/EA, 10:1) as a dark-red oil.

Chemical formula: C₁₅H₁₅NO

Molecular weight: 225.29 g/mol

DC (SiO₂): R_f = 0.45 (PE/EA, 10:1)

**¹H NMR**

(500 MHz, CDCl₃): δ [ppm] = 8.80 (s, 1 H, H₄), 8.61 (d, ³J = 5.3 Hz, 1 H, H₂), 7.33-7.28 (m, 3 H, H_{3,Ph}), 7.25-7.15 (m, 3 H, H_{Ph}), 4.98 (q, ³J = 7.1 Hz, 1 H, H₅), 2.46 (s, 3 H, COCH₃), 1.63 (d, ³J = 7.1 Hz, 3 H, CH₃).

¹³C NMR

(125 MHz, CDCl₃): δ [ppm] = 201.36 (1 C, C=O), 155.31 (1 C, C_{3a}), 151.72 (1 C, C₂), 148.92 (1 C, C₄), 144.36 (1 C, C_{5a}), 134.43 (1 C, C_{3b}), 128.65 (2 C, C_{7,9}), 128.21 (2 C, C_{6,10}), 126.69 (1 C, C₈), 123.40 (1 C, C₃), 39.45 (1 C, C₅), 30.44 (1 C, COCH₃), 21.33 (1 C, CH₃).

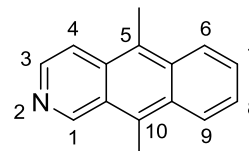
4.3.3 Synthesis of 5,10-dimethyl-2-azaanthracene (3)

2 (106 mg, 0.47 mmol, 1.0 eq) was dissolved in MSA (2 ml) and stirred for 24 h at room temperature. The reaction mixture was poured onto ice, neutralised with aqueous NaHCO₃ solution and extracted with DCM (3x 25 ml). The combined organic phases were dried over MgSO₄, filtrated and the solvent was removed under reduced pressure. A column chromatographic work-up (PE/EA, 1:1 → 1:3) yielded the desired product (90 mg, 0.43 mmol, 92%), obtained as a yellow solid.

Chemical formula: C₁₅H₁₃N

Molecular weight: 207.27 g/mol

DC (SiO₂): R_f = 0.15 (PE/EA, 1:1)



¹H NMR

(300 MHz, CDCl₃): δ [ppm] = 9.81 (s, 1 H, H₁), 8.44 (d, ³J = 6.4 Hz, 1 H, H₃), 8.34 (dd, ³J = 7.9, ⁴J = 1.7 Hz, 1 H, H₆/H₉), 8.29 (dd, ³J = 8.1, ⁴J = 1.8 Hz, 1 H, H₆/H₉), 7.97 (d, ³J = 6.4 Hz, 1 H, H₄), 7.66-7.53 (m, 2 H, H_{7,8}), 3.16 (s, 3 H, CH₃), 3.00 (s, 3 H, CH₃).

¹³C NMR

(75 MHz, CDCl₃): δ [ppm] = 151.71 (1 C, C₁), 138.82 (1 C, C₃), 132.83 (1 C, C_{quart}), 131.98 (1 C, C_{quart}), 130.81 (1 C, C_{quart}), 130.67 (1 C, C_{quart}), 128.05 (1 C, C_{quart}), 127.28 (1 C, C₇/C₈), 125.83 (1 C, C₇/C₈), 125.80 (1 C, C₆/C₉), 125.44 (1 C, C₆/C₉), 124.72 (1 C, C_{quart}), 117.71 (1 C, C₄), 13.74 (1 C, CH₃), 13.50 (1 C, CH₃).

EI MS

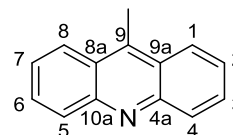
m/z (%): *m/z* (%) = 207 (50) [M]⁺, 192 (100) [M-CH₃]⁺, 178 (6) [M-(CH₃)₂]⁺.

4.3.4 Synthesis of 9-methylacridine (4)

Diphenylamine (20.08 g, 118.6 mmol, 1.0 eq) and zinc chloride (80.0 g, 587.0 mmol, 4.9 eq) was treated with glacial acetic acid (25 ml, 437.1 mmol, 3.7 eq). The reaction mixture was stirred for one day at an oil bath temperature of 200 °C. After cooling to room temperature, aqueous 2 M NaOH solution was added and the product was extracted with DCM (4x 600 ml). The gathered organic phases were dried over MgSO₄, filtrated and the solvent was removed under removed pressure. The product (13.1 g, 67.8 mmol, 57.2%) could be obtained as a yellow powder.

Chemical formula: C₁₄H₁₂N

Molecular weight: 193.22 g/mol



DC (SiO₂): $R_f = 0.35$ (PE/EA, 30:1)

¹H NMR

(300 MHz, CDCl₃): δ [ppm] = 8.29-8.21 (m, 4 H, H_{1,8,4,5}), 7.77 (ddd, ³ $J = 8.7$ Hz, 6.6 Hz, ⁴ $J = 1.2$ Hz, 2 H, H_{3,6}), 7.56 (ddd, ³ $J = 8.7$ Hz, 6.6 Hz, ⁴ $J = 1.2$ Hz, 2 H, H_{2,7}), 3.13 (s, 3 H, CH₃).

¹³C NMR

(75 MHz, CDCl₃): δ [ppm] = 148.21 (2 C, C_{4a,10a}), 130.13 (2 C, C_{3,6}), 130.06 (2 C, C_{4,5}), 125.64 (2 C, C_{2,7}), 124.70 (2 C, C_{1,8}), 13.85 (1 C, CH₃).

EI MS

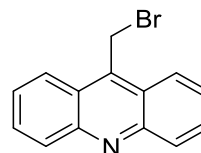
m/z (%): 193 (100) [M]⁺.

4.3.5 Synthesis of 9-(bromomethylene)acridine (5)

4 (0.84 g, 4.35 mmol, 1.0 eq), *N*-bromosuccinimide (0.83 g, 4.66 mmol, 1.1 eq), and benzoic peroxide (72 mg, 301 μ mol, 7 mol%) were dissolved in chloroform and heated to 65 °C for 3 h. When the reaction mixture was cooled to room temperature, a recrystallisation from ethanol was applied. A pure, yellow product was obtained (0.65 g, 2.40 mmol, 55.2%) after a column chromatographic work-up (PE/EA, 5:1).

Chemical formula: C₁₄H₁₀BrN

Molecular weight: 272.15 g/mol



¹H NMR

(300 MHz, CDCl₃): δ [ppm] = 8.34 (d, ³ $J = 8.7$ Hz, 2 H, H_{4,5}), 8.27 (d, ³ $J = 8.7$ Hz, 2 H, H_{1,8}), 7.82 (ddd, ³ $J = 8.7$ Hz, 6.6 Hz, ⁴ $J = 1.2$ Hz, 2 H, H_{3,6}), 7.69 (ddd, ³ $J = 8.7$ Hz, 6.6 Hz, ⁴ $J = 1.2$ Hz, 2 H, H_{2,7}), 5.41 (s, 2 H, CH₂).

¹³C NMR

(75 MHz, CDCl₃): δ [ppm] = 147.93 (2 C, C_{4a,10a}), 140.72 (1 C, C₉), 131.07 (2 C, C_{3,6}), 129.64 (2 C, C_{4,5}), 127.22 (2 C, C_{2,7}), 124.01 (2 C, C_{8a,9a}), 123.63 (2 C, C_{1,8}), 22.96 (1 C, CH₂).

EI MS

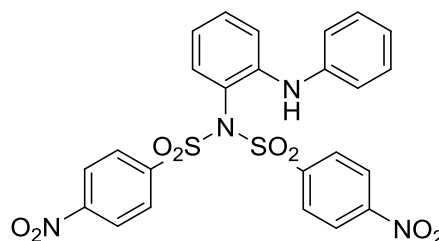
m/z (%): 271 (10) [M]⁺, 192 (100) [M-Br]⁺.

4.3.6 Synthesis of 2-bis(*p*-nitrobenzenesulfonyl)aminodiphenylamine (6)

A suspension of *p*-nitrobenzenesulfonyl chloride (1.80 g, 8.12 mmol, 3.0 eq) in DCM (5 ml) was given to a solution of 2-aminodiphenylamine (0.50 g, 2.69 mmol, 1.0 eq) and trimethylamine (1.15 ml, 8.30 mmol, 3.1 eq) in DCM (20 ml). After 1 h at room temperature, the solvent was removed under reduced pressure and the obtained solid was treated with CHCl₃ (7 ml). The resulting suspension was heated, filtrated and the residue was washed with DCM. The target compound (1.11 g, 2.00 mmol, 74.3%) was obtained as orange powder.

Chemical formula: C₂₄H₁₈N₄O₈S₂

Molecular weight: 554.55 g/mol



¹H NMR

(300 MHz, DMSO-*d*₆): δ [ppm] = 8.35 (d, ³*J* = 8.9 Hz, 4 H), 8.14 (d, ³*J* = 9.1 Hz, 4 H), 7.43 (ddd, ³*J* = 8.5 Hz, 7.0 Hz, ⁴*J* = 1.7 Hz, 1 H), 7.29 (dd, ³*J* = 8.3 Hz, ⁴*J* = 1.4 Hz, 1 H), 7.12 (t, ³*J* = 7.9 Hz, 2 H), 6.99 (ddd, ³*J* = 8.5 Hz, 7.1 Hz, ⁴*J* = 1.5 Hz, 1 H), 6.91 (dd, ³*J* = 7.9 Hz, ⁴*J* = 1.7 Hz, 1 H), 6.84-6.74 (m, 3 H), 6.42 (s, 1 H, NH).

EI MS

m/z (%): 554 (16) [M]⁺, 368 (20) [M-(Nos)]⁺, 181 (100) [M-2(Nos)H]⁺.

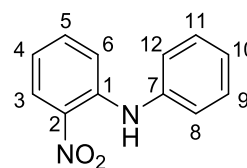
4.3.7 Synthesis of 2-nitrodiphenylamine (7)

2-Nitroaniline (0.55 g, 4.00 mmol, 1.0 eq), K₂CO₃ (1.11 g, 8.00 mmol, 2.0 eq), CuI (76 mg, 0.40 mmol, 10 mol%), and *L*-proline (92 mg, 0.80 mmol, 20 mol%) were treated with an excess of bromobenzene (7 ml) which was used as reagent and solvent. Due to the poor solubility of the starting materials, DMSO was added (3 ml). The mixture was heated to 125 °C for 48 h, then the solvent was removed under reduced pressure at 40 °C. Brine was added and the solution was extracted three times with ethyl acetate. The gathered organic layers were washed two times with brine. The organic phase was dried over MgSO₄, filtrated and the solvent was again removed under reduced pressure. The crude product was purified by column chromatography (PE/EA, 40:1) to give **7** (0.57 g, 2.66 mmol, 66.5%) as a yellow powder.

Chemical formula: C₁₂H₁₀N₄O₄

Molecular weight: 274.24 g/mol

DC (SiO₂): R_f = 0.38 (PE/EA, 20:1)



¹H NMR

(300 MHz, CDCl₃): δ [ppm] = 9.49 (s, 1 H, NH), 8.21 (dd, ³*J* = 8.5 Hz, ⁴*J* = 1.3 Hz, 1 H, H₃), 7.47-7.35 (m, 2 H, H_{Ph}), 7.38-7.33 (m, 1 H, H₅), 7.28 (d, ³*J* = 8.2 Hz, 2 H, H_{Ph}), 7.23 (d, ³*J* = 7.6 Hz, 2 H, H₆), 6.77 (ddd, ³*J* = 8.5 Hz, ³*J* = 7.0 Hz, ⁴*J* = 1.3 Hz, 1 H, H₄).

¹³C NMR

(75 MHz, CDCl₃): δ [ppm] = 143.20 (1 C, C₁), 138.85 (1 C, C₇), 135.77 (1 C, C₅), 133.36 (1 C, C₂), 129.85 (2 C, C_{Ph}), 126.78 (1 C, C₃), 125.77 (1 C, C_{Ph}), 124.50 (2 C, C_{Ph}), 117.61 (1 C, C₄), 116.17 (1 C, C₆).

EI MS

m/z (%): 214.1 (100) [M]⁺, 197.2 (12) [M-O]⁺, 180.2 (22) [M-HO₂]⁺, 167.2 (64) [M-HNO₂]⁺.

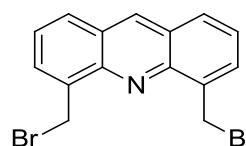
4.3.8 Synthesis of 4,5-bis(bromomethylene)acridine (8)

A solution of acridine (4.06 g, 22.6 mmol, 1.0 eq) in conc. H₂SO₄ (50 ml) was heated up to 50 °C when BMME (7.4 ml, 90.6 mmol, 4.0 eq) was added. After stirring for 17 h at this temperature, the reaction mixture was cooled to room temperature and the formed excess of bromine gas was discharged through an aqueous solution of thiosulfate. The crude product was crushed out by pouring onto ice (400 g) and stirring for 1 h. The yellow precipitate was filtered, washed several times with dem. water and dissolved with chloroform (400 ml). The solution was washed with brine (3x 200 ml) and the gathered aqueous phases were extracted with chloroform (100 ml). The organic phases were dried over MgSO₄, filtered and the solvent was removed under reduced pressure. For purification, the crude dark yellow product was recrystallised from chloroform two times to obtain a light yellow powder (2.54 g, 6.96 mmol, 30.7%).

Chemical formula: C₁₅H₁₁Br₂N

Molecular weight: 365.06 g/mol

DC (SiO₂): R_f = 0.62 (MeOH)

**¹H NMR**

(300 MHz, CDCl₃): δ [ppm] = 8.78 (s, 1 H, H₉), 7.99 (d, ³*J* = 8.5 Hz, 2 H, H_{1,8}), 7.94 (d, ³*J* = 6.8 Hz, 2 H, H_{3,6}), 7.51 (dd, ³*J* = 8.5 Hz, 6.9 Hz, 2 H, H_{2,7}), 5.43 (s, 4 H, CH₂).

¹³C NMR

(75 MHz, CDCl₃): δ [ppm] = 145.81 (2 C, C_{4a,10a}), 136.75 (1 C, C₉), 136.54 (2 C, C_{4,5}), 131.34 (2 C, C_{3,6}), 129.18 (2 C, C_{1,8}), 126.93 (2 C, C_{8a,9a}), 125.99 (2 C, C_{2,7}), 30.27 (2 C, CH₂).

EI MS

m/z (%): 365 (34) [M]⁺, 286/284 (76/76) [M-Br]⁺, 205 (100) [M-2Br]⁺.

Elemental analysis

in % (calculated): C: 48.86 (49.35), H: 3.06 (3.04), N: 3.78 (3.84), Br: 43.30 (43.78).

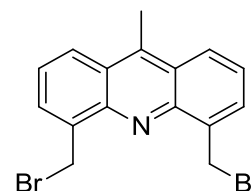
4.3.9 Synthesis of 4,5-bis(bromomethylene)-9-methylacridine (9)

The synthesis of **9** is the same as for **8**, with **4** (5.0 g, 25.88 mmol, 1.0 eq), BMME (9.3 ml, 114.0 mmol, 4.4 eq) and conc. H₂SO₄ (70 ml). The crude product was purified by column chromatography (PE/EA, 10:1) which resulted in a yellow powder (5.28 g, 13.96 mmol, 53.9%). The crystallisation of **9** was performed in DCM at -30 °C.

Chemical formula: C₁₆H₁₃Br₂N

Molecular weight: 379.09 g/mol

DC (SiO₂): R_f = 0.11 (PE/EA, 10:1)

**¹H NMR**

(300 MHz, CDCl₃): δ [ppm] = 8.22 (dd, ³J = 8.9 Hz, ⁴J = 1.1 Hz, 2 H, H_{1,8}), 7.91 (dd, ³J = 6.8 Hz, ⁴J = 1.1 Hz, 2 H, H_{3,6}), 7.51 (dd, ³J = 8.9 Hz, 6.8 Hz, 2 H, H_{2,7}), 5.44 (s, 4 H, CH₂), 3.07 (s, 3 H, CH₃)

¹³C NMR

(75 MHz, CDCl₃): δ [ppm] = 145.15 (2 C, C_{4a,10a}), 143.01 (1 C, C₉), 137.15 (2 C, C_{4,5}), 130.75 (2 C, C_{3,6}), 125.80 (2 C, C_{1,8}), 125.62 (2 C, C_{8a,9a}), 125.55 (2 C, C_{2,7}), 30.80 (2 C, CH₂), 14.10 (1 C, CH₃).

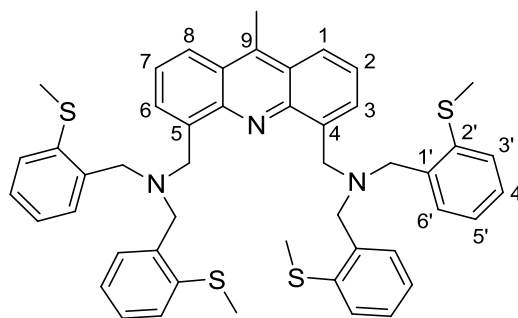
EI MS

m/z (%): 379 (45) [M]⁺, 298 (85) [M-Br]⁺, 219 (100) [M-2Br]⁺.

4.3.10 Synthesis of 4,5-bis(di(2'-methylthiobenzyl)aminomethylene)-9-methylacridine (10)

9 (0.54 g, 1.43 mmol, 1.0 eq), bis(2-methylthiobenzyl)amine (0.82 g, 2.85 mmol, 2.0 eq) and K₂CO₃ (0.79 g, 5.72 mmol, 4.0 eq) were dissolved in MeCN (22 ml) and heated up to 85 °C for 3 h. After cooling to room temperature, the solvent was decanted and the crude product was washed with hexane and dissolved again in toluene. The insoluble inorganic salts were filtered off after what the solvent was removed under reduced pressure. The desired compound (0.54 g, 0.68 mmol, 47.6%) could be obtained as a bright yellow powder. Suitable crystals for X-ray analysis were obtained after recrystallisation from a pentane/ethyl acetate mixture.

Chemical formula: C₄₈H₄₉N₃S₄
Molecular weight: 795.28 g/mol
DC (SiO₂): R_f = 0.2 (PE/EA, 20:1)



¹H NMR
 (300 MHz, CDCl₃): δ [ppm] = 8.25 (d, ³J = 7.7 Hz, 2 H, H_{1,8}), 7.98 (d, ³J = 6.5 Hz, 2 H, H_{3,6}), 7.67-7.61 (m, 4 H, H_{6'}), 7.63-7.56 (m, 2 H, H_{2,7}), 7.27-7.17 (m, 8 H, H_{3',4'}), 7.15-7.07 (m, 4 H, H_{5'}), 4.51 (s, 4 H, 4,5-CH₂), 3.73 (s, 8 H, NCH₂), 3.08 (s, 3 H, 9-CH₃), 2.40 (s, 12 H, SCH₃).

¹³C NMR
 (75 MHz, CDCl₃): δ [ppm] = 145.60 (2 C, C_{4a,10a}), 137.41 (4 C, C_{2'}), 136.89 (2 C, C_{4,5}), 136.46 (4 C, C_{1'}), 128.69 (2 C, C_{3,6}), 128.04 (4 C, C_{6'}), 127.38 (4 C, C_{3'}), 125.30 (2 C, C_{2,7}), 124.94 (4 C, C_{4'}), 124.59 (2 C, C_{8a,9a}), 124.48 (4 C, C_{5'}), 123.67 (2 C, C_{1,8}), 55.27 (4 C, NCH₂), 52.68 (2 C, 4,5-CH₂), 14.91 (4 C, SCH₃), 13.74 (1 C, 9-CH₃).

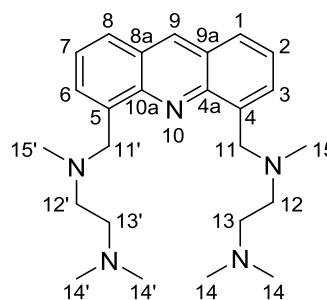
EI MS

m/z (%): 795.2 (100) [M]⁺, 780.2 (24) [M-Me]⁺.

4.3.11 Synthesis of 4,5-bis(*N,N',N'*-trimethylethylenediaminemethylene)acridine (11)

K₂CO₃ (1.35 g, 13.23 mmol, 3.5 eq) and **8** (1.38 g, 3.78 mmol, 1.0 eq) formed a yellow suspension with MeCN (60 ml). When *N,N',N'*-trimethylethylenediamine (1.00 ml, 7.75 mmol, 2.1 eq) was added, the temperature was increased to 85 °C and the reaction mixture was stirred for 8 h. The volatile compounds were removed under reduced pressure and ethyl acetate and brine was added to the crude product. The organic phase was separated and washed with brine. The aqueous phases were extracted five times with ethyl acetate and all gathered organic layers were again washed with brine. The solvent was dried over MgSO₄, filtered and removed in vacuo. The target compound was obtained as brown oil (212 mg, 520 μmol, 13.8%).

Chemical formula: C₂₅H₃₇N₅
Molecular weight: 407.61 g/mol
DC (Al₂O₃): R_f = 0.38 (EA/MeOH, 2:1).



¹H NMR

(300 MHz, CDCl₃): δ [ppm] = 8.69 (s, 1 H, H₉), 7.92-7.82 (m, 4 H, H_{1,3,6,8}), 7.50 (dd, ³J = 8.4 Hz, 6.9 Hz, 2 H, H_{2,7}), 4.46 (s, 4 H, H_{11,11'}), 2.82-8.73 (m, 4 H, H_{12,12'}), 2.68-2.59 (m, 4 H, H_{13,13'}), 2.42 (s, 6 H, H_{15,15'}), 2.30 (s, 12 H, H_{14, H14'}).

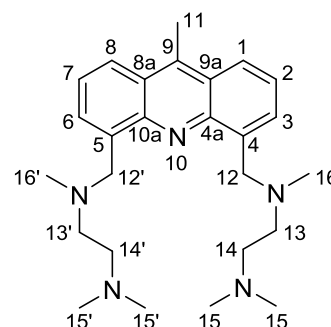
¹³C NMR

(75 MHz, CDCl₃): δ [ppm] = 147.09 (2 C, C_{4a,10a}), 136.97 (2 C, C_{4,5}), 136.13 (1 C, C₉), 129.72 (2 C, C_{3,6}), 127.05 (2 C, C_{1,8}), 126.37 (2 C, C_{8a,9a}), 125.49 (2 C, C_{2,7}), 57.19 (2 C, C_{11,11'}), 57.03 (2 C, C_{13,13'}), 55.44 (2 C, C_{12,12'}), 45.34 (4 C, C_{14,14'}), 43.03 (2 C, C_{15,15'}).

4.3.12 Synthesis of 4,5-bis(*N,N',N'*-trimethylethylenediaminemethylene)-9-methylacridine (**12**)

The formation of the methyl derivative **9** (396 mg, 1.04 mmol, 1.0 eq) with *N,N',N'*-trimethylethylenediamine (0.29 ml, 2.23 mmol, 2.1 eq) and K₂CO₃ (0.55 g, 3.98 mmol, 3.8 eq) was performed in MeCN (40 ml) at 50 °C. The reaction mixture was stirred for 16 hours and afterwards purified by column chromatography on alumina (EA/MeOH, 1:0 → EA/MeOH, 20:1). **12** (75 mg, 178 μ mol, 17.1%) could be obtained as a yellow solid.

Chemical formula: C₂₆H₃₉N₅
Molecular weight: 421.32 g/mol
DC (Al₂O₃): R_f = 0.17 (EA/MeOH, 10:1)

**¹H NMR**

(300 MHz, CDCl₃): δ [ppm] = 8.11 (d, ³J = 8.6 Hz, 2 H, H_{1,8}), 7.87 (d, ³J = 6.7 Hz, 2 H, H_{3,6}), 7.50 (dd, ³J = 8.6 Hz, 6.7 Hz, 2 H, H_{2,7}), 4.46 (s, 4 H, H_{12,12'}), 3.07 (s, 3 H, H₁₁), 2.72 (dd, ³J = 8.4 Hz, 5.7 Hz, 4 H, H_{13,13'}), 2.53 (dd, ³J = 8.4 Hz, 5.7 Hz, 4 H, H_{14,14'}), 2.24 (s, 6 H, H_{16,16'}), 2.17 (s, 12 H, H_{15,15'}).

¹³C NMR

(75 MHz, CDCl₃): δ [ppm] = 146.37 (2 C, C_{4a,10a}), 141.84 (1 C, C₉), 138.03 (2 C, C_{4,5}), 129.03 (2 C, C_{3,6}), 125.23 (2 C, C_{1,8}), 125.17 (2 C, C_{8a,9a}), 123.22 (2 C, C_{2,7}), 57.85 (2 C, C_{12,12'}), 57.62 (2 C, C_{14, 14'}), 56.24 (2 C, C_{13,13'}), 46.05 (4 C, C_{15,15'}), 43.27 (2 C, C_{16,16'}), 14.00 (1 C, C₁₁).

EI MS

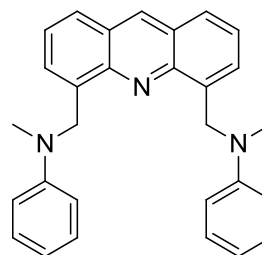
m/z (%): 421 (10) [M]⁺, 363 (65) [M-(NMe₂)₂]⁺, 319 (30) [M-(NMeC₂H₄NMe₂)]⁺, 220 (100) [M-(NMeC₂H₄NMe₂)₂]⁺.

4.3.13 Synthesis of 4,5-bis(*N*-methyl-*N*-phenylaminemethylene)acridine (**13**)

To a suspension of **8** (0.50 g, 1.37 mmol, 1.0 eq) and K_2CO_3 (0.66 g, 4.78 mmol, 3.5 eq) in MeCN (30 ml), methylphenylamine (0.30 ml, 2.76 mmol, 2.0 eq) was added. After stirring the reaction mixture for 4 h at room temperature, the volatile components were removed under reduced pressure. The crude product was dissolved in ethyl acetate and washed three times with brine. The aqueous phases were again extracted with ethyl acetate and the gathered organic layers were dried over $MgSO_4$, filtrated and the solvent was removed in vacuo. For further purification, a recrystallisation from methanol was implemented. Thereby, the impurities were dissolved and filtrated off. **13** (0.49 mg, 1.17 mmol, 85.4%) could be obtained as a yellow solid.

Chemical formula: $C_{29}H_{27}N_3$

Molecular weight: 417.55 g/mol



1H NMR

(300 MHz, $DMSO-d_6$): δ [ppm] = 9.15 (s, 1 H, H_9), 8.07 (d, $^3J = 8.3$ Hz, 2 H, $H_{1,8}$), 7.55 (dd, $^3J = 8.3$ Hz, 6.9 Hz, 2 H, $H_{2,7}$), 7.47 (d, $^3J = 6.9$ Hz, 2 H, $H_{3,6}$), 7.12 (dd, $^3J = 8.6$ Hz, 7.2 Hz, 4 H, *meta* H_{Ph}), 6.73 (d, $^3J = 8.6$ Hz, 4 H, *ortho* H_{Ph}), 6.58 (t, $^3J = 7.2$ Hz, 2 H, *para* H_{Ph}), 5.38 (s, 4 H, CH_2), 3.19 (s, 6 H, CH_3).

^{13}C NMR

(75 MHz, $DMSO-d_6$): δ [ppm] = 149.15 (2 C, *ipso* C_{Ph}), 145.76 (2 C, $C_{4a,10a}$), 136.73 (1 C, C_9), 135.68 (2 C, $C_{4,5}$), 128.98 (4 C, *meta* C_{Ph}), 127.01 (2 C, $C_{1,8}$), 126.79 (2 C, $C_{3,6}$), 126.10 (2 C, $C_{8a,9a}$), 125.64 (2 C, $C_{2,7}$), 115.59 (2 C, *para* C_{Ph}), 111.66 (4 C, *ortho* C_{Ph}), 52.55 (2 C, CH_2), 38.87 (2 C, CH_3).

EI MS

m/z (%): 417.2 (14) $[M]^{++}$, 310.1 (100) $[M-NMePh]^{++}$, 205.1 (84) $[M-(NMePh)_2]^{++}$.

Elemental analysis

in % (calculated): C: 82.31 (83.42), H: 6.33 (6.52), N: 9.92 (10.06).

4.3.14 Synthesis of 4,5-bis(*N*-methyl-*N*-phenylaminemethylene)acridine hydrochloride (**14**)

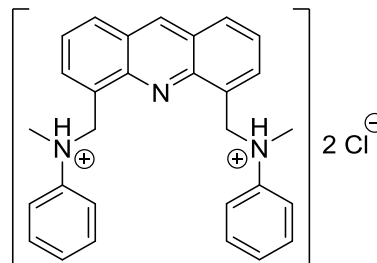
13 (125 mg, 300 μ mol, 1.0 eq) was suspended in ethanol (10 ml) and conc. aqueous HCl was added (10 ml, 120 mmol, 400 eq). The reaction mixture was stirred at room temperature for 30 min whereby it became a clear solution. After adding dem. H_2O (10 ml), the solution was extracted with hexane (2x 20 ml). The organic phases were discarded and the volatile compounds

were removed under reduced pressure. The product (106 mg, 216 μmol , 72.0%) could be obtained as a yellow solid.

14 was dissolved in a boiling ethanol/hexane (1:1) mixture. Suitable crystals for X-ray analysis were obtained after storing the crystals for four weeks at room temperature.

Chemical formula: $\text{C}_{29}\text{H}_{29}\text{N}_3\text{Cl}_2$

Molecular weight: 490.47 g/mol



^1H NMR

(300 MHz, $\text{DMSO-}d_6$): δ [ppm] = 9.17 (s, 1 H, H_9), 8.14 (d, $^3J = 8.0$ Hz, 2 H, $\text{H}_{1,8}$), 7.82-7.70 (m, 2 H, $\text{H}_{3,6}$), 7.59 (dd, $^3J = 8.3$ Hz, 6.9 Hz, 2 H, $\text{H}_{2,7}$), 7.29-7.08 (m, 8 H, *meta* H_{Ph} , *ortho* H_{Ph}), 6.97-6.84 (m, 2 H, *para* H_{Ph}), 5.48 (s, 4 H, CH_2), 3.28 (s, 6 H, CH_3).

EI MS

m/z (%): 417.2 (14) $[\text{M}-(\text{HCl})_2]^+$, 310.1 (100) $[\text{M}-\text{NMePh}(\text{HCl})_2]^+$, 205.1 (84) $[\text{M}-(\text{NMePh})_2(\text{HCl})_2]^+$.

Elemental analysis

in % (calculated): **14**: C: 65.94 (71.02), H: 6.40 (5.96), N: 7.94 (8.57), Cl: 17.50 (14.46).

Chemical composition gained by X-ray analysis: **14** + H_3O^+ + Cl^- + EtOH: C: 65.94 (63.00), H: 6.40 (6.48), N: 7.94 (7.11), Cl: 17.50 (17.99).

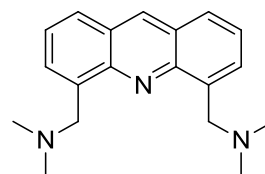
4.3.15 Synthesis of 4,5-bis(dimethylaminomethylene)acridine (**15**)

The synthesis procedure for **15** is the same as for **13** with **8** (1.55 g, 4.25 mmol, 1.0 eq), K_2CO_3 (1.76 g, 12.75 mmol, 3.0 eq), dimethylamine in THF (2.0 M, 4.5 ml, 9.0 mmol, 2.1 eq) and MeCN (40 ml). In this case, no recrystallisation was needed to obtain the product (0.78 g, 2.66 mmol, 62.6%) as a yellow-brown solid.

Chemical formula: $\text{C}_{19}\text{H}_{23}\text{N}_3$

Molecular weight: 293.41 g/mol

DC (Al_2O_3): $R_f = 0.13$ (EA/MeOH, 10:1).



^1H NMR

(300 MHz, $\text{DMSO-}d_6$): δ [ppm] = 9.09 (s, 1 H, H_9), 8.08 (dd, $^3J = 8.5$ Hz, $^4J = 1.6$ Hz, 2 H, $\text{H}_{1,8}$), 7.86 (dd, $^3J = 6.8$ Hz, $^4J = 1.3$ Hz, 2 H, $\text{H}_{3,6}$), 7.61 (dd, $^3J = 8.5$,

6.8 Hz, 2 H, H_{2,7}), 4.28 (s, 4 H, CH₂), 2.35 (s, 12 H, CH₃).

¹³C NMR

(75 MHz, DMSO-*d*₆): δ [ppm] = 146.22 (2 C, C_{4a,10a}), 136.60 (2 C, C_{4,5}), 135.92 (1 C, C₉), 129.96 (2 C, C_{3,6}), 127.42 (2 C, C_{1,8}), 125.89 (2 C, C_{8a,9a}), 125.55 (2 C, C_{2,7}), 58.24 (2 C, CH₂), 45.40 (4 C, CH₃).

¹⁵N NMR

(40.6 MHz, DMF-*d*₇): δ [ppm] = -81.2 (N_{arom}), -355.3 (NMe₂) (taken from ¹H, ¹⁵N-HMBC).

EI MS

m/z (%): 293 (4) [M]⁺, 250 (64) [M-NMe₂]⁺, 205 (100) [M-(NMe₂)₂]⁺.

Elemental analysis

in % (calculated): C: 76.45 (77.78), H: 7.77 (7.90), N: 13.94 (14.32).

4.3.16 Synthesis of 4,5-bis(dimethylaminemethylene)acridine hydrochloride (**16**)

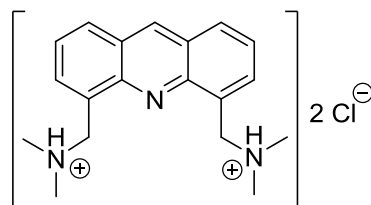
Conc. HCl (0.4 ml, 4.8 mmol, 4.8 eq) was added dropwise to a solution of **15** (293 mg, 1 mmol, 1.0 eq) in toluene (15 ml). After stirring for 15 min at room temperature, a dark yellow precipitate was formed which was filtered and washed with toluene (3x 5 ml). The pure product (342 mg, 934 μmol, 93.4%) was dried under reduced pressure to obtain a bright yellow powder.

Suitable crystals for X-ray analysis were formed after a recrystallisation from methanol.

Reverse reaction to 15: The deprotonation of **16** (235 mg, 641 μmol, 1.0 eq) was carried out in a saturated aqueous NaHCO₃ solution (10 ml, 11.4 mmol, 17.8 eq) which was stirred for 30 min. The product was extracted with ethyl acetate (20 ml) and the organic phase was washed with aqueous NaHCO₃ solution (2x 10 ml). The organic phase was dried over MgSO₄, filtered and the volatile compounds were removed under reduced pressure. **15** (155 mg, 528 μmol, 82.4%) could be reobtained as a yellow-brown solid.

Chemical formula: C₁₉H₂₅N₃Cl₂

Molecular weight: 366.33 g/mol



¹H NMR

(300 MHz, DMSO-*d*₆): δ [ppm] = 10.42 (s, 2 H, NH₂), 9.36 (s, 1 H, H₉), 8.38 (d, ³J = 8.2 Hz, 2 H, H_{1,8}), 8.17 (d, ³J = 6.4 Hz, 2 H, H_{3,6}), 7.77 (dd, ³J = 8.2, 7.0 Hz, 2 H, H_{2,7}), 5.16 (d, ³J = 5.7 Hz, 2 H, CH₂), 2.91 (d, ³J = 4.8 Hz, 12 H, CH₃).

¹³C NMR

(75 MHz, DMSO-*d*₆): δ [ppm] = 146.06 (2 C, C_{4a,10a}), 138.56 (1 C, C₉), 135.77 (2 C, C_{3,6}), 131.17 (2 C, C_{1,8}), 128.07 (2 C, C_{4,5}), 126.45 (2 C, C_{8a,9a}), 125.70 (2 C, C_{2,7}), 55.90 (2 C, CH₂), 42.54 (4 C, CH₃).

ESI MS

m/z (%): 400 (27) [M+Cl]⁻, 364 (18) [M-H]⁻.

Elemental analysis

in % (calculated): C: 61.46 (62.29), H: 6.61 (6.88), N: 11.18 (11.47), Cl: 20.35 (19.36).

4.3.17 Synthesis of 4,5-bis(dimethylaminemethylene)acridine dibromido zinc(II) (17)

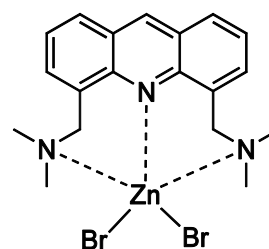
15 (175 mg, 596 μ mol, 1.0 eq) was dissolved in THF (1 ml) and a solution of ZnBr₂ (134 mg, 596 μ mol, 1.0 eq) in THF (0.2 ml) was added dropwise. Thereby, the zinc complex precipitated immediately. The suspension was filtrated and washed several times with THF. The pure product (145 mg, 280 μ mol, 47.0%) could be obtained as a yellow powder.

17 was dissolved in a THF/DMF (9.3:1) mixture and heated up to the boiling point of THF. After two weeks at room temperature, suitable crystals for X-ray analysis could be obtained.

Reverse reaction to 15: **17** (139 mg, 268 μ mol, 1.0 eq) was suspended in an aq. NaHCO₃ solution (5%, 10 ml) when Na₂H₂EDTA (360 mg, 1.07 mmol, 4.0 eq), dissolved in an aq. NaHCO₃ solution (10%, 6 ml), was added. The suspension was stirred at room temperature for 45 min. The product was extracted with ethyl acetate (2x 4 ml) and the gathered organic phases were washed with an aq. saturated NaHCO₃ solution (3x 10 ml). The organic phases were dried over MgSO₄ and filtered. After the solvent was removed under reduced pressure, **15** (74 mg, 252 μ mol, 94%) was reobtained as a yellow-brown solid.

Chemical formula: C₁₉H₂₃N₃ZnBr₂

Molecular weight: 518.61 g/mol

**¹H NMR**

(400 MHz, DMF-*d*₇, 80 °C): δ [ppm] = 9.25 (s, 1 H, H₉), 8.22 (d, ³*J* = 8.3 Hz, 2 H, H_{1,8}), 8.01 (d, ³*J* = 7.1 Hz, 2 H, H_{3,6}), 7.69 (dd, ³*J* = 8.3, 7.1 Hz, 2 H, H_{2,7}), 4.52 (4 H, CH₂), 2.62 (s, 12 H, CH₃).

(400 MHz, DMF-*d*₇, -30 °C): δ [ppm] = 9.57 (s, 1 H, H₉), 8.39 (dd, ³*J* = 8.0 Hz, ⁴*J* = 1.6 Hz, 2 H, H_{1,8}), 8.11 (dd, ³*J* = 6.1 Hz, ⁴*J* = 1.3 Hz, 2 H, H_{3,6}), 7.76 (dd, ³*J* = 8.4, 6.8 Hz, 2 H, H_{2,7}), 5.46 (d, ²*J* = 11.9 Hz, 2 H, CH₂), 3.86 (d,

$^2J = 12.1$ Hz, 2 H, CH₂), 3.19 (s, 6 H, CH₃), 2.38 (s, 6 H, CH₃).

¹³C NMR

(100 MHz, DMF-*d*₇, -30 °C): δ [ppm] = 148.65 (2 C, C_{4a,10a}), 141.97 (1 C, C₉), 135.45 (2 C, C_{3,6}), 130.52 (2 C, C_{1,8}), 127.68 (2 C, C_{8a,9a}), 126.44 (2 C, C_{2,7}), 63.13 (2 C, CH₂), 48.91 (2 C, CH₃), 46.37 (2 C, CH₃).

¹⁵N NMR

(40.6 MHz, DMF-*d*₇, -30 °C): δ [ppm] = -346.7 (taken from ¹H, ¹⁵N-HMBC).

Elemental analysis

in % (calculated): C: 44.00 (44.00), H: 4.50 (4.47), N: 8.10 (8.10), Br: 30.00 (30.81).

TOF ESI MS

m/z (%): 957.01 (0.6) [(C₁₉H₂₃N₃)₂Zn₂Br₃]⁺, 813.15 (1.8) [(C₁₉H₂₃N₃)₂ZnBr₂H]⁺, 438.05 (100) [C₁₉H₂₃N₃ZnBr]⁺, 300.22 (34) [C₁₉H₂₃N₃Li]⁺, 294.20 (93) [C₁₉H₂₄N₃]⁺.

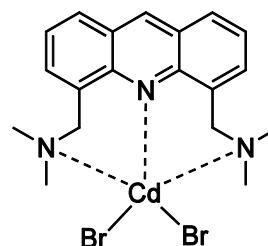
4.3.18 Synthesis of 4,5-bis(dimethylaminemethylene)acridine dibromido cadmium(II) (19)

15 (141 mg, 480 μ mol, 1.0 eq) was dissolved in methanol (0.5 ml) and a solution of CdBr₂ (131 mg, 480 μ mol, 1.0 eq) in methanol (1.5 ml) was poured into. During the addition, the cadmium complex precipitated immediately. Another 5 ml of methanol was added and the suspension was filtrated. The residue was washed several times with methanol (3x 5 ml) and dried under reduced pressure. The pure product (245 mg, 433 μ mol, 90.2%) was obtained as a yellow powder.

Suitable crystals for X-ray diffraction were obtained through crystallisation from a THF/DMF (1.5:1) mixture by slowly cooling the boiling solution to room temperature.

Chemical formula: C₁₉H₂₃N₃CdBr₂

Molecular weight: 565.63 g/mol



¹H NMR

(400 MHz, DMF-*d*₇, 80 °C): δ [ppm] = 9.32 (s, 1 H, H₉), 8.28 (d, ³J = 8.5 Hz, 2 H, H_{1,8}), 8.08-7.99 (m, 2 H, H_{3,6}), 7.71 (dd, ³J = 8.5, 6.8 Hz, 2 H, H_{2,7}), 4.56 (s, 4 H, CH₂), 2.74 (s, 12 H, CH₃).

^{113}Cd NMR

(66.6 MHz, DMF- d_7 , δ [ppm] = -345.5 (taken from ^1H , ^{113}Cd -HMBC).
-30 °C):

TOF ESI MS

m/z (%): 1050.96 (0.4) $[(\text{C}_{19}\text{H}_{23}\text{N}_3)_2\text{Cd}_2\text{Br}_3]^+$, 861.15 (1.2)
 $[(\text{C}_{19}\text{H}_{23}\text{N}_3)_2\text{CdBr}_2\text{H}]^+$, 587.40 (9.2) $[(\text{C}_{19}\text{H}_{23}\text{N}_3)_2\text{H}]^+$, 542.34 (10.8)
 $[\text{C}_{36}\text{H}_{40}\text{N}_5]^+$, 486.02 (15) $[(\text{C}_{19}\text{H}_{23}\text{N}_3)\text{CdBr}]^+$, 294.21 (100)
 $[(\text{C}_{19}\text{H}_{23}\text{N}_3)\text{H}]^+$.

Elemental analysis

in % (calculated): C: 40.28 (40.35), H: 4.31 (4.10), N: 7.20 (7.43), Cd: 19.00 (19.87).

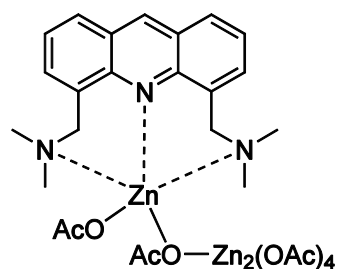
4.3.19 Synthesis of 4,5-bis(dimethylaminemethylene)acridine tetrakis(μ -acetate) bis(acetate) zinc(II) (**20**)

Anhydrous zinc acetate (100 mg, 545 μmol , 1.6 eq) was dissolved in dem. water (0.5 ml) and added to a solution of **15** (100 mg, 341 μmol , 1.0 eq) in methanol. The volatile compounds of the resulting suspension were removed in vacuo and a mixture of toluene with DMF was used to dissolve the product at room temperature. Suitable crystals for X-ray analysis were formed at -30 °C after ten days.

Reverse reaction to 15: The free ligand was reobtained by the application of the same procedure to **20** as for **17**. A direct yield cannot be reported since **20** was not completely isolated before. Nevertheless, 78% (78 mg, 266 μmol) of the used ligand **15** was gained back.

Chemical formula: $\text{C}_{31}\text{H}_{41}\text{N}_3\text{O}_{12}\text{Zn}_3$

Molecular weight: 843.82 g/mol



5. CRYSTALLOGRAPHIC SECTION

5.1 Crystal selection and manipulation

Suitable single crystals for X-ray structural analysis were selected from a *Schlenk* flask under an argon atmosphere and covered with perfluorated polyether oil on a microscope slide, which was cooled with a nitrogen gas flow using the *X-TEMP2* device.^[159] An appropriate crystal was selected using a polarising microscope, mounted on the tip of a *MiTeGen MicroMount*, fixed to a goniometer head and shock-cooled by the crystal cooling device.

5.2 Data collection and processing

The data for the determined structures were collected on four different diffractometers. The datasets using Cu-K α radiation ($\lambda = 1.54178 \text{ \AA}$) were recorded on a *Bruker MacScience* rotating anode diffractometer equipped with a *SMART6000* CCD detector. In the case of Mo-K α radiation ($\lambda = 0.71073 \text{ \AA}$), either an *Incoatec* Mo microsource^[160] with mirror optics or a rotating anode with turbo X-ray source was used. The smallest wavelength with $\lambda = 0.56086 \text{ \AA}$ is generated by an *Incoatec* Ag microfocus source with *Incoatec Quazar* mirror optics. The Mo and Ag diffractometers were equipped with an *APEX II* detector mounted on a three circle D8 goniometer. A low-temperature device was used in every case keeping the crystal temperature at 100 K during the experiment. The data were integrated with *SAINTE*^[161] and an empirical absorption correction was applied (*SADABS*)^[83]. *XPREF*^[162] was used to for the examination of data statistics and space group determination.

5.3 Structure solution and refinement

The structures were solved by direct methods using *SHELXT*^[163] and refined by full-matrix least-squares methods against F^2 (*SHELXL*)^[164] within the *ShelXle* GUI.^[165] All non-hydrogen atoms were refined with anisotropic displacement parameters. The C-bonded hydrogen atoms were refined isotropically on calculated positions using a riding model with their U_{iso} values constrained to equal 1.5 times the U_{eq} of their pivot atoms for terminal sp³ carbon atoms and 1.2 times for all other carbon atoms. The positions of hydrogen atoms attached to heteroatoms were found in the Fourier-density-difference map. They were refined either with the *DFIX* command to set the distance to tabulated values or if similar bonding situations were present (N–H, O–H), the restraint *SADI* was used to align the distances.^[84]

In the absence of restraints, the only data the structural model is refined against are the measured intensities in the form of squared structure factors. Structure factors are calculated from the atomic model and the so-calculated intensities are then compared with the measured intensities, and the best model is the one that minimises $M(p_i, k)$ (Eq. 5.1) using the weights w defined in Eq. 5.2 (p_i : structural parameter; k : scale factor).

$$\text{Eq. 5.1} \quad M(p_i, k) = \sum w[k|F_{\text{obs}}|^2 - |F_{\text{calc}}|^2]^2 = \min$$

$$\text{Eq. 5.2} \quad w^{-1} = \sigma^2(F_{\text{obs}}^2) + (g1 \times P)^2 + g2 \times P \quad \text{with } P = \left(\frac{\text{Max}(F_{\text{obs}}^2, 0) + 2F_{\text{calc}}^2}{3} \right)$$

The results of the refinements were verified by comparison of the calculated and the observed structure factors. Commonly used criteria are the residuals R_1 (Eq. 5.3) and wR_2 (Eq. 5.4). The wR_2 is more significant because the model is refined against F^2 .

$$\text{Eq. 5.3} \quad R_1 = \frac{\sum |F_{\text{obs}}| - |F_{\text{calc}}|}{\sum |F_{\text{obs}}|}$$

$$\text{Eq. 5.4} \quad wR_2 = \sqrt{\frac{\sum w(F_{\text{obs}}^2 - F_{\text{calc}}^2)^2}{\sum w(F_{\text{obs}}^2)^2}}$$

Additionally, the goodness-of-fit (GoF) a figure of merit showing the relation between deviation of F_{calc} from F_{obs} and the over-determination of refined parameters is calculated (Eq. 5.5; N_R : number of reflections; N_P : number of parameters).

$$\text{Eq. 5.5} \quad \text{GoF} = \sqrt{\frac{\sum w(F_{\text{obs}}^2 - F_{\text{calc}}^2)^2}{N_R - N_P}}$$

The residual densities from difference Fourier analysis should be low. Due to the model restrictions, the residuals are normally found in the bonding regions. Higher residuals for heavy scatterers are acceptable as they arise mainly from absorption effects and Fourier truncation errors due to the limited recorded resolution range. The highest peak and deepest hole from difference Fourier analysis are listed in the crystallographic tables.

Additionally, the orientation, size and ellipticity of the ADPs show the quality of the model. Ideally, the ADPs should be oriented perpendicular to the bonds, be equal in size and show little ellipticity.^[166] All graphics were generated and plotted with the XP ^[167] program at the 50% probability level.

5.4 Treatment of disorder

Structures containing disordered fragments were refined using constraints and restraints. Constraints used within this work are, for example, the site occupation factor and the AFIX instruction, which defines and constrains rigid groups. Mathematically, restraints are treated as additional experimental observations, thus increasing the number of data to refine against. In the presence of restraints, the minimisation function changes as follows:

$$\text{Eq. 5.6} \quad M = \sum w(F_{\text{obs}}^2 - F_{\text{calc}}^2)^2 + \sum w_r(R_{\text{target}} - R_{\text{calc}})^2,$$

whereby R_{calc} is the actual value of the restrained quantity.

The geometries of chemically equivalent but crystallographically independent fragments can be fitted to each other by distance restraints. Especially, the 1,2-distances (bond lengths) and 1,3-distances (bond angles) are set to be equal within their effective standard deviations. This is helpful for refining disordered positions as the averaging of equivalent fragments implements chemical information and stabilises the refinement. Within this work, disordered moieties were refined using distance restraints (SADI and SAME) and anisotropic displacement parameter restraints (SIMU and RIGU).^[84]

5.5 Determined structures

5.5.1 4,5-Bis(bromomethylene)-9-methylacridine (9)

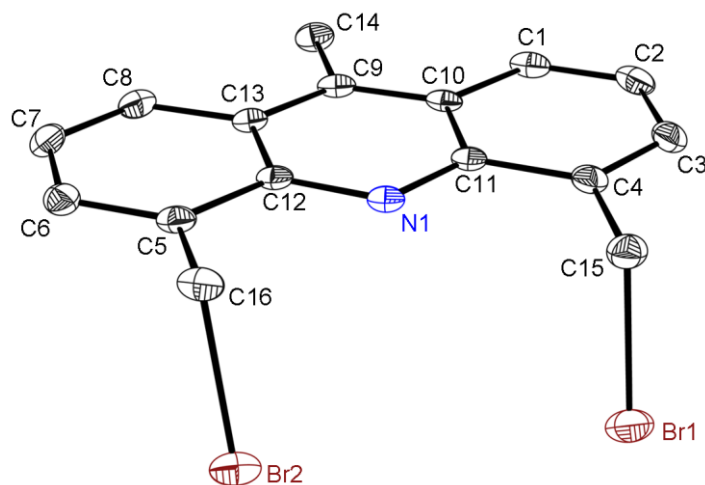


Figure 5.1: Solid state structure of **9**. The anisotropic displacement parameters are depicted at the 50% probability level. All hydrogen atoms are omitted for clarity.

Table 5.1: Crystallographic information of **9**.

CCDC No.	n/a	Density (calculated)	1.836 Mg/m ³
Structure code	9-MeAcrCH ₂ Br	Absorption coefficient	5.896 mm ⁻¹
Empirical formula	C ₁₆ H ₁₃ Br ₂ N	<i>F</i> (000)	744
Formula weight	379.09	Crystal size	0.185 x 0.150 x 0.122 mm ³
Temperature	100(2) K	θ range for data collection	2.313 to 27.875°
Wavelength	0.71073 Å	Reflections collected	37295
Crystal system	monoclinic	Independent reflections	3268 [<i>R</i> _{int} = 0.0238]
Space group	<i>P</i> 2 ₁ / <i>n</i>	Completeness to θ_{\max}	99.9%
Unit cell dimensions	<i>a</i> = 9.598(2) Å <i>b</i> = 8.378(2) Å <i>c</i> = 17.193(3) Å α = 90° β = 97.32(2)° γ = 90°	Max. and min. transmission	0.4308 and 0.3717
Volume	1.3713(5) nm ³	Data / restraints / parameters	3268 / 0 / 173
<i>Z</i>	4	Goodness-of-fit on <i>F</i> ²	1.060
		Final <i>R</i> indices [<i>I</i> > 2σ(<i>I</i>)]	<i>R</i> ₁ = 0.0198, w <i>R</i> ₂ = 0.0529
		<i>R</i> indices (all data)	<i>R</i> ₁ = 0.0216, w <i>R</i> ₂ = 0.0536
		Absolute structure parameter	n/a
		Extinction coefficient	n/a
		Largest diff. peak and hole	0.923 and -0.698 eÅ ⁻³

5.5.2 4,5-Bis(di(2'-methylthiobenzyl)aminemethylene)-9-methylacridine (10)

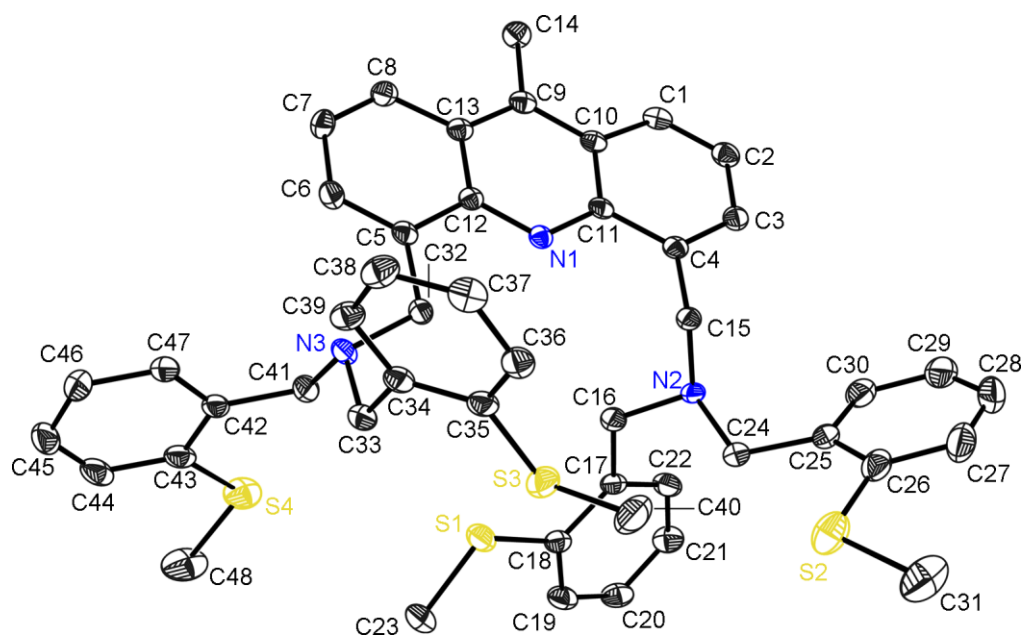


Figure 5.2: Solid state structure of **10**. The anisotropic displacement parameters are depicted at the 50% probability level. All hydrogen atoms are omitted for clarity. In proximity to C2 and C7 unusual residual electron density was noticed. This phenomenon could not be explained reasonable but was also observed at a solid state structure of an acridine unit treated with bromine. Maybe C2 and C7 are brominated by approx. 1% due to the forming of HBr during the reaction process to **10**. Furthermore, the electron density at two of the four sulfur atoms (S1 and S3) is described too high.

Table 5.2: Crystallographic information of **10**.

CCDC No.	n/a	Density (calculated)	1.294 Mg/m ³
Structure code	AcrNBnSMe	Absorption coefficient	0.271 mm ⁻¹
Empirical formula	C ₄₈ H ₄₉ N ₃ S ₄	<i>F</i> (000)	844
Formula weight	796.14	Crystal size	0.460 x 0.220 x 0.060 mm ³
Temperature	100(2) K	θ range for data collection	1.210 to 26.037°
Wavelength	0.71073 Å	Reflections collected	38266
Crystal system	triclinic	Independent reflections	7945 [<i>R</i> _{int} = 0.0255]
Space group	<i>P</i> $\bar{1}$	Completeness to θ_{\max}	98.5%
Unit cell dimensions	<i>a</i> = 10.709(2) Å <i>b</i> = 11.638(2) Å <i>c</i> = 17.300(3) Å α = 93.28(2)° β = 101.85(2)° γ = 103.02(2)°	Max. and min. transmission	0.7453 and 0.7081
Volume	2.0438(7) nm ³	Data / restraints / parameters	7945 / 24 / 501
<i>Z</i>	2	Goodness-of-fit on <i>F</i> ²	1.026
		Final <i>R</i> indices [<i>I</i> > 2σ(<i>I</i>)]	<i>R</i> ₁ = 0.0383, w <i>R</i> ₂ = 0.0912
		<i>R</i> indices (all data)	<i>R</i> ₁ = 0.0499, w <i>R</i> ₂ = 0.0989
		Absolute structure parameter	n/a
		Extinction coefficient	n/a
		Largest diff. peak and hole	1.080 and -0.388 eÅ ⁻³

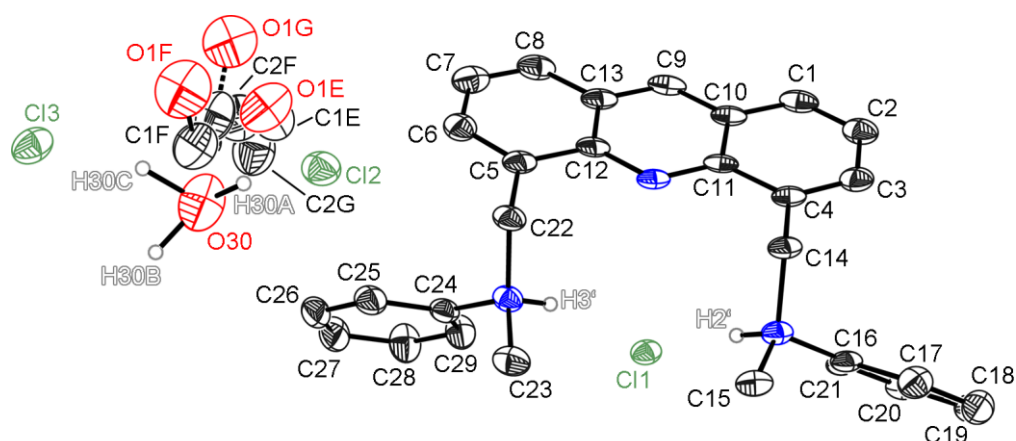
5.5.3 4,5-Bis(*N*-methyl-*N*-phenylaminemethylene)acridine hydrochloride (14)

Figure 5.3: Solid state structure of **14**. The anisotropic displacement parameters are depicted at the 50% probability level. Not freely refined hydrogen atoms are omitted for clarity. The chlorine atom Cl13 lies on a special position with a site occupation factor (*sof*) of 0.5 and the ethanol solvent molecule is disordered over three positions (*sof*: 0.762(3), 0.131(3), 0.107(3)). Therefore, the hydrogen atoms of the oxygen atoms (O1) could not be refined. The position of the hydrogen atoms at O30 were refined freely but more residual electron density could be found in its environment. Probably, the H₃O⁺ molecule is disordered, too, or one hydrogen atom is connected to the Cl2 atom, resulting in the neutral compounds H₂O and HCl. This issue could not be solved with the available data.

Table 5.3: Crystallographic information of **14**.

CCDC No.	n/a	Density (calculated)	1.270 Mg/m ³
Structure code	AcrNMePh_HCl	Absorption coefficient	0.157 mm ⁻¹
Empirical formula	C ₆₂ H ₇₆ Cl ₅ N ₆ O ₄	<i>F</i> (000)	2420
Formula weight	1146.54	Crystal size	0.196 x 0.087 x 0.044 mm ³
Temperature	100(2) K	θ range for data collection	1.927 to 18.233°
Wavelength	0.56086 Å	Reflections collected	91533
Crystal system	monoclinic	Independent reflections	4343 [<i>R</i> _{int} = 0.0723]
Space group	<i>C</i> 2/ <i>c</i>	Completeness to θ _{max}	99.7%
Unit cell dimensions	<i>a</i> = 24.851(3) Å <i>b</i> = 11.214(2) Å <i>c</i> = 24.692(3) Å α = 90° β = 119.56(2)° γ = 90°	Max. and min. transmission	0.7442 and 0.6867
Volume	5.9855(18) nm ³	Data / restraints / parameters	4343 / 221 / 426
<i>Z</i>	8	Goodness-of-fit on <i>F</i> ²	1.030
		Final <i>R</i> indices [<i>I</i> > 2σ(<i>I</i>)]	<i>R</i> ₁ = 0.0416, w <i>R</i> ₂ = 0.0954
		<i>R</i> indices (all data)	<i>R</i> ₁ = 0.0531, w <i>R</i> ₂ = 0.1029
		Absolute structure parameter	n/a
		Extinction coefficient	n/a
		Largest diff. peak and hole	0.547 and -0.443 eÅ ⁻³

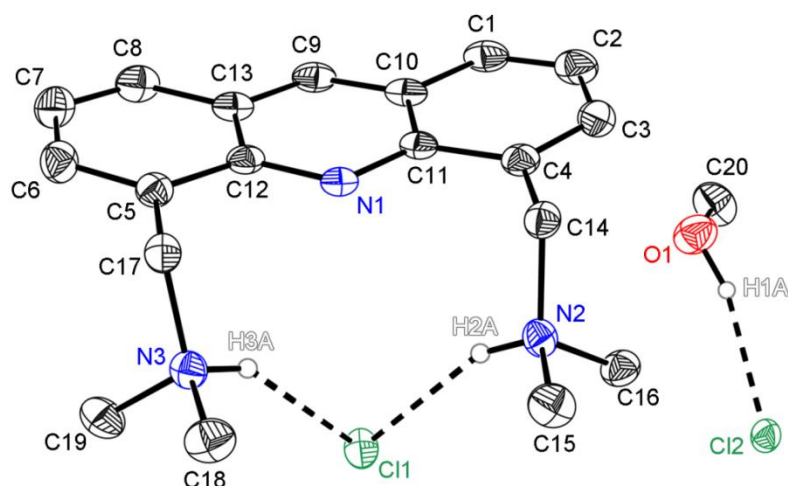
5.5.4 [(Me₂NHCH₂)₂Acr]Cl₂·(MeOH) (16)

Figure 5.4: Solid state structure of **16**. The anisotropic displacement parameters are depicted at the 50% probability level. The positions of the hydrogen atoms H1A, H2A and H3A were refined freely whereas the remaining hydrogen atoms are omitted for clarity. The structure is published in *Dalton Trans.* **2016**, *45*, 5689–5699.^[111]

Table 5.4: Crystallographic information of **16**.

CCDC No.	1423219	Density (calculated)	1.271 Mg/m ³
Structure code	AcrNMe ₂ _HCl	Absorption coefficient	2.905 mm ⁻¹
Empirical formula	C ₂₀ H ₂₉ Cl ₂ N ₃ O	<i>F</i> (000)	848
Formula weight	398.36 g/mol	Crystal size	0.10 x 0.10 x 0.05 mm ³
Temperature	100(2) K	θ range for data collection	28.413 to 66.420°
Wavelength	1.54178 Å	Reflections collected	3602
Crystal system	orthorhombic	Independent reflections	1723 [<i>R</i> _{int} = 0.0163]
Space group	<i>Pna</i> 2 ₁	Completeness to θ_{\max}	79.2% ^(a)
Unit cell dimensions	<i>a</i> = 16.700(3) Å <i>b</i> = 11.503(2) Å <i>c</i> = 10.836(3) Å α = 90° β = 90° γ = 90°	Max. and min. transmission	0.7528 and 0.6427
Volume	2.0816(6) nm ³	Data / restraints / parameters	1723 / 2 / 252
<i>Z</i>	4	Goodness-of-fit on <i>F</i> ²	1.040
		Final <i>R</i> indices [<i>I</i> > 2σ(<i>I</i>)]	<i>R</i> ₁ = 0.0184, <i>wR</i> ₂ = 0.0433
		<i>R</i> indices (all data)	<i>R</i> ₁ = 0.0193, <i>wR</i> ₂ = 0.0436
		Absolute structure parameter	0.008(11)
		Extinction coefficient	n/a
		Largest diff. peak and hole	0.105 and -0.090 eÅ ⁻³

(a): The low completeness of the data set is due to a blockage of the cooling system during the measurement along with the loss of the crystal.

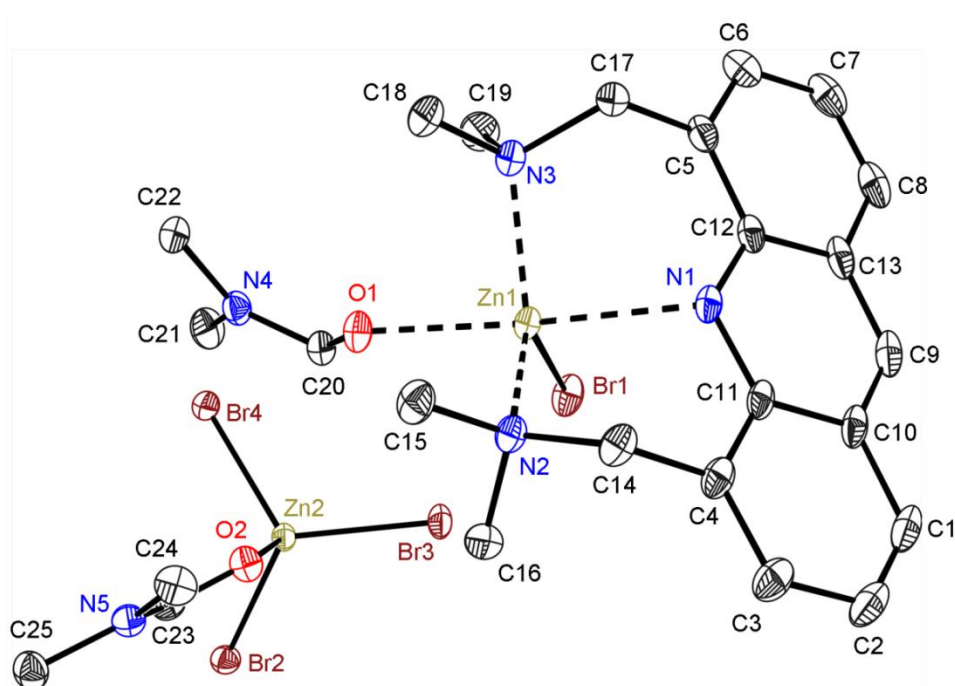
5.5.5 $[(\text{dmf})\text{ZnBr}\{(\text{Me}_2\text{NCH}_2)_2\text{Acr}\}][(\text{dmf})\text{ZnBr}_3]$ (**18**)

Figure 5.5: Solid state structure of **18**. The anisotropic displacement parameters are depicted at the 50% probability level. All hydrogen atoms are omitted for clarity. The structure is published in *Dalton Trans.* **2016**, *45*, 5689–5699.^[111]

Table 5.5: Crystallographic information of **18**.

CCDC No.	1061423	Density (calculated)	1.840 Mg/m ³
Structure code	AcrNMe ₂ -ZnDMF	Absorption coefficient	6.499 mm ⁻¹
Empirical formula	C ₂₅ H ₃₇ Br ₄ N ₅ O ₂ Zn ₂	<i>F</i> (000)	1752
Formula weight	889.97 g/mol	Crystal size	0.212 x 0.179 x 0.076 mm ³
Temperature	100(2) K	θ range for data collection	1.042 to 27.891°
Wavelength	0.71073 Å	Reflections collected	194567
Crystal system	monoclinic	Independent reflections	7674 [<i>R</i> _{int} = 0.0355]
Space group	<i>P</i> 2 ₁ / <i>c</i>	Completeness to θ_{max}	99.9%
Unit cell dimensions	<i>a</i> = 20.985(3) Å <i>b</i> = 9.749(2) Å <i>c</i> = 16.858(2) Å α = 90° β = 111.33(2)° γ = 90°	Max. and min. transmission	0.5631 and 0.3815
Volume	3.2126(10) nm ³	Data / restraints / parameters	7674 / 0 / 351
<i>Z</i>	4	Goodness-of-fit on <i>F</i> ²	1.046
		Final <i>R</i> indices [<i>I</i> > 2σ(<i>I</i>)]	<i>R</i> ₁ = 0.0204, <i>wR</i> ₂ = 0.0528
		<i>R</i> indices (all data)	<i>R</i> ₁ = 0.0236, <i>wR</i> ₂ = 0.0542
		Absolute structure parameter	n/a
		Extinction coefficient	n/a
		Largest diff. peak and hole	1.419 and -0.667 eÅ ⁻³

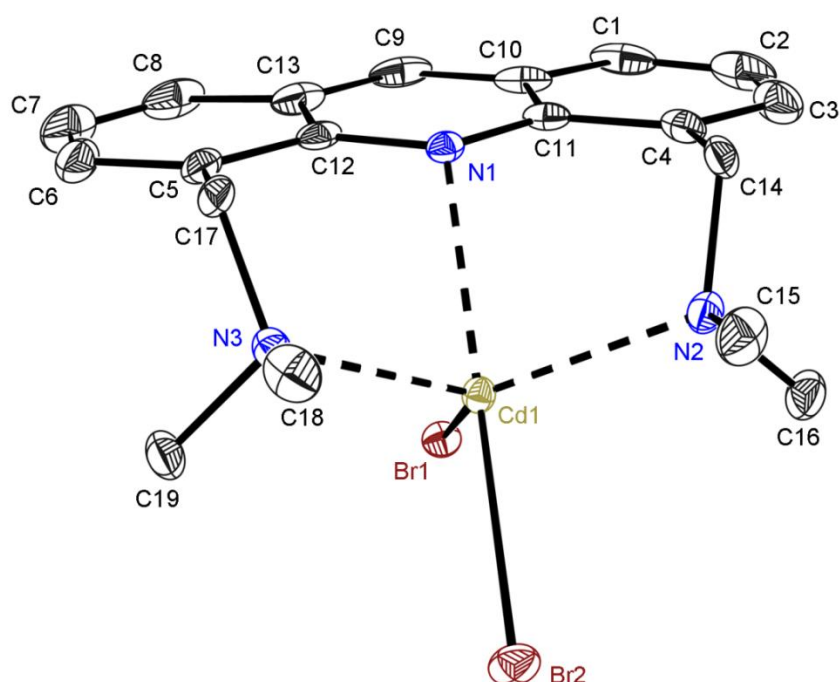
5.5.6 [CdBr₂{(Me₂NCH₂)₂Acr}] (19)

Figure 5.6: Solid state structure of **19**. The anisotropic displacement parameters are depicted at the 50% probability level. All hydrogen atoms are omitted for clarity. The structure is published in *Dalton Trans.* **2016**, *45*, 5689–5699.^[111]

Table 5.6: Crystallographic information of **19**.

CCDC No.	1061424	Density (calculated)	1.866 Mg/m ³
Structure code	AcrNMe ₂ _Cd	Absorption coefficient	2.706 mm ⁻¹
Empirical formula	C ₁₉ H ₂₃ Br ₂ CdN ₃	<i>F</i> (000)	1104
Formula weight	565.62 g/mol	Crystal size	0.225 x 0.222 x 0.185 mm ³
Temperature	100(2) K	θ range for data collection	1.690 to 21.684°
Wavelength	0.56086 Å	Reflections collected	77405
Crystal system	orthorhombic	Independent reflections	4810 [<i>R</i> _{int} = 0.0392]
Space group	<i>P</i> 2 ₁ 2 ₁ 2 ₁	Completeness to θ_{\max}	99.9%
Unit cell dimensions	<i>a</i> = 11.135(2) Å <i>b</i> = 13.332(2) Å <i>c</i> = 13.562(3) Å α = 90° β = 90° γ = 90°	Max. and min. transmission	0.7447 and 0.6799
Volume	2.0133(6) nm ³	Data / restraints / parameters	4810 / 0 / 231
<i>Z</i>	4	Goodness-of-fit on <i>F</i> ²	1.014
		Final <i>R</i> indices [<i>I</i> > 2σ(<i>I</i>)]	<i>R</i> ₁ = 0.0121, w <i>R</i> ₂ = 0.0261
		<i>R</i> indices (all data)	<i>R</i> ₁ = 0.0129, w <i>R</i> ₂ = 0.0263
		Absolute structure parameter	0.014(3)
		Extinction coefficient	0.00180(13)
		Largest diff. peak and hole	0.241 and -0.190 eÅ ⁻³

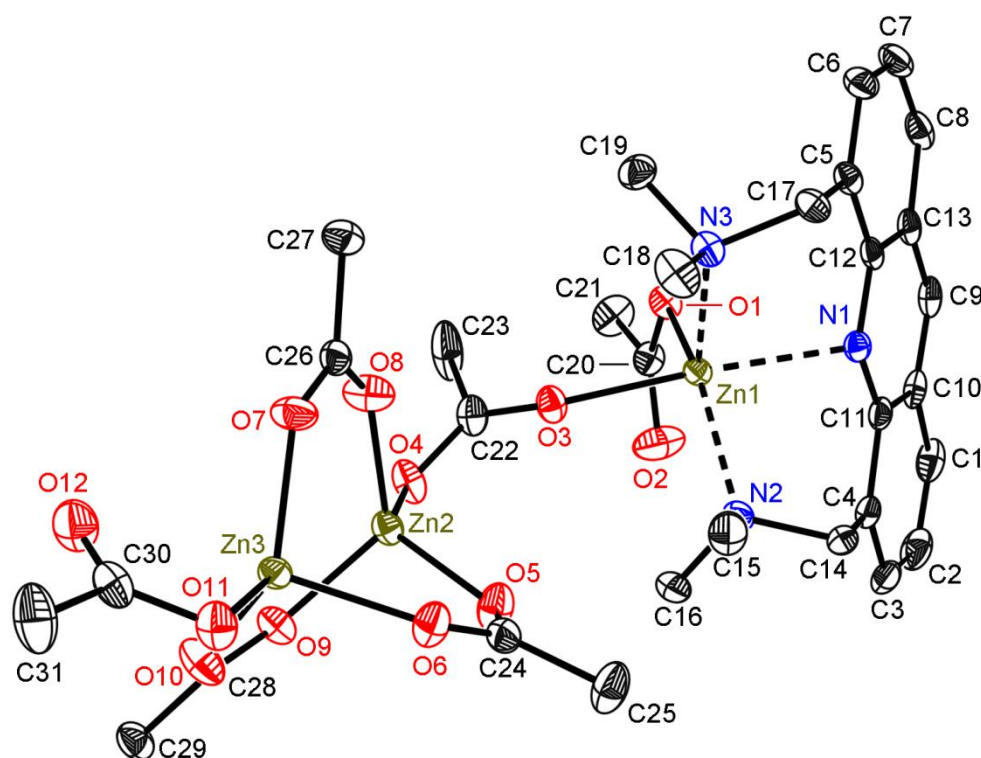
5.5.7 $[\text{Zn}_3(\mu\text{-OAc})_4(\text{OAc})_2\{(\text{Me}_2\text{NCH}_2)_2\text{Acr}\}]$ (**20**)

Figure 5.7: Solid state structure of **20**. The anisotropic displacement parameters are depicted at the 50% probability level. All hydrogen atoms are omitted for clarity. The structure is published in *Dalton Trans.* **2016**, *45*, 5689–5699.^[111]

Table 5.7: Crystallographic information of **20**.

CCDC No.	1423218	Density (calculated)	1.602 Mg/m ³
Structure code	AcrNMe ₂ _ZnOAc	Absorption coefficient	1.111 mm ⁻¹
Empirical formula	C ₃₁ H ₄₁ N ₃ O ₁₂ Zn ₃	<i>F</i> (000)	1736
Formula weight	843.78 g/mol	Crystal size	0.179 x 0.168 x 0.122 mm ³
Temperature	100(2) K	θ range for data collection	1.940 to 20.553°
Wavelength	0.56086 Å	Reflections collected	178761
Crystal system	monoclinic	Independent reflections	7163 [<i>R</i> _{int} = 0.0485]
Space group	<i>P</i> 2 ₁ / <i>c</i>	Completeness to θ_{max}	99.4%
Unit cell dimensions	<i>a</i> = 8.449(2) Å <i>b</i> = 20.113(2) Å <i>c</i> = 21.008(3) Å α = 90° β = 101.42(2)° γ = 90°	Max. and min. transmission	0.5599 and 0.5243
Volume	3.4993(11) nm ³	Data / restraints / parameters	7163 / 0 / 452
<i>Z</i>	4	Goodness-of-fit on <i>F</i> ²	1.037
		Final <i>R</i> indices [<i>I</i> > 2σ(<i>I</i>)]	<i>R</i> ₁ = 0.0214, w <i>R</i> ₂ = 0.0526
		<i>R</i> indices (all data)	<i>R</i> ₁ = 0.0252, w <i>R</i> ₂ = 0.0544
		Absolute structure parameter	n/a
		Extinction coefficient	n/a
		Largest diff. peak and hole	0.646 and -0.458 eÅ ⁻³

5.5.8 $[\text{Zn}_2(\mu\text{-OMe})_{1.16}\text{Br}_{2.84}\{(\text{Me}_2\text{NCH}_2)_2\text{Acr}\}]\cdot(\text{thf})$ (**21**)

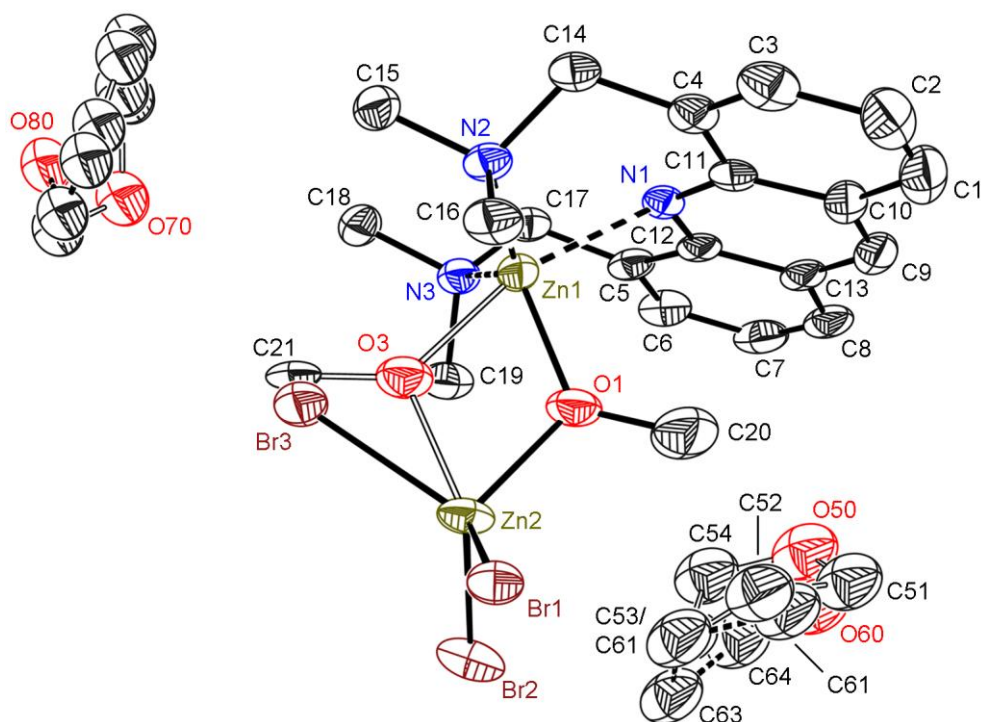


Figure 5.8: Solid state structure of **21**. The anisotropic displacement parameters are depicted at the 50% probability level. All hydrogen atoms are omitted for clarity. Both THF solvent molecules lie on an inversion centre and are disordered over two positions (*sof*: 0.277(6), 0.223(6), 0.244(8), 0.256(8)). The methoxide O3–C21 is disordered with Br3 (*sof*: 0.160(3) and 0.840(3)). The compound was formed during the attempt to crystallise ZnBr₂ with **15** from a THF/MeOH mixture, whereby parts of the methanol solvent molecules were deprotonated.

Table 5.8: Crystallographic information of **21**.

CCDC No.	n/a	Density (calculated)	1.816 Mg/m ³
Structure code	AcrNMe2_ZnOMe	Absorption coefficient	3.113 mm ⁻¹
Empirical formula	C _{24.16} H _{34.47} Br _{2.84} N ₃ O _{2.16} Zn ₂	<i>F</i> (000)	3017
Formula weight	759.21	Crystal size	0.131 x 0.094 x 0.076 mm ³
Temperature	100(2) K	θ range for data collection	1.334 to 19.543°
Wavelength	0.56086 Å	Reflections collected	52354
Crystal system	monoclinic	Independent reflections	4945 [<i>R</i> _{int} = 0.0559]
Space group	<i>C</i> 2/ <i>c</i>	Completeness to θ_{max}	99.8%
Unit cell dimensions	<i>a</i> = 16.197(2) Å <i>b</i> = 18.066(2) Å <i>c</i> = 19.015(3) Å α = 90° β = 93.450(2)° γ = 90°	Max. and min. transmission	1.0000 and 0.8220
Volume	5.5540(13) nm ³	Data / restraints / parameters	4945 / 674 / 468
<i>Z</i>	8	Goodness-of-fit on <i>F</i> ²	1.056
		Final <i>R</i> indices [<i>I</i> > 2σ(<i>I</i>)]	<i>R</i> ₁ = 0.0386, w <i>R</i> ₂ = 0.0932
		<i>R</i> indices (all data)	<i>R</i> ₁ = 0.0595, w <i>R</i> ₂ = 0.1055
		Absolute structure parameter	n/a
		Extinction coefficient	n/a
		Largest diff. peak and hole	1.068 and -0.603 eÅ ⁻³

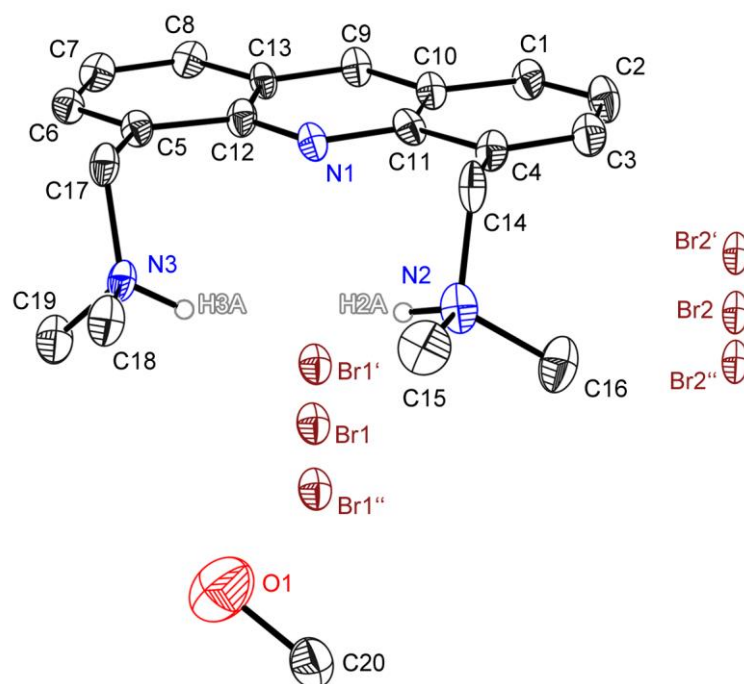
5.5.9 [(Me₂NHCH₂)₂Acr]Br₂·(MeOH) (22)

Figure 5.9: Solid state structure of **22**. The anisotropic displacement parameters are depicted at the 50% probability level. Not freely refined hydrogen atoms are omitted for clarity. Both bromide anions are disordered over three positions (*sof*: Br1: 0.941(2), 0.033(2), 0.026(2); Br2: 0.905(3), 0.074(2), 0.021(2)). The hydrogen atom at the oxygen (O1) could not be refined. The compound was formed during the attempt to crystallise SnBr₂ with **15**. Due to the Lewis acid properties of the metal salt, the ligand got protonated at its amines in a solution of methanol. The two bromide anions act as counter anions to the two-fold positive organic ligand.

Table 5.9: Crystallographic information of **22**.

CCDC No.	n/a	Density (calculated)	1.556 Mg/m ³
Structure code	AcrNMe2_SnBr2	Absorption coefficient	3.912 mm ⁻¹
Empirical formula	C ₂₀ H ₂₉ Br ₂ N ₃ O	<i>F</i> (000)	992
Formula weight	487.28	Crystal size	0.189 x 0.114 x 0.077 mm ³
Temperature	100(2) K	θ range for data collection	2.163 to 25.403°
Wavelength	0.71073 Å	Reflections collected	38418
Crystal system	orthorhombic	Independent reflections	3825 [<i>R</i> _{int} = 0.0640]
Space group	<i>P</i> 2 ₁ 2 ₁ 2 ₁	Completeness to θ_{\max}	100.0%
Unit cell dimensions	<i>a</i> = 11.135(2) Å <i>b</i> = 11.608(2) Å <i>c</i> = 16.088(3) Å α = 90° β = 90° γ = 90°	Max. and min. transmission	0.4288 and 0.3715
Volume	2.0795(4) nm ³	Data / restraints / parameters	3825 / 182 / 266
<i>Z</i>	4	Goodness-of-fit on <i>F</i> ²	1.136
		Final <i>R</i> indices [<i>I</i> > 2σ(<i>I</i>)]	<i>R</i> ₁ = 0.0435, w <i>R</i> ₂ = 0.0992
		<i>R</i> indices (all data)	<i>R</i> ₁ = 0.0517, w <i>R</i> ₂ = 0.1022
		Absolute structure parameter	0.50(3)
		Extinction coefficient	n/a
		Largest diff. peak and hole	0.967 and -0.574 eÅ ⁻³

6. CRYSTAL STRUCTURE DETERMINATION IN COLLABORATIONS

6.1 Structures determined for Mykyta Tretiakov (Prof. Dr. H. W. Roesky)

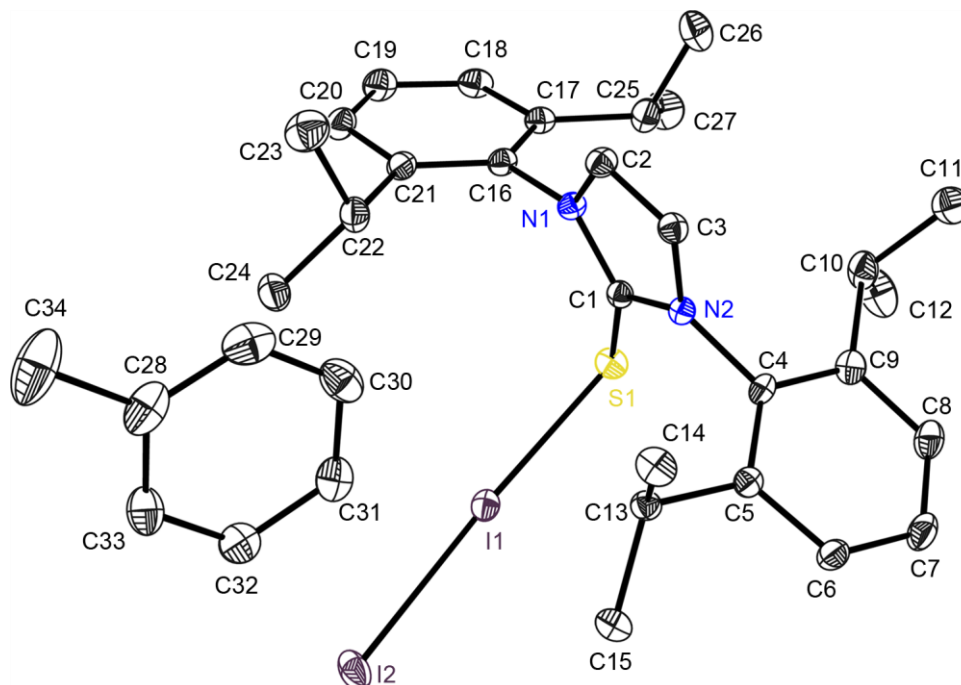
6.1.1 $I_2S=C[N(2,6\text{-}iPr_2\text{-}C_6H_3)CH]_2$ (**23**)

Figure 6.1: Solid state structure of **23**. The anisotropic displacement parameters are depicted at the 50% probability level. All hydrogen atoms are omitted for clarity. The structure is published in *Dalton Transaction* **2013**, 42, 12940-12946.^[168]

Table 6.1: Crystallographic information of **23**.

CCDC No.	933418	Density (calculated)	1.494 Mg/m ³
Structure code	AV_SN82	Absorption coefficient	1.027 mm ⁻¹
Empirical formula	C ₃₄ H ₄₄ I ₂ N ₂ S	<i>F</i> (000)	3072
Formula weight	766.57	Crystal size	0.178 x 0.133 x 0.063 mm ³
Temperature	100(2) K	θ range for data collection	0.867 to 23.633°
Wavelength	0.56086 Å	Reflections collected	103802
Crystal system	monoclinic	Independent reflections	10410 [<i>R</i> _{int} = 0.0635]
Space group	<i>C</i> 2/ <i>c</i>	Completeness to θ_{\max}	100.0%
Unit cell dimensions	<i>a</i> = 37.684(3) Å <i>b</i> = 11.414(2) Å <i>c</i> = 16.103(2) Å α = 90.00° β = 100.24(2)° γ = 90.00°	Max. and min. transmission	0.7449 and 0.6452
Volume	6816.0(16) Å ³	Data / restraints / parameters	10410 / 0 / 361
<i>Z</i>	8	Goodness-of-fit on <i>F</i> ²	1.027
		Final <i>R</i> indices [<i>I</i> > 2σ(<i>I</i>)]	<i>R</i> ₁ = 0.0304, <i>wR</i> ₂ = 0.0654
		<i>R</i> indices (all data)	<i>R</i> ₁ = 0.0397, <i>wR</i> ₂ = 0.0687
		Absolute structure parameter	n/a
		Extinction coefficient	n/a
		Largest diff. peak and hole	1.439 and -0.997 eÅ ⁻³

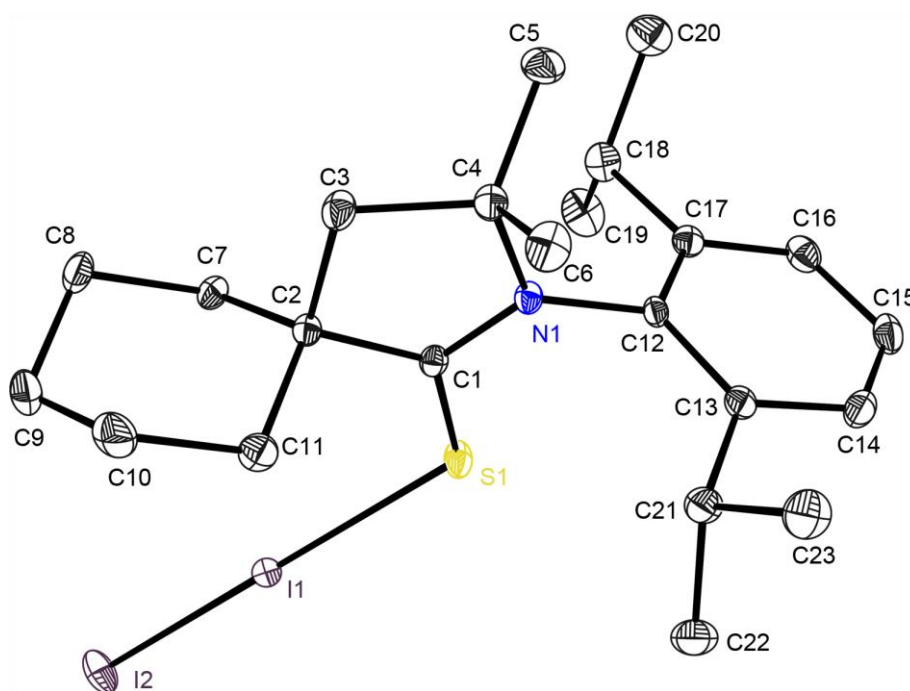
6.1.2 $\text{I}_2\text{S}=\text{C}(\text{CH}_2)(\text{CMe}_2)(\text{C}_6\text{H}_{10})\text{N}-2,6\text{-}i\text{Pr}_2\text{-C}_6\text{H}_3$ (**24**)

Figure 6.2: Solid state structure of **24**. The anisotropic displacement parameters are depicted at the 50% probability level. All hydrogen atoms are omitted for clarity. The structure is published in *Dalton Transaction* **2013**, *42*, 12940-12946.^[168]

Table 6.2: Crystallographic information of **24**.

CCDC No.	933419	Density (calculated)	1.657 Mg/m ³
Structure code	AV_SN84_1	Absorption coefficient	1.412 mm ⁻¹
Empirical formula	C ₂₃ H ₃₅ I ₂ NS	<i>F</i> (000)	604
Formula weight	611.38	Crystal size	0.118 x 0.102 x 0.088 mm ³
Temperature	100(2) K	θ range for data collection	1.351 to 25.679°
Wavelength	0.56086 Å	Reflections collected	50088
Crystal system	triclinic	Independent reflections	9450 [<i>R</i> _{int} = 0.0454]
Space group	<i>P</i> $\bar{1}$	Completeness to θ_{max}	100.0%
Unit cell dimensions	<i>a</i> = 9.520(2) Å <i>b</i> = 11.141(2) Å <i>c</i> = 12.138(2) Å α = 91.69(2)° β = 100.62(2)° γ = 103.70(2)°	Max. and min. transmission	1.0000 and 0.8996
Volume	1225.7(4) Å ³	Data / restraints / parameters	9450 / 0 / 250
<i>Z</i>	2	Goodness-of-fit on <i>F</i> ²	1.054
		Final <i>R</i> indices [<i>I</i> > 2σ(<i>I</i>)]	<i>R</i> ₁ = 0.0255, <i>wR</i> ₂ = 0.0527
		<i>R</i> indices (all data)	<i>R</i> ₁ = 0.0357, <i>wR</i> ₂ = 0.0552
		Absolute structure parameter	n/a
		Extinction coefficient	n/a
		Largest diff. peak and hole	1.162 and -0.947 eÅ ⁻³

6.1.3 $\text{I}_2\text{Te}=\text{C}(\text{CH}_2)(\text{CMe}_2)_2\text{N}-2,6\text{-}^i\text{Pr}_2\text{-C}_6\text{H}_3$ (**25**)

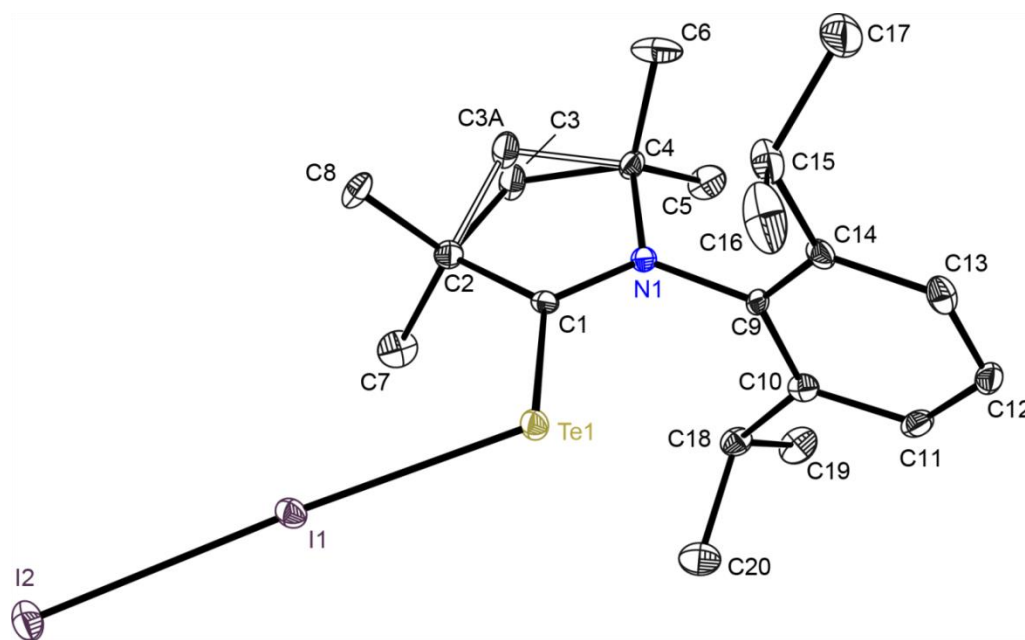


Figure 6.3: Solid state structure of **25**. The anisotropic displacement parameters are depicted at the 50% probability level. All hydrogen atoms are omitted for clarity. C3 is disordered over two positions (*sof*: 0.878(18)). The structure is published in *Dalton Transaction* **2013**, 42, 12940-12946.^[168]

Table 6.3: Crystallographic information of **25**.

CCDC No.	933421	Density (calculated)	1.930 Mg/m ³
Structure code	AV_SN94	Absorption coefficient	2.116 mm ⁻¹
Empirical formula	C ₂₀ H ₃₁ I ₂ NTe	<i>F</i> (000)	1264
Formula weight	666.86	Crystal size	0.090 x 0.085 x 0.058 mm ³
Temperature	100(2) K	θ range for data collection	1.609 to 24.813°
Wavelength	0.56086 Å	Reflections collected	108910
Crystal system	monoclinic	Independent reflections	8016 [<i>R</i> _{int} = 0.0922]
Space group	<i>P</i> 2 ₁ / <i>n</i>	Completeness to θ_{max}	100.0%
Unit cell dimensions	<i>a</i> = 11.108(2) Å <i>b</i> = 16.440(2) Å <i>c</i> = 12.754(2) Å α = 90.00° β = 99.76(2)° γ = 90.00°	Max. and min. transmission	0.8140 and 0.7503
Volume	2295.4(6) Å ³	Data / restraints / parameters	8016 / 3 / 230
Z	4	Goodness-of-fit on <i>F</i> ²	1.064
		Final <i>R</i> indices [<i>I</i> > 2σ(<i>I</i>)]	<i>R</i> ₁ = 0.0313, w <i>R</i> ₂ = 0.0458
		<i>R</i> indices (all data)	<i>R</i> ₁ = 0.0484, w <i>R</i> ₂ = 0.0492
		Absolute structure parameter	n/a
		Extinction coefficient	0.00047(6)
		Largest diff. peak and hole	0.829 and -0.748 eÅ ⁻³

6.2 Structures determined for Bastian Milde (Prof. Dr. D. B. Werz)

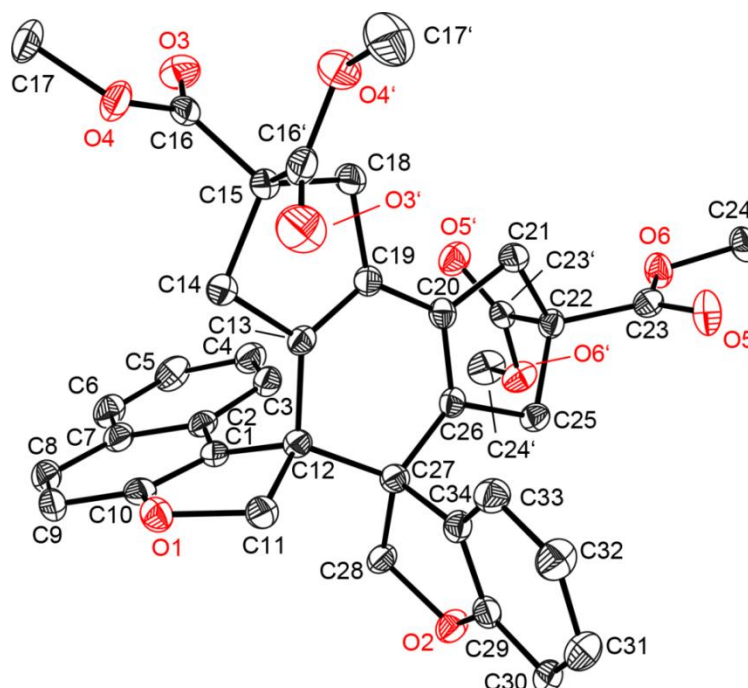
6.2.1 Dispirane: $C_6H_4CCH_2O-(C_5H_4(CO_2Me)_2)_2-C_{10}H_6CCH_2O$ (**26**)

Figure 6.4: Solid state structure of **26**. The anisotropic displacement parameters are depicted at the 50% probability level. All hydrogen atoms are omitted for clarity. The structure is published in *Chem.-Eur. J.* **2015**, *21*, 16136-16146.^[169]

Table 6.4: Crystallographic information of **26**.

CCDC No.	1053289	Density (calculated)	1.364 Mg/m ³
Structure code	BM2_04	Absorption coefficient	0.099 mm ⁻¹
Empirical formula	C ₃₈ H ₃₄ O ₁₀	<i>F</i> (000)	1368
Formula weight	650.65	Crystal size	0.119 x 0.117 x 0.076 mm ³
Temperature	100(2) K	θ range for data collection	1.263 to 26.385°
Wavelength	0.71073 Å	Reflections collected	38399
Crystal system	orthorhombic	Independent reflections	6496 [<i>R</i> _{int} = 0.0482]
Space group	<i>P</i> 2 ₁ 2 ₁ 2 ₁	Completeness to θ_{\max}	99.9%
Unit cell dimensions	<i>a</i> = 9.221(2) Å <i>b</i> = 10.655(2) Å <i>c</i> = 32.257(2) Å α = 90.00° β = 90.00° γ = 90.00°	Max. and min. transmission	0.7446 and 0.7319
Volume	3.1692(9) nm ³	Data / restraints / parameters	6496 / 0 / 437
<i>Z</i>	4	Goodness-of-fit on <i>F</i> ²	1.080
		Final <i>R</i> indices [<i>I</i> > 2σ(<i>I</i>)]	<i>R</i> ₁ = 0.0376, <i>wR</i> ₂ = 0.0893
		<i>R</i> indices (all data)	<i>R</i> ₁ = 0.0450, <i>wR</i> ₂ = 0.0925
		Absolute structure parameter	0.0(3)
		Extinction coefficient	n/a
		Largest diff. peak and hole	0.187 and -0.175 eÅ ⁻³

6.2.2 Dispirane: $C_{12}H_{12}(CO_2Me)_4(CH_2OC_6H_3(CO_2Me))_2$ (**27**)

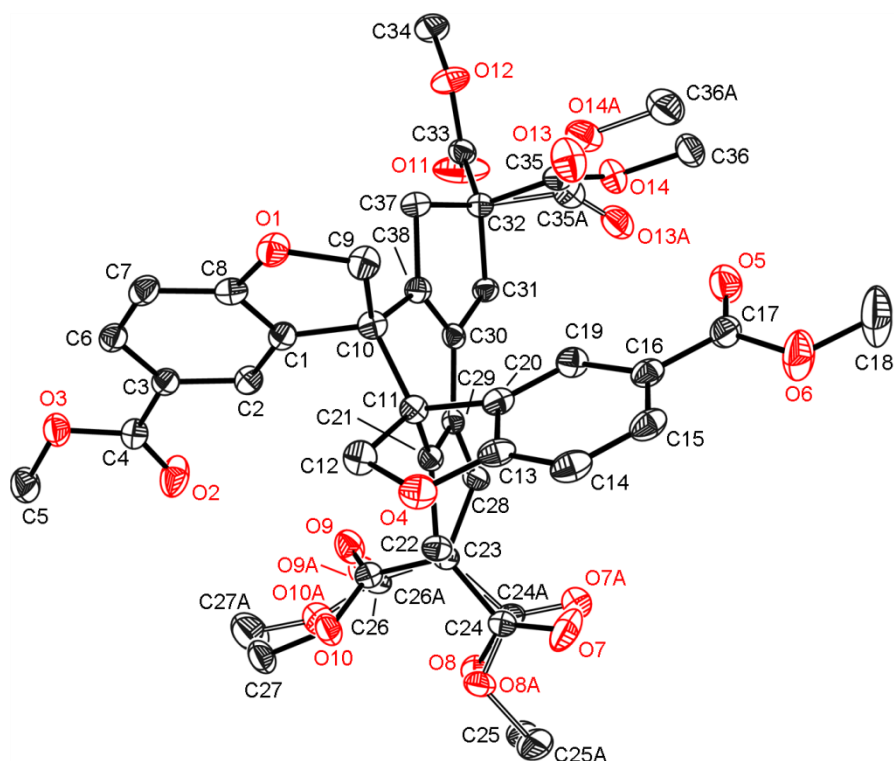


Figure 6.5: Solid state structure of **27**. The anisotropic displacement parameters are depicted at the 50% probability level. All hydrogen atoms are omitted for clarity. The ester groups at C22, C23, and C32 are disordered over two positions (*sof*: 0.883(17), 0.763(14), and 0.935(4), respectively). The structure is published in *Chem.-Eur. J.* **2015**, *21*, 16136-16146.^[169]

Table 6.5: Crystallographic information of **27**.

CCDC No.	1053290	Density (calculated)	1.436 Mg/m ³
Structure code	BM2_871b	Absorption coefficient	0.929 mm ⁻¹
Empirical formula	C ₃₈ H ₃₆ O ₁₄	<i>F</i> (000)	1504
Formula weight	716.67	Crystal size	0.09 x 0.07 x 0.02 mm ³
Temperature	100(2) K	θ range for data collection	5.541 to 70.071°
Wavelength	1.54178 Å	Reflections collected	91199
Crystal system	orthorhombic	Independent reflections	6147 [<i>R</i> _{int} = 0.0388]
Space group	<i>Pca</i> 2 ₁	Completeness to θ_{max}	98.1%
Unit cell dimensions	<i>a</i> = 17.674(2) Å <i>b</i> = 7.983(2) Å <i>c</i> = 23.492(2) Å α = 90.00° β = 90.00° γ = 90.00°	Max. and min. transmission	0.8644 and 0.7943
Volume	3314.5(10) Å ³	Data / restraints / parameters	6147 / 639 / 587
Z	4	Goodness-of-fit on <i>F</i> ²	1.079
		Final <i>R</i> indices [<i>I</i> > 2σ(<i>I</i>)]	<i>R</i> ₁ = 0.0289, w <i>R</i> ₂ = 0.0798
		<i>R</i> indices (all data)	<i>R</i> ₁ = 0.0295, w <i>R</i> ₂ = 0.0800
		Absolute structure parameter	0.38(2)
		Extinction coefficient	n/a
		Largest diff. peak and hole	0.207 and -0.140 eÅ ⁻³

6.3 Structures determined for Tobias Schneider (Prof. Dr. D. B. Werz)

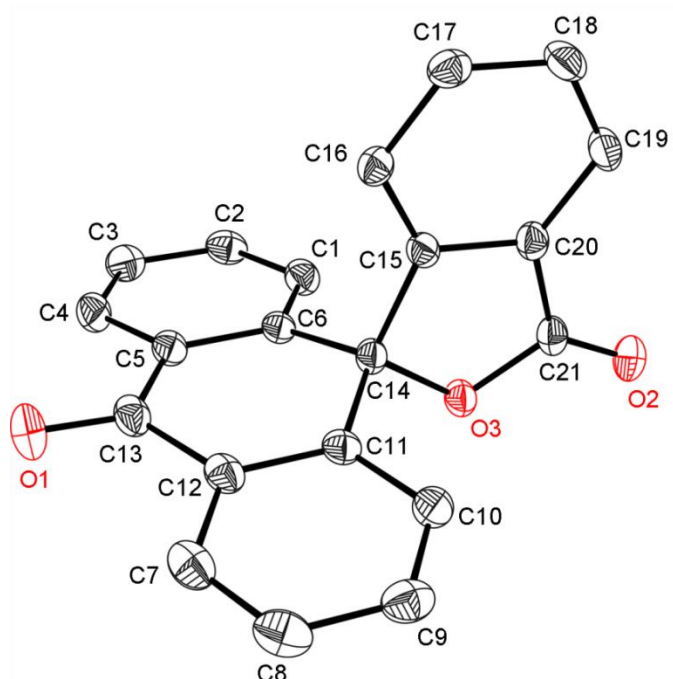
6.3.1 Spiro[anthracene-9(10*H*),1'(3'*H*)-isobenzofuran]-3'10-dione (**28**)

Figure 6.6: Solid state structure of **28**. The anisotropic displacement parameters are depicted at the 50% probability level. All hydrogen atoms are omitted for clarity.

Table 6.6: Crystallographic information of **28**.

CCDC No.	n/a	Density (calculated)	1.449 Mg/m ³
Structure code	ST5_01	Absorption coefficient	0.097 mm ⁻¹
Empirical formula	C ₂₁ H ₁₂ O ₃	<i>F</i> (000)	324
Formula weight	312.31	Crystal size	0.182 x 0.125 x 0.057 mm ³
Temperature	100(2) K	θ range for data collection	1.974 to 25.349°
Wavelength	0.71073 Å	Reflections collected	11019
Crystal system	triclinic	Independent reflections	2617 [<i>R</i> _{int} = 0.0238]
Space group	<i>P</i> $\bar{1}$	Completeness to θ_{\max}	99.9%
Unit cell dimensions	<i>a</i> = 8.635(2) Å <i>b</i> = 9.075(2) Å <i>c</i> = 10.553(2) Å α = 78.25(2)° β = 81.78(2)° γ = 62.31(2)°	Max. and min. transmission	1.0000 and 0.9285
Volume	715.8(3) Å ³	Data / restraints / parameters	2617 / 0 / 217
<i>Z</i>	2	Goodness-of-fit on <i>F</i> ²	1.038
		Final <i>R</i> indices [<i>I</i> > 2σ(<i>I</i>)]	<i>R</i> ₁ = 0.0338, w <i>R</i> ₂ = 0.0881
		<i>R</i> indices (all data)	<i>R</i> ₁ = 0.0386, w <i>R</i> ₂ = 0.0910
		Absolute structure parameter	n/a
		Extinction coefficient	n/a
		Largest diff. peak and hole	0.236 and -0.168 eÅ ⁻³

6.3.2 10,15-Dihydro-5H-tribenzo[*a,d,g*]cyclononen-5-ol (29)

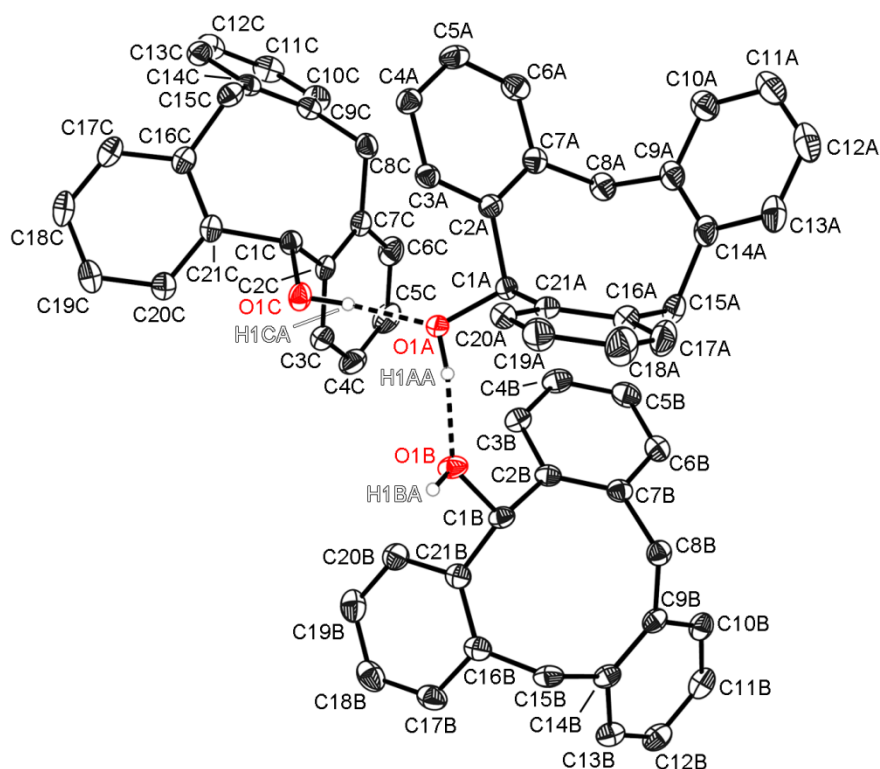


Figure 6.7: Solid state structure of **29**. The anisotropic displacement parameters are depicted at the 50% probability level. Not freely refined hydrogen atoms are omitted for clarity.

Table 6.7: Crystallographic information of **29**.

CCDC No.	n/a	Density (calculated)	1.204 Mg/m ³
Identification code	ST4-X13	Absorption coefficient	0.072 mm ⁻³
Empirical formula	C ₆₃ H ₅₄ O ₃	<i>F</i> (000)	1824
Formula weight	859.06	Crystal size	0.408 x 0.300 x 0.072 mm ³
Temperature	100(2) K	θ range for data collection	1.606 to 27.282°
Wavelength	0.71073 Å	Reflections collected	87786
Crystal system	monoclinic	Independent reflections	10546 [<i>R</i> _{int} = 0.0332]
Space group	<i>P</i> 2 ₁ / <i>n</i>	Completeness to θ _{max}	100.0%
Unit cell dimensions	<i>a</i> = 16.786(2) Å <i>b</i> = 16.518(3) Å <i>c</i> = 17.202(2) Å α = 90.00° β = 96.58(2)° γ = 90.00°	Max. and min. transmission	1.0000 and 0.9490
Volume	4.7382(12) nm ³	Data / restraints / parameters	10546 / 3 / 605
<i>Z</i>	4	Goodness-of-fit on <i>F</i> ²	1.062
		Final <i>R</i> indices [<i>I</i> > 2σ(<i>I</i>)]	<i>R</i> ₁ = 0.0404, w <i>R</i> ₂ = 0.0999
		<i>R</i> indices (all data)	<i>R</i> ₁ = 0.0466, w <i>R</i> ₂ = 0.1033
		Absolute structure parameter	n/a
		Extinction coefficient	0.0022(2)
		Largest diff. peak and hole	0.287 and -0.217 eÅ ⁻³

6.4 Structures determined for Matheus Bukala

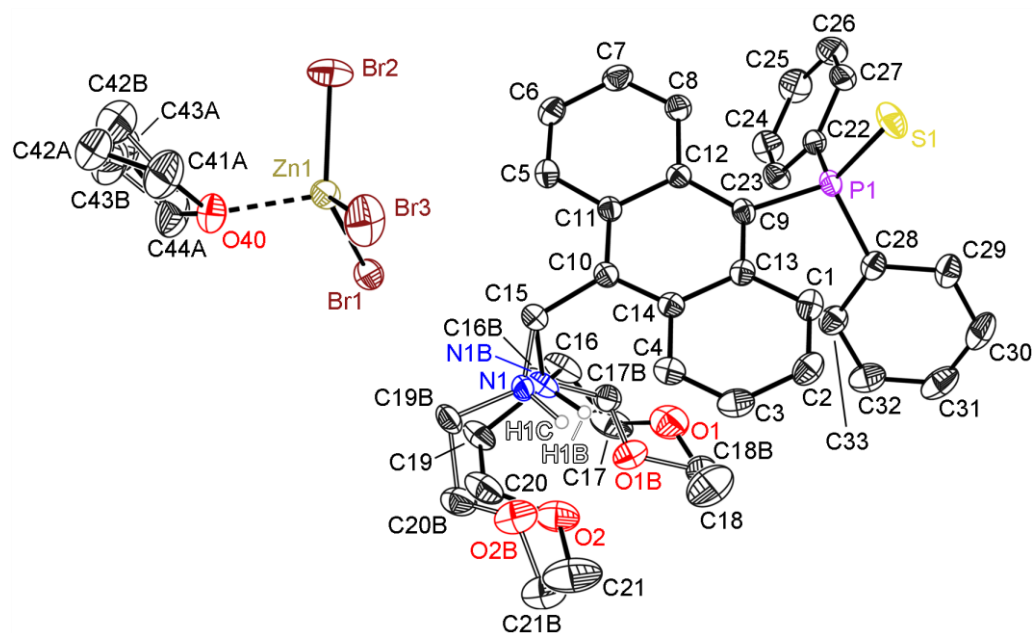
6.4.1 $[\text{Ph}_2\text{SP}(\text{C}_{14}\text{H}_8)\text{CH}_2\text{NH}((\text{CH}_2)_2\text{OCH}_3)_2]^+[(\text{thf})\text{ZnBr}_3]^-$ (30)

Figure 6.8: Solid state structure of **30**. The anisotropic displacement parameters are depicted at the 50% probability level. Not freely refined hydrogen atoms are omitted for clarity. The amine group (N1) and the THF molecule are disordered over two positions (*sof*: 0.897(4) and 0.742(21), respectively).

Table 6.8: Crystallographic information of **30**.

CCDC No.	n/a	Density (calculated)	1.554 Mg/m ³
Structure code	SPAnAmin_Zn	Absorption coefficient	2.035 mm ⁻¹
Empirical formula	C ₃₇ H ₄₃ Br ₃ NO ₃ PSZn	<i>F</i> (000)	924
Formula weight	917.85	Crystal size	0.425 x 0.319 x 0.269 mm ³
Temperature	170(2) K	θ range for data collection	1.531 to 20.594 °
Wavelength	0.56086 Å	Reflections collected	71266
Crystal system	triclinic	Independent reflections	8086 [<i>R</i> _{int} = 0.0223]
Space group	<i>P</i> $\bar{1}$	Completeness to θ_{max}	100.0%
Unit cell dimensions	<i>a</i> = 10.544(2) Å <i>b</i> = 13.126(2) Å <i>c</i> = 15.345(3) Å α = 79.08(2)° β = 70.18(2)° γ = 85.37(3)°	Max. and min. transmission	0.7445 and 0.6315
Volume	1.9615(7) nm ³	Data / restraints / parameters	8086 / 584 / 531
<i>Z</i>	2	Goodness-of-fit on <i>F</i> ²	1.024
		Final <i>R</i> indices [<i>I</i> > 2σ(<i>I</i>)]	<i>R</i> ₁ = 0.0289, <i>wR</i> ₂ = 0.0679
		<i>R</i> indices (all data)	<i>R</i> ₁ = 0.0337, <i>wR</i> ₂ = 0.0713
		Absolute structure parameter	n/a
		Extinction coefficient	n/a
		Largest diff. peak and hole	1.300 and -1.026 eÅ ⁻³

6.5 Structures determined for Lianrong Liu

6.5.1 9,9'-Ethenediylidiacridine (31)

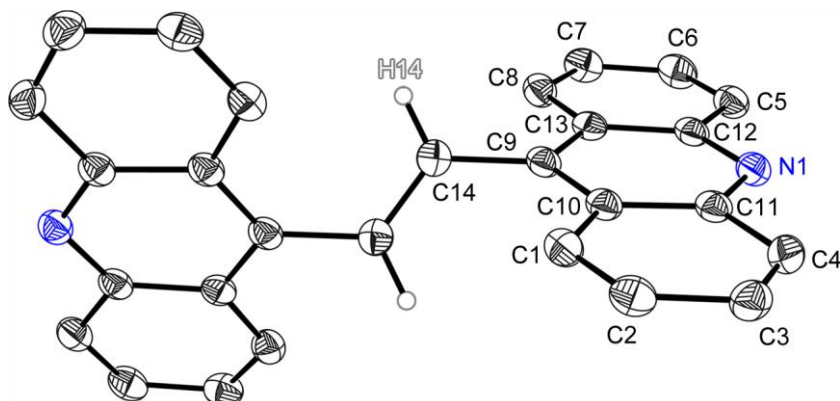


Figure 6.9: Solid state structure of **31**. The anisotropic displacement parameters are depicted at the 50% probability level. The hydrogen atoms at the aromatic system have been omitted for clarity. Only the half of the molecule is present in the asymmetric unit. The other half is generated by a symmetry operation ($1-x, +y, 3/2-z$).

Table 6.9: Crystallographic information of **31**.

CCDC No.	n/a	Density (calculated)	1.384 Mg/m ³
Structure code	LL14	Absorption coefficient	0.081 mm ⁻¹
Empirical formula	C ₂₈ H ₁₈ N ₂	$F(000)$	800
Formula weight	382.44	Crystal size	0.350 x 0.256 x 0.146 mm ³
Temperature	100(2) K	θ range for data collection	2.393 to 25.367°
Wavelength	0.71073 Å	Reflections collected	71266
Crystal system	monoclinic	Independent reflections	1674 [$R_{\text{int}} = 0.0256$]
Space group	$C2/c$	Completeness to θ_{max}	99.9%
Unit cell dimensions	$a = 13.550(3)$ Å	Max. and min. transmission	0.7452 and 0.7091
	$b = 12.211(2)$ Å	Data / restraints / parameters	1674 / 0 / 136
	$c = 12.660(2)$ Å	Goodness-of-fit on F^2	1.075
	$\alpha = 90^\circ$	Final R indices [$I > 2\sigma(I)$]	$R_1 = 0.0387, wR_2 = 0.1049$
	$\beta = 118.83(2)^\circ$	R indices (all data)	$R_1 = 0.0420, wR_2 = 0.1083$
	$\gamma = 90^\circ$	Absolute structure parameter	n/a
Volume	1.8351(7) nm ³	Extinction coefficient	n/a
Z	4	Largest diff. peak and hole	0.263 and -0.188 eÅ ⁻³

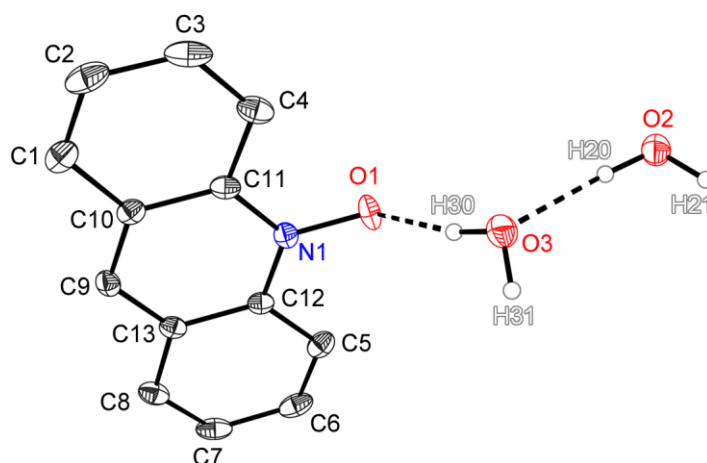
6.5.2 Acridine-10-oxide·2H₂O (32)

Figure 6.10: Solid state structure of **32**. The anisotropic displacement parameters are depicted at the 50% probability level. Not freely refined hydrogen atoms have been omitted for clarity.

Table 6.10: Crystallographic information of **32**.

CCDC No.	n/a	Density (calculated)	1.385 Mg/m ³
Structure code	LL17	Absorption coefficient	0.062 mm ⁻¹
Empirical formula	C ₁₃ H ₁₃ NO ₃	<i>F</i> (000)	488
Formula weight	231.24	Crystal size	0.529 x 0.332 x 0.156 mm ³
Temperature	100(2) K	θ range for data collection	1.707 to 20.308 °
Wavelength	0.56086 Å	Reflections collected	44220
Crystal system	monoclinic	Independent reflections	2198 [<i>R</i> _{int} = 0.0434]
Space group	<i>P</i> 2 ₁ / <i>n</i>	Completeness to θ_{\max}	99.9%
Unit cell dimensions	<i>a</i> = 11.565(3) Å <i>b</i> = 6.762(2) Å <i>c</i> = 14.254(3) Å <i>a</i> = 90° <i>β</i> = 95.83(2)° <i>γ</i> = 90°	Max. and min. transmission	0.7445 and 0.6561
Volume	1.1089(5) nm ³	Data / restraints / parameters	2198 / 6 / 171
Z	4	Goodness-of-fit on <i>F</i> ²	1.070
		Final <i>R</i> indices [<i>I</i> > 2σ(<i>I</i>)]	<i>R</i> ₁ = 0.0375, w <i>R</i> ₂ = 0.1104
		<i>R</i> indices (all data)	<i>R</i> ₁ = 0.0437, w <i>R</i> ₂ = 0.1155
		Absolute structure parameter	n/a
		Extinction coefficient	0.006(3)
		Largest diff. peak and hole	0.311 and -0.233 eÅ ⁻³

7. SUPPLEMENT

7.1 Lifetime measurement of **17**

The measurements were carried out during a workshop of the company *Horiba Scientific* in Essen 2014 at an exhibited spectrometer of the DeltaFlex series. Unfortunately, the company only handed over a screenshot of the results without any raw data. This is why no clear graph could be prepared. In Figure 7.1, the abscissa represents the measured channels and the counts are given on the vertical axis. A value of 13.9 ns was received for the lifetime of **17**.

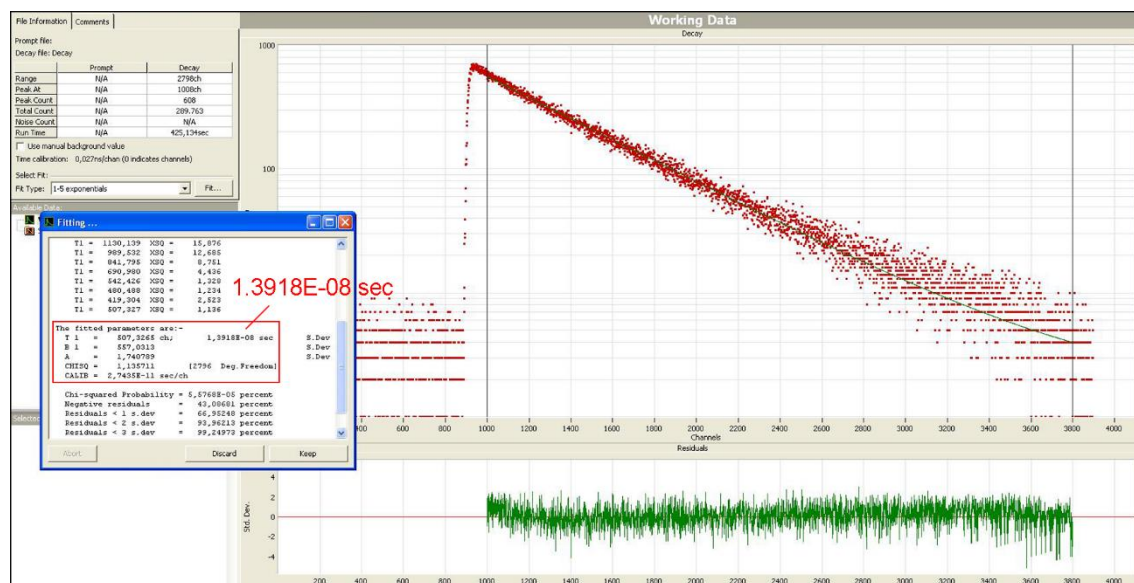


Figure 7.1: Lifetime measurement of **17** in methanol (10^{-5} M).

7.2 NMR spectra

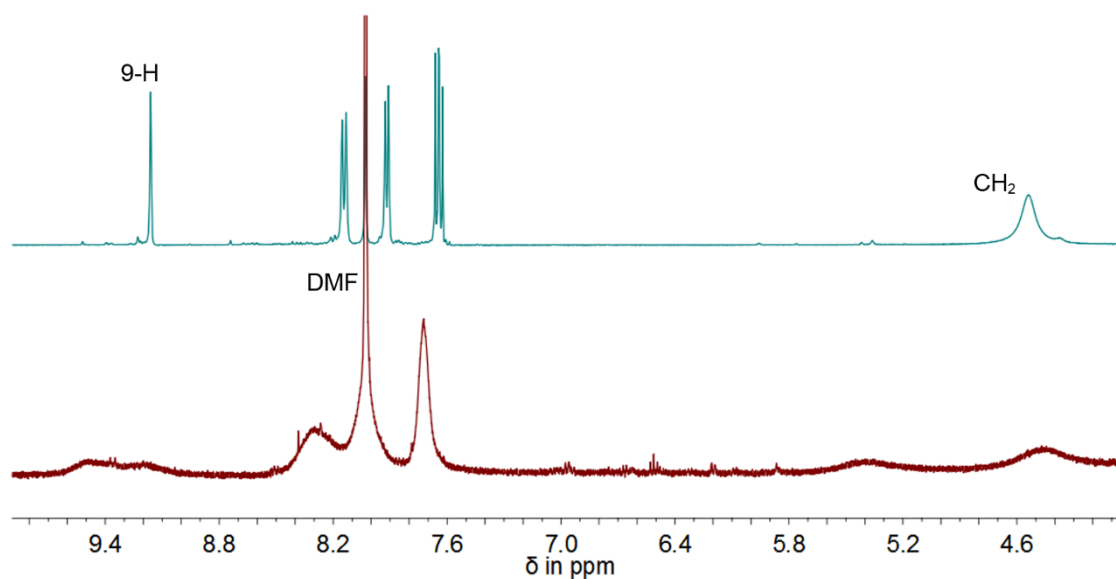


Figure 7.2: Stacked ^1H NMR spectra of **17** without (red) and with addition of 10 eq NaBr (turquoise) in DMF- d_7 at ambient temperature. The signals are no longer broadened after the addition of NaBr which is why the dynamic processes can be attributed to the DMF/bromide exchange.

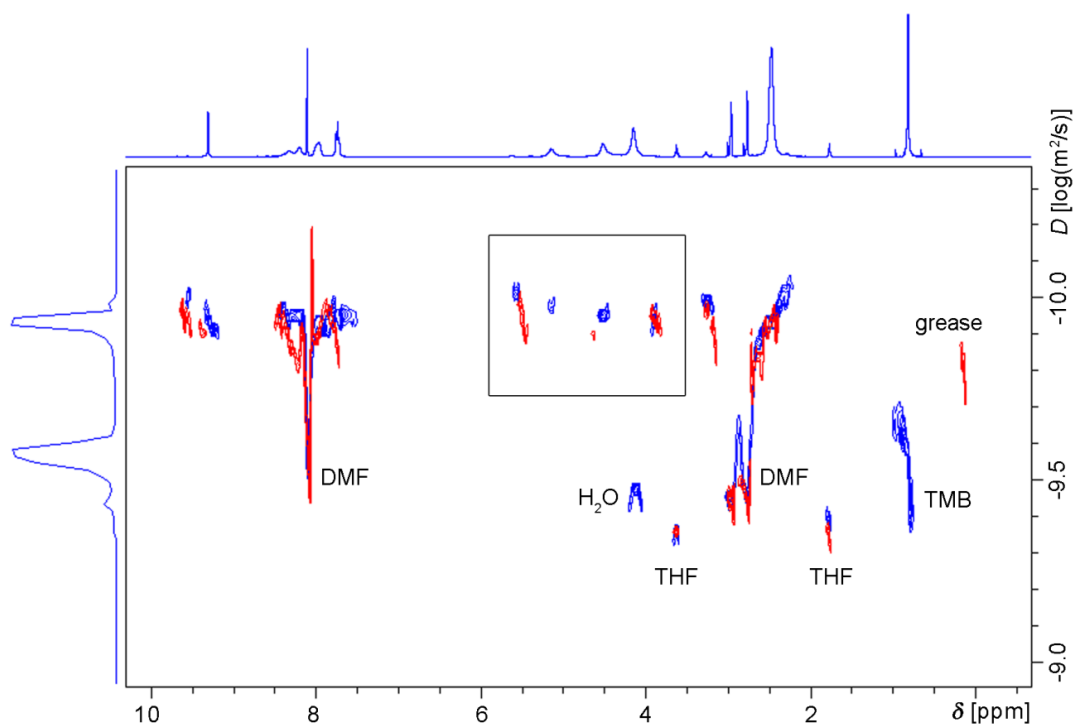


Figure 7.3: Overlay of ^1H -DOSY NMR full spectra of **17** without (red) and with addition of 10 eq NaBr (blue) in $\text{DMF-}d_7$ at 243 K.

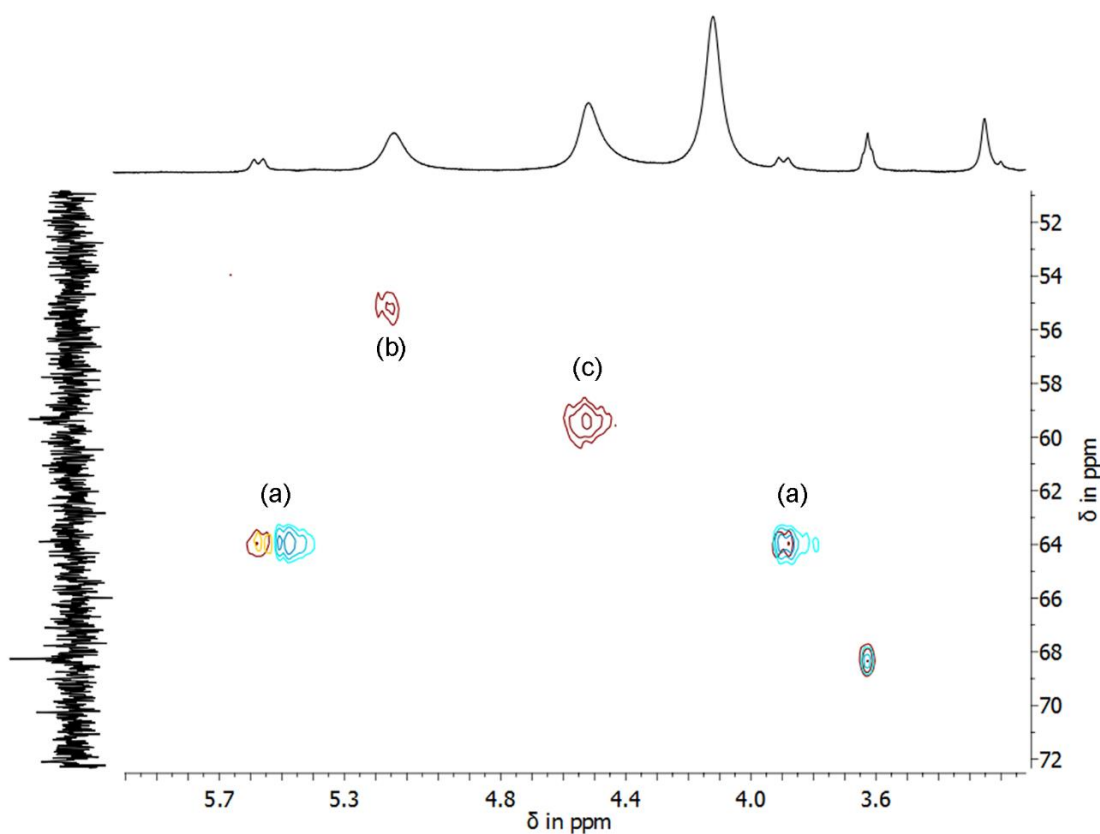


Figure 7.4: Superimposed ^1H , ^{13}C -HSQC NMR spectra of **17** without (turquoise) and with addition of 10 eq NaBr (brown) in $\text{DMF-}d_7$ at 243 K; a) $[(\text{dmf})_2\text{Zn}\{(\text{Me}_2\text{NCH}_2)_2\text{Acr}\}]^{2+}$; b) $[(\text{dmf})\text{ZnBr}\{(\text{Me}_2\text{NCH}_2)_2\text{Acr}\}]^+$; c) $[\text{ZnBr}_2\{(\text{Me}_2\text{NCH}_2)_2\text{Acr}\}]$. This spectrum is in line with the theory of generating different species by adding NaBr to the NMR sample. The protons of (a), (b), and (c) couple to different carbon atoms and do not belong to one compound.

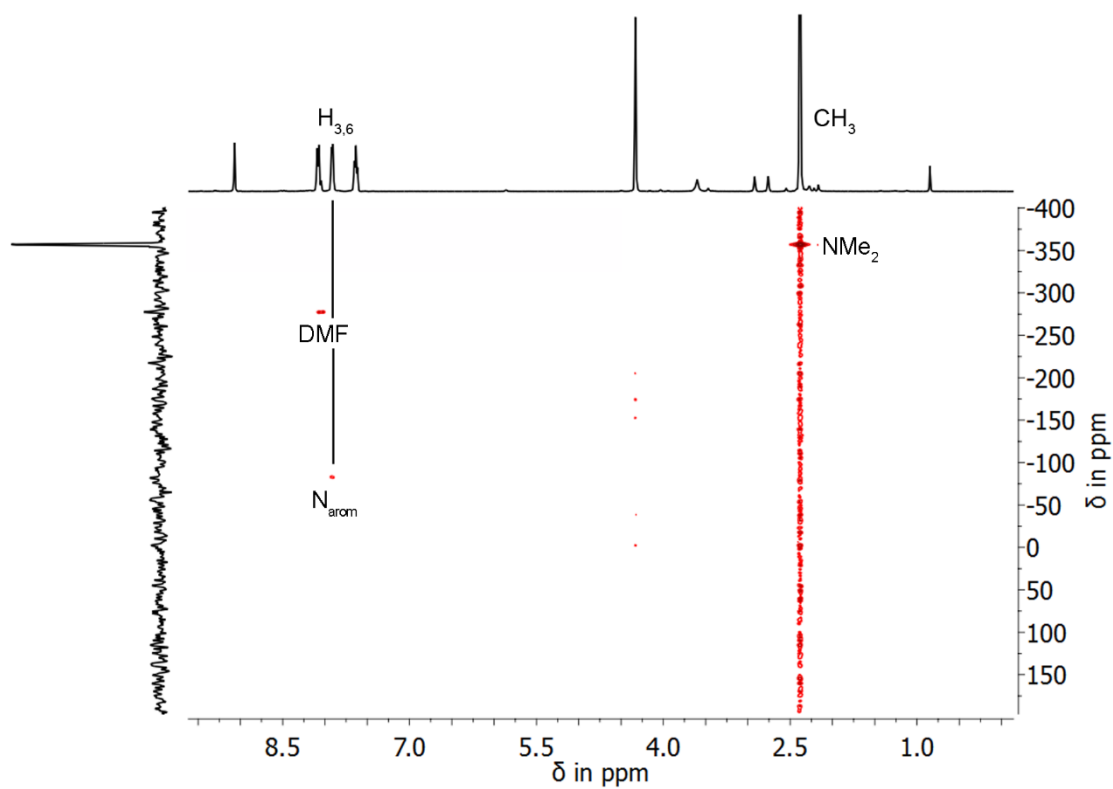


Figure 7.5: ^1H , ^{15}N -HMBC NMR spectrum of **15** in $\text{DMF-}d_7$ at 273 K.

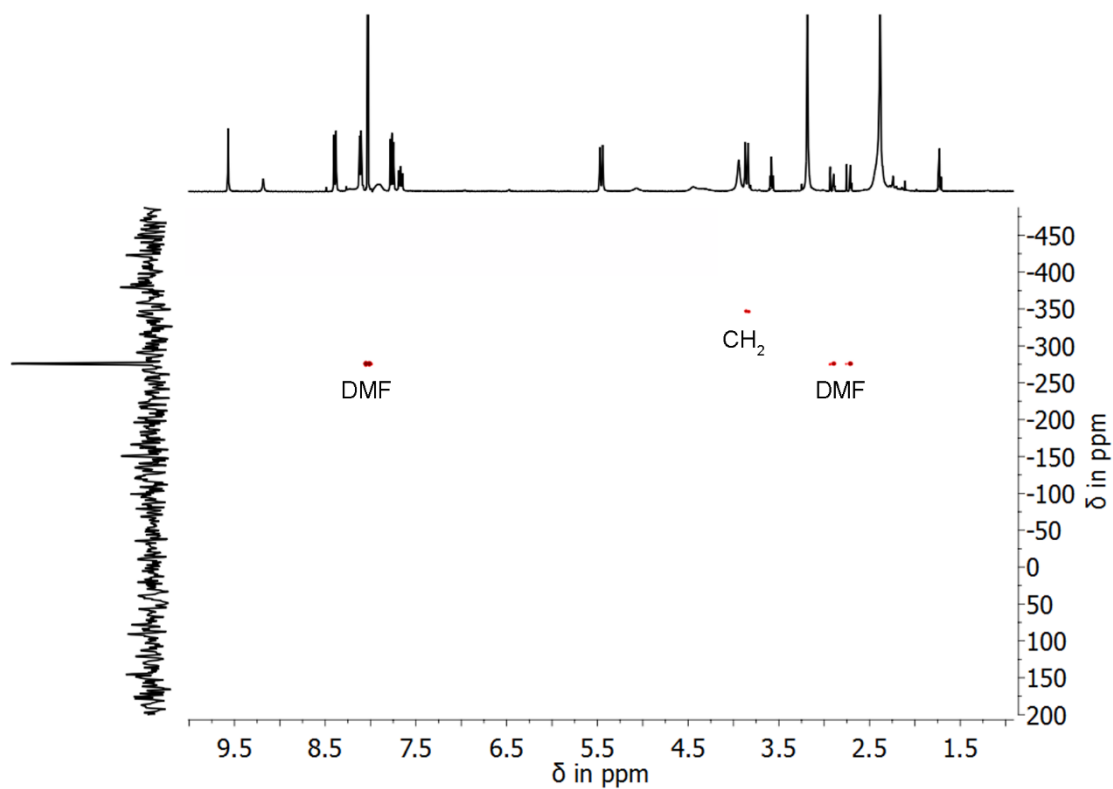


Figure 7.6: ^1H , ^{15}N -HMBC NMR spectrum of **17** in $\text{DMF-}d_7$ at 243 K.

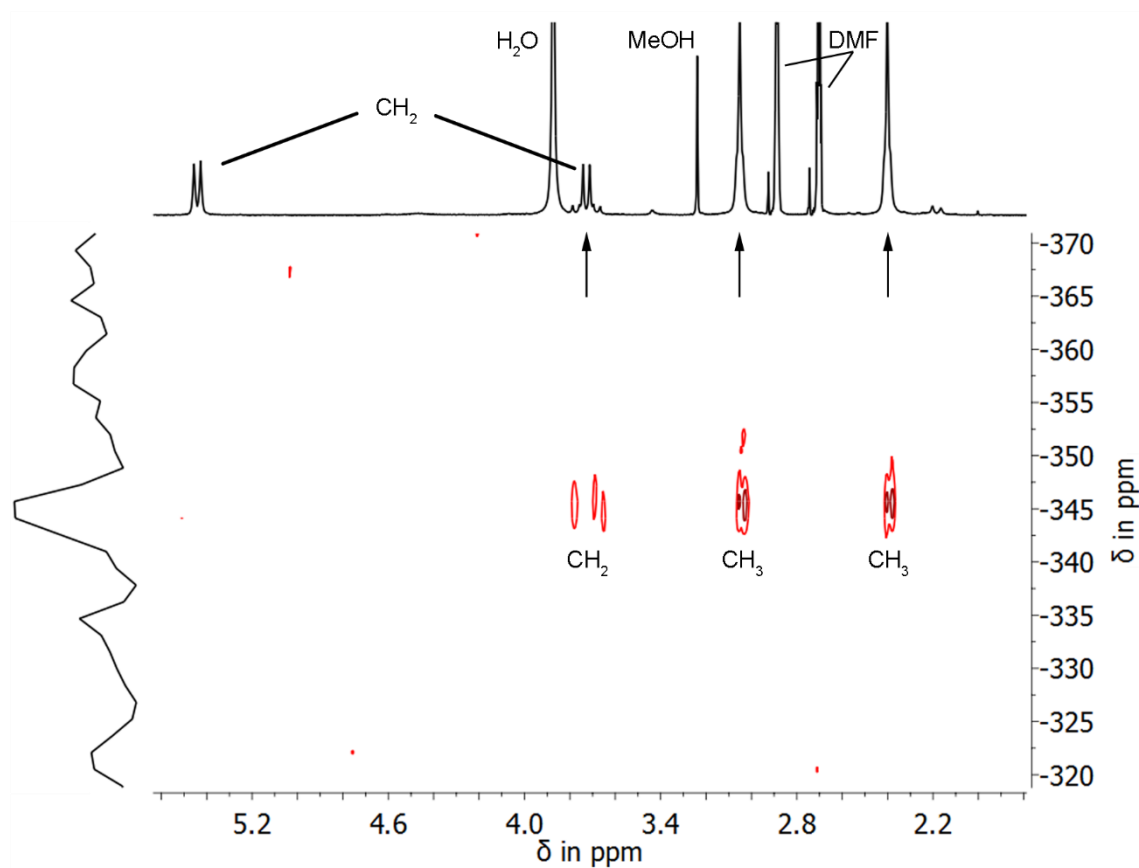


Figure 7.7: $^1\text{H},^{113}\text{Cd}$ -HMBC NMR spectrum of **19** in $\text{DMF-}d_7$ at 243 K. Only one proton of each CH_2 group is coupled to the ^{113}Cd nucleus ($\delta = -345$ ppm).

7.3 Mass spectra

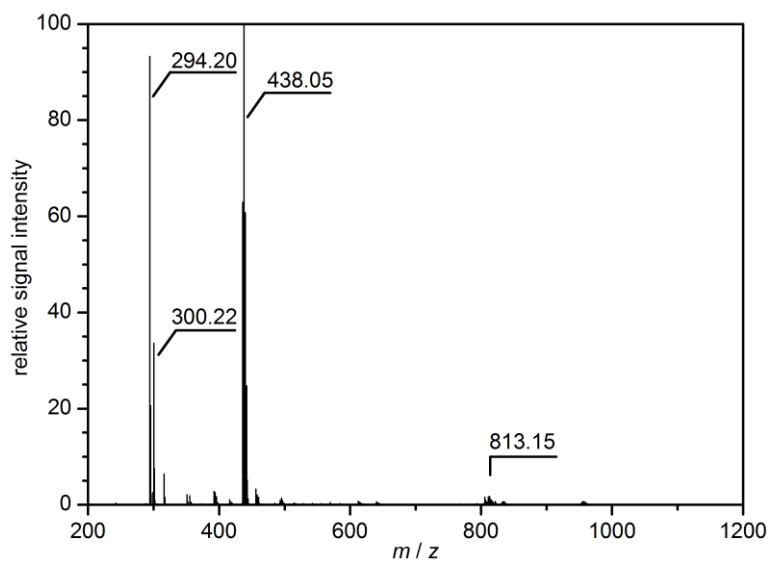


Figure 7.8: Positive-ion mode ESI-TOF mass spectrum of a solution of **17** in THF.

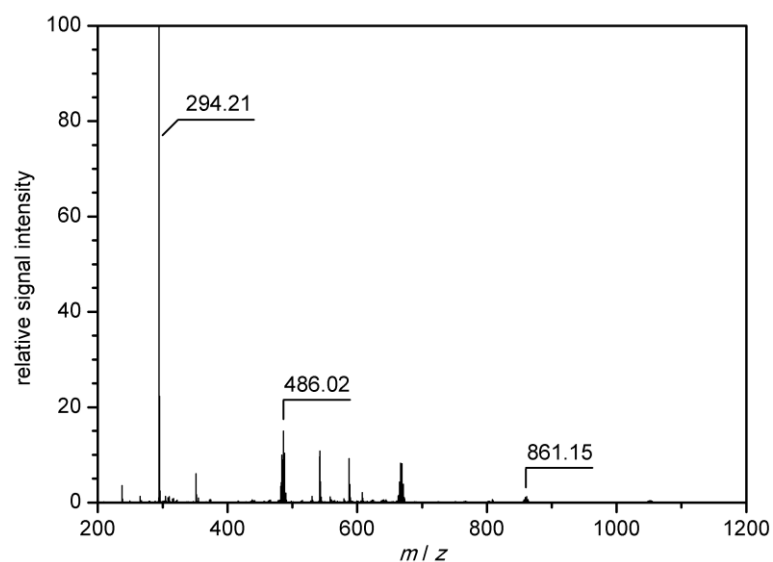


Figure 7.9: Positive-ion mode ESI-TOF mass spectrum of a solution of **19** in a THF/H₂O mixture.

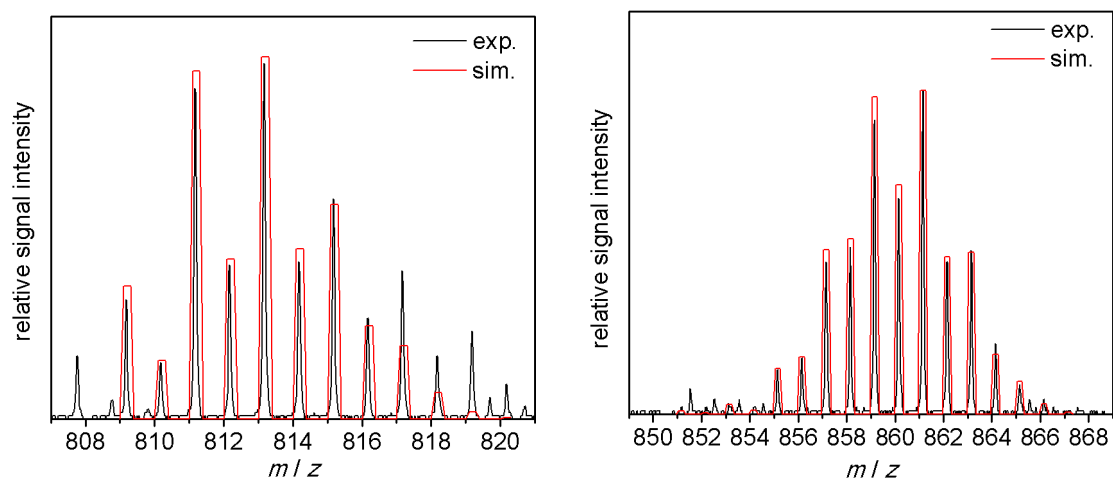


Figure 7.10: Parts of the mass spectra showing the simulated (red) and the experimental (black) isotope pattern of the cationic $[(C_{19}H_{23}N_3)_2HZnBr_2]^+$ (left) and $[(C_{19}H_{23}N_3)_2HCdBr_2]^+$ (right).

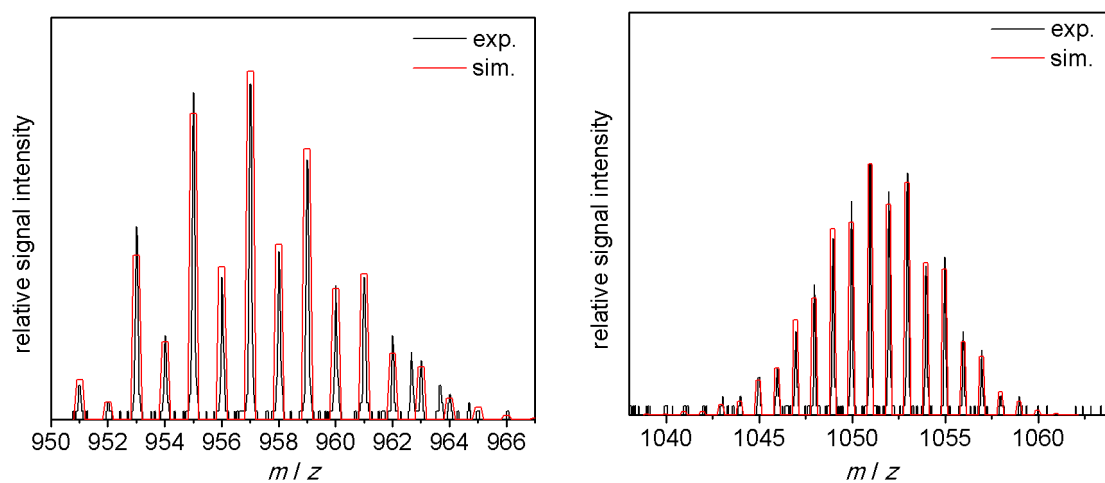


Figure 7.11: Parts of the mass spectra showing the simulated (red) and the experimental (black) isotope pattern of the cationic $[(C_{19}H_{23}N_3)_2Zn_2Br_3]^+$ (left) and $[(C_{19}H_{23}N_3)_2Cd_2Br_3]^+$ (right).

8. REFERENCES

- [1] B. Valeur, M. N. Berberan-Santos, *J. Chem. Educ.* **2011**, *88*, 731-738.
- [2] A. U. Acuña, F. Amat-Guerri, in *Fluorescence of Supermolecules, Polymers, and Nanosystems, Vol. 4* (Ed.: M. N. Berberan-Santos), Springer, Berlin, Heidelberg, **2008**, pp. 3-20.
- [3] A. U. Acuña, F. Amat-Guerri, P. Morcillo, M. Liras, B. Rodríguez, *Org. Lett.* **2009**, *11*, 3020-3023.
- [4] (a) J. F. W. Herschel, *Phil. Trans. R. Soc. London* **1845**, *135*, 143-145; (b) D. Brewster, *Phil. Mag.* **1848**, *32*, 401-412.
- [5] G. G. Stokes, *Phil. Trans. R. Soc. London* **1852**, *142*, 463-562.
- [6] G. G. Stokes, *Phil. Trans. R. Soc. London* **1853**, *143*, 385-396.
- [7] J. R. Lakowicz, *Principles of Fluorescence Spectroscopy* 3rd ed., Springer, New York, **2006**, pp. 1-26.
- [8] E. Becquerel, *Ann. Chim. Phys.* **1842**, *9*, 257-322.
- [9] A. Jabłoński, *Z. Physik* **1935**, *94*, 38-46.
- [10] M. Kasha, *Discuss. Faraday Soc.* **1950**, *9*, 14-19.
- [11] N. J. Turro, V. Ramamurthy, J. C. Scaiano, *Modern Molecular Photochemistry of Organic Molecules*, 1st ed., University Science Books, Sausalito, **2010**.
- [12] (a) J. Franck, E. G. Dymond, *Trans. Faraday Soc.* **1926**, *21*, 536-542; (b) E. Condon, *Phys. Rev.* **1926**, *28*, 1182-1201.
- [13] M. Sauer, J. Hofkens, J. Enderlein, *Handbook of Fluorescence Spectroscopy and Imaging: From Single Molecules to Ensembles*, Wiley-VCH, Weinheim, **2011**, pp. 1-30.
- [14] (a) A. P. de Silva, D. B. Fox, A. J. M. Huxley, N. D. McClenaghan, J. Roiron, *Coord. Chem. Rev.* **1999**, *185-186*, 297-306; (b) W.-Y. Wong, K. C.-F. Leung, J. F. Stoddart, *Org. Biomol. Chem.* **2010**, *8*, 2332-2343; (c) J. T. Hutt, J. Jo, A. Olasz, C.-H. Chen, D. Lee, Z. D. Aron, *Org. Lett.* **2012**, *14*, 3162-3165.
- [15] A. P. de Silva, H. Q. N. Gunaratne, T. Gunnlaugsson, A. J. M. Huxley, C. P. McCoy, J. T. Rademacher, T. E. Rice, *Chem. Rev.* **1997**, *97*, 1515-1566.
- [16] (a) R. A. Bissell, A. P. de Silva, H. Q. N. Gunaratne, P. L. M. Lynch, G. E. M. Maguire, K. R. A. S. Sandanayake, *Chem. Soc. Rev.* **1992**, *21*, 187-195; (b) J. F. Callan, A. P. de Silva, J. Ferguson, A. J. M. Huxley, A. M. O'Brien, *Tetrahedron* **2004**, *60*, 11125-11131; (c) A. Kumar, V. Kumar, K. K. Upadhyay, *Analyst* **2013**, *138*, 1891-1897.
- [17] Y. Li, T. Liu, H. Liu, M.-Z. Tian, Y. Li, *Acc. Chem. Res.* **2014**, *47*, 1186-1198.
- [18] T. Saha, A. Sengupta, P. Hazra, P. Talukdar, *Photochem. Photobiol. Sci.* **2014**, *13*, 1427-1433.
- [19] J. B. Birks, *Photophysics of Aromatic Molecules*, 1st ed., Wiley - Interscience, London, New York, Sydney, Toronto, **1970**.
- [20] (a) R. A. Bissel, A. P. de Silva, H. Q. N. Gunaratne, P. L. M. Lynch, G. E. M. Maguire, C. P. McCoy, K. R. A. S. Sandanayake, in *Photoinduced Electron Transfer V, Vol. 168* (Ed.: J. Mattay), Springer, Berlin, Heidelberg, **1993**, pp. 229-230; (b) K. Kubo, in *Topics in Fluorescence Spectroscopy, Vol. 9* (Eds.: C. D. Geddes, J. R. Lakowicz), Springer US, **2005**, pp. 219-247; (c) A. P. de Silva, *J. Phys. Chem. Lett.* **2011**, *2*, 2865-2871.
- [21] M. Asha Jhonsi, A. Kathiravan, *J. Lumin.* **2014**, *145*, 188-193.
- [22] J. C. Beeson, M. E. Huston, D. A. Pollard, T. K. Venkatachalam, A. W. Czarnik, *J. Fluoresc.* **1993**, *3*, 65-68.
- [23] R. S. Davidson, K. R. Trethewey, *J. Chem. Soc., Chem. Commun.* **1976**, 827-829.
- [24] (a) G. Greiner, I. Maier, *J. Chem. Soc., Perkin Trans. 2* **2002**, 1005-1011; (b) A. P. de Silva, S. Uchiyama, in *Luminescence Applied in Sensor Science*, 1st ed. (Eds.: L. Prodi, M. Montalti, Z. Nelsi), Springer, Heidelberg, **2011**.
- [25] (a) Z. Fei, N. Kocher, C. J. Mohrschladt, H. Ihmels, D. Stalke, *Angew. Chem. Int. Ed.* **2003**, *42*, 783-787; *Angew. Chem.* **2003**, *115*, 807-811; (b) G. Schwab, Dissertation, *Göttingen*, **2008**; (c) D. Stern, Dissertation, *Göttingen*, **2009**; (d) N. Finkelmeier, Dissertation, *Göttingen*, **2013**; (e) S. Wandtke, Dissertation, *Göttingen*, **2014**.
- [26] N. Nijegorodov, R. Mabbs, D. P. Winkoun, *Spectrochim. Acta, Part A* **2003**, *59*, 595-606.
- [27] (a) *SciFinder*, 2016; Chemical Abstracts Service: Columbus, OH, (accessed Feb 03, 2016); (b) The *SciFinder* search was refined by 'document types' with the filter categories 'book', 'journal', 'letter', 'report', and 'review'.
- [28] A. Philips, *Ber. Dtsch. Chem. Ges.* **1895**, *28*, 1658-1660.

- [29] N. Beeharry, A. G. L. Di Rora, M. R. Smith, T. J. Yen, *Cancer Biol. Ther.* **2015**, *16*, 1397-1406.
- [30] A. Opitz, E. Roemer, W. Haas, H. Görls, W. Werner, U. Gräfe, *Tetrahedron* **2000**, *56*, 5147-5155.
- [31] (a) W. E. Rhine, J. Davis, G. Stucky, *J. Am. Chem. Soc.* **1975**, *97*, 2079-2085; (b) L.-J. Fan, Y. Zhang, W. E. Jones Jr., *Macromolecules* **2005**, *38*, 2844-2849.
- [32] Y. Zou, D. D. Young, A. Cruz-Montanez, A. Deiters, *Org. Lett.* **2008**, *10*, 4661-4664.
- [33] E. Campaigne, J. Ashby, *J. Heterocycl. Chem.* **1971**, *8*, 487-488.
- [34] (a) J. v. Braun, J. Nelles, *Ber. Dtsch. Chem. Ges.* **1937**, *70B*, 1760-1766; (b) N. S. Prostakov, V. I. Kuznetsov, *Chem. Heterocycl. Compd.* **1980**, *5*, 525-529; (c) A.-S. Rebstock, F. Mongin, F. Trecourt, G. Queguiner, *Org. Biomol. Chem.* **2004**, *2*, 291-295.
- [35] C. Graebe, H. Caro, *J. Prakt. Chem.* **1870**, *2*, 183-185.
- [36] (a) A. Bernthsen, *Ber. Dtsch. Chem. Ges.* **1883**, *16*, 767-769; (b) A. Bernthsen, *Liebigs Ann. Chem.* **1884**, *224*, 1-56.
- [37] (a) O. Tsuge, M. Nishinohara, M. Tashi, *Bull. Chem. Soc. Jpn.* **1963**, *36*, 1477-1485; (b) J. Joseph, E. Kuruvilla, A. T. Achuthan, D. Ramaiah, G. B. Schuster, *Bioconjugate Chem.* **2004**, *15*, 1230-1235; (c) J. Khalafy, R. H. Prager, N. M. Puspawati, *Turk. J. Chem.* **2008**, *32*, 755-763.
- [38] (a) R. Fukuda, S. Takenaka, M. Takagi, *J. Chem. Soc., Chem. Commun.* **1990**, 1028-1030; (b) E. Kikuta, M. Murata, N. Katsube, T. Koike, E. Kimura, *J. Am. Chem. Soc.* **1999**, *121*, 5426-5436; (c) K. E. Sifers, M. A. Fountain, J. R. Morrow, *Inorg. Chem.* **2014**, *53*, 11540-11551.
- [39] W. Kikuth, *Dtsch. Med. Wochenschr.* **1932**, *58*, 530-531.
- [40] Z. Ma, J. R. Choudhury, M. W. Wright, C. S. Day, G. Saluta, G. L. Kucera, U. Bierbach, *J. Med. Chem.* **2008**, *51*, 7574-7580.
- [41] J. Chiron, J.-P. Galy, *Synlett* **2003**, *15*, 2349-2350.
- [42] V. Sourdon, S. Mazoyer, V. Pique, J.-P. Galy, *Molecules* **2001**, *6*, 673-682.
- [43] (a) W. N. Lipscomb, N. Sträter, *Chem. Rev.* **1996**, *96*, 2375-2434; (b) R. McRae, P. Bagchi, S. Sumalekshmy, C. J. Fahrni, *Chem. Rev.* **2009**, *109*, 4780-4827.
- [44] (a) J.-Y. Koh, S. W. Suh, B. J. Gwag, Y. Y. He, C. Y. Hsu, D. W. Choi, *Science* **1996**, *272*, 1013-1016; (b) A. I. Bush, *Curr. Opin. Chem. Biol.* **2000**, *4*, 184-191.
- [45] (a) M. Cortesi, E. Fridman, A. Volkov, S. S. Shilstein, R. Chechik, A. Breskin, D. Vartsky, N. Kleinman, G. Kogan, E. Moriel, V. Gladyshev, M. Huszar, J. Ramon, G. Raviv, *The Prostate* **2008**, *68*, 994-1006; (b) Z. Medarova, S. K. Ghosh, M. Vangel, R. Drake, A. Moore, *Am. J. Cancer Res.* **2014**, *4*, 385-393.
- [46] (a) J. M. Berg, Y. Shi, *Science* **1996**, *271*, 1081-1085; (b) N. Wellinghausen, M. Martin, L. Rink, *Eur. J. Immunol.* **1997**, *27*, 2529-2535; (c) M. J. Salgueiro, M. Zubillaga, A. Lysionek, M. I. Sarabia, R. Caro, T. De Paoli, A. Hager, R. Weill, J. Boccio, *Nutr. Res.* **2000**, *20*, 737-755.
- [47] (a) K. Nogawa, A. Ishizaki, E. Kobayashi, *Environ. Res.* **1979**, *18*, 397-409; (b) C. Tohyama, Z. A. Shaikh, K. Nogawa, E. Kobayashi, R. Honda, *Arch. Toxicol.* **1982**, *50*, 159-166.
- [48] (a) A. Ajayaghosh, P. Carol, S. Sreejith, *J. Am. Chem. Soc.* **2005**, *127*, 14962-14963; (b) K. Ono, J. K. Klosterman, M. Yoshizawa, K. Sekiguchi, T. Tahara, M. Fujita, *J. Am. Chem. Soc.* **2009**, *131*, 12526-12527; (c) Z. Xu, J. Yoon, D. R. Spring, *Chem. Soc. Rev.* **2010**, *39*, 1996-2006; (d) H. Woo, S. Cho, Y. Han, W.-S. Chae, D.-R. Ahn, Y. You, W. Nam, *J. Am. Chem. Soc.* **2013**, *135*, 4771-4787; (e) M. Yamashina, M. M. Sartin, Y. Sei, M. Akita, S. Takeuchi, T. Tahara, M. Yoshizawa, *J. Am. Chem. Soc.* **2015**, *137*, 9266-9269.
- [49] M. S. Park, K. M. K. Swamy, Y. J. Lee, H. N. Lee, Y. J. Jang, Y. H. Moon, J. Yoon, *Tetrahedron Lett.* **2006**, *47*, 8129-8132.
- [50] H. N. Lee, K. M. K. Swamy, S. K. Kim, J.-Y. Kwon, Y. Kim, S.-J. Kim, Y. J. Yoon, J. Yoon, *Org. Lett.* **2007**, *9*, 243-246.
- [51] W. Scenger, *Principles of Nucleic Acid Structure*, Springer, New York, **1998**.
- [52] S. Szarvas, Z. Majer, P. Huszthy, B. Vermes, M. Hollósi, *Enantiomer* **2002**, *7*, 241-249.
- [53] J. Kertész, I. Móczár, A. Kormos, P. Baranyai, M. Kubinyi, K. Tóth, P. Huszthy, *Tetrahedron: Asymmetry* **2011**, *22*, 684-689.
- [54] T. Németh, S. Lévai, A. Kormos, J. Kupai, T. Tóth, G. T. Balogh, P. Huszthy, *Chirality* **2014**, *26*, 651-654.
- [55] I. Móczár, P. Huszthy, A. Mezei, M. Kádár, J. Nyitrai, K. Tóth, *Tetrahedron* **2010**, *66*, 350-358.
- [56] J. Kertész, B. Bognár, A. Kormos, I. Móczár, P. Baranyai, M. Kubinyi, T. Kálai, K. Hideg, P. Huszthy, *Tetrahedron* **2011**, *67*, 8860-8864.

- [57] Y. Wang, X. Hu, L. Wang, Z. Shang, J. Chao, W. Jin, *Sens. Actuators, B* **2011**, *156*, 126-131.
- [58] E. V. Solovyeva, L. A. Myund, G. L. Starova, E. M. Dem'yanchuk, A. A. Makarov, A. S. Denisova, *J. Mol. Struct.* **2014**, *1063*, 235-241.
- [59] E. V. Solovyeva, G. L. Starova, L. A. Myund, A. S. Denisova, *Polyhedron* **2016**, *106*, 1-9.
- [60] R. Ghosh, A. Nandi, D. K. Palit, *Phys. Chem. Chem. Phys.* **2016**, *18*, 7661-7671.
- [61] Y. Jiao, B. Zhu, J. Chen, X. Duan, *Theranostics* **2015**, *5*, 173-187.
- [62] N. Dash, A. Malakar, M. Kumar, B. B. Mandal, G. Krishnamoorthy, *Sens. Actuators, B* **2014**, *202*, 1154-1163.
- [63] A. Visscher, Master thesis, *Göttingen*, **2011**.
- [64] A. P. Krapcho, T. P. Gilmor, *J. Heterocycl. Chem.* **1998**, *35*, 669-674.
- [65] A. A. Leon, G. Daub, I. R. Silverman, *J. Org. Chem.* **1984**, *49*, 4544-4545.
- [66] (a) S. M. Duan, J. Turk, J. Speigle, J. Corbin, J. Masnovi, R. J. Baker, *J. Org. Chem.* **2000**, *65*, 3005-3009; (b) R. Brückner, *Reaktionsmechanismen, Vol. 3*, Elsevier, München, **2004**.
- [67] R. M. Acheson, *The Chemistry of Heterocyclic Compounds, Acridines*, 2nd ed., John Wiley & Sons, Toronto, **2009**.
- [68] J.-P. Galy, J. Chiron, *Synthesis* **2004**, *3*, 313-325.
- [69] K. Fukui, T. Yonezawa, C. Nagata, H. Shingu, *J. Chem. Phys.* **1954**, *22*, 1433-1442.
- [70] (a) U. Groth, L. Richter, U. Schöllkopf, *Liebigs Ann. Chem.* **1992**, *1992*, 199-202; (b) J. K. Ray, B. C. Roy, G. K. Kar, *J. Org. Chem.* **1996**, *61*, 1863-1866.
- [71] J. J. Gassensmith, E. Arunkumar, L. Barr, J. M. Baumes, K. M. DiVittorio, J. R. Johnson, B. C. Noll, B. D. Smith, *J. Am. Chem. Soc.* **2007**, *129*, 15054-15059.
- [72] G. A. Olah, R. Malhotra, S. C. Narang, *Nitration: Methods and Mechanisms*, Wiley-VCH, New York, **1989**.
- [73] C. Graebe, H. Caro, *Liebigs Ann. Chem.* **1871**, *158*, 265-281.
- [74] R. M. Acheson, *The Chemistry of Heterocyclic Compounds, Acridines*, 2nd ed., John Wiley & Sons, Toronto, **2009**, pp. 1-8.
- [75] R. M. Acheson, B. Adcock, G. M. Glover, L. E. Sutton, *J. Chem. Soc.* **1960**, 3367-3371.
- [76] K. Lehmsstedt, *Ber. Dtsch. Chem. Ges.* **1938**, *71*, 808-814.
- [77] P. Strazzolini, A. G. Giumanini, A. Runcio, *Tetrahedron Lett.* **2001**, *42*, 1387-1389.
- [78] M. J. Plater, P. Barnes, L. K. McDonald, S. Wallace, N. Archer, T. Gelbrich, P. N. Horton, M. B. Hursthouse, *Org. Biomol. Chem.* **2009**, *7*, 1633-1641.
- [79] S. M. S. Chauhan, R. Singh, Geetanjali, *Synth. Commun.* **2003**, *33*, 2899-2906.
- [80] (a) H. Rao, Y. Jin, H. Fu, Y. Jiang, Y. Zhao, *Chem.-Eur. J.* **2006**, *12*, 3636-3646; (b) X. Guo, H. Rao, H. Fu, Y. Jiang, Y. Zhao, *Adv. Synth. Catal.* **2006**, *348*, 2197-2202.
- [81] (a) K. Shimi, G. Boyer, J.-P. Finet, J.-P. Galy, *Lett. Org. Chem.* **2004**, *1*, 34-36; (b) M. Binaschi, A. Boldetti, M. Gianni, C. A. Maggi, M. Gensini, M. Bigioni, M. Parlani, A. Giolitti, M. Fratelli, C. Valli, M. Terao, E. Garattini, *ACS Med. Chem. Lett.* **2010**, *1*, 411-415.
- [82] Y. Kitahara, T. Mizuno, A. Kubo, *Tetrahedron* **2004**, *60*, 4283-4288.
- [83] L. Krause, R. Herbst-Irmer, G. M. Sheldrick, D. Stalke, *J. Appl. Cryst.* **2015**, *48*, 3-10.
- [84] P. Müller, R. Herbst-Irmer, A. L. Spek, T. R. Schneider, M. R. Sawaya, in *Crystal Structure Refinement - A Crystallographer's Guide to SHELXL*, 1st ed. (Ed.: P. Müller), Oxford University Press, New York, **2006**.
- [85] (a) H. Langhals, T. Potrawa, H. Nöth, G. Linti, *Angew. Chem. Int. Ed.* **1989**, *28*, 478-480; *Angew. Chem.* **1998**, *110*, 497-499; (b) X.-H. Bu, M.-L. Tong, J.-R. Li, H.-C. Chang, L.-J. Li, S. Kitagawa, *CrystEngComm* **2005**, *7*, 411-416; (c) B. Dong, M. Wang, C. Xu, Q. Feng, Y. Wang, *Cryst. Growth Des.* **2012**, *12*, 5986-5993; (d) M. Yamamura, S. Ikuma, T. Nabeshima, *J. Mol. Struct.* **2015**, *1093*, 59-64.
- [86] (a) A. Mukherjee, S. Tothadi, G. R. Desiraju, *Acc. Chem. Res.* **2014**, *47*, 2514-2524; (b) G. R. Desiraju, R. Parthasarathy, *J. Am. Chem. Soc.* **1989**, *111*, 8725-8726.
- [87] A. Bondi, *J. Phys. Chem.* **1964**, *68*, 441-451.
- [88] (a) A. Achari, S. Neidle, *Acta Cryst. B* **1977**, *33*, 3269-3270; (b) A. J. Adamson, Y. Archambeau, R. E. Banks, B. Beagley, *Acta Cryst. C* **1994**, *50*, 967-971.
- [89] T. Steiner, *Angew. Chem. Int. Ed.* **2002**, *41*, 48-76; *Angew. Chem.* **2002**, *114*, 50-80.

- [90] F. Karagöz, O. Güney, M. Kandaz, A. T. Bilgiçi, *J. Lumin.* **2012**, *132*, 2736-2740.
- [91] W. B. Jensen, *The Lewis Acid-Base Concepts. An Overview*, John Wiley & Sons, New York, **1980**.
- [92] (a) Y. Umezawa, S. Tsuboyama, H. Takahashi, J. Uzawa, M. Nishio, *Tetrahedron* **1999**, *55*, 10047-10056; (b) M. Nishio, Y. Umezawa, K. Honda, S. Tsuboyama, H. Suezawa, *CrystEngComm* **2009**, *11*, 1757-1788.
- [93] M. Kasha, *Radiat. Res.* **1960**, *2*, 243-275.
- [94] J. B. Birks, L. G. Christophorou, *Spectrochim. Acta* **1963**, *19*, 401-410.
- [95] B. Cadioli, E. Gallinella, C. Coulombeau, H. Jobic, G. Berthier, *J. Phys. Chem.* **1993**, *97*, 7844-7856.
- [96] M. D. Hanwell, D. E. Curtis, D. C. Lonie, T. Vandermeersch, E. Zurek, G. R. Hutchison, *J. Cheminform.* **2012**, *4*, 1-17.
- [97] M. E. Huston, K. W. Haider, A. W. Czarnik, *J. Am. Chem. Soc.* **1988**, *110*, 4460-4462.
- [98] (a) J. Hicks, E. J. Underhill, C. E. Kefalidis, L. Maron, C. Jones, *Angew. Chem. Int. Ed.* **2015**, *54*, 10000-10004; *Angew. Chem.* **2015**, *127*, 10138-10142; (b) B. Roy, A. K. Ghosh, S. Srivastava, P. D'Silva, P. S. Mukherjee, *J. Am. Chem. Soc.* **2015**, *137*, 11916-11919.
- [99] M. Laronze-Cochard, Y.-M. Kim, B. Brassart, J.-F. Riou, J.-Y. Laronze, J. Sapi, *Eur. J. Med. Chem.* **2009**, *44*, 3880-3888.
- [100] J. F. Mammone, S. K. Sharma, M. Nicol, *J. Phys. Chem.* **1980**, *84*, 3130-3134.
- [101] R. K. Haynes, S. C. Vonwiller, M. R. Luderer, in *e-EROS Encyclopedia of Reagents for Organic Synthesis*, John Wiley & Sons, **2006**.
- [102] U. Knips, F. Huber, *Z. Naturforsch.* **1983**, *38b*, 434-436.
- [103] (a) A. Gafni, L. Brand, *Chem. Phys. Lett.* **1978**, *58*, 346-350; (b) J. R. Lakowicz, A. Balter, *Biophys. Chem.* **1982**, *16*, 117-132.
- [104] D. D. Pant, G. C. Joshi, H. B. Tripathi, *J. Phys.* **1986**, *27*, 161-170.
- [105] (a) P. Gangola, N. B. Joshi, D. D. Pant, *Chem. Phys. Lett.* **1979**, *60*, 329-331; (b) M. K. Sarangi, D. Dey, S. Basu, *J. Phys. Chem. A* **2011**, *115*, 128-135.
- [106] (a) M. Kasha, *J. Chem. Phys.* **1952**, *20*, 71-74; (b) A. Martin, R. Narayanaswamy, *Sens. Actuators, B* **1997**, *39*, 330-333.
- [107] J. R. Lakowicz, *Principles of Fluorescence Spectroscopy* 3rd ed., Springer, New York, **2006**, pp. 205-235.
- [108] M. Hofmann, H. Graener, *Chem. Phys.* **1996**, *206*, 129-137.
- [109] F. Neese, *WIREs Comput. Mol. Sci.* **2012**, *2*, 73-78.
- [110] V. P. Zvolinskii, N. I. Nizhegorodov, V. V. Nikiforov, V. V. Dorogov, A. N. Gusarov, *Sov. Phys. J.* **1977**, *20*, 701-706.
- [111] A. Visscher, S. Bachmann, C. Schnegelsberg, T. Teuteberg, R. A. Mata, D. Stalke, *Dalton Trans.* **2016**, *45*, 5689-5699.
- [112] I. Negrón-Encarnación, R. Arce, M. Jiménez, *J. Phys. Chem. A* **2005**, *109*, 787-797.
- [113] J. N. Murrell, *Proc. Phys. Soc. A* **1955**, *68*, 969-975.
- [114] P. Nikolov, H. Görner, *J. Photochem. Photobiol., A* **1996**, *101*, 137-144.
- [115] B. Ma, F. Zeng, X. Li, S. Wu, *Chem. Commun.* **2012**, *48*, 6007-6009.
- [116] (a) S. Karuppanan, J.-C. Chambron, *Chem. Asian J.* **2011**, *6*, 964-984; (b) M. Shellaiah, Y.-H. Wu, A. Singh, M. V. Ramakrishnam Raju, H.-C. Lin, *J. Mat. Chem. A* **2013**, *1*, 1310-1318.
- [117] H. Friebolin, *Basic One- and Two-Dimensional NMR Spectroscopy*, 5th ed., Wiley-VCH Verlag, Weinheim, **2011**.
- [118] J. Keeler, *Understanding NMR Spectroscopy*, 2nd ed., John Wiley & Sons, **2010**, pp. 300-303526.
- [119] T. Steiner, *Acta Cryst. B* **1998**, *54*, 456-463.
- [120] G. A. Jeffrey, *An Introduction to Hydrogen Bonding*, Oxford University Press, Oxford, **1997**.
- [121] Y. Wang, L. Shi, H. S. Sun, Z. Shang, J. Chao, W. Jin, *J. Lumin.* **2013**, *139*, 16-21.
- [122] HORIBA, *FluoroMax-4 Spectrofluorometer Operation Manual* **2006**, 2.2-2.6.
- [123] G. A. Carlson, J. P. McReynolds, F. H. Verhoek, *J. Am. Chem. Soc.* **1945**, *67*, 1334-1339.
- [124] R. D. Shannon, *Acta Cryst. A* **1976**, *32*, 751-767.
- [125] H. Irving, R. J. P. Williams, *J. Chem. Soc.* **1953**, 3192-3210.

- [126] (a) V. Balzani, *Tetrahedron* **1992**, *48*, 10443-10514; (b) L. Fabbrizzi, M. Licchelli, P. Pallavicini, A. Perotti, A. Taglietti, D. Sacchi, *Chem.-Eur. J.* **1996**, *2*, 75-82; (c) V. V. Volchkov, V. L. Ivanov, B. M. Uzhinov, *J. Fluoresc.* **2009**, *20*, 299-303.
- [127] (a) J. D. Hoeschele, J. E. Turner, M. W. England, *Sci. Total Environ.* **1991**, *109/110*, 477-492; (b) R. M. Izatt, K. Pawlak, J. S. Bradshaw, R. L. Bruening, *Chem. Rev.* **1991**, *91*, 1721-2085.
- [128] (a) C. Gunanathan, L. J. W. Shimon, D. Milstein, *J. Am. Chem. Soc.* **2009**, *131*, 3146-3147; (b) X. Ye, P. N. Plessow, M. K. Brinks, M. Schelwies, T. Schaub, F. Rominger, R. Paciello, M. Limbach, P. Hofmann, *J. Am. Chem. Soc.* **2014**, *136*, 5923-5929.
- [129] Cambridge Structural Database, v5.37 (November 2015), Cambridge, UK, 2015.
- [130] U. Flierler, D. Stalke, in *Structure and Bonding*, Vol. 146 (Ed.: D. Stalke), Springer, Berlin, New York, **2012**, pp. 1-20.
- [131] (a) A. D. Becke, *Phys. Rev. A* **1988**, *38*, 3098-3100; (b) C. Lee, W. Yang, R. G. Parr, *Phys. Rev. B* **1988**, *37*, 785-789; (c) A. D. Becke, *J. Chem. Phys.* **1993**, *98*, 5648-5652; (d) P. J. Stephens, F. J. Devlin, C. F. Chabalowski, M. J. Frisch, *J. Phys. Chem.* **1994**, *98*, 11623-11627; (e) F. Weigend, R. Ahlrichs, *Phys. Chem. Chem. Phys.* **2005**, *7*, 3297-3305; (f) S. Grimme, J. Antony, S. Ehrlich, H. Krieg, *J. Chem. Phys.* **2010**, *132*, 154104-154119.
- [132] (a) J. P. Foster, F. Weinhold, *J. Am. Chem. Soc.* **1980**, *102*, 7211-7218; (b) A. E. Reed, R. B. Weinstock, F. Weinhold, *J. Chem. Phys.* **1985**, *83*, 735-746; (c) E. D. Glendening, J. K. Badenhop, A. E. Reed, J. E. Carpenter, J. A. Bohmann, C. M. Morales, F. Weinhold, *GenNBO 5.9*, University of Wisconsin, Madison, **2009**.
- [133] A. E. Reed, L. A. Curtiss, F. Weinhold, *Chem. Rev.* **1988**, *88*, 899-926.
- [134] C. Maaß, D. M. Andrada, R. A. Mata, R. Herbst-Irmer, D. Stalke, *Inorg. Chem.* **2013**, *52*, 9539-9548.
- [135] A. Klamt, G. Schüürmann, *J. Chem. Soc., Perkin Trans. 2* **1993**, 799-805.
- [136] R. Neufeld, D. Stalke, *Chem. Sci.* **2015**, *6*, 3354-3364.
- [137] (a) H. Gornitzka, D. Stalke, *Eur. J. Inorg. Chem.* **1998**, 311-317; (b) T. E. Wood, B. Berno, C. S. Beshara, A. Thompson, *J. Org. Chem.* **2006**, *71*, 2964-2971.
- [138] M. Karplus, *J. Am. Chem. Soc.* **1963**, *85*, 2870-2871.
- [139] X. Lang, L. Li, Y. Chen, Q. Sun, Q. Wu, F. Liu, C. Tan, H. Liu, C. Gao, Y. Jiang, *Bioorg. Med. Chem.* **2013**, *21*, 4170-4177.
- [140] (a) P. Job, *Ann. Chim. Appl.* **1928**, *9*, 113-203; (b) J. S. Renny, L. L. Tomasevich, E. H. Tallmadge, D. B. Collum, *Angew. Chem. Int. Ed.* **2013**, *52*, 11998-12013; *Angew. Chem.* **2013**, *125*, 12218-12234.
- [141] C. Steinmetzger, Master thesis, *Göttingen*, **2015**.
- [142] P. Molz, H. J. Skrzypczyk, H. Luebbers, H. Strecker, G. Schnorr, T. Kinkel, Ger. Offen. DE 3628573, **1988**; *Chem. Abstr.* **1988**, 109: 89359.
- [143] O. S. Radchenko, E. N. Sigida, N. N. Balaneva, P. S. Dmitrenok, V. L. Novikov, *J. Heterocycl. Chem.* **2011**, *48*, 209-214.
- [144] L. Liu, Master thesis, *Göttingen*, **2015**.
- [145] C.-J. J. Wu, C. Xue, Y.-M. Kuo, F.-T. Luo, *Tetrahedron* **2005**, *61*, 4735-4741.
- [146] (a) W. Schlenk, A. Thal, *Ber. Dtsch. Chem. Ges.* **1913**, *46*, 2840-2854; (b) T. T. Tidwell, *Angew. Chem. Int. Ed.* **2001**, *40*, 331-337; *Angew. Chem.* **2001**, *113*, 343-349; (c) Georg-August-University Göttingen, *Virtuelles Labor*, www.stalke.chemie.uni-goettingen.de/virtuelles_labor/en.html; access at 23/03/2016.
- [147] A. Schäfer, H. Horn, R. Ahlrichs, *J. Chem. Phys.* **1992**, *97*, 2571-2577.
- [148] S. Grimme, S. Ehrlich, L. Goerigk, *J. Comput. Chem.* **2011**, *32*, 1456-1465.
- [149] (a) A. D. Becke, E. R. Johnson, *J. Chem. Phys.* **2005**, *123*, 154101; (b) E. R. Johnson, A. D. Becke, *J. Chem. Phys.* **2005**, *123*, 024101; (c) E. R. Johnson, A. D. Becke, *J. Chem. Phys.* **2006**, *124*, 174104.
- [150] E. F. Valeev, LIBINT: A library for the evaluation of molecular integrals of many-body operators over Gaussian functions, Version 2.1.0 (beta), 2014; <http://libint.valeev.net/>.
- [151] K. Eichkorn, F. Weigend, O. Treutler, R. Ahlrichs, *Theor. Chem. Acc.* **1997**, *97*, 119-124.
- [152] D. Andrae, U. Häußermann, M. Dolg, H. Stoll, H. Preuß, *Theor. Chim. Acta* **1990**, *77*, 123-141.
- [153] (a) E. J. Baerends, D. E. Ellis, P. Ros, *Chem. Phys.* **1973**, *2*, 41-51; (b) J. L. Whitten, *J. Chem. Phys.* **1973**, *58*, 4496-4501; (c) F. Neese, F. Wennmohs, A. Hansen, U. Becker, *Chem. Phys.* **2009**, *356*, 98-109.
- [154] J. R. Lakowicz, *Principles of Fluorescence Spectroscopy* 3rd ed., Springer, New York, **2006**, pp. 27-61.
- [155] HORIBA, FluorEssence v3.0, Edison, 2008.

- [156] H. J. Svec, *Int. J. Mass Spectrom. Ion Processes* **1985**, *66*, 3-29.
- [157] J. F. d. l. Mora, G. J. Van Berkel, C. G. Enke, R. B. Cole, M. Martinez-Sanchez, J. B. Fenn, *J. Mass Spectrom.* **2000**, *35*, 939-952.
- [158] H. E. Gottlieb, V. Kotlyar, A. Nudelman, *J. Org. Chem.* **1997**, *62*, 7512-7515.
- [159] (a) T. Kottke, D. Stalke, *J. Appl. Cryst.* **1993**, *26*, 615-619; (b) T. Kottke, R. J. Lagow, D. Stalke, *J. Appl. Cryst.* **1996**, *29*, 465-468; (c) D. Stalke, *Chem. Soc. Rev.* **1998**, *27*, 171-178.
- [160] T. Schulz, K. Meindl, D. Leusser, D. Stern, J. Graf, C. Michaelsen, M. Ruf, G. M. Sheldrick, D. Stalke, *J. Appl. Cryst.* **2009**, *42*, 885-891.
- [161] Bruker AXS Inc., SAINT v8.30C, Bruker Apex CCD, SAINT v8.30C, Madison, WI, USA, 2013.
- [162] G. M. Sheldrick, XPREP in SHELXTL 2014/2, Madison, WI, USA, 2014.
- [163] G. M. Sheldrick, *Acta Cryst. A* **2015**, *71*, 3-8.
- [164] G. M. Sheldrick, SHELXL in SHELXTL v2014/7, Madison, WI, USA, 2014.
- [165] C. B. Huebschle, G. M. Sheldrick, B. Dittrich, *J. Appl. Cryst.* **2011**, *44*, 1281-1284.
- [166] (a) F. Hirshfeld, *Acta Cryst. A* **1976**, *32*, 239-244; (b) K. N. Trueblood, J. D. Dunitz, *Acta Cryst. B* **1983**, *39*, 120-133.
- [167] G. M. Sheldrick, XP in SHELXTL v2014/7, Madison, WI, USA, 2014.
- [168] M. Tretiakov, Y. G. Shermolovich, A. P. Singh, P. P. Samuel, H. W. Roesky, B. Niepötter, A. Visscher, D. Stalke, *Dalton Trans.* **2013**, *42*, 12940-12946.
- [169] B. Milde, M. Leibelng, A. Hecht, P. G. Jones, A. Visscher, D. Stalke, J. Grunenberg, D. B. Werz, *Chem.-Eur. J.* **2015**, *21*, 16136-16146.

CURRICULUM VITAE

Name: Arne Visscher Geburtsdatum: 03.02.1986
Anschrift: Kreuzberggring 68 Geburtsort: Burgwedel
37075 Göttingen Familienstand: verheiratet
Email: avisscher@gwdg.de



AKADEMISCHE AUSBILDUNG

01/2011 – heute **Promotion** im Arbeitskreis von Prof. Dr. Dietmar Stalke, Institut für Anorganische Chemie, Georg-August-Universität Göttingen:
„*Fluorescence Studies of Amine-substituted Azaanthracene Metal Complexes*“
10/2009 – 11/2011 Studium der Chemie an der Georg-August-Universität Göttingen,
Abschluss als M.Sc. mit der Masterarbeit „*Azaanthracene als Chemosensoren*“ (Note: 1,0)
10/2006 – 08/2009 Studium der Chemie an der Georg-August-Universität Göttingen,
Abschluss als B.Sc. mit der Bachelorarbeit „*Von lithiierten Phenanthrenen zu Phosphanen*“ (Note: 1,0)

ERFAHRUNG AUßERHALB UNIVERSITÄRER FORSCHUNG

01/2012 – 06/2015 Wissenschaftlicher Mitarbeiter am Institut für Anorganische Chemie, Georg-August-Universität Göttingen
10/2009 – 06/2015 Betreuung von Praktika und Durchführung von Seminaren für Studierende mit Haupt- oder Nebenfach Chemie
11/2012 – 03/2014 Gewählter Sprecher der Promovierenden im Vorstand von GAUSS (*Georg-August University School of Science*)
03/2012 – 03/2014 Gewählter Sprecher der Promovierenden der Fakultät für Chemie
10/2013 Experimentelle Messungen an Röntgendiffraktometern, Firma *Incoatec*, Geesthacht
04/2011 – 03/2012 Planung, Projektleitung und Umsetzung des Lehrvideoprojekts „*Virtuelles Labor*“ http://www.stalke.chemie.uni-goettingen.de/virtuelles_labor/nmr/de.html

ABITUR UND ZIVILDIENTST

05/2006 – 07/2006	Angestellter bei der gGIS (gemeinnützige Gesellschaft für integrative Sozialdienste) in Hannover
08/2005 – 05/2006	Zivildienst bei der gGIS (gemeinnützige Gesellschaft für integrative Sozialdienste) in Hannover
08/1998 – 07/2005	Abitur am Gymnasium Isernhagen (Note: 2,1)

ZUSATZQUALIFIKATIONEN UND AUSZEICHNUNGEN

07/2015	Erhalt des Lehrpreises für die „ <i>beste nicht-selbstständige Lehre im Institut für Anorganische Chemie</i> “
09/2013	Seminarteilnahme „ <i>Interkulturelle Zusammenarbeit</i> “
12/2012	Teilnahme am Hochschuldidaktikkurs „ <i>Meine Rolle als Lehrender</i> “
06/2012 – 05/2015	Durchführung von Einkristall-Diffraktionsexperimenten von Service-Partnern des Arbeitskreises
06/2008	Erhalt des Sachkundenachweises nach §5 ChemVerbotsV

METHODEN UND FACHKENNTNISSE

Analytik	Röntgendiffraktometrie, 1D/2D NMR-, IR-, UV-vis- und Fluoreszenzspektroskopie, Massenspektrometrie
Labor	(Metall-)Organische Synthese unter Inertbedingungen, Optimierungsverfahren, chromatographische Trennmethoden

SPRACH- UND EDV-KENNTNISSE

Sprachkenntnisse	Deutsch: Muttersprache
	Englisch: fließend in Wort und Schrift
	Französisch: Grundkenntnisse (A1)
EDV-Kenntnisse	sicherer Umgang mit MS Office
	sicherer Umgang mit Chemie Programmen (ChemDraw, Origin, MestreNova, TopSpin)
	sicherer Umgang mit kristallographischen Programmen (APEXII, SHELX Suite, Mercury)

TEILNAHME AN KONFERENZEN

- 10/2014 9. Treffen des Center for Materials Crystallography, Århus (DK);
Vortrag: "Sensing Metal Ions with Acridine Amines"
- 03/2014 8. Treffen des Center for Materials Crystallography, Göttingen
- 02/2014 Central European Conference on Photochemistry, Bad Hofgastein
(AU); Posterpräsentation: „New Acridinyl Amines as Potential
Chemosensors“
- 11/2012 6. Treffen des Center for Materials Crystallography, Göttingen
- 10/2012 Workshop der Firma Sartorius GmbH, Göttingen; Posterpräsentation:
„Virtuelles Labor“
- 09/2012 16. Vortragstagung der Wöhler-Vereinigung, Göttingen;
Posterpräsentation: „Virtuelles Labor“
- 07/2012 5. JungChemikerForum der GDCh, Göttingen; Posterpräsentation
- 06/2011 3. Treffen des Center for Materials Crystallography, Århus (DK)
- 04/2010 1. Treffen des Center for Materials Crystallography, Århus (DK)

VERÖFFENTLICHUNGEN

A. Visscher, S. Bachmann, C. Schnegelsberg, T. Teuteberg, R. Mata, D. Stalke „Highly selective and sensitive fluorescence detection of Zn^{2+} and Cd^{2+} ions by using an acridine sensor” in *Dalton Trans.* **2016**, 45, 5689-5699.

N. Finkelmeier, A. Visscher, S. Wandtke, R. Herbst-Irmer, D. Stalke „Deprotonation of 9-Methylantracene under Mild Conditions to give a Localized Carbanion” in *Chem. Commun.* **2016**, 52, 5440-5442.

B. Milde, M. Leibelng, A. Hecht, P. G. Jones, A. Visscher, D. Stalke, J. Grunenberg, D. B. Werz „Oligoene-Based π -Helicenes or Dispiranes? Winding up Oligoene Chains by a Multiple Carbopalladation/Stille/(Electrocyclization) Cascade” in *Chem. Eur. J.* **2015**, 21, 16136-16146.

M. Tretiakov, Y. G. Shermolovich, A. P. Singh, P. P. Samuel, H. W. Roesky, B. Niepötter, A. Visscher, D. Stalke „Lewis-base stabilized diiodine adducts with N-heterocyclic chalcogenamides” in *Dalton Trans.* **2013**, 42, 12940-12946.

Göttingen, den 26.04.2016



